



HAL
open science

Ion diffusion mechanisms derived from atomic simulations in fast ion conductors

Chenyi Li

► **To cite this version:**

Chenyi Li. Ion diffusion mechanisms derived from atomic simulations in fast ion conductors. Materials and structures in mechanics [physics.class-ph]. Université Paris-Saclay, 2020. English. NNT : 2020UPAST044 . tel-04565786

HAL Id: tel-04565786

<https://theses.hal.science/tel-04565786>

Submitted on 2 May 2024

HAL is a multi-disciplinary open access archive for the deposit and dissemination of scientific research documents, whether they are published or not. The documents may come from teaching and research institutions in France or abroad, or from public or private research centers.

L'archive ouverte pluridisciplinaire **HAL**, est destinée au dépôt et à la diffusion de documents scientifiques de niveau recherche, publiés ou non, émanant des établissements d'enseignement et de recherche français ou étrangers, des laboratoires publics ou privés.

Mécanismes de diffusion d'ions dérivés de simulations atomiques dans des conducteurs superioniques

Thèse de doctorat de l'Université Paris-Saclay

École doctorale n° 573, Approches interdisciplinaires:
fondements, applications et innovation (INTERFACES)
Spécialité de doctorat: Physique
Unité de recherche : Université Paris-Saclay, CentraleSupélec, CNRS,
Laboratoire SPMS, 91190, Gif-sur-Yvette, France)
Réfèrent : CentraleSupélec

**Thèse présentée et soutenue à Gif-sur-Yvette, le 30
Novembre 2020, par**

Chenyi LI

Composition du Jury

Rose Nöelle VANNIER Professeur, Ecole Nationale Supérieure de Chimie de Lille	Présidente
Mathieu SALANNE Professeur, Sorbonne Université	Rapporteur
Xavier ROCQUEFELTE Professeur, Université de Rennes 1	Rapporteur
Emilie AMZALLAG Enseignant-Chercheur, SP2M, Université Paris-Saclay	Examinatrice
Guilhem DEZANNEAU Directeur du laboratoire SPMS, Université Paris-Saclay	Directeur de thèse
Charles PAILLARD Maître de conférences, Université Paris- Saclay	Invité

ACKNOWLEDGEMENTS

To begin with, I would express my deepest and sincere appreciation to my supervisor Dr. Guilhem Dezanneau. I am so so so fortunate to work with you. I will never forget that when I was in the hardest time, it is you that warm me and give me the opportunity to continue research. You are so knowledgeable, patient, comprehensible, and warm-hearted. There is a saying in Chinese called “nobleman in life”. You are my nobleman in my life. Thank you, Guilhem, for everything, for your endless patience in guiding me, for your faith and support on me, for your comprehension and invaluable help for me...I really feel sorry I will leave you and our lab.

I would like to thank all the members of the jury. I would like to thank M. Mathieu Salanne and M. Xavier Rocquefelte for accepting to read this thesis and to be rapporteurs. I would like to thank Mme. Rose Noëlle Vannier for accepting to be president. I also thank Mme. Emilie Amzallag and M. Charles Paillard for agreeing to attend the presentation of this work. I would also thank M. Mathieu Salanne again for participating my mini-soutenance and your kind encouragement.

I want to thank Mme. Suzanne Thuron and Mme. Pascale le Gall. Thank you, Suzanne, for consistently helping me with the paperwork. I always feel warm and happy chatting with you. I am also very grateful to Mme. Pascale le Gall for her great help and advice during my most difficult period. I am also very thankful to M. Yves Dumont for your kind attention and encouragement.

I would thank all our SPMS laboratory members for all the marvelous memories we have together. I am grateful to M. Hichem Dammak and Charles Paillard for the enlightening discussions on our articles. I would also thank M. Igor Kornev for the help about VASP. I am impressed by M. Brahim Dkhil for the inspiring courses and his jokes. I was touched by Christine Vinée-Jacquín for your thoughtful attention and help. I would also acknowledge Céline Freydier for all the works you do for me. I would appreciate Fabienne Karolak for the happy lunchtime every day. I would appreciate Agnès Benard for the professional informatic supports. I am grateful for Christine

Bogicevic for her kind help in experiments at the University Paris-Sud. I am also grateful to Pascale Salvini for her patience with the complicated reimbursement problems. And also many great thanks to Pascale Gemeiner, Nicolas Guiblin, Vincent Boemare, Thierry Martin, Claire Roussel... Please forgive my plain language, but it is the true voice from the bottom of my heart. *No matter where I am, I would always send my best wishes to the SPMS family and wish you all healthy, happy forever.*

I would thank all the SPMS friends, desiree, vitoria, cintia, charles, rossen, henri, halyna, yang, xiaofei, zeyin, xianwu, hainan, zechao, jiacheng, shenglan, minghai, jingye, milad, daniel, for your company and our friendship. Bon courage, everyone!

I am deeply grateful to all my family and friends who stay far away from me. Your loves and encouragements are the sources of my strength.

Five years have passed quickly. France has become my second home. Five years of Ph.D. career has made me more mature, calmer, more optimistic, and more confident to face my future life. In the past five years, I have met too many lovely people and too many unforgettable things. The five years of Ph.D. study time is my life's wealth and will be memorized forever.

Abstract

The development of new types of ion conductors with high conductivity may have a significant impact on the emergence a new generation of electrochemical devices. This is particularly true for hydrogen technologies, which are expected to play a major role in our society in the near future. The understanding of ionic conductors has largely benefited from progress in both simulation and experiments in the last years. Simulation can, for instance, reasonably predict the diffusion path of moving ions in materials, evaluate diffusion coefficient, and detect potential anisotropic of diffusion. Therefore, simulations can guide materials developers efficiently to identify diffusion bottlenecks and design new formulations. Within this context, the main purpose of this thesis is to study the anion diffusion mechanism of various materials by using molecular dynamics simulation and first-principles calculations. Our objective is also to propose original tools for extracting all subtleties of simulations to provide a deeper understanding of the atomic-scale mechanisms.

The research objects at the center of this thesis are a variety of ion conductors, among which one, NdBaInO_4 , can be applied to Solid Oxide Fuel Cells. We also focus on a new family of hydride ion conductors, namely the LaHO family and the $\text{LaH}_{3-2x}\text{O}_x$ family. In this last case, the potential application is still to be explored more deeply. Concerning methodological developments, we proposed two classification methods for processing molecular dynamics ion trajectories, namely the convex hull classification method and a DBSCAN machine learning algorithm, which can associate the trajectory of each ion efficiently to the crystallographic sites. Furthermore, other relevant information is deduced from this analysis, such as the diffusion paths, the occupancy rates of all sites, the jumps rates, and the residence time analysis. These two methods are simple and effective and can be applied to all ion conductors.

After a general introduction on the study of diffusion mechanisms, we present two chapters dealing with the influence of aliovalent doping in NdBaInO_4 . In chapter 2, we study $\text{Nd}_{1-x}\text{AE}_x\text{BaInO}_{4-x/2}$ ($\text{AE} = \text{Ca}, \text{Sr}, \text{Ba}$) and we determine precisely the oxygen vacancy diffusion mechanism. In chapter 3, we suggest that the oxygen diffusion in

donor-doped $\text{NdBaIn}_{1-x}\text{M}_x\text{O}_{4+x/2}$ ($\text{M}=\text{Ti}, \text{Zr}$) is based on an interstitialcy diffusion mechanism. In chapter 4, firstly, we calculated the crystal structures and the elastic tensors of the six materials $\alpha\text{-LaHO}$, $\beta\text{-LaHO}$, $\gamma\text{-LaHO}$, $\delta\text{-LaHO}$, La_2O_3 , and LaH_3 through first-principle calculations. Secondly, we created a new force field for the La-H-O system by fitting DFT information. The new-born force fields were further adopted to explore the diffusion mechanism of the two most stable forms in the LaHO family ($\alpha\text{-LaHO}$, $\beta\text{-LaHO}$). The results show that the force field provides important information about diffusion pathways in both materials. This force field potentially provides a powerful research tool for lanthanide oxyhydrides. In chapter 5, we studied the $\text{LaH}_{3-2x}\text{O}_x$ family based on the interatomic potentials developed during chapter 4. We prove that the incorporation of oxygen ions strongly affects the hydride ion diffusion mechanism, making it highly anisotropic. Finally, chapter 6 summarizes the most relevant conclusions derived in this work.

Keywords: Molecular dynamic simulation; DFT; Oxygen-ion conductors; Oxyhydrides; Ion diffusion mechanism.

Résumé

Le développement de nouveaux types de conducteurs d'ions à haute conductivité pourrait avoir un impact significatif sur l'émergence d'une nouvelle génération de dispositifs électrochimiques. Cela est particulièrement vrai pour les technologies de l'hydrogène, qui devraient jouer un rôle majeur dans notre société dans un avenir proche. La compréhension des conducteurs ioniques a déjà largement bénéficié des progrès réalisés ces dernières années, tant sur le plan théorique que sur le plan expérimental. Les simulations, par exemple, de prédire raisonnablement le chemin de diffusion des ions mobiles dans le matériau, d'évaluer le coefficient de diffusion et l'anisotropie éventuelle de la diffusion. Par conséquent, les simulations peuvent guider efficacement les concepteurs de matériaux pour identifier les goulets d'étranglement du phénomène de diffusion et pour concevoir de nouvelles formulations. Dans ce contexte, l'objectif principal de cette thèse est d'étudier le mécanisme de diffusion anionique dans divers matériaux en utilisant la simulation par dynamique moléculaire et les calculs *ab initio*. Notre objectif est également de proposer des outils originaux permettant d'extraire toutes les subtilités des simulations afin de mieux comprendre les mécanismes à l'échelle atomique.

Les objets de recherche au cœur de cette thèse sont une variété de conducteurs ioniques, parmi lesquels NdBaInO_4 pouvant être appliqué aux piles à combustible à oxyde solide. Nous nous concentrons également sur deux nouvelles familles de conducteurs par ions hydrures, à savoir la famille LaHO et la famille $\text{LaH}_{3-2x}\text{O}_x$. Dans ces derniers cas, l'application potentielle doit encore être étudiée plus en profondeur. En ce qui concerne les développements méthodologiques, nous avons proposé deux méthodes de classification pour le traitement des trajectoires des ions en dynamique moléculaire, à savoir la méthode de classification de l'enveloppe convexe et un algorithme d'apprentissage machine DBSCAN, qui peuvent associer efficacement la trajectoire de chaque ion aux différents sites cristallographiques. En outre, d'autres informations pertinentes sont déduites de cette analyse, telles que les trajectoires de diffusion, les taux d'occupation de tous les sites, les taux de sauts et l'analyse du temps de séjour. Ces

deux méthodes sont simples et efficaces et peuvent être appliquées à tous les conducteurs ioniques.

Après une introduction générale sur l'étude des mécanismes de diffusion, nous présentons deux chapitres traitant de l'influence du dopage aliovalent dans la phase NdBaInO_4 . Dans le chapitre 2, nous étudions les composés $\text{Nd}_{1-x}\text{AE}_x\text{BaInO}_{4-x/2}$ ($\text{AE} = \text{Ca}, \text{Sr}, \text{Ba}$) et nous déterminons précisément le mécanisme de diffusion de la lacune d'oxygène. Dans le chapitre 3, nous suggérons que la diffusion de l'oxygène dans les composés $\text{NdBaIn}_{1-x}\text{M}_x\text{O}_{4+x/2}$ ($\text{M}=\text{Ti}, \text{Zr}$) dits « dopé donneur » est basée sur un mécanisme de diffusion interstitielle. Dans le chapitre 4, nous avons tout d'abord calculé les structures cristallines et les tenseurs élastiques des six matériaux α -LaHO, β -LaHO, γ -LaHO, δ -LaHO, La_2O_3 et LaH_3 par des calculs de premier principe. Ensuite, nous avons créé un nouveau champ de force pour le système La-H-O en ajustant les informations issues des calculs DFT. Les nouveaux champs de force créés ont été adoptés pour explorer le mécanisme de diffusion des deux formes les plus stables de LaHO (α -LaHO, β -LaHO). Les résultats de dynamique moléculaire fournissent des informations importantes sur les chemins et mécanismes de diffusion dans ces deux matériaux. Par ailleurs, le champ de force développé fournit potentiellement un outil de recherche puissant pour d'autres oxyhydrides de lanthanides. Au chapitre 5, nous avons étudié la famille $\text{LaH}_{3-2x}\text{O}_x$ en nous basant sur les potentiels interatomiques développés au chapitre 4. Nous prouvons que l'incorporation d'ions oxygène affecte fortement le mécanisme de diffusion des ions hydrides, le rendant hautement anisotrope. Enfin, le chapitre 6 résume les conclusions les plus pertinentes tirées de ce travail.

Mots clés: dynamique moléculaire; DFT; Conducteurs d'ions oxygène; Oxyhydrides; Mécanisme de diffusion ionique.

Contents

Chapter I Introduction.....	5
I.1 Diffusion mechanisms in fast ion conductors	5
I.1.1 Interstitial Mechanism.....	5
I.1.2 Vacancy Mechanism.....	7
I.1.3 Collective Mechanisms.....	9
I.1.4 Interstitialcy Mechanism.....	10
I.2 Computational methods for detecting diffusion mechanisms in fast ion conductors	11
I.2.1 Molecular dynamic simulations for diffusion mechanism.....	11
I.2.1.1 Molecular dynamic simulation (MD)	11
I.2.1.2 Data processing method for MD simulation	12
I.2.1.2.1 Ion density map	12
I.2.1.2.2 Local cation environment analysis.....	13
I.2.1.2.3 K-means clustering algorithm	15
I.2.2 Density functional theory (DFT) for diffusion mechanism.....	17
I.2.2.1 Regular NEB and climbing image NEB method	18
I.3 Several fast ion conductors and their diffusion mechanisms	20
I.3.1.2 Diffusion mechanisms of oxygen ion conductors in SOFC cathodes.....	21
I.3.1.2.1 Perovskite crystal structure $ABO_{3-\delta}$	21
I.3.1.2.2 Ruddlesden Popper (RP) series of layered oxides ($A_{n+1}B_nO_{3n+1}$).....	22
I.3.1.2.3 Double perovskites ($AA'B_2O_{5+\delta}$)	23
I.3.1.2.4 layered cobaltites	25

I.3.2 Proton conductors	26
I.4 Objective and outline	28
I.5 Reference	30
Chapter II Oxygen diffusion mechanism in acceptor-doped NBIO	43
II.1 Introduction	44
II.2 Methods	46
II.2.1 MD simulation details	47
II.2.2 Data processing methods	48
II.2.2.1 Producing one complete information cell	48
II.2.2.2 Classification methods.....	50
II.2.2.2.1 Convex hull classification method (CHC).....	50
II.2.2.2.2 Density-based spatial clustering of applications with noise (DBSCAN)	51
II.3 Results and discussions	53
II.4 Conclusions	66
II.5 Notes and references	68
II.6 Supporting information	73
Chapter III oxygen diffusion mechanism in donor-doped NBIO	85
III.1 Introduction	86
III.2 Methods	87
III.2.1 Bond valence summation (BVS).....	87
III.2.2 Molecular dynamic simulation.....	88
III.2.3 Density-based spatial clustering of applications with noise (DBSCAN).....	89
III.3 Results and discussions	90
III.4 Conclusions	100
III.5 Notes and references	100

III.6 Supporting information	105
Chapter IV Hydride diffusion mechanism in LaHO family ...	111
IV.1 Introduction.....	112
IV.2 Computational techniques	114
IV.2.1 First-principle calculation	114
IV.2.2 Derivation of Interatomic potentials.....	115
IV.2.3 Molecular dynamic simulation	117
IV.3 Results and discussion	118
IV.3.1 General results of MD simulations in α -LaHO and β - LaHO phases	118
IV.3.2 Hydride diffusion mechanism in non-defective α - LaHO	120
IV.3.3 Hydride diffusion mechanism in non-defective β - LaHO	128
IV.3.4 Influence of defects on hydride diffusion mechanisms in α and β -LaHO.....	131
IV.4 Conclusion	134
IV.5 Notes and references	135
IV.6 Supporting information.....	141
Chapter V Hydride diffusion mechanism in $\text{LaH}_{3-2x}\text{O}_x$	163
V.1 Introduction	164
V.2 Molecular dynamic simulation	165
V.3 Results and discussions.....	167
V.4 Conclusion.....	176
V.5 Notes and references	177
V.6 Supporting information	179
Chapter VI General Conclusion.....	183

Chapter I Introduction

Fast ion conductors, also named as superionic conductors, are solids with high ionic conductivities. The value of the conductivity of one fast ion conductor is in the range 10^{-3} to 10^1 S cm⁻¹, which is even close to the value of ionic solids at the melting point. For comparison, Cu at room temperature has an electronic conductivity of 6×10^6 S cm⁻¹, and Alkali halide crystals near the melting point have a 10^{-4} S cm⁻¹ ionic conductivity.[1]

Fast ion conductors usually meet several conditions. Firstly, the mobile ions are usually light, but not necessarily small, and have a low formal charge, *e.g.*, H⁺ and O²⁻. Secondly, the lattice structure should present a structure that favours ion diffusion *i.e.* short jump distance and highly symmetrical pathways or highly open structures. Thirdly, the elements of fast ion conductors would ideally be inexpensive and would be obtained easily, this to favour their use in applications such as Li-ion batteries or Solid Oxide Fuel Cells.[1] Fast ion conductors can be classified in different ways, considering either the nature of mobile ions (oxide ion, proton, hydride), the type of structure (fluorite, perovskite, pyrochlore,...) or the type of applications (fuel cells, electrolysis cells, sensors, ...). Another interesting viewpoint consists of classifying the fast ion conductors by considering the ion diffusion mechanism, as explained here.[2]

I.1 Diffusion mechanisms in fast ion conductors

The diffusion mechanisms in fast ion conductors depend on many factors, such as the crystal structure, the size and chemical properties of the diffusing and host atoms, and the type and amount of defects. The diffusion of atoms usually occurs via the jumps of the diffusing atom from one crystallographic site to another. There are mainly four mechanisms for fast ion conduction, namely interstitial, vacancy, collective, and interstitialcy mechanism, that we will describe here below. [1]

I.1.1 Interstitial Mechanism

Solute atoms, which are usually smaller than the host atoms, stay at the interstitial

Chapter I Introduction

sites of the host lattice, which constitute the interstitial solid solutions. The interstitial sites play a crucial role in the diffusion process, as an interstitial solute can jump from one interstitial site to the other neighbouring one directly, as shown in **Figure 1.1**. Therefore, in the interstitial mechanism, the interstitial atoms jump only among the interstitial sites without interacting much with the host atoms. This mechanism is the simplest diffusion mechanism. It is also named as the direct interstitial mechanism. It has to be distinguished from the interstitialcy mechanism discussed below, which is also named as the indirect interstitial mechanism. In this mechanism, defects are unnecessary. Besides, no defect concentration term enters the diffusivity, and no defect formation energy contributes to the activation energy of diffusion. The interstitial atom does not need the presence of a vacancy to jump, and the diffusion coefficients of direct interstitial mechanism tend to be relatively high. This mechanism is relevant for the diffusion of small foreign atoms such as H, C, N, and O in metals. Small atoms fit in interstitial sites, and they do not significantly displace the atoms from their normal lattice sites.

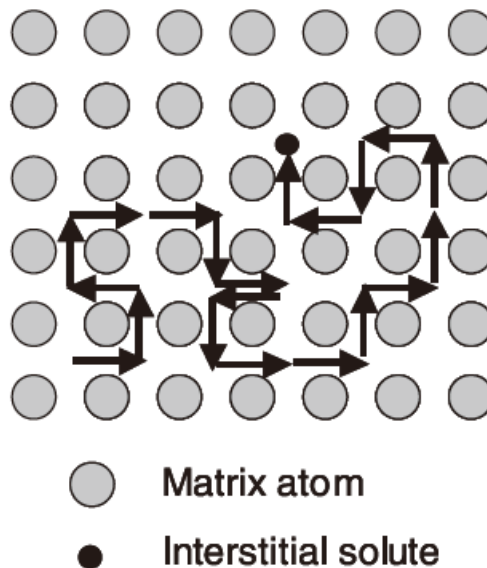


Figure 1.1 interstitial mechanism (direct interstitial mechanism) in fast ion conductor.

[1]

This type of diffusion mechanism is frequent in intermetallic compounds or in oxides with small diffusing cations (Li-ion batteries, Na-batteries...). It occurs less in O^{2-} containing compounds due to the significant size (1.35-1.4 Å) of the oxide ion. It can be considered to occur in proton-conducting oxides, even if the proton

Chapter I Introduction

is in this case associated to an oxide ion to form an -OH group. This proton may jump from one oxide ion to another. The proton movement is strongly dependant from the movement of host ions, in particular oxide ions. The mechanism is thus different from the one found in intermetallic compounds. Proton diffusion through interstitial sites is found in doped BaZrO_3 , BaCeO_3 and BaSnO_3 used as electrolytes in proton-conducting fuel cells.

I.1.2 Vacancy Mechanism

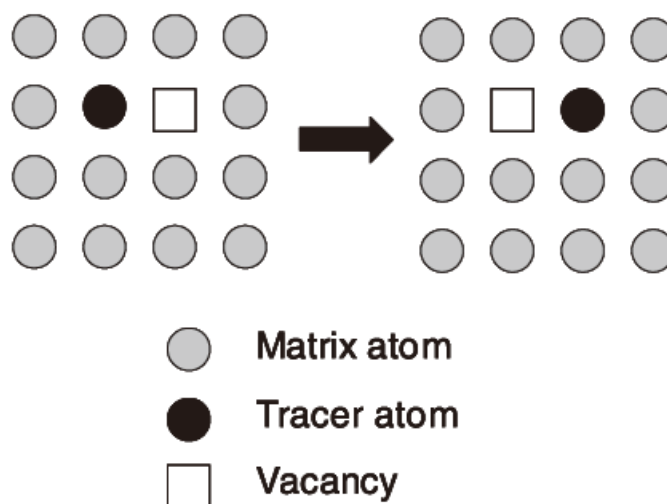


Figure 1.2 vacancy mechanism in fast ion conductor. [1]

The real crystals are never perfect, and the vacancies are the most important form of thermally induced atomic defects in the fast ion conductors. The energy barrier for moving an atom to an empty crystal site can be lower than that of moving into an interstitial site, particularly if the atom is of significant size. In the late 1940s, the vacancy mechanism has been considered as the most dominant mechanism in solid materials.[3] External conditions like high energy particle irradiation can induce vacancy formation, which is usually applied as an important way to investigate the effects of vacancies. As shown in **Figure 1.2**, the tracer atom will jump to the neighboring vacancy. Since, in the following chapters (chapter 2 and chapter 5), the vacancy mechanism of two different materials will be thoroughly discussed, some basic thermal equilibrium theory will be presented here. At thermal equilibrium, we have:

Chapter I Introduction

$$C_{1V}^{eq} = \frac{n_{1V}^{eq}}{N+n_{1V}^{eq}} \quad (1.1)$$

Where C_{1V}^{eq} is the site fraction of monovacancies, n_{1V}^{eq} is the vacant lattice sites (monovacancies, index 1V) and N is the number of system atoms. The equilibrium site fraction also has the relationship in **Eq. (1.2)**

$$C_{1V}^{eq} \propto \exp\left(-\frac{G_{1V}^F}{k_B T}\right) = \exp\left(\frac{S_{1V}^F}{k_B}\right) \exp\left(-\frac{H_{1V}^F}{k_B T}\right) \quad (1.2)$$

Where G_{1V}^F is the Gibbs free energy of vacancy formation, k_B is the Boltzmann constant, S_{1V}^F and H_{1V}^F are the formation entropy and the formation enthalpy of a vacancy, respectively. The vacancy formation enthalpy can also be given by

$$H_{1V}^F = -k_B \frac{\partial \ln C_{1V}^{eq}}{\partial (1/T)} \quad (1.3)$$

The exchange jump rate Γ of a vacancy-mediated jump of a matrix atom to a particular neighboring site

$$\Gamma = \omega_{1V} C_{1V}^{eq} = \nu^0 \exp\left(\frac{S_{1V}^F + S_{1V}^M}{k_B}\right) \exp\left(-\frac{H_{1V}^F + H_{1V}^M}{k_B T}\right) \quad (1.4)$$

Where ω_{1V} denotes the exchange rate between an atom and a vacancy and ν^0 the pertinent attempt frequency. H_{1V}^M and S_{1V}^M denote the migration enthalpy and entropy of vacancy migration, respectively.[1]

Vacancy-driven mechanism is found in many oxide materials for Solid Oxide Fuel/Electrolysis cells, at the core of our thesis project. To name just a few considered as efficient electrolyte materials, we can cite doped zirconia, doped ceria, doped lanthanum gallate [4]–[7], in which the doping action consists precisely in substituting a host cation by a dopant with a lower charge, in order to induce the creation of oxygen vacancies by charge compensation. It is worth noting that the original lattice usually consists of a dense packing of oxide ions, by which an interstitial mechanism would be impossible. Besides the lower charge of the dopant, this one is chosen so as to present an ionic radius similar to that of the original host cation to minimize local distortions. Several theoretical and experimental studies have nevertheless shown that the optimal dopant radius is slightly bigger than that of the host cation. As an example, the best dopant in zirconia is known to be Sc^{3+} , which presents an ionic radius of 0.87 Å to be compared with the value of 0.84 Å for Zr^{4+} . Similarly, the best dopants in ceria are known to be Sm^{3+} and Gd^{3+} , which present an ionic radius of 1.079 Å and 1.053 Å respectively slightly greater than that of Ce^{+4} equal to 0.97 Å.[8]

Vacancy-based diffusion mechanism is also the one found in most air electrode

Chapter I Introduction

materials for SOFCs. Namely, $\text{La}_{1-x}\text{Sr}_x\text{Co}_{1-y}\text{Fe}_y\text{O}_{3-d}$ is known to present a mixed valence on transition metal ions and oxygen vacancies simultaneously. This dual state allows defining the compound as a mixed ion-electron conductor and makes it play a role as electrons collector/provider and oxide ion diffusor, which leads to enhanced electrode properties [9], [10]. Similar properties are observed in the double perovskite $\text{GdBaCo}_2\text{O}_{5+x}$ explained in a later part.

I.1.3 Collective Mechanisms

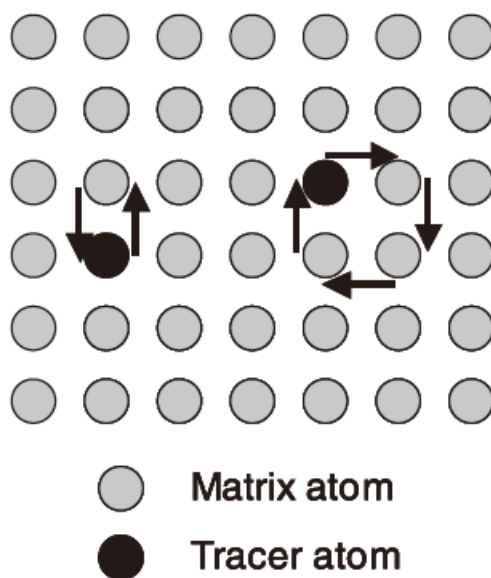


Figure 1.3 direct change and ring diffusion mechanism in fast ion conductor.[1]

Collective mechanisms, including direct change and ring diffusion mechanism (see above), involve the simultaneous motion of several atoms. They surprisingly appear to be quite common in fast ion-conducting systems.[11],[12] For the direct exchange mechanism, as shown in **Figure 1.3**, two neighbouring atoms exchange their positions simultaneously. In a close-packed lattice, this mechanism requires large distortions to squeeze the atoms through. This entails a high activation barrier and makes this process energetically unfavourable. The ring mechanism of diffusion was proposed for crystalline solids by the American metallurgist Jeffries already in the 1920s and advocated by Zener in the 1950s. [1],[13] The ring mechanism corresponds to a rotation of 3 (or more) atoms as a group by one atom distance. The required lattice distortions are not as great as in a direct exchange. Ring versions of atomic exchanges have lower

Chapter I Introduction

activation energies but increase the amount of collective atomic motion.

I.1.4 Interstitialcy Mechanism

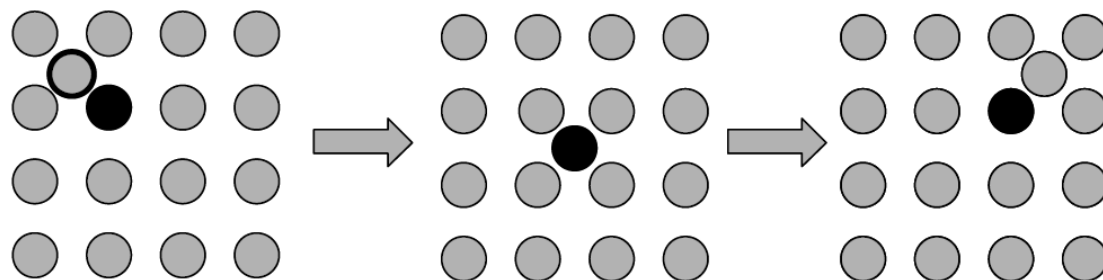


Figure 1.4 Interstitialcy mechanism of diffusion (colinear jumps) in fast ion conductor.

[1]

When an interstitial atom is nearly equal in size to the lattice atoms (or the lattice atoms on a given sublattice in a compound), diffusion may occur by the interstitialcy mechanism. **Figure 1.4** illustrates a (collinear) interstitialcy mechanism. Both atoms move in unison: a self-interstitial replaces an atom on a substitutional site, which then becomes itself interstitial. Interstitialcy mechanisms are collective mechanisms because at least two atoms move simultaneously. The interstitialcy mechanism is important for radiation-induced diffusion. When a crystal is irradiated with energetic particles (protons, neutrons, electrons...), lattice atoms are knocked-out from their lattice positions. The knocked-out atom leaves behind a vacancy. The atom itself is deposited in the lattice as a self-interstitial. In this way, pairs of vacancies and self-interstitials (Frenkel pairs) are formed. When these defects become mobile, they both mediate diffusion and give rise to radiation-induced diffusion, also linked to radiation damage in crystals.

Interstitialcy mechanism is also known to occur in oxide materials for SOFCs. Two important materials can be cited involving this mechanism. Firstly, the lanthanum silicate $\text{La}_{9.33+x}\text{Si}_6\text{O}_{26+1.5x}$ present interstitial oxide ions for $x > 0$. In this case, an enhanced oxide ion diffusion is observed whose exact mechanism has been debated [14], [15] but involves in all cases an interstitialcy mechanism. Another important material is the Ruddlesden-Popper nickelate $\text{La}_2\text{NiO}_{4+d}$ which presents at 650-800°C a

Chapter I Introduction

slight oxygen excess. This oxygen excess also leads to an interstitialcy mechanism at the origin of the mixed electron-ion conduction in this compound and of its excellent air electrode performance[16]–[18].

I.2 Computational methods for detecting diffusion mechanisms in fast ion conductors

For exploring the diffusion mechanism of fast ion conductors, classical molecular dynamic simulations (MD)[19] and density functional theory (DFT)[20] frameworks are usually adopted. Besides, after MD simulation producing long and large scale trajectories, specific analysis methods are adopted to analyze precisely the trajectories of the mobile atom. Here we present three of these methods, including density map, local environment analysis, and K-means clustering algorithm.[21]–[23] These data analyses can give precious details about the ion diffusion process. Under the frame of DFT, the nudged elastic band method (NEB) [24] and ab initio molecular dynamics[25], [26] are also widely used tools. Concerning the theoretical background of MD and DFT, we will not enter into details since many textbooks have been published with exhaustive description[19], [20], [27].

I.2.1 Molecular dynamic simulations for diffusion mechanism

I.2.1.1 Molecular dynamic simulation (MD)

The classical potential-based MD method is a widely used technique to study ion diffusion. In MD, the state of the system is defined according to the positions and the momenta of all the particles. Newton's equations of motion for an ensemble of particles are solved iteratively. These particles interact via potential energy functions, which are described by a long-range Coulombic term and by a short-range parameterized pair potential such as the Buckingham potential.[28] In MD simulation, due to the need for a lighter computational resource, the size of the systems that can be simulated is orders of magnitude greater compared to DFT.

The most widely used integration algorithms in MD simulations are based on the Verlet scheme, including Verlet's original method, the Verlet leapfrog algorithm, and the velocity Verlet.[29] The system may be coupled to a heat bath to ensure that the average

Chapter I Introduction

system temperature is maintained close to the requested temperature. Three different thermostats are usually used, including Nosé-Hoover[30], Berendsen[31], and Gaussian constraints[32]. Some popular software used for ionic MD simulations includes DL_POLY [33], LAMMPS [34], NAMD [35], CHARMM [36], GROMACS [37], and AMBER [38]. All our simulations in this thesis are performed using the DL_POLY classical code[33].

I.2.1.2 Data processing method for MD simulation

After MD simulation, the trajectories of all ions in the system can be obtained. A lot of powerful software (such as NmolDyn[39] and VMD[40]) were invented to analyze the ion diffusion, based on the data processing of ion trajectories. However, even if these codes are very general and can produce efficiently properties like mean square displacements, coordination numbers ..., they usually do not incorporate tools to analyse the diffusion mechanisms locally. Home-made codes are thus necessary to provide this detailed analysis of trajectories.

I.2.1.2.1 Ion density map

Chroneos *et al.*[21] performed Molecular dynamics simulations to study oxygen transport in tetragonal $\text{La}_2\text{NiO}_{4+\delta}$. They predict an interstitialcy mechanism with an activation energy of migration of 0.51 eV in the temperature range 800–1100 K. The prevalence of oxygen diffusion in the *a-b* (001) plane accounts for the anisotropy observed in tetragonal $\text{La}_2\text{NiO}_{4+\delta}$. After MD simulation, they extracted all the trajectories of every oxygen ion at every time step. Then, according to the coordinates of all oxygen ions, they obtained a density map of oxygen ions, as shown in **Figure 1.5**, reflecting the probability to find an oxygen ion at specific positions.

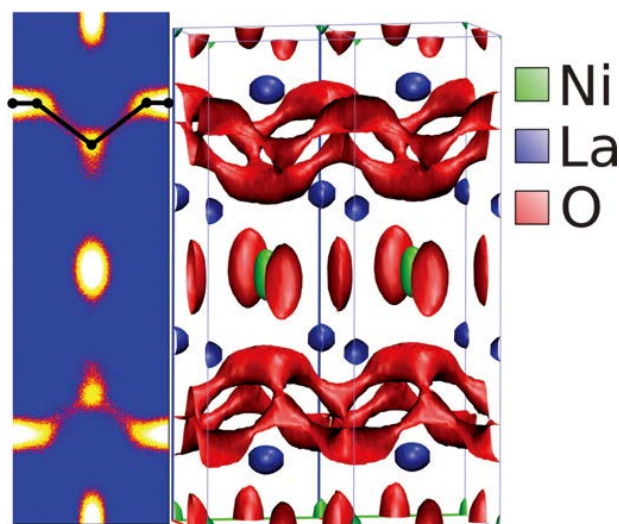


Figure 1.5 Oxygen ion density in the (010) plane (left) and the isosurface connecting the oxygen conduction sites (right) from a simulation at 900K of $\text{La}_2\text{NiO}_{4+\delta}$ and $\delta= 0.09$. Highlighted on the left is the proposed interstitial conduction mechanism.[21]

The density map allows for identifying the ion diffusion path directly. The red isosurface, which represented the oxygen ions, is oriented mainly in a - b plane, indicating the diffusion happened in this plane. This method is direct and intuitive, which is often used to detect the ion diffusion path.[41]–[43]. Nevertheless, a lot of jump information is lost, such as jumps frequency from site to site, the residence time of ions at each site. Thus the method gives no quantitative information on the diffusion bottlenecks even if a thinner zone of the isosurface might be associated with a more difficult pathway. Additional analysis tools are thus needed where all the jump information is kept and is made much more prosperous.

I.2.1.2.2 Local cation environment analysis

Chapter I Introduction

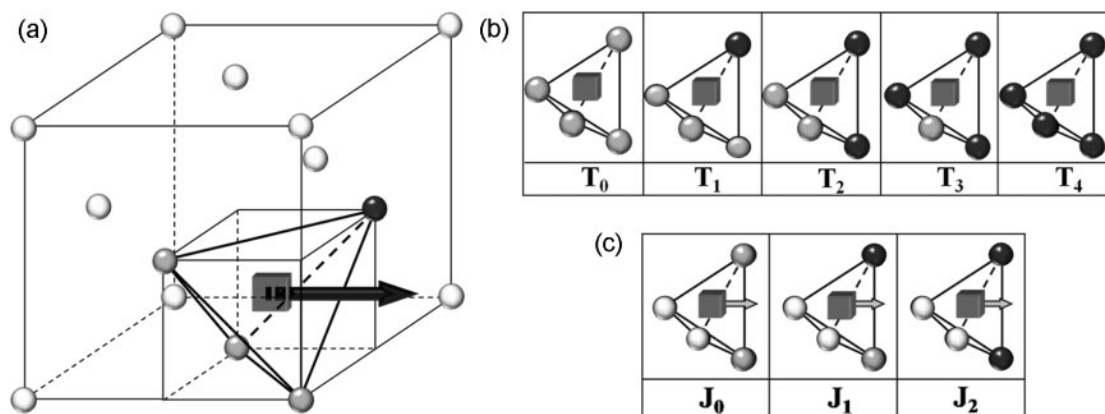


Figure 1.6 Oxygen (grey cube) migration pathway between two cations, host (dark grey) and dopant (black), at the vertexes of the edge of the tetrahedral site in a fluorite structure. Up to (b) five tetrahedral environments (T₀, T₁, T₂, T₃, and T₄) and (c) three jump environments (J₀, J₁, J₂) can be defined.[22]

Tarancón *et al.*[22] studied the effect of the dopant distribution on the oxygen diffusion in two doped fluorites structure (yttria-stabilized zirconia (YSZ) and gadolinia-doped ceria). They propose a new methodology based on the analysis of local environments. With this method, preferred vacancy migration pathways, most suitable conduction models, energy landscapes, and jump efficiency were found. As shown in **Figure 1.6**, in the fluorite oxides, oxygen occupies the tetrahedral sites formed by the fcc lattice of cations. There are five different tetrahedral environments can be defined depending on the number of dopant cations present in the tetrahedron, *i.e.* T₀, T₁, T₂, T₃ and T₄ (**Figure 1.6**). Since oxygen ions are located inside cation tetrahedrons, the jump of an oxygen ion from one site to another can also be identified by two cations located at the vertexes of the tetrahedral edge. Therefore, there are three different jump environments, *i.e.* J₀, J₁ and J₂ depending on the number of dopants present.

Their home-made code includes four steps: (i) localization of oxygen vacancies on oxygen positions; (ii) monitoring of each vacancy evolution on time; (iii) construction of a matrix containing all the vacancy jumps labelled with departure-tetrahedron, jump environment, and arrival-tetrahedron site; (iv) determination of the vacancy residence time in each tetrahedral type and the hopping rate for each jump environment. In brief, their method is to analyze the jumps of oxygen vacancies with the evolution of time for five different environments, which can be extended to all doped ionic systems. In this case, oxygen ions were associated with a specific tetrahedral site after measuring their distance to the centres of the tetrahedra. Double occupancy on one tetrahedron was

Chapter I Introduction

resolved by considering the nearest neighbour tetrahedron.

I.2.1.2.3 K-means clustering algorithm

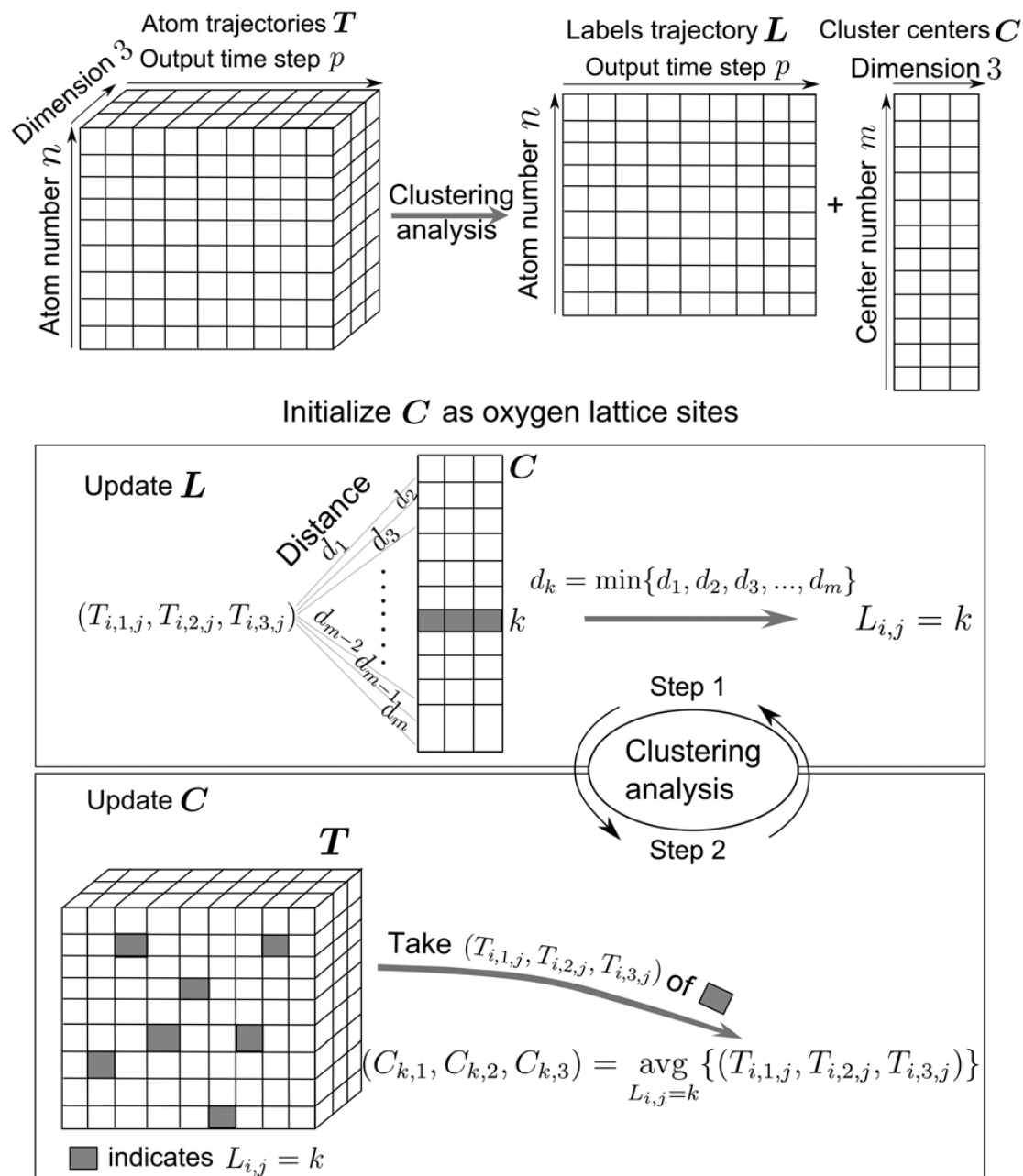


Figure 1.7 K-means clustering algorithm. This method illustrates the clustering analysis as applied to MD trajectories. Clustering aims to reduce the tensor T containing the trajectory data into two matrices L and C . L stores the labels' trajectory, and matrix C contains the coordinates of the cluster centers. The algorithm follows a two-step process by updating the labels and cluster centers iteratively.[23]

Chapter I Introduction

Ciucci *et al.*[23] explored the oxygen ion diffusion in A-site ordered perovskite $\text{PrBaCo}_2\text{O}_{5.5}$ by MD simulation. They suggest a machine learning algorithm, namely the K-means clustering. K-means clustering method can allow the tracking of each individual oxygen jump along with its corresponding location, *i.e.*, oxygen sites in BaO , $\text{PrO}_{0.5}$, and CoO_2 layers. The oxygen occupancy fraction of the different layers were determined. Additionally, the activation enthalpies of oxygen jump from layer to layer were obtained. Finally, they suggested that oxygen transport is fast within the CoO_2 layers, while the $\text{PrO}_{0.5}$ layers work as oxygen vacancy reservoirs. The K-means clustering algorithm [44] is widely used in solving unsupervised machine learning problems. In this work of Ciucci *et al.*, this method was for the first time proposed for MD simulation analyses. As shown in **Figure 1.7**, the trajectories of oxygen atoms are stored in a $n \times 3 \times p$ tensor T , where n is the number of oxygen atoms, and p is the number of MD output steps. Herein, each cluster means the grouped oxygen atoms which can be associated to the same oxygen site. For details, L is a $n \times p$ matrix that stores the cluster labels of the n atoms at each of the p steps output by the MD simulations. The labels are used to distinguish different clusters and are integers ranging from 1 to m , where m is the total number of clusters or oxygen sites. The coordinates of the cluster centres (one for each label) are stored in C , an $m \times 3$ matrix. Each row is mapped to a specific cluster centre, and the columns indicate x , y , and z coordinates.

The clustering analysis includes two iterative processes.

1. Initially, the centres (total number is m) are the crystallographic oxygen lattice sites.
2. Secondly, the distance between one oxygen ion and m centres are computed, then this minimum distance (among m distances) is confirmed, and this oxygen ion belongs to its closest centre.
3. After all the oxygen ions found their centre, the coordinates (x, y, z) of all centres will be updated by the mean values of their clustered oxygen ions coordinates. Therefore, all the coordinates of m centres will be updated, Then step 2 restarts and the oxygen ions of next timestep will find their new belonged centres.
4. The loops continue between 2 and 3 until all the oxygen ions of each time step have been associated to their centres.

The change of centre labels implies the jump from site to site. Rich diffusion information can be obtained according to the jump statistics. The method proposed by

Chapter I Introduction

Ciucci suggests that data mining methods can be promising in the analysis of the ion diffusion problem. This also inspires us to combine the other data mining method with the MD simulations in Chapter 2.

I.2.2 Density functional theory (DFT) for diffusion mechanism

Density functional theory (DFT) calculations is becoming a standard tool for diverse materials modeling problems in materials science.[20] To overcome these issues and to make the simulation of solids tractable, DFT have been developed since some approximation techniques are made within DFT which can reduce the calculation amount largely.[45] To overcome these issues and to make the simulation of solids tractable, suitable approximation techniques such as DFT have been developed.[46] In DFT, the exchange-correlation energy is described in the local density approximation (LDA) or the generalized gradient approximation (GGA). Another way of approximating the exchange-correlation energy is with the use of hybrid functionals that incorporate a part of the exact exchange from the Hartree–Fock theory.[47] Generally, a plane-wave basis set is used with the pseudopotential method. In this, the core electrons are described by effective potentials (pseudopotentials), and the valence electrons may evolve explicitly. Important recent developments include the introduction of the U-parameter (onsite Coulomb interaction parameter) for open-shell transition metal compounds.[48],[49] The limitation of DFT is the relatively small simulation size that is typically on the order of only a few hundred atoms at the present time. Within the DFT framework, the activation energy of diffusion can be calculated coupled with techniques to identify the minimum energy path, such as the nudged elastic band method.[24] Besides, the Ab Initio Molecular Dynamics (AIMD) [50] is another powerful tool to study the diffusion mechanism in different fast ionic materials. Ab initio molecular dynamics unifies approximate ab initio electronic structure theory and classical molecular dynamics. AIMD comes in two fundamentally distinct flavours, including Born–Oppenheimer Molecular Dynamics (BOMD) and Car–Parrinello Molecular Dynamics (CPMD). More theoretical background can be found in the references [51]–[53] Herein, the theoretical backgrounds of NEB are presented.

Chapter I Introduction

I.2.2.1 Regular NEB and climbing image NEB method

The nudged elastic band (NEB) method is an efficient method for finding the minimum energy path (MEP) between a given initial and final state of a transition.[54] The MEP can be used to estimate the activation energy barrier for transitions between the initial and final states. NEB has become widely used for estimating transition rates within the harmonic transition state theory approximation. The method has been used both in conjunction with electronic structure calculations, in particular, plane wave-based DFT calculations.[55]–[59] The MEP is found by constructing a set of images of the system, typically on the order of 4~20, between the initial and final state. A spring interaction between adjacent images is added to ensure continuity of the path, thus mimicking an elastic band. An optimization of the band, involving the minimization of the force acting on the images, brings the band to the MEP.

An elastic band with $N+1$ images can be denoted by $[\mathbf{R}_0, \mathbf{R}_1, \mathbf{R}_2, \dots, \mathbf{R}_N]$, where the end points, \mathbf{R}_0 and \mathbf{R}_N , are fixed and given by the energy minima corresponding to the initial and final states. The $N-1$ intermediate images are adjusted by the optimization algorithm. In the NEB method, the total force acting on an image is the sum of the spring force along the local tangent and the true force perpendicular to the local tangent

$$\mathbf{F}_i = \mathbf{F}_i^s|_{\parallel} - \nabla E(\mathbf{R}_i)|_{\perp} \quad (1.7)$$

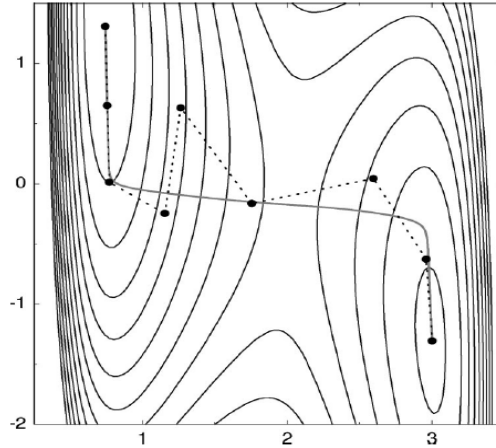
Where the true force is:

$$\nabla E(\mathbf{R}_i)|_{\perp} = \nabla E(\mathbf{R}_i) - \nabla E(\mathbf{R}_i) \cdot \hat{\mathbf{t}}_i \quad (1.8)$$

Here, E is the energy of the system, a function of all the atomic coordinates, and $\hat{\mathbf{t}}_i$ is the normalized local tangent at image i . The spring force is:

$$\mathbf{F}_i^s|_{\parallel} = k(|\mathbf{R}_{i+1} - \mathbf{R}_{i-1}| - |\mathbf{R}_i - \mathbf{R}_{i-1}|)\hat{\mathbf{t}}_i \quad (1.9)$$

where k is the spring constant.



Chapter I Introduction

Figure 1.8 Illustration for the regular nudged elastic band method. The band does not converge to the minimum energy path (solid line).[54]

An illustration of this is given in **Fig. 1.8**. The potential surface is a two-dimensional combination of a LEPS potential [54] and a harmonic oscillator. Initially, the seven movable images were placed equispaced along the straight line between the minima. A minimization algorithm was then applied, moving the images in the direction of the force given by **Eq. 1.7**. A projected velocity Verlet algorithm was used for the minimization. The velocity projection is carried out at each time step and ensures that only the component of the velocity parallel to the force is included in the dynamics. When the force and projected velocity point in the opposite direction (indicating that the system has gone over the energy ridge), the velocity is zeroed. This projected velocity verlet algorithm has been found to be an efficient and simple minimization algorithm.[54] After a few iterations, the images are close to the MEP, but, once convergence is reached, the magnitude of the force on the images does not evolve more. An essential feature of the method, which distinguishes it from other elastic band methods [60],[61] is a force projection which ensures that the spring forces do not interfere with the convergence of the elastic band to the MEP, as well as ensuring that the true force does not affect the distribution of images along with the MEP.

The climbing image NEB (CI-NEB) method constitutes a small modification to the NEB method.[24], [54] Information about the shape of the MEP is retained, but a rigorous convergence to a saddle point is also obtained. This additional feature does not add any significant computational effort. After a few iterations with the regular NEB, the image with the highest energy i_{max} is identified. The force on this one image is not given by **Eq. 1.7** but rather by

$$\mathbf{F}_{i_{max}} = -\nabla E(\mathbf{R}_{i_{max}}) + 2\nabla E(\mathbf{R}_{i_{max}})|_{||} \quad (1.10)$$

This is the full force due to the potential with the component along with the elastic band inverted. The maximum energy image is not affected by the spring forces at all. The true force at this image along the tangent is inverted. In this way, the image tries to maximize its energy along with the band and minimize it in all other directions. When this image converges, it will be at the exact saddle point.

I.3 Several fast ion conductors and their diffusion mechanisms

The oil crisis of the 1970s and the need for energy conservation further increased the number of studies on fast ion conduction with a significant focus on battery and sensor technology and on fuel cells. [1] According to the difference of mobile ion, several new fast ion conductors were reported, notably, the oxygen ion conductors used for SOFCs [28], proton conduction materials [62], lithium-ion conductors [63], sodium β -alumina and related materials [64].

I.3.1 Oxygen ion conductors

I.3.1.1 Solid Oxide Fuel Cells (SOFCs)

Solid Oxide Fuel Cells (SOFCs) are electrochemical devices that convert chemical energy into electricity and heat, which can be used for stationary and mobile applications.[65]–[67] They are great technologies due to their high efficiency, high energy density, and environmental friendliness.[68]–[70]

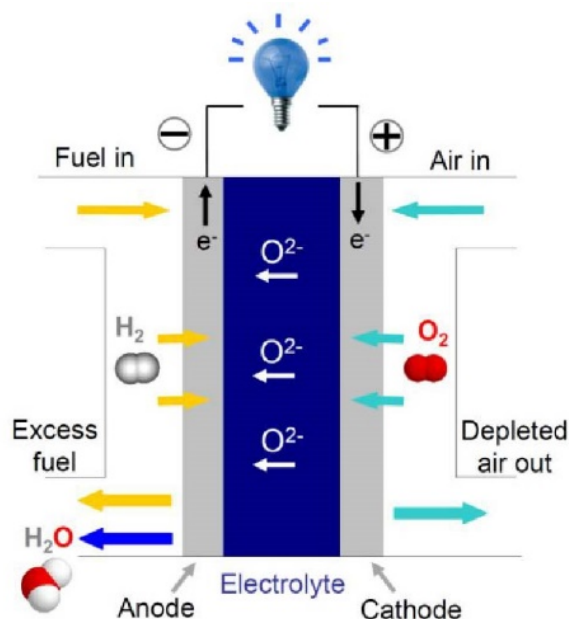


Figure 1.9 Schematic representations of the reactions taking place in a SOFC. [71]

The schematics of SOFCs is shown in **Figure 1.9**. The oxidant, air or oxygen, is sent to the cathode, and the oxygen atoms get electrons to undergo a reduction reaction. Hydrogen loses electrons at the anode and undergoes an oxidation reaction. The oxygen ions migrate from the cathode to the anode through the oxide-ion conducting electrolyte

Chapter I Introduction

and combine with protons to form water. The electron flow in the external circuit from the anode to the cathode generates direct-current electricity. SOFCs are composed of solid-state ceramics and require operating temperatures ranging between 500 and 1000 °C. The best established SOFC systems are those based on an yttria-stabilized zirconia (YSZ) electrolyte, which requires operating temperatures between 800 - 1000 °C [65]–[67] to achieve sufficient ionic conductivity in order to assure the efficient transport of O²⁻. These high operating temperatures are the main limitations of SOFCs, which lie mainly in their unsatisfactory durability and reduced lifetime.[72] To overcome such disadvantages, lowering the working temperature to 500 - 700 °C becomes an important challenge in improving SOFC technology.[66]

The cathodes for SOFCs should perform well for both ionic and electronic conduction, while electrolytes should exhibit high ionic conductivity with very low electronic conductivity. Most of the cathode materials in SOFCs are based on the perovskite crystal structure ABO_{3-δ}. [67], [73][74][75] Nevertheless, novel materials that do not rely only on oxygen vacancies and show promising oxygen diffusion properties, are reported, including the Ruddlesden Popper (RP) series of layered oxides (formula A_{n+1}B_nO_{3n+1}), [76][77] the double perovskites (formula AA'B₂O_{5+δ}) [78]–[82], and layered cobaltites and ferrites exemplified by Sr_{1-x}Y_xCoO_{3-δ} [83]–[87] and Sr₄Fe₆O₁₃ [88]–[92] respectively. The electrolyte materials may also present a great diversity of structures, ranging from the traditional cubic-like-symmetry isotropic systems, the yttria-stabilized zirconia (YSZ), [93]–[96] the Gadolinium- or Samarium-doped ceria (CGO or CSO) [97], [98] and La_{1-x}Sr_xGa_{1-y}Mg_yO₃ (LSGM) [99]–[101], to the non-cubic systems as the Brownmillerites structure (*e.g.*, BaInO_{2.5}) [102]–[106] and Apatites (Ln₁₀(XO₄)₆O_{2-y}, Ln is a rare-earth or alkaline earth metal, and X is P, Si or Ge) [14], [107]–[109].

I.3.1.2 Diffusion mechanisms of oxygen ion conductors in SOFC cathodes

Here, several diffusion mechanisms of cathodes materials are presented, mainly based on theoretical approaches.

I.3.1.2.1 Perovskite crystal structure ABO_{3-δ}

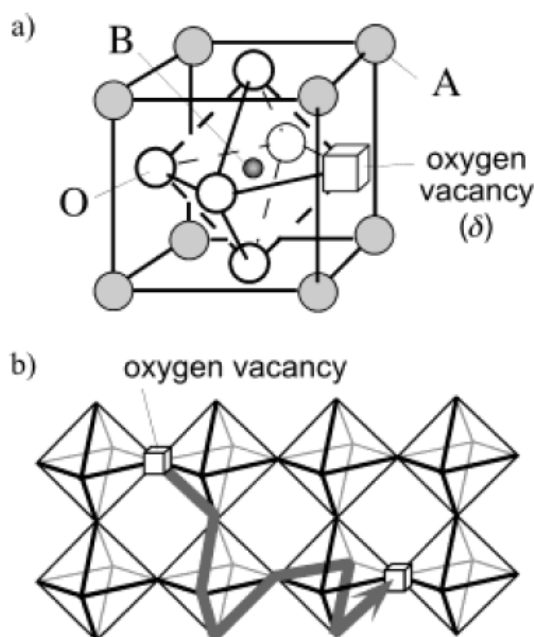


Figure 1.10 Atomic structure and oxygen transport in mixed conducting perovskites $ABO_{3-\delta}$. (a) Basic structural element, consisting of a corner-sharing BO_6 octahedron surrounded by charge-compensating A-site cations. (b) Bulk oxygen transport mechanism, involving random hopping of oxygen ion vacancies on the oxygen sublattice.[65]

Figure 1.10 illustrates the general perovskite crystal structure $ABO_{3-\delta}$ as it relates to the electronic and ionic transport properties of some transition metal oxides. The B sites are the reducible transition metal such as Co or Fe, and the A-site cation is a mixture of the rare and alkaline earth element, *e.g.*, La and Sr. The octahedral symmetry around the transition metal (B-site) often promotes a metallic or semiconducting band structure at high temperatures, leading to high electronic conduction. Besides, the perovskite structure is quite stable compared with the other crystalline phases, and a good choice of A and B cations can produce a large number of oxygen vacancies, thus facilitating the oxygen ions transport. **Figure 1.10(b)** shows the jump path of oxygen vacancies along the edges of the octahedron in the perovskite phase.

I.3.1.2 Ruddlesden Popper (RP) series of layered oxides ($A_{n+1}B_nO_{3n+1}$)

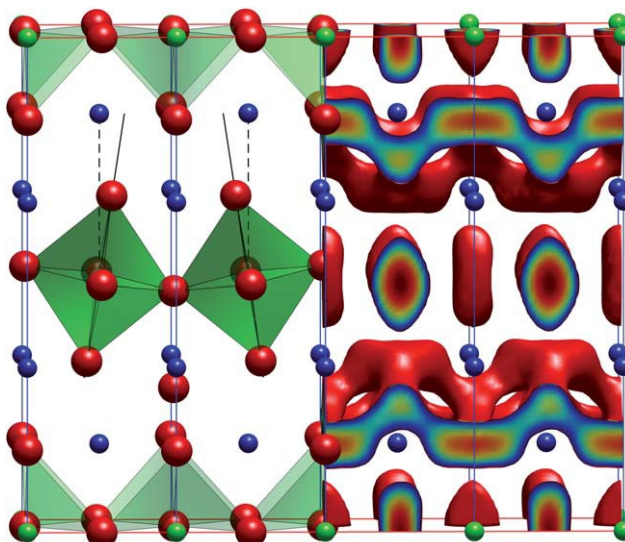


Figure 1.11 The tetragonal crystal structure of $\text{Pr}_2\text{NiO}_{4+\delta}$ (O in red, NiO_6 octahedra in green and Ni in blue) and the isosurface connecting the O diffusion sites in a - b plane (the c -axis in the vertical axis) from the MD calculations at 1100 K and $\delta=0.09875$. [43]

As mentioned above, Chroneos explored the oxygen diffusion mechanism in $\text{La}_2\text{NiO}_{4+\delta}$ through classical molecular dynamics simulations. In the RP family materials, including $\text{La}_2\text{NiO}_{4+\delta}$, $\text{Pr}_2\text{NiO}_{4+\delta}$, and $\text{La}_2\text{CoO}_{4+\delta}$, oxygen diffusion takes place in the a - b plane via a highly anisotropic interstitialcy mechanism (**Figure 1.11**) [21], [43], [110], [111] In the temperature range 800–1500 K, the activation energy for migration varied between 0.49 eV ($\delta = 0.025$) and 0.64 eV ($\delta = 0.20$). Excellent agreements between the calculated values and experimental ones are observed in their simulation. [18], [43] Beyond $\delta = 0.02$, the diffusivity levels off. The physical meaning of this process can be attributed to the rise in the effective migration barrier due to the increased formation energy of oxygen interstitials (*i.e.*, due to the presence of other pre-existing neighboring interstitials) and the stiffening of the lattice.

I.3.1.2.3 Double perovskites ($\text{AA}'\text{B}_2\text{O}_{5+\delta}$)

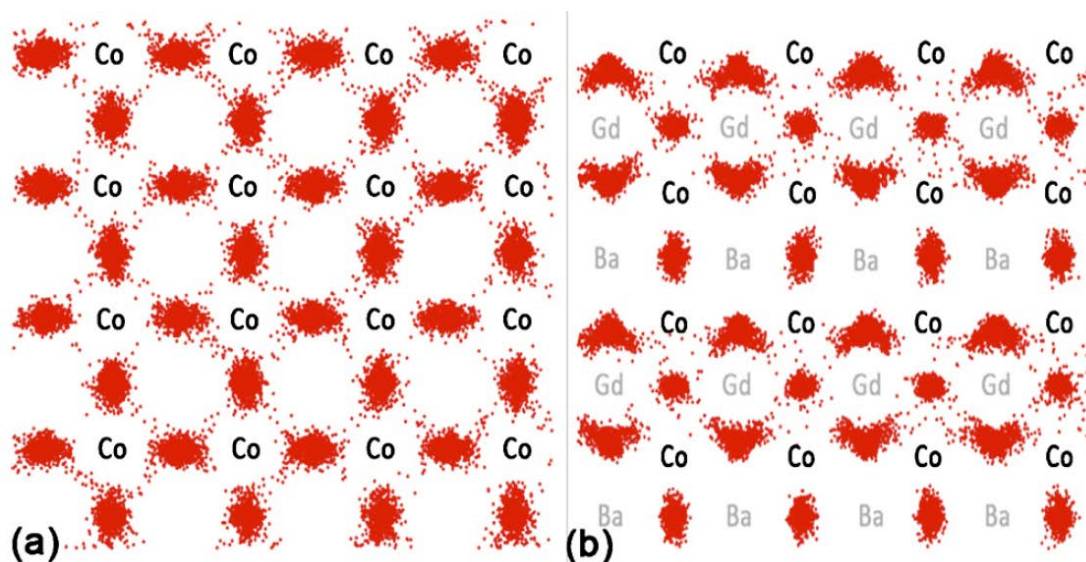


Figure 1.12 Calculated oxygen-density profiles in $\text{GdBaCo}_2\text{O}_{5.5}$ at 1200 K along (a) the c -axis in the cobalt planes, and (b) the b -axis in the cobalt planes.[112]

Ordered double perovskites with general formula $\text{AA}'\text{B}_2\text{O}_{5+\delta}$, where A is rare earth, A' is alkaline earth, and B is Co, Mn, have been recently proposed as next-generation of intermediate temperature SOFCs cathodes due to their excellent performance.[42], [80]–[82], [112]–[118] These double perovskite materials derive from aliovalent substitution on the A-site of a simple perovskite oxide (ABO_3), with the general formula, $\text{A}_{0.5}\text{A}'_{0.5}\text{BO}_{3-\delta}$, which generates oxygen vacancies. For a significant size mismatch between the two A-site cations, the simple perovskite structure tends to adopt a layered arrangement with an A-site cation ordering, and the formula for the material is then rewritten in the double perovskite manner, $\text{AA}'\text{B}_2\text{O}_{5+\delta}$. The mechanisms of oxygen diffusion in $\text{GdBaCo}_2\text{O}_{5.5}$ compound are discussed here as an example.

MD simulation [41],[112], oxygen diffusion in $\text{GdBaCo}_2\text{O}_{5.5}$ was confirmed to be bidimensional occurring mainly in the a - b plane, while diffusion along the c axis was limited. Between 1000 and 1600 K, the self-activation energy for diffusion is about 0.6 eV. Vacancies are mainly located in the gadolinium planes (95%), while a relatively small amount of them is in the cobalt planes (5%). Oxygen ions spend most of their time in the cobalt planes and occasionally jump into gadolinium planes where they stay only for a few picoseconds, while they can remain up to some nanoseconds in cobalt planes. As shown in **Figure 1.12**, oxygen atoms located originally in Barium planes remain at their original site and do not diffuse in the neighbouring cobalt planes. The diffusion occurs mainly in the cobalt planes, while most of the oxygen vacancies are

held in the Gd planes (**Figure 1.12**). Gd planes were then identified as source-sink for the oxygen vacancies rather than as fast pathways, as proposed previously.

I.3.1.2.4 layered cobaltites

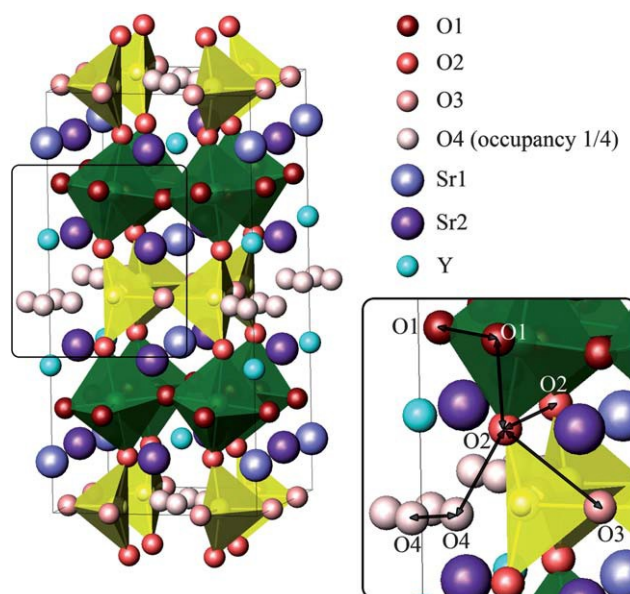


Figure 1.13 The crystal structure of $\text{Sr}_{0.7}\text{Y}_{0.3}\text{CoO}_{2.62}$. The CoO_6 octahedra layers alternate with oxygen-deficient layers (O3, O4) and Co atoms. [87]

Cobalt-based oxides are another important category of materials that can be employed for SOFCs cathodes, oxygen separation membranes, and other applications due to their high electrochemical stability and in spite of their lower stability. [83]–[87] The structure and properties of $\text{Sr}_{1-x}\text{Ln}_x\text{CoO}_{3-\delta}$ ($\text{Ln} = \text{Y}$, rare-earth cations) have been studied exhaustively. [83]–[87] As an example, $\text{Sr}_{0.7}\text{Y}_{0.3}\text{CoO}_{2.62}$, originally studied by Istomin *et al.* [86], exhibits the tetragonal symmetry with space group $I4/mmm$. In $\text{Sr}_{0.7}\text{Y}_{0.3}\text{CoO}_{2.62}$, the layers of CoO_6 octahedra alternate with the oxygen-deficient layers (**Figure 1.13**). One of the oxygen sites (the O4) has a partial occupancy of 1/4, with only one of the four adjacent positions being occupied. Rupasov *et al.* [87] investigated the oxygen diffusion mechanism in $\text{Sr}_{0.7}\text{Y}_{0.3}\text{CoO}_{2.62}$. Their calculation shows that oxygen transport is isotropic with an activation energy of 1.56 eV in the temperature range of 1000–1400 K. This activation energy is in excellent agreement with the experimental value of about 1.5 eV. The diffusion mechanism consists of O2 atoms moving to the partially occupied O4 sites creating vacancies at O2 sites. These vacancies move to the Co-O1/O2 octahedra (*a-b* plane migration) and along the O2-

O1-O2 pathway (*c*-axis migration).

I.3.2 Proton conductors

A growing interest has concerned proton conductors, which are expected to present a high ion conduction at low temperature due to the smaller activation energy associated with the diffusion process. The most efficient proton-conductors for fuel cells are known to belong to the perovskite family. Two principal mechanisms are usually recognized to describe the transport of protons, namely, the vehicle mechanism and the Grotthuss mechanism.[119]–[122] For the vehicle mechanism, the proton moves together with a “vehicle” as a passenger on a larger ion (H_3O^+ , NH_4^+ , OH^-), which mainly happens in aqueous solution, and compounds with small molecules. For the Grotthuss mechanism, which is observed in solid acid salts and proton-conducting oxides, the proton diffusion occurs mainly by rotational diffusion of a proton around an oxygen ion, followed by proton transfer toward a neighbouring oxide ion.

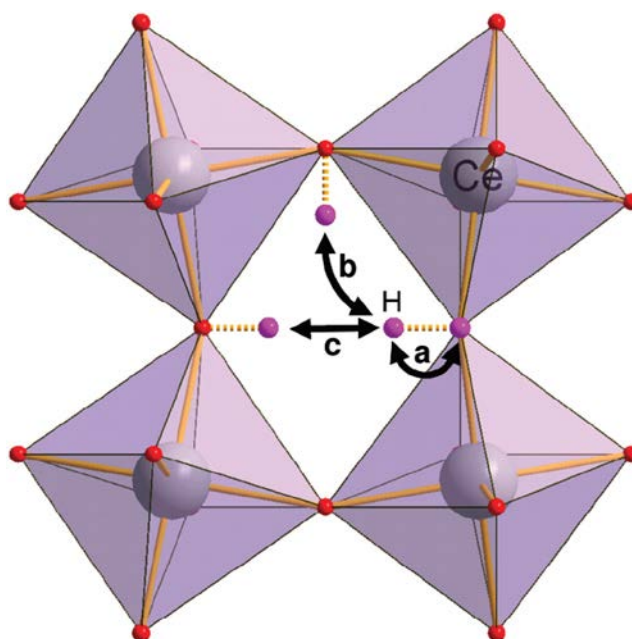
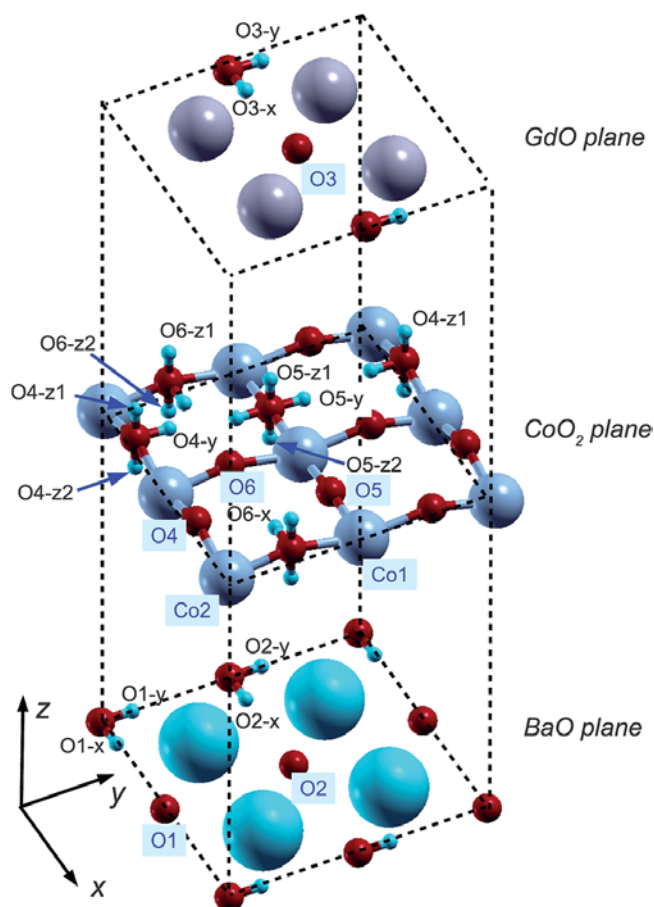


Figure 1.14 Possible motions of the proton in the perovskite $Pnma$ structure: (a) reorientation, (b) intra-octahedral hopping, and (c) inter-octahedral hopping. The Ce, O, and H atoms are represented with white, red, and violet color.[123]

Chapter I Introduction

Many perovskites (*e.g.*, BaZrO₃, BaCeO₃, and BaSnO₃) doped by elements of lower valence on their B site (*e.g.*, Y, In, and Gd in substitution of Zr, Ce, and Sn) can be used as electrolytes in Protonic Ceramic Fuel Cells (PCFCs).[123]–[126] After DFT calculation of Gd-doped BaCeO₃ (BaCe_{1-x}Gd_xO_{3-x/2}), Geneste *et al.* proposed that in a cubic perovskite, there are two kinds of processes for the proton motion: reorientation (**Figure 1.14 a** path) and transfer (or hopping). Actually, the hoppings can be divided in two kinds, intra-octahedral and inter-octahedral. In a cubic structure, intra-octahedral hoppings are the most probable. In this case, the two initial and final oxygen positions belong to the same octahedron (**Figure 1.14 b** path). In distorted perovskites (*e.g.*, *Pnma* structure), when there is a set of tilts of oxygen octahedra, inter-octahedral hopping mechanism may appear (**Figure 1.14 c** path). One inter-octahedral hopping may be equivalent to two intra-octahedral hoppings in terms of distance. This direct jump to another octahedron might strengthen the proton diffusion in *Pnma* structure compared to cubic perovskites and explains why doped BaCeO₃, of orthorhombic structure, presents a higher proton conductivity compared to the cubic BaZrO₃.



Chapter I Introduction

Figure 1.15 The different positions of the proton in the GBCO supercell. The BaO, CoO₂ and GdO_{0.5} planes are spaced out for clarity.[127]

REBaCo₂O_{5+δ} (RE = Gd, Sm, Pr, Nd, Y) materials have been presented as promising cathode material for SOFCs, as discussed above in section 1.3.1.1.3. Besides, they are also found able to be potential mixed proton-electrode cathode materials.[82], [127] Geneste *et al.* employ density-functional calculations in the Hubbard framework (DFT+U) to investigate the structure, magnetism, and chemical reactivity of GdBaCo₂O_{5.5} with respect to hydration, oxidation, and reduction.[127] The possible migration paths of protons were proposed by examining the protonic energy landscape (**Figure 1.15**).

- (i) Along **a**: this path exists passing through the sites attached to oxygens O4 and O6 in the CoO₂ plane, namely: O4-y→O6-x→O6-z1→O6-x→O4-y, involving the traditional succession of hopping and reorientation motions of the OH group. Only very stable sites join in this path joins, and thus this path is probably very favourable.
- (ii) Along **b**: it is more difficult for the proton to diffuse along **b** because the O5 oxygens are associated with unstable sites (O5-y). However, these sites could be avoided by passing through the O2-x and O2-y sites of the BaO plane, which would involve only stable or very stable sites, as O4-y→O6-x→O6-z2→O2-y→O2-x→O2-y→O6-z2→O6-x→O4-y.
- (iii) Along **c**: diffusion along **c** must necessarily pass by the sites attached to the O3. This path exhibits high energy barriers, indicating many difficulties.

Based on these arguments, protonic diffusion in GBCO could be very anisotropic, with probably favourable paths along with **a** and **b**, not along with **c**. The experimental proof of proton diffusion in double cobaltites is still the subject of debate, mainly linked with the difficulty to evaluate hydration rates (due to competitive oxidation reaction) and to measure proton conductivity due to electron conductivity screening.[128], [129]

I.4 Objective and outline

As summarized above, the current understanding of ionic diffusion in solids is based on classical diffusion models, which describes ionic transport as the hopping of

Chapter I Introduction

individual ions from one lattice site to another through inter-connected diffusion channels in the crystalline structure framework. The crystalline structure framework defines the energy landscape of the ion migration. Understanding fundamental aspects of ion diffusion in solid-state ionic systems is important for the discovery of new fast ion conductors or for improving already known compounds.

In this thesis, we provide direct atomic-scale insights on the ion transport mechanisms and conduction properties of NdBaInO_4 [130]–[132], LaHO and their family members [133]–[135] by operating MD and DFT simulation. NdBaInO_4 is a promising O^{2-} conductor, which could be used as electrolyte material in SOFCs. With substituting Nd by alkaline-earth elements (Ca, Sr, Ba), $\text{Nd}_{1-x}\text{AE}_x\text{BaInO}_{4-x/2}$ ($\text{AE} = \text{Ca}, \text{Sr}, \text{Ba}$) is obtained, which is dominated by oxygen vacancy diffusion mechanism. On the other hand, substituting Nd by Ti and Zr will produce $\text{NdBaIn}_{1-x}\text{RE}_x\text{O}_{4+x/2}$ ($\text{RE}=\text{Ti}, \text{Zr}$), which is expected to present an interstitialcy diffusion behaviour. These oxygen ion diffusion mechanisms of acceptor and donor-doped NdBaInO_4 are discussed thoroughly in chapter 2 and 3, respectively. LaHO is a novel hydride ion conductor, which was shown to present enhanced ion conduction properties at ~ 600 K [133], [134]. Unfortunately, the diffusion mechanisms in this LaHO compound are poorly known. We propose here to explore such mechanisms by combining both classical MD and DFT calculation. However, due to the lack of the interatomic potential for H, MD simulations could not be performed straightforwardly. Therefore, in chapter 4, we developed specifically a force field describing all interatomic interactions in LaHO and we studied the hydride ion diffusion mechanisms in different LaHO family members. Finally, in chapter 5, we explored the hydride ion diffusion mechanism of $\text{LaH}_{3-2x}\text{O}_x$ based on the force field obtained in chapter 4. Details are as followed:

Chapter 1 (this chapter) illustrates the concept of fast ion conductors, the ion diffusion mechanism, the basic concept of atomic-scale simulation methods, and a literature review of different fast ion conductors applied in SOFCs.

Chapter 2 proposes two general clustering methods (convex hull classification method and a DBSCAN machine learning algorithm) to identify oxygen ion diffusion pathways. These two methods aim at associating each ion coordinate of MD output files to a fixed ionic site. Furthermore, relevant details are provided for efficient use of these two approaches during MD analysis of ion conductors, *e.g.*, oxygen site occupation, jump times analysis, diffusion path, correlation factor, and residence time analysis. The mechanism of oxygen diffusion in $\text{Nd}_{1-x}\text{AE}_x\text{BaInO}_{4-x/2}$ ($\text{AE} = \text{Ca}, \text{Sr}, \text{Ba}$) compounds

Chapter I Introduction

is exhaustively studied. As a whole, the two classification approaches could be extrapolated to other ion conductors to gather detailed information about the diffusion processes.

Chapter 3 describes the O^{2-} diffusion mechanism donor-doped $NdBaInO_4$, *i.e.*, $NdBaIn_{1-x}RE_xO_{4+x/2}$ ($RE=Ti, Zr$). Bond valence summation (BVS) was used as an additional tool to find the possible oxygen interstitial position. MD simulations results are in good agreement with the BVS calculations. Finally, a DBSCAN machine learning algorithm was adopted to track the trajectory of each oxygen ion and further obtain the oxygen diffusion path. An interstitialcy mechanism was found in the temperature range 1500K-1900K.

Chapter 4 describes an accurate fitted interatomic potential for the Lanthanide oxyhydrides LaHO. The potential is obtained by fitting the experimental and DFT calculation results of 4 compounds (α -LaHO, β -LaHO, LaH_3 , and La_2O_3) by GULP. The potential was also tested to describe the high-pressure forms of LaHO, namely γ -LaHO and δ -LaHO. Finally, this potential has been employed to study the hydride diffusion mechanisms in α -LaHO and β -LaHO. Potential strategies to improve the ionic conductivity for α - and β -LaHO are suggested.

In Chapter 5, we adopt the same H^- force field developed in chapter 4 and apply it to $LaH_{3-2x}O_x$ to investigate the hydride diffusion path. A particular focus concerns the influence of oxygen content on the anisotropy and the evolution of diffusion coefficient.

Chapter 6 presents the conclusion of this work.

I.5 Reference

- [1] H. Mehrer, "Diffusion in solids: fundamentals, methods, materials, diffusion-controlled processes," *Springer Ser. solid-state Sci.*, 2007.
- [2] CRA.Catlow, "Atomistic Mechanisms of Ionic Transport in Fast-ion Conductors," *j.chem.soc.faraday.trans*, vol. 86, no. 8, pp. 1167–1176, 1990.
- [3] K. Janssens, D. Raabe, E. Kozeschnik, M. Miodownik, and B. Nestler, *Computational Materials Engineering 1st Edition*. 2007.
- [4] C. Périllat-Merceroz, G. Gauthier, P. Roussel, M. Huvé, P. Gélín, and R. N. Vannier, "Synthesis and study of a Ce-doped La/Sr titanate for solid oxide fuel cell anode operating directly on methane," *Chem. Mater.*, vol. 23, no. 6, pp.

Chapter I Introduction

- 1539–1550, 2011.
- [5] S. Guillot, S. Beaudet-Savignat, S. Lambert, P. Roussel, and R. N. Vannier, “Effect of the dopant nature on the conductivity of oxygen overstoichiometric oxyapatites with controlled microstructures,” *Solid State Ionics*, vol. 185, no. 1, pp. 18–26, 2011.
- [6] M. Benamira *et al.*, “Gadolinia-doped ceria mixed with alkali carbonates for solid oxide fuel cell applications: I. A thermal, structural and morphological insight,” *J. Power Sources*, vol. 196, no. 13, pp. 5546–5554, 2011.
- [7] M. Benamira *et al.*, “Structural and Electrical Properties of Gadolinia-doped Ceria Mixed with Alkali Earth Carbonates for SOFC Applications,” *ECS Trans.*, vol. 7, no. 1, pp. 2261–2268, 2019.
- [8] R. D. Shannon, “Revised Effective Ionic Radii and Systematic Studies of Interatomic Distances in Halides and Chalcogenides,” *Acta Crystallogr.*, vol. 32, p. 751, 1976.
- [9] S. J. Skinner and M. A. Laguna-Bercero, “Advanced Inorganic Materials for Solid Oxide Fuel Cells,” *Energy Mater.*, pp. 33–94, 2011.
- [10] H. J. M. Bouwmeester, M. W. Den Otter, and B. A. Boukamp, “Oxygen transport in $\text{La}_{0.6}\text{Sr}_{0.4}\text{Co}_{1-y}\text{Fe}_y\text{O}_{3-\delta}$,” *J. Solid State Electrochem.*, vol. 8, no. 9, pp. 599–605, 2004.
- [11] H. Teichler, “Structural dynamics on the μs scale in molecular-dynamics simulated, deeply undercooled, glass-forming $\text{Ni}_{10.5}\text{Zr}_{0.5}$,” *J. Non. Cryst. Solids*, vol. 293–295, no. 1, pp. 339–344, 2001.
- [12] K. Rätzke and F. Faupel, “Diffusion in metallic glasses and undercooled metallic melts,” *Rev. Mod. Phys.*, vol. 95, no. 10, pp. 956–960, 2004.
- [13] C. Zener, “Ring diffusion in metals,” *Acta Crystallogr.*, vol. 3, no. 5, pp. 346–354, 1950.
- [14] J. R. Tolchard, M. S. Islam, and P. R. Slater, “Defect chemistry and oxygen ion migration in the apatite-type materials $\text{La}_{9.33}\text{Si}_6\text{O}_{26}$ and $\text{La}_8\text{Sr}_2\text{Si}_6\text{O}_{26}$,” *J. Mater. Chem.*, vol. 13, no. 8, pp. 1956–1961, 2003.
- [15] K. Fukuda *et al.*, “Anisotropy of oxide-ion conduction in apatite-type lanthanum silicate,” *Solid State Ionics*, vol. 217, pp. 40–45, 2012.
- [16] F. Mauvy *et al.*, “Electrode properties of $\text{Ln}_2\text{NiO}_{4+\delta}$ (Ln=La, Nd, Pr),” *J. Electrochem. Soc.*, vol. 153, no. 8, p. A1547, 2006.
- [17] F. Mauvy *et al.*, “Oxygen reduction on porous $\text{Ln}_2\text{NiO}_{4+\delta}$ electrodes,” *J. Eur.*

Chapter I Introduction

- Ceram. Soc.*, vol. 25, no. 12 SPEC. ISS., pp. 2669–2672, 2005.
- [18] E. Boehm, J. M. Bassat, P. Dordor, F. Mauvy, J. C. Grenier, and P. Stevens, “Oxygen diffusion and transport properties in non-stoichiometric $\text{Ln}_{2-x}\text{NiO}_{4+\delta}$ oxides,” *Solid State Ionics*, vol. 176, no. 37–38, pp. 2717–2725, 2005.
- [19] D. C. Rapaport, R. L. Blumberg, S. R. McKay, and W. Christian, “The Art of Molecular Dynamics Simulation,” *Comput. Phys.*, 1996.
- [20] D. S. Sholl and J. A. Steckel, *Density Functional Theory: A Practical Introduction*. 2009.
- [21] A. Chroneos, D. Parfitt, J. A. Kilner, and R. W. Grimes, “Anisotropic oxygen diffusion in tetragonal $\text{La}_2\text{NiO}_{4+\delta}$: Molecular dynamics calculations,” *J. Mater. Chem.*, vol. 20, no. 2, pp. 266–270, 2010.
- [22] A. Tarancón, A. Morata, F. Peiró, and G. Dezanneau, “A molecular dynamics study on the oxygen diffusion in doped fluorites: The effect of the dopant distribution,” *Fuel Cells*, vol. 11, no. 1, pp. 26–37, 2011.
- [23] C. Chen, D. Chen, and F. Ciucci, “A molecular dynamics study of oxygen ion diffusion in A-site ordered perovskite $\text{PrBaCo}_2\text{O}_{5.5}$: Data mining the oxygen trajectories,” *Phys. Chem. Chem. Phys.*, vol. 17, no. 12, pp. 7831–7837, 2015.
- [24] G. Henkelman, B. P. Uberuaga, and H. Jónsson, “Climbing image nudged elastic band method for finding saddle points and minimum energy paths,” *J. Chem. Phys.*, vol. 113, pp. 9901–9904, 2000.
- [25] G. Kresse, “Ab initio molecular dynamics for liquid metals,” *J. Non. Cryst. Solids*, vol. 47, no. 1, p. 558, 1995.
- [26] G. Kresse and J. Hafner, “Ab initio molecular-dynamics simulation of the liquid-metalamorphous- semiconductor transition in germanium,” *Phys. Rev. B*, vol. 49, no. 20, p. 14251, 1994.
- [27] L. Noodleman, T. Lovell, W. G. Han, T. Liu, R. A. Torres, and F. Himo, *Density Functional Theory An Advanced Course*, vol. 2. 2004.
- [28] A. Chroneos, B. Yildiz, A. Tarancón, D. Parfitt, and J. A. Kilner, “Oxygen diffusion in solid oxide fuel cell cathode and electrolyte materials: Mechanistic insights from atomistic simulations,” *Energy Environ. Sci.*, vol. 4, no. 8, pp. 2774–2789, 2011.
- [29] R. Scott, M. P. Allen, and D. J. Tildesley, “Computer Simulation of Liquids,” *Math. Comput.*, 1991.
- [30] D. J. Evans and B. L. Holian, “The Nose-Hoover thermostat,” *J. Chem. Phys.*,

Chapter I Introduction

- vol. 83, no. 8, pp. 4069–4074, 1985.
- [31] H. J. C. Berendsen, J. P. M. Postma, W. F. Van Gunsteren, A. Dinola, and J. R. Haak, “Molecular dynamics with coupling to an external bath,” *J. Chem. Phys.*, vol. 81, pp. 3684–3690, 1984.
- [32] D. J. Evans and G. P. Morris, “Molecular dynamics of carbon nanotube bundles as molecular sieves,” *Comput. Phys. reports*, vol. 1, pp. 297–343, 1984.
- [33] W. Smith and T. R. Forester, “DL-POLY-2.0: A general-purpose parallel molecular dynamics simulation package,” *J. Mol. Graph.*, vol. 174, no. 7, pp. 560–568, 1996.
- [34] P. S. Crozier, “LAMMPS Molecular Dynamics Simulator,” *Tutorial*, 2011. .
- [35] J. C. Phillips *et al.*, “Scalable molecular dynamics with NAMD,” *J. Comput. Chem.*, vol. 26, no. 16, pp. 1781–1802, 2005.
- [36] B. R. Brooks *et al.*, “CHARMM: The biomolecular simulation program,” *J. Comput. Chem.*, vol. 30, no. 10, pp. 1545–1614, 2009.
- [37] H. J. C. Berendsen, D. van der Spoel, and R. van Drunen, “GROMACS: A message-passing parallel molecular dynamics implementation,” *Comput. Phys. Commun.*, vol. 91, no. 1–3, pp. 43–56, 1995.
- [38] D. A. Case *et al.*, “The Amber biomolecular simulation programs,” *J. Comput. Chem.*, vol. 26, no. 16, pp. 1668–1688, 2005.
- [39] T. Róg, M. K., H. K., and G. R. Kneller, “nMoldyn : A Program Package for a Neutron Scattering,” *J. Comput. Chem.*, vol. 24, no. 5, pp. 657–667, 2003.
- [40] W. Humphrey, A. Dalke, and K. Schulten, “VMD: Visual molecular dynamics,” *J. Mol. Graph.*, vol. 14, pp. 33–38, 1996.
- [41] Y. Hu *et al.*, “Oxygen diffusion mechanism in the mixed ion-electron conductor $\text{NdBaCo}_2\text{O}_{5+x}$,” *J. Mater. Chem.*, vol. 22, no. 36, pp. 18744–18747, 2012.
- [42] D. Parfitt, A. Chroneos, A. Tarancón, and J. A. Kilner, “Oxygen ion diffusion in cation ordered/disordered $\text{GdBaCo}_2\text{O}_{5+\delta}$,” *J. Mater. Chem.*, vol. 21, no. 7, pp. 2183–2186, 2011.
- [43] D. Parfitt, A. Chroneos, J. A. Kilner, and R. W. Grimes, “Molecular dynamics study of oxygen diffusion in $\text{Pr}_2\text{NiO}_{4+\delta}$,” *Phys. Chem. Chem. Phys.*, vol. 12, no. 25, pp. 6834–6836, 2010.
- [44] D. Steinley, “K-means clustering: A half-century synthesis,” *Br. J. Math. Stat. Psychol.*, vol. 59, no. 1, pp. 1–34, 2006.
- [45] M. D. Segall *et al.*, “First-principles simulation: Ideas, illustrations and the

Chapter I Introduction

- CASTEP code,” *J. Phys. Condens. Matter*, vol. 14, p. 2717, 2002.
- [46] P. Hohenberg and W. Kohn, “Inhomogeneous electron gas,” *Phys. Rev.*, vol. 136, no. 3B, p. B864, 1964.
- [47] W. Koch and M. C. Holthausen, *A Chemist’s Guide to Density Functional Theory*. 2001.
- [48] V. I. Anisimov, J. Zaanen, and O. K. Andersen, “Band theory and Mott insulators: Hubbard U instead of Stoner I,” *Phys. Rev. B*, vol. 44, no. 3, pp. 943–954, 1991.
- [49] S. A. Tolba, K. M. Gameel, B. A. Ali, H. A. Almossalami, and N. K. Allam, “The DFT+U: Approaches, Accuracy, and Applications,” *Density Funct. Calc. - Recent Progresses Theory Appl.*, pp. 3–30, 2018.
- [50] E. Paquet and H. L. Viktor, “Computational Methods for Ab Initio Molecular Dynamics,” *Adv. Chem.*, vol. 2018, pp. 1–14, 2018.
- [51] T. D. Kühne, “Second generation Car-Parrinello molecular dynamics,” *Wiley Interdiscip. Rev. Comput. Mol. Sci.*, vol. 4, no. 4, pp. 391–406, 2014.
- [52] R. Car and M. Parrinello, “Unified Approach for Molecular Dynamics and Density-Functional Theory,” *Phys. Rev. Lett.*, vol. 55, p. 2471, 1985.
- [53] D. Marx and J. Hutter, *Ab initio molecular dynamics: Basic theory and advanced methods*. 2009.
- [54] G. Henkelman and H. Jónsson, “Improved tangent estimate in the nudged elastic band method for finding minimum energy paths and saddle points,” *J. Chem. Phys.*, vol. 113, no. 22, pp. 9978–9985, 2000.
- [55] B. P. Uberuaga, M. Leskovar, A. P. Smith, H. Jónsson, and M. Olmstead, “Diffusion of Ge below the Si(100) surface: Theory and experiment,” *Phys. Rev. Lett.*, vol. 84, p. 2441, 2000.
- [56] W. Windl, M. M. Bunea, R. Stumpf, S. T. Dunham, and M. P. Masquelier, “First-principles study of boron diffusion in silicon,” *Phys. Rev. Lett.*, vol. 83, p. 4345, 1999.
- [57] C. Tracy and C. Liu, “Retardation of O diffusion through polycrystalline Pt by Be doping,” *Phys. Rev. B - Condens. Matter Mater. Phys.*, vol. 59, p. 16047, 1999.
- [58] T. C. Shen, J. A. Steckel, and K. D. Jordan, “Electron-stimulated bond rearrangements on the H/Si(100)-3×1 surface,” *Surf. Sci.*, vol. 446, no. 3, pp. 211–218, 2000.
- [59] T. Rasmussen, K. W. Jacobsen, T. Leffers, O. B. Pedersen, S. G. Srinivasan, and H. Jónsson, “Atomistic Determination of Cross-Slip Pathway and Energetics,”

Chapter I Introduction

- Phys. Rev. Lett.*, vol. 79, no. 19, p. 3676, 1997.
- [60] R. E. Gillilan and K. R. Wilson, "Shadowing, rare events, and rubber bands. A variational Verlet algorithm for molecular dynamics," *J. Chem. Phys.*, vol. 97, no. 3, pp. 1757–1772, 1992.
- [61] R. Elber and M. Karplus, "A method for determining reaction paths in large molecules: Application to myoglobin," *Chem. Phys. Lett.*, vol. 139, no. 5, pp. 375–380, 1987.
- [62] E. Fabbri, D. Pergolesi, and E. Traversa, "Materials challenges toward proton-conducting oxide fuel cells: A critical review," *Chem. Soc. Rev.*, vol. 39, no. 11, pp. 4355–4369, 2010.
- [63] Y. Zhu, X. He, and Y. Mo, "First principles study on electrochemical and chemical stability of solid electrolyte-electrode interfaces in all-solid-state Li-ion batteries," *J. Mater. Chem. A*, vol. 4, no. 9, pp. 3253–3266, 2016.
- [64] M. A. Subramanian, G. Aravamudan, and G. V. Subba Rao, "Oxide pyrochlores - A review," *Prog. Solid State Chem.*, vol. 15, no. 2, pp. 55–143, 1983.
- [65] S. B. Adler, "Factors governing oxygen reduction in solid oxide fuel cell cathodes," *Chem. Rev.*, vol. 104, no. 10, pp. 4791–4843, 2004.
- [66] D. J. L. Brett, A. Atkinson, N. P. Brandon, and S. J. Skinner, "Intermediate temperature solid oxide fuel cells," *Chem. Soc. Rev.*, vol. 37, no. 8, pp. 1568–1578, 2008.
- [67] N. P. Brandon, S. Skinner, and B. C. H. Steele, "Recent Advances in Materials for Fuel Cells," *Annu. Rev. Mater. Res.*, vol. 33, no. 1, pp. 182–213, 2003.
- [68] L. Malavasi, C. A. J. Fisher, and M. S. Islam, "Oxide-ion and proton conducting electrolyte materials for clean energy applications: Structural and mechanistic features," *Chemical Society Reviews*. pp. 4370–4387, 2010.
- [69] A. Boudghene Stambouli and E. Traversa, "Fuel cells, an alternative to standard sources of energy," *Renewable and Sustainable Energy Reviews*. 2002.
- [70] E. Traversa, "Toward the miniaturization of solid oxide fuel cells," in *Electrochemical Society Interface*, 2009.
- [71] D. C. Matamoros, "Thermo-mechanical properties of materials for fuel cells," 2017.
- [72] F. Lefebvre-Joud, G. Gauthier, and J. Mougín, "Current status of proton-conducting solid oxide fuel cells development," *J. Appl. Electrochem.*, vol. 39, no. 4, pp. 535–543, 2009.

Chapter I Introduction

- [73] S. J. Skinner, "Recent advances in perovskite-type materials for solid oxide fuel cell cathodes," *Int. J. Inorg. Mater.*, vol. 3, no. 2, pp. 113–121, 2001.
- [74] B. C. H. Steele, "Materials for IT-SOFC stacks - 35 years R&D: The inevitability of gradualness" *Solid State Ionics*, vol. 134, no. 1–2, pp. 3–20, 2000.
- [75] H. U. Anderson, "Review of p-type doped perovskite materials for SOFC and other applications," *Solid State Ionics*, vol. 52, no. 1–3, pp. 33–41, 1992.
- [76] H. Tsai *et al.*, "High-efficiency two-dimensional ruddlesden-popper perovskite solar cells," *Nature*, vol. 536, no. 7616, pp. 312–316, 2016.
- [77] G. Amow and S. J. Skinner, "Recent developments in Ruddlesden-Popper nickelate systems for solid oxide fuel cell cathodes," *J. Solid State Electrochem.*, vol. 10, no. 8, pp. 538–546, 2006.
- [78] A. A. Taskin, A. N. Lavrov, and Y. Ando, "Achieving fast oxygen diffusion in perovskites by cation ordering," *Appl. Phys. Lett.*, vol. 86, p. 91910, 2005.
- [79] A. Tarancón, S. J. Skinner, R. J. Chater, F. Hernández-Ramírez, and J. A. Kilner, "Layered perovskites as promising cathodes for intermediate temperature solid oxide fuel cells," *J. Mater. Chem.*, vol. 17, p. 3175, 2007.
- [80] G. Kim, S. Wang, A. J. Jacobson, L. Reimus, P. Brodersen, and C. A. Mims, "Rapid oxygen ion diffusion and surface exchange kinetics in $\text{PrBaCo}_2\text{O}_{5+x}$ with a perovskite related structure and ordered a cations," *J. Mater. Chem.*, vol. 17, p. 2500, 2007.
- [81] A. Tarancón, M. Burriel, J. Santiso, S. J. Skinner, and J. A. Kilner, "Advances in layered oxide cathodes for intermediate temperature solid oxide fuel cells," *J. Mater. Chem.*, vol. 20, p. 3799, 2010.
- [82] A. Tarancón *et al.*, " $\text{GdBaCo}_2\text{O}_{5+x}$ layered perovskite as an intermediate temperature solid oxide fuel cell cathode," *J. Power Sources*, vol. 174, p. 255, 2007.
- [83] S. Carter, A. Selcuk, R. J. Chater, J. Kajda, J. A. Kilner, and B. C. H. Steele, "Oxygen transport in selected nonstoichiometric perovskite-structure oxides," *Solid State Ionics*, vol. 197, pp. 53–59, 1992.
- [84] J. E. Sunstrom IV, K. V. Ramanujachary, M. Greenblatt, and M. Croft, "The Synthesis and Properties of the Chemically Oxidized Perovskite, $\text{La}_{1-x}\text{Sr}_x\text{CoO}_{3-\delta}$ ($0.5 \leq x \leq 0.9$)," *J. Solid State Chem.*, vol. 139, p. 388, 1998.
- [85] E. V. Antipov, A. M. Abakumov, and S. Y. Istomin, "Target-aimed synthesis of anion-deficient perovskites," *Inorganic Chemistry*. 2008.

Chapter I Introduction

- [86] S. Y. Istomin *et al.*, “Crystal Structure of the Novel Complex Cobalt Oxide $\text{Sr}_{0.7}\text{Y}_{0.3}\text{CoO}_{2.62}$,” *Chem. Mater.*, vol. 15, p. 4012, 2003.
- [87] D. Rupasov *et al.*, “Oxygen diffusion in $\text{Sr}_{0.75}\text{Y}_{0.25}\text{CoO}_{2.625}$: A molecular dynamics study,” *Phys. Rev. B - Condens. Matter Mater. Phys.*, vol. 79, no. 17, pp. 6–9, 2009.
- [88] C. A. J. Fisher and M. S. Islam, “Mixed ionic/electronic conductors $\text{Sr}_2\text{Fe}_2\text{O}_5$ and $\text{Sr}_4\text{Fe}_6\text{O}_{13}$: Atomic-scale studies of defects and ion migration,” *J. Mater. Chem.*, vol. 15, no. 31, pp. 3200–3207, 2005.
- [89] J. H. Kim, M. Cassidy, J. T. S. Irvine, and J. Bae, “Electrochemical investigation of composite cathodes with $\text{SmBa}_{0.5}\text{Sr}_{0.5}\text{Co}_2\text{O}_{5-\delta}$ cathodes for intermediate temperature-operating solid oxide fuel cell,” *Chem. Mater.*, vol. 22, p. 883, 2010.
- [90] M. Y. Avdeev, M. V. Patrakeev, V. V. Kharton, and J. R. Frade, “Oxygen vacancy formation and ionic transport in $\text{Sr}_4\text{Fe}_6\text{O}_{13+\delta}$,” *J. Solid State Electrochem.*, vol. 6, p. 217, 2002.
- [91] M. V. Patrakeev, E. B. Mitberg, I. A. Leonidov, and V. L. Kozhevnikov, “Electrical characterization of the intergrowth ferrite $\text{Sr}_4\text{Fe}_6\text{O}_{13+\delta}$,” *Solid State Ionics*, vol. 139, p. 325, 2001.
- [92] R. Bredesen, T. Norby, A. Bardal, and V. Lynam, “Phase relations, chemical diffusion and electrical conductivity in pure and doped $\text{Sr}_4\text{Fe}_6\text{O}_{13}$ mixed conductor materials,” *Solid State Ionics*, vol. 135, p. 687, 2000.
- [93] C. Korte, A. Peters, J. Janek, D. Hesse, and N. Zakharov, “Ionic conductivity and activation energy for oxygen ion transport in superlattices-the semicoherent multilayer system YSZ ($\text{ZrO}_2 + 9.5 \text{ mol\% Y}_2\text{O}_3$)/ Y_2O_3 ,” *Phys. Chem. Chem. Phys.*, vol. 10, no. 31, pp. 4623–4635, 2008.
- [94] A. Cavallaro *et al.*, “Electronic nature of the enhanced conductivity in YSZ-STO multilayers deposited by PLD,” *Solid State Ionics*, vol. 181, no. 13–14, pp. 592–601, 2010.
- [95] J. Garcia-Barriocanal *et al.*, “Colossal ionic conductivity at interfaces of epitaxial $\text{ZrO}_2\text{:Y}_2\text{O}_3/\text{SrTiO}_3$ heterostructures,” *Science (80-.)*, vol. 321, no. 5889, pp. 676–680, 2008.
- [96] O. H. Kwon and G. M. Choi, “Electrical conductivity of thick film YSZ,” *Solid State Ionics*, vol. 177, no. 35–36, pp. 3057–3062, 2006.
- [97] D. Pérez-Coll and G. C. Mather, “Electrical transport at low temperatures in dense nanocrystalline Gd-doped ceria,” *Solid State Ionics*, vol. 181, no. 1–2, pp.

Chapter I Introduction

- 20–26, 2010.
- [98] M. Cherry, M. Saiful Islam, and C. R. A. Catlow, “Oxygen Ion Migration in Perovskite-Type oxides,” *J. Solid State Chem.*, vol. 118, no. 1, pp. 125–132, 1995.
- [99] M. Yashima, K. Nomura, H. Kageyama, Y. Miyazaki, N. Chitose, and K. Adachi, “Conduction path and disorder in the fast oxide-ion conductor $(\text{La}_{0.8}\text{Sr}_{0.2})(\text{Ga}_{0.8}\text{Mg}_{0.15}\text{Co}_{0.05})\text{O}_{2.8}$,” *Chem. Phys. Lett.*, vol. 380, no. 3–4, pp. 391–396, 2003.
- [100] O. Ion, C. La, and S. Ga, “High-Temperature Powder Neutron Diffraction Study,” *J. Solid State Chem.*, vol. 143, no. 139, pp. 135–143, 1998.
- [101] A. J. Jacobson, “Materials for solid oxide fuel cells,” *Chem. Mater.*, vol. 22, no. 3, pp. 660–674, 2010.
- [102] A. Nemudry, M. Weiss, I. Gainutdinov, V. Boldyrev, and R. Schöllhorn, “Room Temperature Electrochemical Redox Reactions of the Defect Perovskite $\text{SrFeO}_{2.5+x}$,” *Chem. Mater.*, vol. 10, no. 9, pp. 2403–2411, 1998.
- [103] R. Le Toquin, W. Paulus, A. Cousson, C. Prestipino, and C. Lamberti, “Time-resolved in situ studies of oxygen intercalation into $\text{SrCoO}_{2.5}$, performed by neutron diffraction and X-ray absorption spectroscopy,” *J. Am. Chem. Soc.*, vol. 128, no. 40, pp. 13161–13174, 2006.
- [104] C. Didier, J. Claridge, and M. Rosseinsky, “Crystal structure of brownmillerite $\text{Ba}_2\text{InGaO}_5$,” *J. Solid State Chem.*, vol. 218, pp. 38–43, 2014.
- [105] A. Muñoz *et al.*, “Crystallographic and magnetic structure of $\text{SrCoO}_{2.5}$ brownmillerite: Neutron study coupled with band-structure calculations,” *Phys. Rev. B - Condens. Matter Mater. Phys.*, vol. 78, no. 5, pp. 1–8, 2008.
- [106] E. Bakken, N. L. Allan, T. H. K. Barron, C. E. Mohn, I. T. Todorov, and S. Stølen, “Order-disorder in grossly non-stoichiometric $\text{SrFeO}_{2.50}$ - A simulation study,” *Phys. Chem. Chem. Phys.*, vol. 5, no. 11, pp. 2237–2243, 2003.
- [107] S. Nakayama, T. Kageyama, and Y. Sadaoka, “Ionic Conductivity of Lanthanoid Silicates, $\text{Ln}_{10}(\text{SiO}_4)_6\text{O}_3$ ($\text{Ln} = \text{La}, \text{Nd}, \text{Sm}, \text{Gd}, \text{Dy}, \text{Y}, \text{Ho}, \text{Er}$ and Yb),” *J. Mater. Chem.*, vol. 5, pp. 1801–1805, 1995.
- [108] A. Jones, P. R. Slater, and M. Saiful Islam, “Local defect structures and ion transport mechanisms in the oxygen-excess apatite $\text{La}_{9.67}(\text{SiO}_4)_6\text{O}_{2.5}$,” *Chem. Mater.*, vol. 20, no. 15, pp. 5055–5060, 2008.
- [109] M. S. Islam, J. R. Tolchard, and P. R. Slater, “An apatite for fast oxide ion

Chapter I Introduction

- conduction,” *Chem. Commun.*, vol. 3, no. 13, pp. 1486–1487, 2003.
- [110] R. Sayers, R. A. De Souza, J. A. Kilner, and S. J. Skinner, “Low temperature diffusion and oxygen stoichiometry in lanthanum nickelate,” *Solid State Ionics*, vol. 181, no. 8–10, pp. 386–391, 2010.
- [111] A. Kushima, D. Parfitt, A. Chroneos, B. Yildiz, J. A. Kilner, and R. W. Grimes, “Interstitialcy diffusion of oxygen in tetragonal $\text{La}_2\text{CoO}_{4+\delta}$,” *Phys. Chem. Chem. Phys.*, vol. 13, no. 6, pp. 2242–2249, 2011.
- [112] J. Hermet, G. Geneste, and G. Dezanneau, “Molecular dynamics simulations of oxygen diffusion in $\text{GdBaCo}_2\text{O}_{5.5}$,” *Appl. Phys. Lett.*, vol. 97, no. 17, p. 174102, 2010.
- [113] E. Chavez, M. Mueller, L. Mogni, and A. Caneiro, “Study of $\text{LnBaCo}_2\text{O}_{6-\delta}$ (Ln = Pr, Nd, Sm and Gd) double perovskites as new cathode material for IT-SOFC,” *J. Phys. Conf. Ser.*, vol. 167, pp. 0–6, 2009.
- [114] J. A. Kilner, “Fast oxygen transport in acceptor doped oxides,” *Solid State Ionics*, vol. 129, no. 1, pp. 13–23, 2000.
- [115] A. A. Taskin, A. N. Lavrov, and Y. Ando, “Fast oxygen diffusion in A-site ordered perovskites,” *Prog. Solid State Chem.*, vol. 35, no. 2–4, pp. 481–490, 2007.
- [116] A. Maignan, C. Martin, D. Pelloquin, N. Nguyen, and B. Raveau, “Structural and Magnetic Studies of Ordered Oxygen-Deficient Perovskites $\text{LnBaCo}_2\text{O}_{5+\delta}$, Closely Related to the ‘112’ Structure,” *J. Solid State Chem.*, vol. 142, no. 2, pp. 247–260, 1999.
- [117] C. Zhu, X. Liu, C. Yi, D. Yan, and W. Su, “Electrochemical performance of $\text{PrBaCo}_2\text{O}_{5+\delta}$ layered perovskite as an intermediate-temperature solid oxide fuel cell cathode,” *J. Power Sources*, vol. 185, no. 1, pp. 193–196, 2008.
- [118] D. Chen, R. Ran, and Z. Shao, “Assessment of $\text{PrBaCo}_2\text{O}_{5+\delta} + \text{Sm}_{0.2}\text{Ce}_{0.8}\text{O}_{1.9}$ composites prepared by physical mixing as electrodes of solid oxide fuel cells,” *J. Power Sources*, vol. 195, no. 21, pp. 7187–7195, 2010.
- [119] K. D. Kreuer, “On the development of proton conducting materials for technological applications,” *Solid State Ionics*, vol. 97, pp. 1–15, 1997.
- [120] K. D. Kreuer, “Proton-Conducting Oxides,” *Annu. Rev. Mater. Res.*, vol. 33, no. 1, pp. 333–359, 2003.
- [121] N. Bonanos, “Transport properties and conduction mechanism in high-temperature protonic conductors,” *Solid State Ionics*, vol. 53–56, no. PART 2,

Chapter I Introduction

- pp. 967–974, 1992.
- [122] K. D. Kreuer, A. Fuchs, and J. Maier, “H D isotope effect of proton conductivity and proton conduction mechanism in oxides,” *Solid State Ionics*, vol. 77, no. C, pp. 157–162, 1995.
- [123] J. Hermet, M. Torrent, F. Bottin, G. Dezanneau, and G. Geneste, “Hydrogen diffusion in the protonic conductor $\text{BaCe}_{1-x}\text{Gd}_x\text{O}_{3-x/2}$ from density functional theory,” *Phys. Rev. B - Condens. Matter Mater. Phys.*, vol. 87, no. 10, pp. 1–9, 2013.
- [124] G. Geneste, A. Ottochian, J. Hermet, and G. Dezanneau, “Proton transport in barium stannate: classical, semi-classical and quantum regimes,” *Phys. Chem. Chem. Phys.*, vol. 17, no. 29, pp. 19104–19118, 2015.
- [125] É. Bévilion and G. Geneste, “Hydration properties of $\text{BaSn}_{0.875}\text{M}_{0.125}\text{O}_{3-\delta}$ substituted by large dopants (M=In, Y, Gd, and Sm) from first principles,” *Phys. Rev. B - Condens. Matter Mater. Phys.*, vol. 77, no. 18, pp. 1–11, 2008.
- [126] J. Hermet, F. Bottin, G. Dezanneau, and G. Geneste, “Thermodynamics of hydration and oxidation in the proton conductor Gd-doped barium cerate from density functional theory calculations,” *Phys. Rev. B - Condens. Matter Mater. Phys.*, vol. 85, no. 20, 2012.
- [127] E. Coulaud, G. Dezanneau, and G. Geneste, “Hydration, oxidation, and reduction of $\text{GdBaCo}_2\text{O}_{5.5}$ from first-principles,” *J. Mater. Chem. A*, vol. 3, no. 47, pp. 23917–23929, 2015.
- [128] F. Briec, G. Dezanneau, M. Hayoun, and H. Dammak, “Proton diffusion mechanisms in the double perovskite cathode material $\text{GdBaCo}_2\text{O}_{5.5}$: A molecular dynamics study,” *Solid State Ionics*, vol. 309, no. July, pp. 187–191, 2017.
- [129] R. Glöckner, M. S. Islam, and T. Norby, “Protons and other defects in BaCeO_3 : a computational study,” *Solid State Ionics*, vol. 122, no. 1–4, pp. 145–156, 1999.
- [130] T. Ishihara, Y. Yan, T. Sakai, and S. Ida, “Oxide ion conductivity in doped NdBaInO_4 ,” *Solid State Ionics*, vol. 288, pp. 262–265, 2016.
- [131] K. Fujii, M. Shiraiwa, Y. Esaki, M. Yashima, S. J. Kim, and S. Lee, “Improved oxide-ion conductivity of NdBaInO_4 by Sr doping,” *J. Mater. Chem. A*, vol. 3, no. 22, pp. 11985–11990, 2015.
- [132] K. Fujii *et al.*, “New Perovskite-Related Structure Family of Oxide-Ion Conducting Materials NdBaInO_4 ,” *Chem. Mater.*, vol. 26, no. 3, pp. 2488–2491,

Chapter I Introduction

- 2014.
- [133] H. Ubukata *et al.*, “Hydride Conductivity in an Anion-Ordered Fluorite Structure LnHO with an Enlarged Bottleneck,” *Chem. Mater.*, vol. 31, no. 18, pp. 7360–7366, 2019.
- [134] T. Broux *et al.*, “High-Pressure Polymorphs of LaHO with Anion Coordination Reversal,” *J. Am. Chem. Soc.*, vol. 141, no. 22, pp. 8717–8720, 2019.
- [135] K. Fukui *et al.*, “Characteristic fast H⁻ ion conduction in oxygen-substituted lanthanum hydride,” *Nat. Commun.*, vol. 10, no. 1, pp. 1–8, 2019.

Chapter I Introduction

Chapter II Oxygen diffusion mechanism in acceptor-doped NBIO

Abstract

Molecular dynamics simulations have been widely adopted to study oxygen ion diffusion mechanisms in materials for Solid Oxide Fuel Cells. Indeed, understanding fundamental aspects of the oxygen diffusion is important to develop new materials for this application. In this work, $\text{Nd}_{1-x}\text{AE}_x\text{BaInO}_{4-x/2}$ (AE = Ca, Sr, Ba) compounds have been studied by MD simulations focusing on oxygen diffusion mechanisms. Two general clustering methods were used, namely a convex hull classification method and a DBSCAN machine learning algorithm, to identify oxygen ion diffusion pathways. Here, relevant details are provided for an efficient use of these two approaches during MD analysis of ion conductors. The calculations show that Ca is the most favorable dopant for substituting Nd in NdBaInO_4 , while Ba is the least desired. The substitution of Nd by Ca hardly changes the pristine lattice parameters of NdBaInO_4 leading to the higher oxygen diffusion coefficient compared to the other dopants. The oxygen vacancies induced by doping mainly locate on two specific oxygen sites over four oxygen sites available. Concerning the diffusion process, jumps involving these two sites play the main role and are associated to smaller migration enthalpies. For the main diffusion path, ions migrate along the *b* (2 routes) and *c* (4 routes) directions. Some other oxygen sites can be considered as barriers for the diffusion process inducing a strong anisotropy in the diffusion process. Additionally, the residence time analysis of oxygen ions confirm that ions in different sites have different motion ability. As a whole the approach presented here can be extrapolated to other ion conductors for gaining detailed information about the diffusion process.

This work is published in Physical Chemistry Chemical Physics

<https://doi.org/10.1039/C9CP03048D>

Identification of oxygen diffusion mechanisms in $\text{Nd}_{1-x}\text{AE}_x\text{BaInO}_{4-x/2}$ (AE = Ca, Sr, Ba) compounds through molecular dynamics

II.1 Introduction

Solid Oxide Fuel Cells (SOFCs) are electrochemical devices operating at temperatures up to 1000 °C that allow converting hydrogen and air into electricity and heat with reduced emission of green-house gases compared to other more conventional power generation routes.[1,2] The high working temperature presents some advantages from the point of view of fuel tolerance and efficiency but also has some significant drawbacks such as an accelerated ageing of components. There is thus a need to find new classes of materials with enhanced electrochemical properties at 700 °C or even at lower temperatures.[3,4]

In SOFCs, understanding fundamental aspects of the oxygen diffusion mechanism is important as the oxygen transport properties at the electrodes and electrolyte play a key role in the overall cell performance.[5-11] Oxygen diffusion is nevertheless a complex process which is influenced by numerous parameters such as materials structure, composition, oxygen stoichiometry, doping, local or macroscopic elastic strain, *etc.*[1] Complementarily to experimental techniques which can be used to measure the oxygen diffusion coefficient, Molecular Dynamics (MD) simulations can also evaluate this oxygen diffusion coefficient and provide a detailed insight of the oxygen diffusion mechanism at the atomistic scale.[12-30] This possibility to correlate the macroscopic properties to atomic scale mechanisms makes MD simulations a unique technique to better understand diffusion properties.

Recently, a novel material, NdBaInO_4 , belonging to a new perovskite-related structure family was reported by Fujii *et al.*[31-33] NdBaInO_4 consists of Nd-O A-rare earth oxide and (Nd,Ba) InO_3 perovskite units and the characteristic feature of this structure is that the edge of InO_6 octahedron faces the Nd-O units.[31] Fujii *et al.* found that Nd^{3+} substitution by Sr^{2+} will decrease the activation energy of oxide-ion conduction and enhance the oxide ion conduction through the creation of oxygen vacancies. The bond valence based energy (BVE) calculations indicated

Chapter II Oxygen diffusion mechanism in acceptor-doped NBIO

two-dimensional oxide-ion diffusion in the $((\text{Nd,Sr})_2\text{O}_3)$ unit.[32] Ishihara *et al.* proved that Ti doping on In site in NdBaInO_4 is effective for increasing the oxide ion conductivity and the optimized amount of Ti was found to be around 20 mol% [34] In this case, due to donor doping effect of Ti, we can anticipate the oxygen diffusion mechanism to occur through oxygen interstitials.

The exploitation of MD simulations data can be performed so as to find the correlation between macroscopic information such as diffusion coefficients and atomic scale mechanism. For instance, mean squared displacement (MSD) analysis of the diffusing atoms is an effective way to extract the diffusion coefficient of this kind of atom.[35,36] However, normally MSD results are just of few bytes while the atoms trajectories represent hundreds of megabytes produced by MD simulations. The large amount of information including the details of atomic jump is by far less exploited [37,38], even if MSD analysis is clearly not sufficient to figure out the detailed oxygen diffusion mechanism. Clarifying oxygen diffusion mechanism remains challenging since the trajectories dataset is rather big (several hundreds of Mb) and the oxygen diffusion pathway may involve different crystallographic sites with non-equivalent contributions. A number of techniques have been developed to reduce the dimensionality of MD simulations, including linear methods such as principal component analysis, and nonlinear methods such as diffusion maps, isomaps, local linear embedding.[39-44] These approaches have been primarily used in the protein folding and nucleic acid simulations. Ciucci *et al.* proposed data-mining molecular dynamics simulations in the case of ion-conducting compounds.[45-47] With this method, atoms trajectories information were much more effectively utilized. In their work, atoms jump between cages of La-substituted A-sites in BaFeO_3 were studied. They found that La tends to decrease the concentration of oxygen vacancies and lowers the activation energy of local oxygen migration.[46] They also used the k-means clustering algorithm to analyze the oxygen atoms jump mechanism in $\text{PrBaCo}_2\text{O}_{5.5}$. Their results suggest that oxygen transport is fast within the CoO_2 layers while $\text{PrO}_{0.5}$ layers work as oxygen vacancy reservoirs.[47] This fine trajectory analysis confirmed and completed previous results obtained also through MD simulations and neutron diffraction on $\text{GdBaCo}_2\text{O}_{5+x}$ and on $\text{NdBaCo}_2\text{O}_{5+x}$ compounds.[13,27,29]

In this work, $\text{Nd}_{1-x}\text{AE}_x\text{BaInO}_{4-x/2}$ ($\text{AE}=\text{Ca}, \text{Sr}, \text{Ba}$) systems are studied by molecular dynamics simulations and has been chosen as a particular case of ion-conducting

Chapter II Oxygen diffusion mechanism in acceptor-doped NBIO

compound. Even if the presence of Indium in this compound represents a clear obstacle for a widespread use in SOFCs, the complexity of its structure constitutes an interesting playground for exploring the efficiency of two MD analysis methods used in this work. Namely, convex hull classification method (CHC) and Density-Based Spatial Clustering of data (DBSCAN) were used to associate precisely oxygen positions to specific crystallographic sites and to analyse the trajectories of diffusing ions. Previous works on doped NdBaInO_4 , in particular the one from Kuang *et al.*, allowed identifying the role played by the different oxygen atoms and already identified an anisotropy in the diffusion process.[33] In the present study, we provide more quantitative information regarding the oxygen diffusion process and a precise description on how to use concretely the two classification methods mentioned above to analyze MD calculations. The use of such classification methods allows obtaining the following parameters in a straightforward way: occupancy rates, jumps between crystallographic sites, specific site-to-site migration enthalpy, residence time. A detailed oxygen ion diffusion mechanism could then be proposed, based on the fine analysis on oxygen ions trajectories and the discussion of dopant influence on the diffusion properties.

II.2 Methods

In NdBaInO_4 (NBIO), as shown in **Figure 2.1**, there are seven independent sites, namely Nd, Ba, In, O1, O2, O3, and O4, which are all in the general Wyckoff positions of the monoclinic structure, with space group $P2_1/c$. Each Wyckoff position will produce 4 equivalent sites *i.e.* 28 ions totally in one-unit cell.[31] The four O1 sites in the cell are named as O1a, O1b, O1c and O1d (The same rule is also adopted for the other oxygen sites).

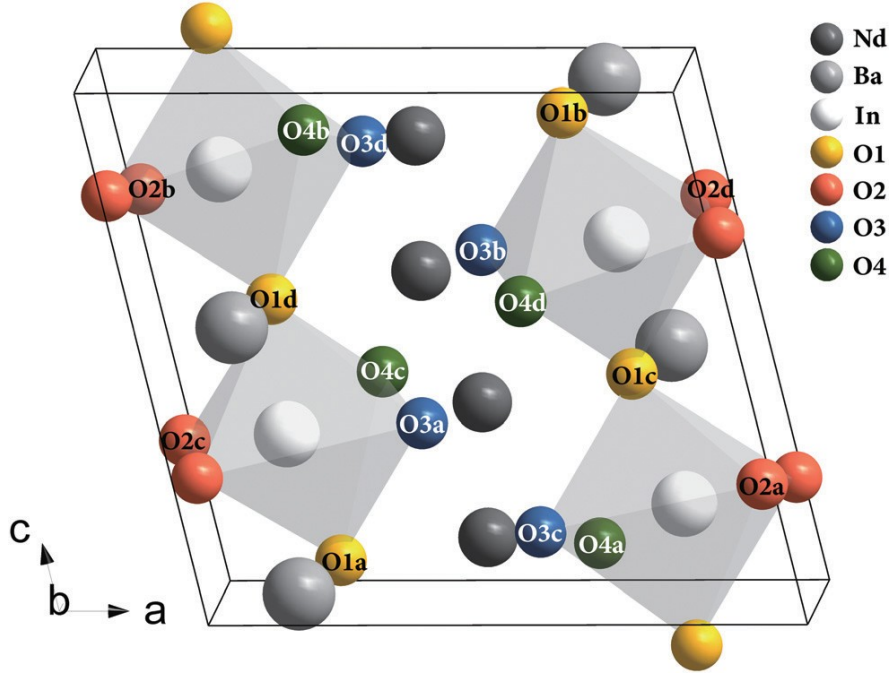


Figure 2.1 The unit cell information of NBIO system.

II.2.1 MD simulation details

MD simulations were performed using the DLPOLY classic code.[48] The chemical formula of the compound was $\text{Nd}_{1-x}\text{AE}_x\text{BaInO}_{4-x/2}$ and simulations were performed in a $3 \times 4 \times 4$ supercell. The elements substituting Nd are the 3 Alkaline Earth metal, Ca, Sr, Ba; the dopant concentrations were $x=6.25\%$, 9.375% , 12.5% , 15.625% and 18.75% . Five simulation temperatures (1500K, 1600K, 1700K, 1800K and 1900K) were adopted. Three starting configurations were employed. Besides dopants and vacancies were distributed randomly in each starting configuration. Averaging the results on different starting configurations were performed to strengthen the calculation reliability. The interactions between ions were described by a long-range Coulombic term calculated by Ewald Summation, and a short-range Buckingham pair potential. For Coulombic interactions, formal charges of +3, +2 +3 and -2 for Nd, AE, In and O ions were used respectively. The Buckingham potential used to describe the short-range interactions is described by:

$$\varphi_{ij} = A_{ij} \exp\left(-\frac{r_{ij}}{\rho_{ij}}\right) - \frac{C_{ij}}{r_{ij}^6} \quad (2.1)$$

Chapter II Oxygen diffusion mechanism in acceptor-doped NBIO

Where r is the distance between the ions i and j , and A_{ij} , ρ_{ij} , C_{ij} are potential parameters specific to each ion pair whose values are given in **Table 2.1**. The set of potentials was taken from previous studies, which were shown to reproduce correctly oxide materials properties.[49-51] As a proof of the potential validity, an energy minimization approach was employed using the GULP code [52] to determine the pristine lattice parameters ($a=9.038 \text{ \AA}$, $b=6.009 \text{ \AA}$, $c=8.308 \text{ \AA}$, $\beta=103.674^\circ$), which are within 0.66% the ones found experimentally ($a=9.095 \text{ \AA}$, $b=6.049 \text{ \AA}$, $c=8.256 \text{ \AA}$, $\beta=103.404^\circ$).[31]

Interactions	A / eV	$\rho / \text{\AA}$	C / eV \AA^6
$\text{Nd}^{3+} - \text{O}^{2-}$	1379.9	0.36072	22.59
$\text{Ca}^{2+} - \text{O}^{2-}$	1228.9	0.3372	0.00
$\text{Sr}^{2+} - \text{O}^{2-}$	959.1	0.3721	0.00
$\text{Ba}^{2+} - \text{O}^{2-}$	931.7	0.3949	0.00
$\text{In}^{3+} - \text{O}^{2-}$	1495.6	0.3310	4.325
$\text{O}^{2-} - \text{O}^{2-}$	22764.30	0.1490	43.00

Table 2.1 Inter-ionic Buckingham potentials used for molecular dynamics calculations. M-O interactions are taken from: Nd-O, O-O [49], Ca-O, Sr-O and Ba-O [50], In-O [51].

Each system was first equilibrated at the desired temperature and zero pressure for 20,000 time steps (with a time step duration of 0.5 fs) in the isothermal-isobaric ($N\sigma T$) ensemble with Nose-Hoover thermostat. Afterwards, the equilibrium lattice parameters were calculated with 80,000 time steps more. Then, simulations were performed in the NVT mode during 100,000 time steps. Finally, NVE simulations were realized for 2,000,000 time steps. All the ions trajectories coordinates were dumped every 1000 time steps to the trajectory file. Some input files examples have been added in the supplementary information file.

II.2.2 Data processing methods

II.2.2.1 Producing one complete information cell

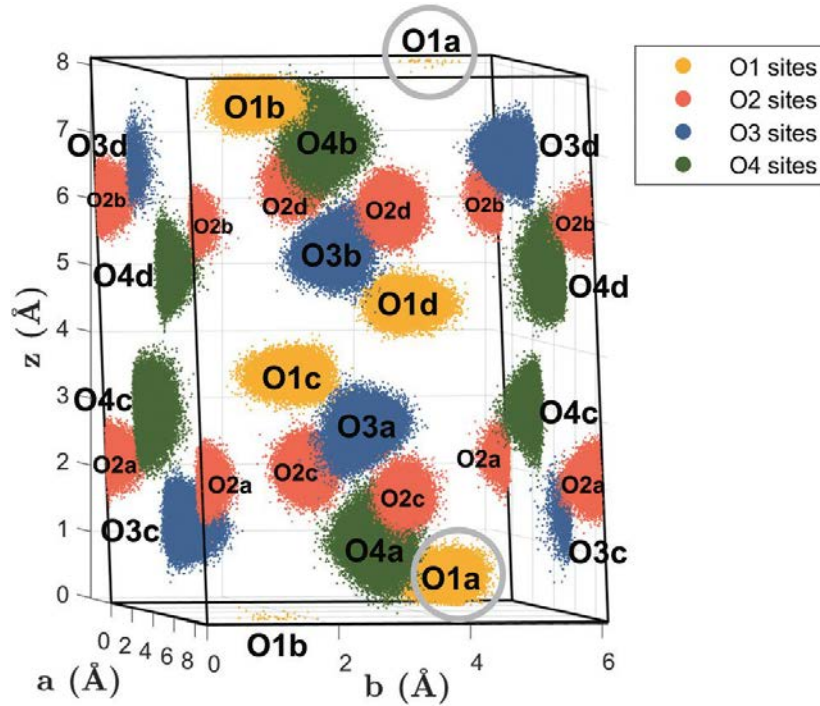


Figure 2.2 The complete information cell of NBIO at 1500K. After *NVE* simulation, a set of trajectories for all ions in the supercell are obtained. When considering ion trajectories and plotting all the ionic positions obtained all along the simulations, a significant amount of “dots” will be observed around crystallographic sites defining the so-called clusters. Moreover, if we refold the supercell to plot all the ionic positions in the original cell, these clusters will become even more obvious.

After *NVE* steps, we obtained all the trajectories coordinates of all ions at each 1000 time steps in the $3 \times 4 \times 4$ supercell. The oxygen ions trajectories could be refolded in the original cell according to periodical boundary conditions, creating the "complete information cell" as shown in **Figure 2.2**. (The matlab code for producing these data is presented in supporting information). In these simulations, considering 16 O ions per unit cell, 48 unit cells in the supercell, and 2000 dumped records, there are $16 \times 48 \times 2000 = 1,536,000$ dots representing oxygen ions positions. In this complete information cell, 30 clusters (see above) can be found: 6, 12, 6, 6 for O1, O2, O3 and O4 respectively, instead of 16 as expected from Wyckoff positions. This difference comes from the fact that several sites split into two or four after applying periodical boundary conditions. For instance, the two clusters in **Figure 2.2** in grey circles belong to the same O1a site. Each site, including O1c, O1d, O3a, O4a and O4b will present just one cluster. Both O2a and

Chapter II Oxygen diffusion mechanism in acceptor-doped NBIO

O2b have 4 clusters because these two ions are close to the edges of unit cell. For the rest of oxygen sites, each site will present 2 clusters.

II.2.2.2 Classification methods

The complete information cell of NcBIO c18.75% at 1500K is shown in **Figure 2.3** and in **Figure 2.4**. Here the notation NcBIO c18.75% stands for a $\text{Nd}_{1-x}\text{AE}_x\text{BaInO}_{4-x/2}$ compound where the Ca concentration is 18.75%. A Similar notation is used for $\text{Nd}_{1-x}\text{Ba}_x\text{BaInO}_{4-x/2}$ (NbBIO) and $\text{Nd}_{1-x}\text{Sr}_x\text{BaInO}_{4-x/2}$ (NsBIO). Once complete information cell was created, two classification methods were used to associate precisely oxygen positions to specific crystallographic sites.

II.2.2.2.1 Convex hull classification method (CHC)

In computational geometry, given P a set of n points in 3D, the convex hull of P, $\text{CH}(P)$, is the smallest polyhedron that contains all the elements of P in the interior of $\text{CH}(P)$. [53] Numerous efficient algorithms were proposed for computing the convex hull, such as Gift wrapping, Graham scan, and Quickhull *etc.* [53,54] Convex hulls were widely applied in a number of research areas, including statistics, pattern recognition, image processing, geographic information system and game theory *etc.*

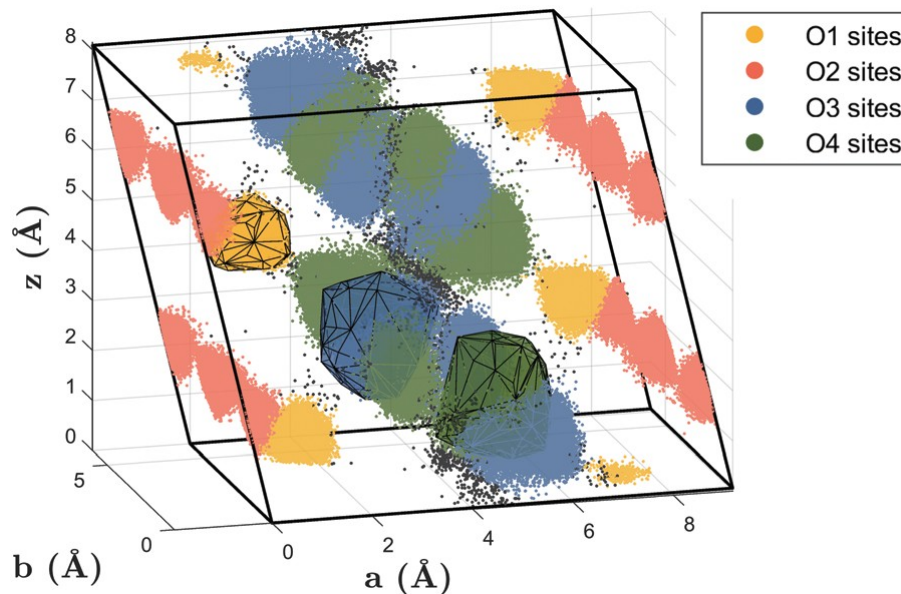


Figure 2.3 This picture is the complete information cell of NcBIO c18.75% at

Chapter II Oxygen diffusion mechanism in acceptor-doped NBIO

1500K. It also shows the clustering result after convex hull classification using the standard NBIO at 1900K. The color of dots represent which convex hull this dot belongs to. The black dots are interstitial ions. Only the convex hull of O1d, O3a and O4a have been drawn, the others are omitted for the sake of clarity.

According to the MSD curves (see below) of the oxygen ions in undoped NBIO, the oxygen ions do not diffuse at any temperature. Therefore, in the complete information cell of pure NBIO at 1500K in **Figure 2.2**, each cluster is a collection of trajectories of oxygen ions that simply vibrate around their equilibrium position. The geometrical boundary of the three-dimensional convex hull formed by ion clusters can thus be used to define the equilibrium positions. Points which are inside or on the surface of the convex hull will be considered as belonging to the crystallographic site. Points which are outside any convex hull will be regarded as interstitials.

Thirty oxygen ion clusters in NBIO at 1900K are found and chosen as the standard convex hulls. (**Figure S2.1**) Once these clusters are chosen, a 15% volume expansion is imposed to convex hulls for ensuring a good association of oxygen ions.

It is worth noting that the definition parameters of standard convex hull has to be tuned. Indeed, with a temperature increase, the amplitude of vibration of oxygen ions on their equilibrium position also increases, resulting in bigger volume for oxygen ions clusters and thus in bigger convex hull. By choosing NBIO 1900K as the standard, we thus ensure that the convex hulls obtained at this higher temperature contain those obtained at lower temperature. The reason for the expansion of convex hull by 15% reflects the fact that the addition of AE will favour the motion of oxygen ions. It is reasonable to slightly expand the volume of the pure NBIO convex hulls to describe the equilibrium position of doped systems while making sure the convex hulls do not overlap. (The matlab code of convex hull classification is annexed in supporting information).

II.2.2.2.2 Density-based spatial clustering of applications with noise (DBSCAN)

DBSCAN is one of the most common clustering algorithms used in unsupervised machine learning to separate clusters of high density from clusters of low

Chapter II Oxygen diffusion mechanism in acceptor-doped NBIO

density.[55] Each cluster is the largest set of points connected by density, and the shape of clusters can be arbitrary. This point is important since it allows defining a crystallographic site without any assumption on the shape of the trajectory followed by a vibrating atom. Interstitials are defined as points in the database not belonging to any cluster. There are two parameters to be defined in the clustering process, *Eps* (distance threshold) and *MinPts* (minimum cluster size, which must be chosen at least 3). [55-57] These two parameters should be modified prudentially. For instance, when the minimum cluster size is unchanged, if the value of distance threshold is too large, it causes many clusters which should be different to merge. If the distance threshold is too small, it will split a unique cluster into several clusters. On the opposite, when the distance threshold is kept fixed, if the value of minimum cluster size is too large, more outliers will be observed and if the minimum cluster size is too small, it will lead to the discovery of a large number of interstitial points. [55,56]

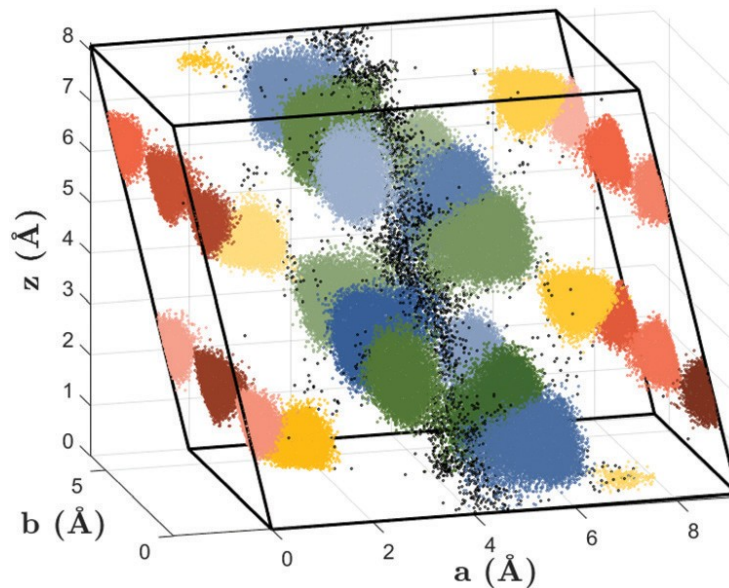


Figure 2.4 This picture is the complete information cell of NcBIO c18.75% at 1500K. It also shows the clustering results after applying DBSCAN. 30 clusters have been found. The color slightly varies in 30 clusters. The O1 is presented by a series of yellow colors, O2 with red series, O3 with blue series, O4 with green series respectively. The black dots are interstitial ions.

In our cases, beside these two parameters, the sample size appears as another important variable parameter. When the sample size is large, *e.g.*, the number of

Chapter II Oxygen diffusion mechanism in acceptor-doped NBIO

dots is 1,500,000 in NcBIO c18.75%, the calculation requires larger memory resulting in a very low clustering speed. DBSCAN is in this case inefficient. It is thus necessary to divide the sample into several sub-samples. The classification process steps using DBSCAN are:

1. Obtaining the complete information cell of a certain doped system at a certain temperature.
2. Adjusting the DBSCAN parameters to have the required number of clusters in the same complete information cell.
3. Associating all clusters to specific crystallographic sites precisely. Oxygen ions not belonging to any cluster are considered as interstitial ions.

As shown in **Figures 2.3** and **2.4**, these two methods will generate similar results. By associating one given oxygen ion with time and identified cluster, the precise trajectory of this ion from site to site can be followed. Furthermore, the analysis of occupancy rates, diffusion mechanism of the oxygen ion and residence time can be implemented in a straightforward way. After a proper adjustment, these two methods can thus be adopted in the analysis of molecular dynamics simulations of any ion-conducting material.

The convex hull method supposes to focus on how to choose the reference convex hull, while DBSCAN supposes to pay more attention on the selection of the clustering parameters. The advantages of the convex hull method are (1) intuitiveness and efficiency. (2) a more accurate definition of oxygen cluster. The main disadvantage is that the selection criteria of the convex hull is not fixed. Besides the position of the standard convex hull needs to be carefully determined when the lattice parameters change greatly. The advantage of DBSCAN is to find spatial clusters of arbitrary shapes; Unlike standard convex hull which should be transposed with care for different compositions, each cluster can be identified and its equilibrium position can be obtained automatically. DBSCAN also has some weaknesses: (1) DBSCAN is inefficient when the sample size is too large since it supposes to consider all the positions for performing a complete clustering (2) It is not easy to find the good combination of adjustable parameters. A bad choice may for instance lead to the collapse of two sites, due to the diffusion process.

II.3 Results and discussions

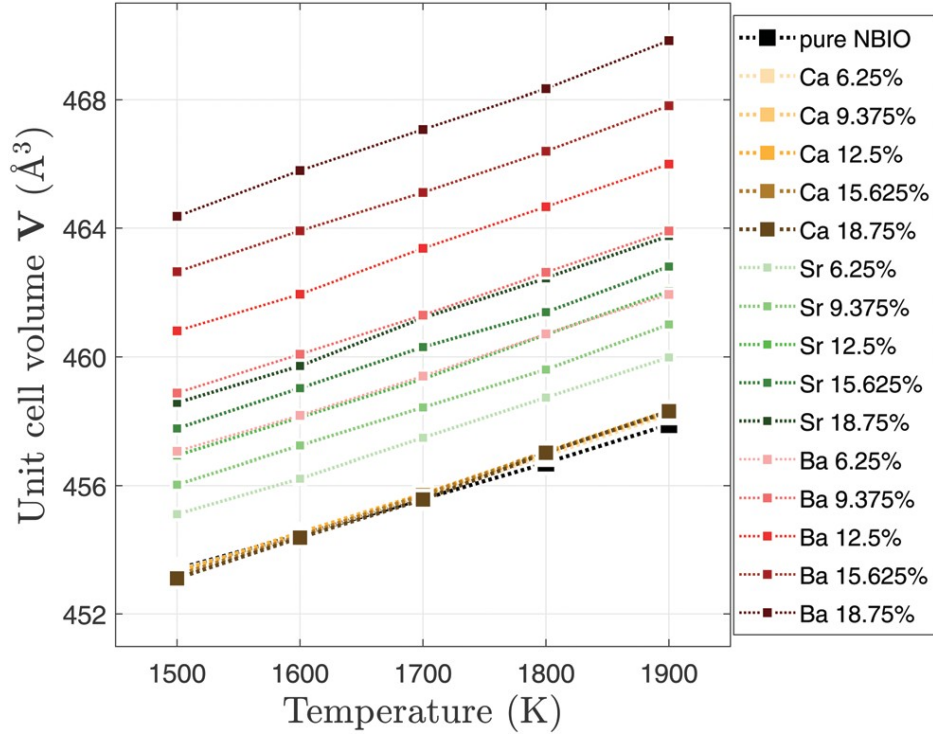


Figure 2.5 The averaged unit cell volume of pure and AE-doped NBIO as a function of temperature and dopant amount from three starting configuration. (AE= Ca, Sr, Ba)

After *NPT* simulations, the lattice parameters and unit cell volume are obtained as a function of dopant concentrations and temperatures. More detailed *a*, *b*, *c* lattice parameters are presented in **Figure S2.2**. As shown in **Figure 2.5**, the volume of the unit cell of all systems increase with temperature and differs with significant differences among the three dopants. The addition of Ca element hardly changes the unit cell volume, while the distortion of unit cell is much more pronounced with the addition of Sr and Ba. Cells parameters evolve accordingly to the difference of ion size between dopant and Nd ion, *i.e.*, $r_{Ba^{2+}} = 1.42 \text{ \AA} > r_{Sr^{2+}} = 1.26 \text{ \AA} > r_{Ca^{2+}} = 1.12 \text{ \AA} \approx r_{Nd^{3+}} = 1.109 \text{ \AA}$ in 8-fold environment. [58] The unit cell volume of pure NBIO at 300K is 441.822 \AA^3 from experimental results of Fujii [31], which fits the NBIO curve trends of **Figure 2.5** well. Besides, the unit cell volume at 300K of $Nd_{0.9}Sr_{0.1}BaInO_{3.95}$ (443.184 \AA^3) is slightly larger than that of $NdBaInO_4$, which also fits the **Figure 2.5**. [32]

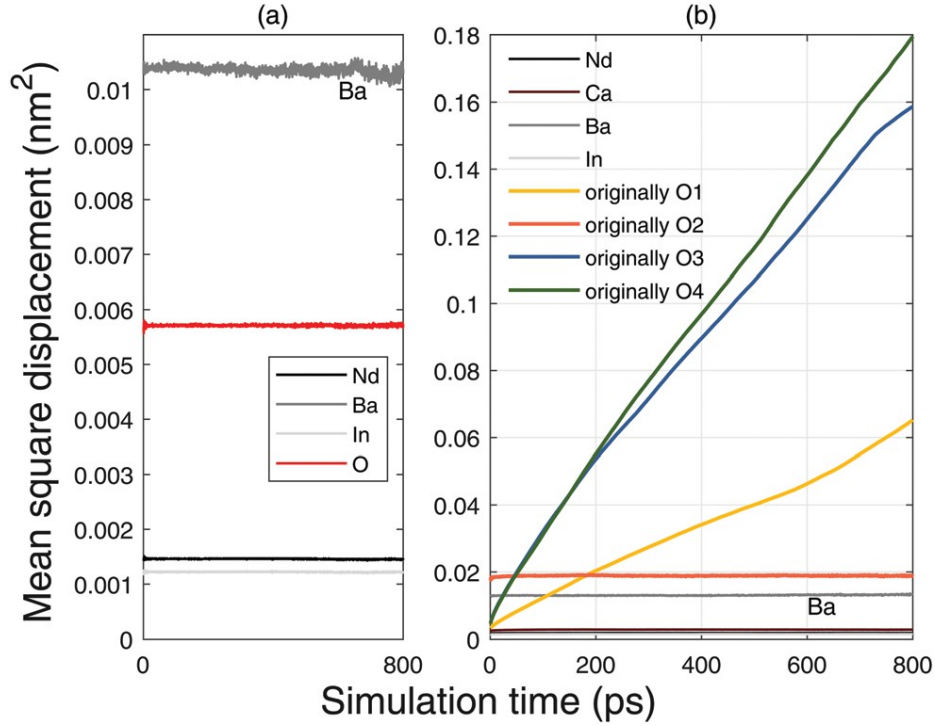


Figure 2.6 (a) The MSD curves of NBIO at 1500K. (b) The MSD curves of NcBIO c18.75% at 1500K.

After *NVE* simulations, the MSD curves were obtained and are drawn in the **Figure 2.6**. It shows that the metal cations only vibrate around their equilibrium position. Compared with pure NBIO, oxygen ions in 18.75% Ca-doped NBIO (NcBIO c18.75%) present a significant diffusion coefficient. The diffusion coefficient of oxygen ions increases with the increase of temperature and the dopant amount. Oxygen diffusion coefficients can be extracted from MSD curves by applying the Einstein law.

$$\langle |r_i(t) - r_i(0)|^2 \rangle = 6Dt + \text{constant} \quad (2.2)$$

Where $r_i(t)$ is the position of the i -th particle at time t , $|r_i(t) - r_i(0)|$ is the displacement of the oxygen ion i from its initial position, t is the simulation time, D is the oxygen diffusion coefficient. The constant value is generally associated with the purely vibrational motion of ions around their crystallographic site. In our case, the diffusion coefficient was fitted in the 200-600 ps time range, where a linear behaviour was observed. Furthermore, D can be expressed as a function of temperature T through:

$$D = D_0 \cdot \exp\left(-\frac{E_A}{k_B T}\right) \quad (2.3)$$

Where k_B being the Boltzmann constant, D_0 a pre-exponential factor and E_A the activation energy of the diffusion process.

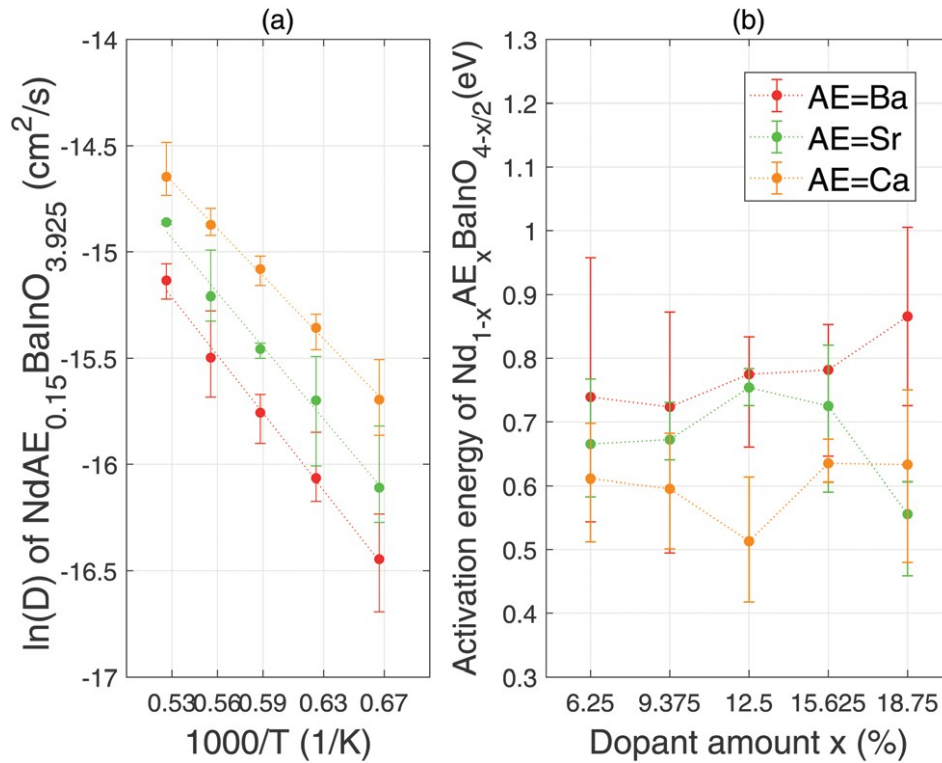


Figure 2.7 (a) Calculated logarithm of oxygen diffusion coefficients as a function of the inverse of temperature as extracted from MD simulations for NbBIO b15.625% (red circle), NsBIO s15.625% (green circle), NcBIO c15.625% (orange circle). **(b)** Activation energy for oxygen diffusion as a function of dopant amount. All these data were averaged by three starting configurations.

The Arrhenius plot for diffusion versus temperature of NbBIO b15.625%, NcBIO c15.625%, and NsBIO s15.625% are shown in **Figure 2.7(a)**. This figure clearly shows that Ca-doping favours more oxygen diffusion compared to Sr-doping, which in turn favours more diffusion compared to Ba-doping. According to **equation 2.3**, the activation energy for oxygen diffusion can be obtained by fitting the logarithm of oxygen diffusion coefficient with the reciprocal of temperature. The activation energy is shown in **Figure 2.7(b)**. The activation energy values of Ca^{2+} doped NBIO are the smallest compared to those of Sr^{2+} and Ba^{2+} -doped compounds. Whatever the dopant is, the activation energy does not evolve monotonically with dopants concentrations. This fit only partially the experimental

Chapter II Oxygen diffusion mechanism in acceptor-doped NBIO

results of Fujii: the total electrical conductivity of $\text{Nd}_{0.9}\text{Sr}_{0.1}\text{BaInO}_{3.95}$ ($\sigma_{ion} = 7.7 \times 10^{-4} \text{ S cm}^{-1}$) is higher than that with higher Sr-doping levels system ($\text{Nd}_{1-x}\text{Sr}_x\text{BaInO}_{4-x/2}$, $x=0.2, 0.3$).[32] Overall, Ca^{2+} is the most favorable dopant to obtain high diffusion coefficient, which can be attributed to the smaller size mismatch between the dopants and the host Neodymium ion.[58]

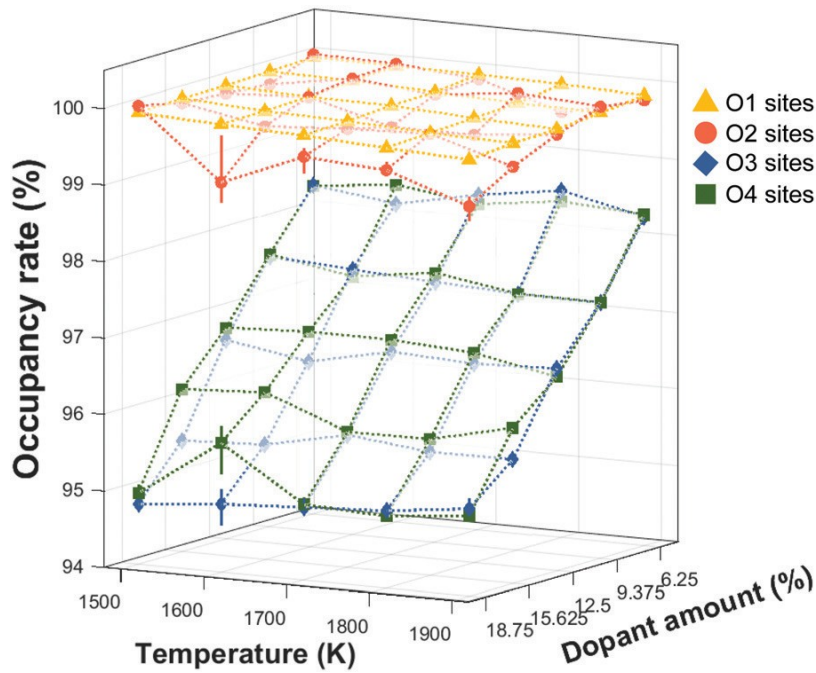
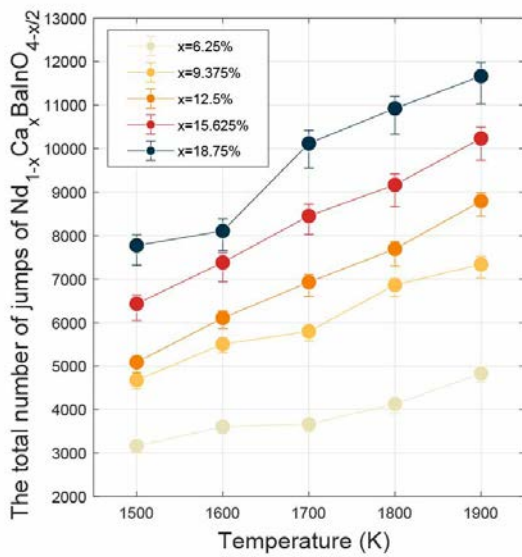


Figure 2.8 The occupation fraction of NbIO systems as a function of dopant amount and system temperature. Error bar are only shown in dopant amount= 18.75% plane.

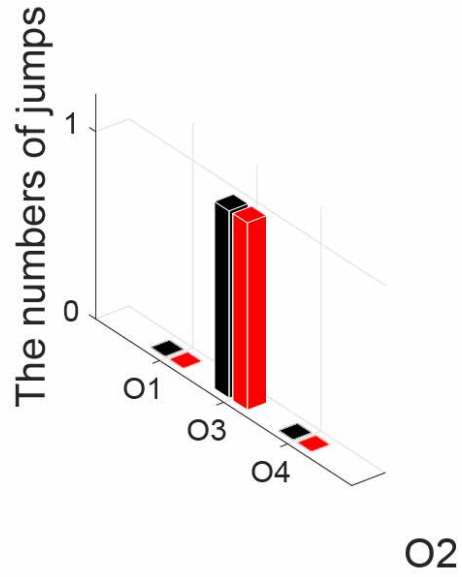
Using convex hull classification and DBSCAN, the trajectories of each oxygen ion could be followed. (one trajectory of a representative oxygen ion was given in **Figure S2.3**.) The mean occupancies of all four oxygen sites in Ca-doped NBIO as a function of temperature and dopant concentration are presented in **Figure 2.8**. As shown previously in **Figure 2.6(b)**, the higher slopes in MSD curves were observed for ions originally located in the O3 and O4 sites, while originally O1 ions show a smaller slope and originally O2 ions show a null-slope MSD curve. One has to keep in mind here that these original labels for oxygen ions lose their meaning if a diffusion process exists. From the occupancy analysis, O1 and O2 sites keep a very high occupancy rate. Concretely, the occupancy rate of O1 diminishes slightly with

Chapter II Oxygen diffusion mechanism in acceptor-doped NBIO

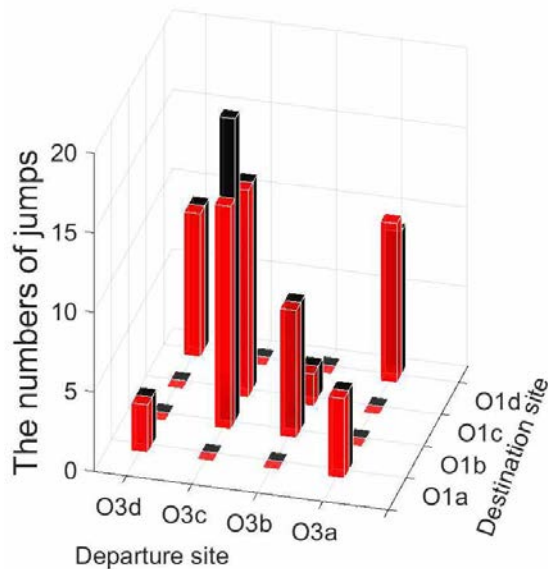
the increase of temperature and dopant amount while the value of O2 occupancy which is very close to 1 fluctuates within a small range. On the contrary, the occupancy rates of O3 and O4 are lower and they decrease linearly with increasing dopant amount. These results indicate that the vacancies concentrate on O3 and O4 sites. This also suggests that O3 and O4 sites play a much more important role than O1 and O2 sites in the diffusion process.



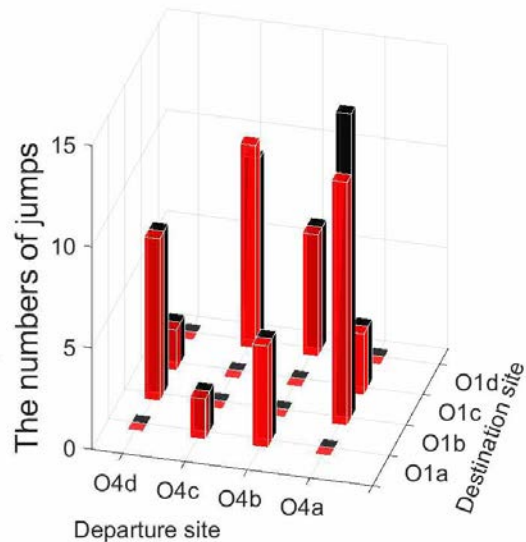
(a)



(b)



(c)



(d)

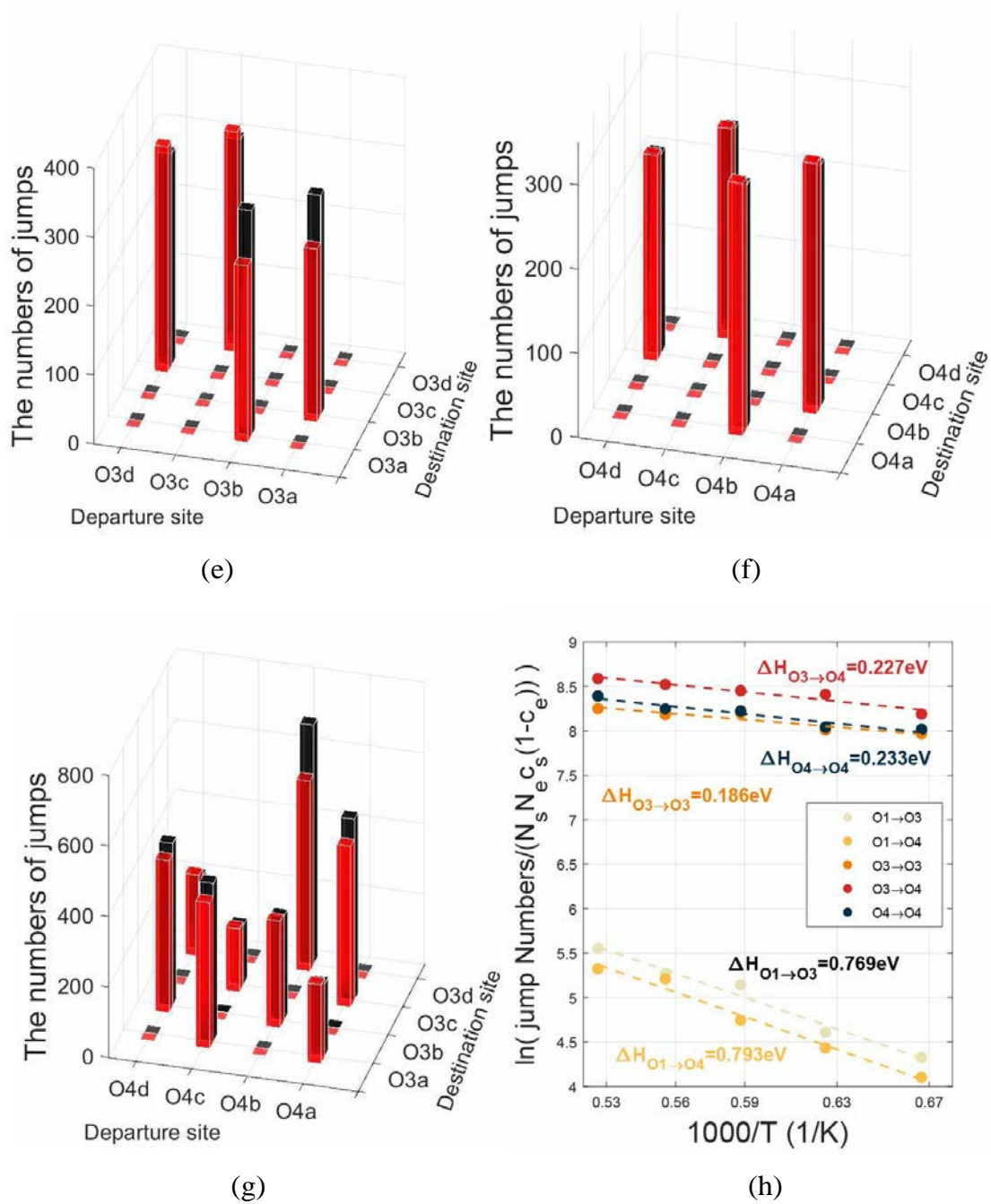


Figure 2.9 (a) Total number of oxygen ions jumps as a function of temperature and dopant amount in the NcBIO system. (b)-(g) Jumps numbers between two different sites in NcBIO c18.75% 1500K. Red columns represent results by convex hull classification methods (CHC), while black columns stand for DBSCAN ones. (h) The Arrhenius representation of total ion plotted number divided by coefficient against the reciprocal of temperature in NcBIO c18.75%.

Chapter II Oxygen diffusion mechanism in acceptor-doped NBIO

To figure out the oxygen diffusion path, NcBIO c18.75% was selected since Ca-doped NBIO has the lowest diffusion activation energy and the highest diffusion coefficient. The trajectories were analysed by making statistics on jumps between different crystallographic sites as a function of temperature and dopant amount in the NcBIO system. Results are shown in **Figure 2.9(a)**. [59] Logically, the total number of jumps increases with temperature and dopant amount. Here we give the precise analysis of jumps for NcBIO c18.75% at 1500K. The figures from **Figure 2.9(b-g)** describe jumps between two different sites, considering both convex hull and DBSCAN classification methods. The results from both methods are very close. In **Figure 2.9(b)**, there is only one jump between O2 and O3 sites (the total jumps number being about 8000) and no jump from O2 to O1, O4 sites, proving that O2 sites have almost no contribution in the diffusion process. The jumps involving O1 sites occupy a small proportion of the total jumps number (about 2.80%), suggesting that ions O1 sites also play a limited role in oxygen ion diffusion. The percentage that O3 ↔ O3 jumps and O4 ↔ O4 jumps over the total number of jumps is 14.39% and 13.63% respectively. Finally, jumps from O4 to O3 sites are shown in **Figure 2.9(g)**. These jumps between O4 and O3 sites undertake a crucial role in the ion conduction. The number of jumps between O3 and O4 indeed represents 69.17% over the total number of jumps. (Similar analysis results for compounds with Ca concentration of 9.375% and 15.625% are provided as supplementary information in **Figure S2.4** and **Figure S2.5**.)

Since the oxygen diffusion is a thermally-activated process, the temperature dependence can be analysed through an Arrhenius law. Previously, it was shown that the total number of jumps can be written as follows: [47,60]

$$T \propto N_s N_e c_s (1 - c_e) \exp\left(-\frac{\Delta H_m}{k_B T}\right) \quad (2.4)$$

Where T is the total number of jumps, the subscript s and e represent the starting sites and ending sites, and N_s and N_e are the numbers of equivalent sites per formula unit. c_s and c_e are the site occupancy fractions which can be obtained from **Figure 2.8**. ΔH_m is the migration enthalpy, k_B is the Boltzmann constant, and T is the system temperature. The Logarithm of total jumps numbers divided by the factor $N_s N_e c_s (1 - c_e)$ versus the reciprocal of the temperature are shown in **Figure 2.9(h)**. The average migration enthalpy from the original sites to destination sites

Chapter II Oxygen diffusion mechanism in acceptor-doped NBIO

can be achieved by fitting the slopes. The calculation results demonstrate that $\Delta H_{O1 \rightarrow O3}$, $\Delta H_{O1 \rightarrow O4}$ are 0.769 eV and 0.793 eV, which are much higher than $\Delta H_{O3 \rightarrow O3}$, $\Delta H_{O3 \rightarrow O4}$ and $\Delta H_{O4 \rightarrow O4}$ equaling to 0.186 eV, 0.227 eV and 0.233 eV, respectively. The values of the latter three migration enthalpies are close to each other, which again confirms the fact that O3 and O4 sites are the main sites involved in the oxygen ion diffusion.

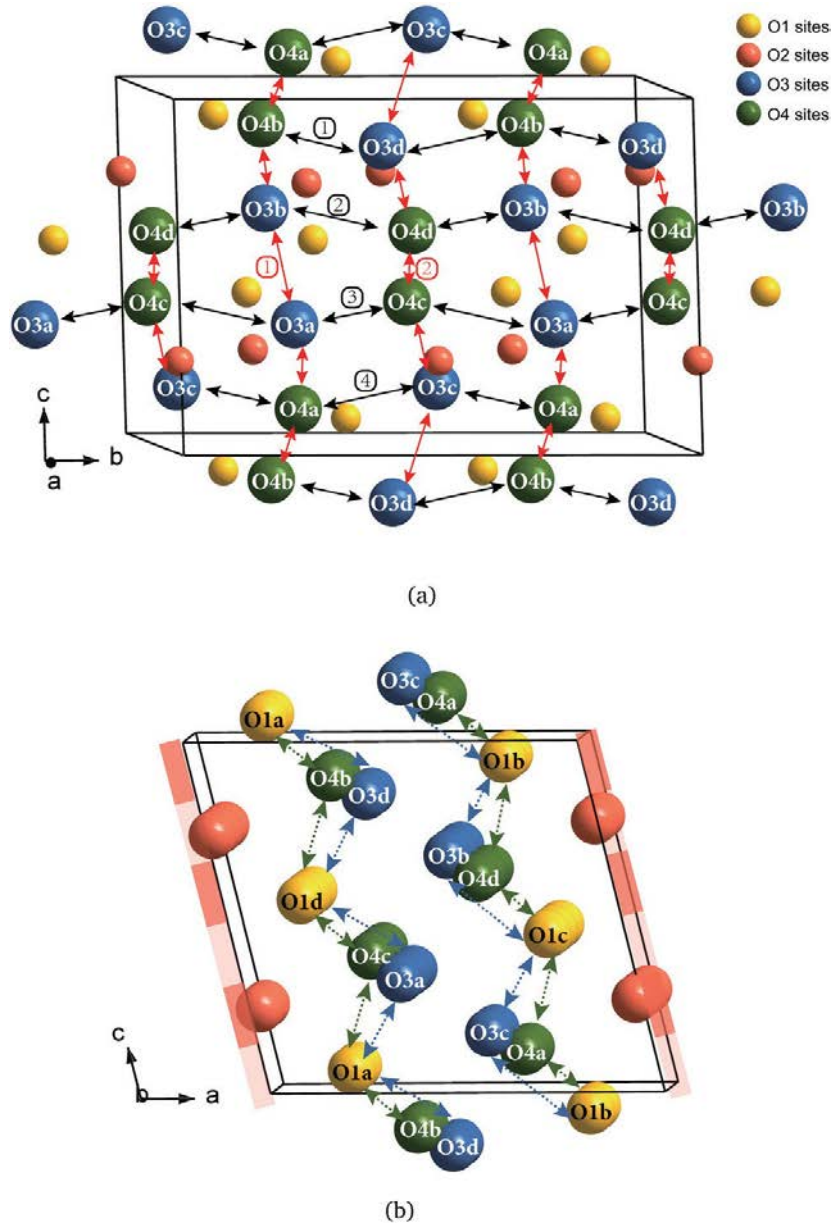


Figure 2.10 (a) Viewing the oxygen diffusion path along the *a* direction. Solid arrows represent the main diffusion path. (b) Viewing the oxygen diffusion path along the *b* direction. Dotted arrows represent secondary diffusion paths. Each O1 site will interact with the most nearest four sites (two O3 and two O4). O2 sites

Chapter II Oxygen diffusion mechanism in acceptor-doped NBIO

(Red ball) block the diffusion along the *a* direction.

Now, a detailed explanation of the diffusion path of oxygen ions in NcBIO can be obtained. $O3 \leftrightarrow O3$, $O3 \leftrightarrow O4$ and $O4 \leftrightarrow O4$ jumps represent more than 97.19% of the total number of jumps. Connecting sites where jumps exist by arrows, the **Figure 2.10(a)** is obtained in which the cell has been expanded along *b* direction for sake of clarity. Two main diffusion paths can be identified: one roughly along *b* direction, represented by black arrows, another along the *c* direction shown by red arrows. Along *b* direction there are four oxygen ions diffusion paths specifically:

1. $O4b \leftrightarrow O3d$
2. $O4d \leftrightarrow O3b$
3. $O4c \leftrightarrow O3a$
4. $O4a \leftrightarrow O3c$

Along the *c* direction, two detailed diffusion paths are:

1. $O4a \leftrightarrow O4b \leftrightarrow O3b \leftrightarrow O3a$
2. $O3c \leftrightarrow O3d \leftrightarrow O4d \leftrightarrow O4c$

The proposed oxygen ion diffusion path is also valid for Sr- and Ba-doped NBIO. In general, the total jump numbers along *b* and *c* directions are not fully equivalent, *e.g.*, the jumps number of *c* direction in NcBIO c18.75% 1500K is larger by 10.88%, comparing to *b* direction. In addition to the main diffusion route of **Figure 2.10(a)**, **Figure 2.10(b)** shows the secondary conduction path involving the O1 sites. O1 sites act as a narrow bridge which connect O3 and O4 sites. Each O1 site will interact with the nearest neighbor O3 and O4 sites. As a whole, the influence of O1 sites in diffusion process is limited but cannot be ignored. For O2 sites ions, they hardly participate to the diffusion process and O2 sites can thus be considered as a barrier that restricts the movement of oxygen ions between the two "walls" shown in **Figure 2.10(b)**. This explains why along *a* direction, no obvious diffusion behavior can be detected. (More comments in **Figure S2.6**) Fujii *et al.* calculated the diffusion pathways of oxide ions in the $Nd_{0.9}Sr_{0.1}BaInO_{3.95}$ and $NdBaInO_4$ at 1073K by the bond valence based energy (BVE). Their results prove that the paths along the *b* and *c* axes have similar energy barriers while the path along the *a*-axis has significantly higher energy barriers than the other two directions. The oxide-ion conduction in $Nd_{0.9}Sr_{0.1}BaInO_{3.95}$ would thus be two dimensional.[31,32] Fujii's results are in good agreement with this work where the oxygen diffusion path is described in more details.

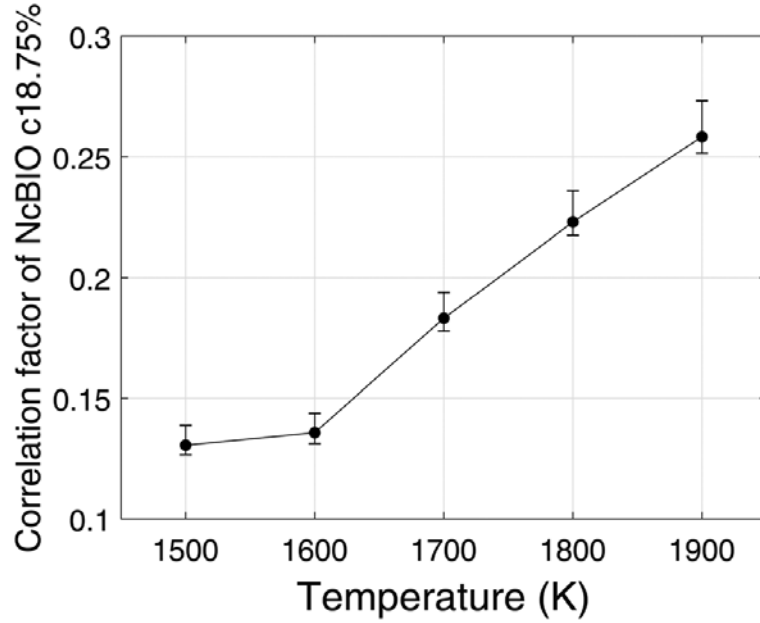


Figure 2.11 The correlation factor as a function of temperature of NbBIO c18.75%.

On the other side, Correlation effects potentially play an important role for any solid-state diffusion process, when point defects act as diffusion vehicles.[61] In pure random-walk diffusion, it is assumed that the jump probabilities of atoms do not depend on the direction of the preceding jump. In real crystals, such a dependence of jump probability is usually observed and successive atom jumps are thus correlated. Instead of following a pure random walk, each atom follows a correlated walk. The correlation factor f is thus introduced. Counting the number of jumps J between (types of) sites provides the mean jump rate (Γ) using:[61,62]

$$\Gamma = \frac{J}{Nt} \quad (2.5)$$

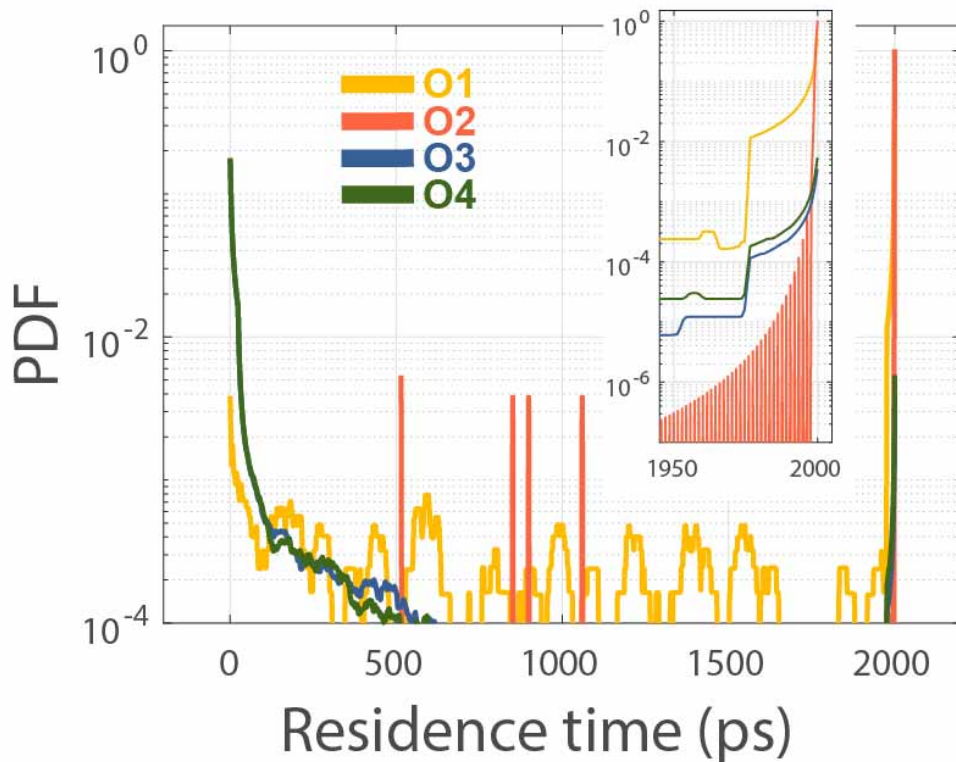
where N is the number of diffusing atoms, and t the simulation time. Using the Einstein-Smoluchowski relation the jump rates are related to the jump rate diffusivity D_j :[62]

$$D_j = \sum_i \frac{\Gamma a_i^2}{2d} \quad (2.6)$$

where i are the different types of jumps, a_i is the jump distance of jump type i , and d the number of diffusion dimensions. To get an estimate of the fraction of jumps which contribute to macroscopic diffusion, the correlation factor (f) is calculated:[62]

$$f = \frac{D^*}{D_j} \quad (2.7)$$

Where D^* is the diffusion coefficient of tagged atoms. If $f = 1$, it suggests the Markovian jump sequence and no diffusion vehicle involved (direct interstitial diffusion). If $f < 1$, it suggests the non-Markovian jump sequence and diffusion vehicle involved (perhaps vacancy, divacancy, self-interstitial, . . . mechanisms).[61] The correlation factor of $\text{Nd}_{1-x}\text{Ca}_x\text{BaInO}_{4-x/2}$ $x=18.75\%$ is presented in the **Figure 2.11**. The correlation factor increases with the increase of temperature, indicating that jumps become less correlated at high temperature. The largest value of correlation factor is about 0.26, suggesting the oxygen diffusion is highly correlated.



(a)

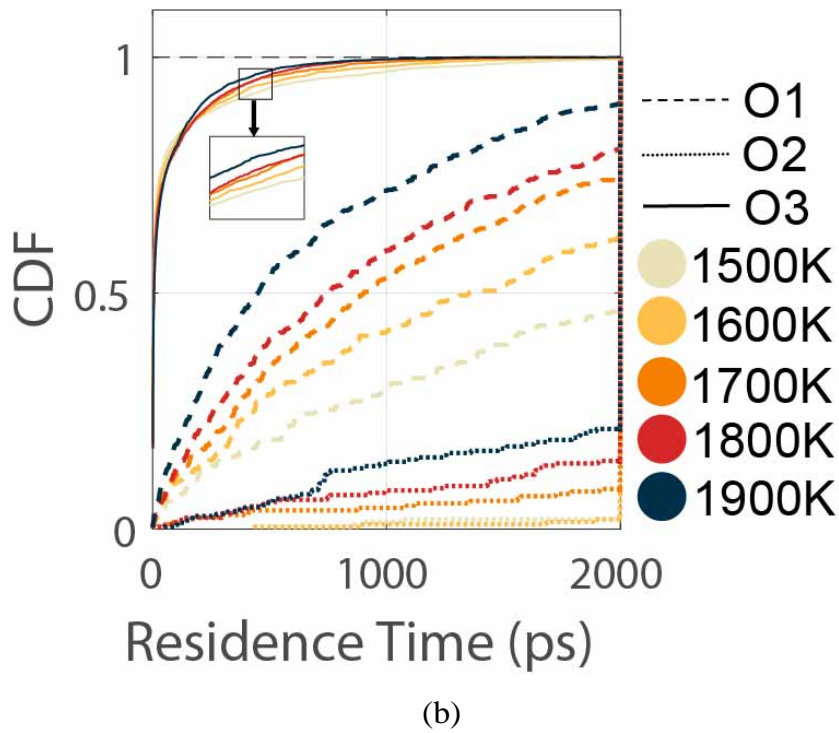


Figure 2.12 (a) PDF of the oxygen residence time of four oxygen sites in NcBIO c15.625% at 1500 K. **(b)** CDF of the oxygen residence time of three oxygen sites in NcBIO c15.625% from 1500K to 1900 K. Solid, dash and dot lines represent for O3, O1 and O2 respectively. The CDF of O3 is very similar to O4, only O3 CDFs are plotted.

Finally, with the help of these two classification methods, we could find out how many oxygen ions visited one fixed oxygen site, and how long each oxygen ion stayed at this site. (also see **Figure S2.3**) In probability and statistics, a random variable is described informally as a variable whose values depend on outcomes of a random phenomenon. Here, the residence time of each oxygen ion staying at this site can be considered as a random variable. The probability distribution function (PDF) and the cumulative distribution function (CDF) of this random variable can be obtained by the Gaussian kernel density estimation with automatic determination of the kernel bandwidth.[47,63] The PDF curves of residence time at different oxygen sites of NcBIO c15.625% at 1500K are shown in **Figure 2.12(a)**. Firstly, the PDF curves of O3 and O4 sites are nearly coincident, meaning the abilities for trapping ions of O3 and O4 sites are close. In addition, the shape of O3 and O4 PDF

Chapter II Oxygen diffusion mechanism in acceptor-doped NBIO

curves from 0 ps to 1999 ps are similar to the right half of the normal distribution whose expectation is 0 ps. Since the PDF is used to specify the probability of the random variable falling within a particular range of values, it suggests that for O3 and O4 sites, a residence time smaller than 200 ps is highly probable, and the oxygen ions are highly mobile on these two sites. Secondly, this residence time random variable in O1 sites is roughly subject to uniform distribution $U(0, 1999)$. It is worth noting that it exists a sudden rise in O1, O3 and O4 PDF curves at $x=2000$ ps, meaning that some oxygen ions will remain on their original sites without jumping. Compared with the PDF of O3 and O4, a lower mobility of oxygen ions is observed for the O1 sites. Finally, the probability that oxygen ions do not escape from O2 sites, *i.e.*, the residence time=2000 ps, is in this case close to 1 (One-point distribution). These results are consistent with the **Figure 2.12(b)** where the CDFs of the residence time at different temperatures of different oxygen sites are shown. The CDF of a continuous random variable can be expressed as the integral of its probability density function. The O3 CDF curve increases at the highest rate than O1 and O2, approaching 1 quickly. Nevertheless, the increasing rate of O2 curve is the slowest, at $x=2000$ ps, there is a sudden rise in the curve, and $x=2000$ is a discontinuity point. $1 - \lim_{t \rightarrow 2000^-} f_{cdf}(t)$ will be the fraction value of O2 ions which never move out of our defined convex hull or clustering results of DBSCAN. Furthermore, it is evident that the curve growth rates of all oxygen sites will increase with the increasing of temperature (This is also true for O3 and O4, which it is shown in the inserted figure of **Figure 2.12(b)**). In summary, our residence time analysis confirms that O3 and O4 sites have the worst ability to constrict the movement of oxygen ions, followed by O1 sites, while O2 sites have the strongest trapping ability, *i.e.*, ions on O2 sites cannot escape easily.

II.4 Conclusions

In this work, oxygen-ion diffusion mechanisms in doped NdBaInO₄ compound were studied. This material was chosen for its high ion conduction properties but also due to its complex structure inducing a non-less complex ion diffusion mechanism. Classical molecular dynamics simulations were performed using well sounded interatomic potentials, which allowed extracting macroscopic diffusion

Chapter II Oxygen diffusion mechanism in acceptor-doped NBIO

coefficients, identifying the best dopant in agreement with experimental results. Concerning atomic scale mechanisms, we present here in details a dual analysis route for clarifying the oxygen ion diffusion pathway. This analysis involves the use of convex hull classification method (CHC) and Density-based spatial clustering of applications with noise (DBSCAN) to associate precisely oxygen ions to specific crystallographic sites. Based on this distribution obtained for every trajectory step, we determined the mean occupancy of each oxygen site, the jump numbers from site to site, the oxygen ion diffusion path and we performed a residence time analysis.

These two clustering methods could be beneficial for understanding intrinsic properties of specific packing of atoms and for the design of materials with enhanced conductivity, by figuring out the diffusion bottlenecks and fast diffusion routes. In this work, $\text{Nd}_{1-x}\text{AE}_x\text{BaInO}_{4-x/2}$ (AE=Ca, Sr, Ba) systems has been chosen as an example to verify the feasibility of our routine. The calculation results show that: Ca is the best dopant in NBIO to favour diffusion, while Ba is the worst. The addition of Ca element hardly changes the lattice parameter of pure NBIO, while the lattice distortion of Ba-doped NBIO is the largest. The diffusion coefficient follows the rule $D_{\text{Ca}(O)} > D_{\text{Sr}(O)} > D_{\text{Ba}(O)}$. Oxygen sites participate differently to the oxygen diffusion process. Their role importance follows $O3 \approx O4 > O1 \gg O2$, as demonstrated by MSD, occupancy rate, detailed jumps, the activation enthalpy of oxygen jumps and residence time analysis. $\Delta H_{O3 \rightarrow O3}$, $\Delta H_{O3 \rightarrow O4}$ and $\Delta H_{O4 \rightarrow O4}$ are 0.186 eV, 0.227 eV and 0.233 eV respectively, which are lower than $\Delta H_{O1 \rightarrow O3}$ 0.769 eV and $\Delta H_{O1 \rightarrow O4}$ 0.793 eV. Diffusing oxygen ions in AE-doped NBIO follow thus a main and a secondary diffusion paths. For the main diffusion path, ions migrate along the **b** and **c** directions on O3 and O4 sites. For the secondary diffusion path, a small proportion of O1 sites will interact with the O3 and O4 sites. Impeding diffusion between slabs along the **a** direction, O2 sites can be considered as barriers for the diffusion process.

This work shows that the proposed approach can deal with complex diffusion mechanisms and can thus be extrapolated to other compounds. Finally, we can also anticipate that diffusion coefficient could probably be increased if we were able to favour diffusion across the identified walls. Partial substitution of Ba by smaller cations like Sr could potentially favour such a diffusion.

II.5 Notes and references

1. A. Chronos, B. Yildiz, A. Tarancon, D. Parfitt and J. A. Kilner, "Oxygen diffusion in solid oxide fuel cell cathode and electrolyte materials: mechanistic insights from atomistic simulations," *Energy Environ. Sci.*, 2011, 4, 2774–2789.
2. B. C. Steele and A. Heinzl, *Materials For Sustainable Energy: A Collection of Peer-Reviewed Research and Review Articles from Nature Publishing Group*, World Scientific, 2011, pp. 224–231.
3. A. J. Jacobson, "Materials for solid oxide fuel cells," *Chem. Mater.*, 2009, 22, 660–674.
4. J. Fleig, Annu. "Solid oxide fuel cell cathodes: Polarization mechanisms and modeling of the electrochemical performance," *Rev. Mater. Res.*, 2003, 33, 361–382.
5. C. Frayret, A. Villesuzanne and M. Pouchard, "Application of density functional theory to the modeling of the mixed ionic and electronic conductor $\text{La}_2\text{NiO}_{4+\delta}$: Lattice relaxation, oxygen mobility, and energetics of frenkel defects," *Chem. Mater.*, 2005, 17, 6538–6544.
6. G. Kim, S. Wang, A. Jacobson, L. Reimus, P. Brodersen and C. Mims, "Rapid oxygen ion diffusion and surface exchange kinetics in $\text{PrBaCo}_2\text{O}_{5+x}$ with a perovskite related structure and ordered A cations," *J. Mater. Chem.*, 2007, 17, 2500–2505.
7. S. Skinner and J. Kilner, "Oxygen diffusion and surface exchange in $\text{La}_{2-x}\text{Sr}_x\text{NiO}_{4+\delta}$," *Solid State Ionics*, 2000, 135, 709–712.
8. A. Tarancon, S. J. Skinner, R. J. Chater, F. Hernandez-Ramirez and J. A. Kilner, "Layered perovskites as promising cathodes for intermediate temperature solid oxide fuel cells," *J. Mater. Chem.*, 2007, 17, 3175–3181.
9. M. Burriel, G. Garcia, J. Santiso, J. A. Kilner, R. J. Chater and S. J. Skinner, "Anisotropic oxygen diffusion properties in epitaxial thin films of $\text{La}_2\text{NiO}_{4+\delta}$," *J. Mater. Chem.*, 2008, 18, 416–422.
10. L. Troncoso, J. Alonso and A. Aguadero, "Low activation energies for interstitial oxygen conduction in the layered perovskites $\text{La}_{1+x}\text{Sr}_{1-x}\text{InO}_{4+\delta}$," *J. Mater. Chem. A*, 2015, 3, 17797–17803.

Chapter II Oxygen diffusion mechanism in acceptor-doped NBIO

11. I. Seymour, A. Chroneos, J. Kilner and R. Grimes, “Defect processes in orthorhombic $\text{LnBaCo}_2\text{O}_{5.5}$ double perovskites,” *Phys. Chem. Chem. Phys.*, 2011, 13, 15305–15310.
12. M. Yashima, M. Enoki, T. Wakita, R. Ali, Y. Matsushita, F. Izumi and T. Ishihara, “Structural disorder and diffusional pathway of oxide ions in a doped Pr_2NiO_4 -based mixed conductor,” *J. Am. Chem. Soc.*, 2008, 130, 2762–2763.
13. J. Hermet, G. Geneste and G. Dezanneau, “Molecular dynamics simulations of oxygen diffusion in $\text{GdBaCo}_2\text{O}_{5.5}$,” *Appl. Phys. Lett.*, 2010, 97, 174102.
14. C. Tealdi, J. Heath and M. S. Islam, “Feeling the strain: enhancing ionic transport in olivine phosphate cathodes for Li- and Na-ion batteries through strain effects,” *J. Mater. Chem. A*, 2016, 4, 6998–7004.
15. E. Olsson, X. Aparicio-Angles and N. H. de Leeuw, “A computational study of the electronic properties, ionic conduction, and thermal expansion of $\text{Sm}_{1-x}\text{A}_x\text{CoO}_3$ and $\text{Sm}_{1-x}\text{A}_x\text{CoO}_{3-x/2}$ ($\text{A}=\text{Ba}^{2+}$, Ca^{2+} , Sr^{2+} , and $x=0.25, 0.5$) as intermediate temperature SOFC cathodes,” *Phys. Chem. Chem. Phys.*, 2017, 19, 13960–13969.
16. O. Tripathy and P. P. Kumar, “Molecular dynamics investigation of oxide ion transport in Sr-doped LaMnO_3 ,” *J. Mater. Sci.*, 2017, 52, 6542–6553.
17. C. Chen, D. Chen, Y. Gao, Z. Shao and F. Ciucci, “Computational and experimental analysis of $\text{Ba}_{0.95}\text{La}_{0.05}\text{FeO}_{3-\delta}$ as a cathode material for solid oxide fuel cells,” *J. Mater. Chem. A*, 2014, 2, 14154–14163.
18. G. Dezanneau, J. Hermet and B. Dupe, “Effects of biaxial strain on bulk 8% yttria-stabilised zirconia ion conduction through molecular dynamics,” *Int. J. Hydrogen Energy*, 2012, 37, 8081–8086.
19. M. Rushton and A. Chroneos, “Impact of uniaxial strain and doping on oxygen diffusion in CeO_2 ,” *Sci. Rep.*, 2014, 4, 6068.
20. A. Piovano, A. Perrichon, M. Boehm, M. Johnson and W. Paulus, “Positional recurrence maps, a powerful tool to de-correlate static and dynamical disorder in distribution maps from molecular dynamics simulations: the case of $\text{Nd}_2\text{NiO}_{4+\delta}$,” *Phys. Chem. Chem. Phys.*, 2016, 18, 17398–17403.
21. R. A. De Souza, A. Ramadan and S. Horner, “Modifying the barriers for oxygen-vacancy migration in fluorite-structured CeO_2 electrolytes through strain: a computer simulation study,” *Energy Environ. Sci.*, 2012, 5, 5445–5453.
22. M. Burbano, S. T. Norberg, S. Hull, S. G. Eriksson, D. Marrocchelli, P. A.

Chapter II Oxygen diffusion mechanism in acceptor-doped NBIO

- Madden and G. W. Watson, "Oxygen vacancy ordering and the conductivity maximum in Y_2O_3 -doped CeO_2 ," *Chem. Mater.*, 2011, 24, 222–229.
23. D. Parfitt, A. Chroneos, A. Taranco'n and J. A. Kilner, "Oxygen ion diffusion in cation ordered/disordered $\text{GdBaCo}_2\text{O}_{5+\delta}$," *J. Mater. Chem.*, 2011, 21, 2183–2186.
24. C. Tealdi, C. Ferrara, P. Mustarelli and M. S. Islam, "Vacancy and interstitial oxide ion migration in heavily doped $\text{La}_{2-x}\text{Sr}_x\text{CoO}_{4\pm\delta}$," *J. Mater. Chem.*, 2012, 22, 8969–8975.
25. D.-S. Byeon, S.-M. Jeong, K.-J. Hwang, M.-Y. Yoon, H.-J. Hwang, S. Kim and H.-L. Lee, "Oxide ion diffusion in Ba-doped LaInO_3 perovskite: A molecular dynamics study," *J. Power Sources*, 2013, 222, 282–287.
26. Y. Wang, E. Bevilion, A. Chesnaud, G. Geneste and G. Dezanneau, "Atomistic simulation of pure and doped BaSnO_3 ," *J. Phys. Chem. C*, 2009, 113, 20486–20492.
27. J. Hermet, B. Dupe and G. Dezanneau, "Simulations of $\text{REBaCo}_2\text{O}_{5.5}$ (RE=Gd, La, Y) cathode materials through energy minimisation and molecular dynamics," *Solid State Ionics*, 2012, 216, 50–53.
28. A. Chroneos, D. Parfitt, J. A. Kilner and R. W. Grimes, "Anisotropic oxygen diffusion in tetragonal $\text{La}_2\text{NiO}_{4+\delta}$: molecular dynamics calculations," *J. Mater. Chem.*, 2010, 20, 266–270.
29. Y. Hu, O. Hernandez, T. Broux, M. Bahout, J. Hermet, A. Ottochian, C. Ritter, G. Geneste and G. Dezanneau, "Oxygen diffusion mechanism in the mixed ion-electron conductor $\text{NdBaCo}_2\text{O}_{5+x}$," *J. Mater. Chem.*, 2012, 22, 18744–18747.
30. J. Xu, S. Bai, Y. Higuchi, N. Ozawa, K. Sato, T. Hashida and M. Kubo, "Multi-nanoparticle model simulations of the porosity effect on sintering processes in Ni/YSZ and Ni/ScSZ by the molecular dynamics method," *J. Mater. Chem. A*, 2015, 3, 21518–21527.
31. K. Fujii, Y. Esaki, K. Omoto, M. Yashima, A. Hoshikawa, T. Ishigaki and J. R. Hester, "New perovskite-related structure family of oxide-ion conducting materials NdBaInO_4 ," *Chem. Mater.*, 2014, 26, 2488–2491.
32. K. Fujii, M. Shiraiwa, Y. Esaki, M. Yashima, S. J. Kim and S. Lee, "Improved oxide-ion conductivity of NdBaInO_4 by Sr doping," *J. Mater. Chem. A*, 2015, 3, 11985–11990.
33. X. Yang, S. Liu, F. Lu, J. Xu and X. Kuang, "Acceptor doping and oxygen

Chapter II Oxygen diffusion mechanism in acceptor-doped NBIO

- vacancy migration in layered Perovskite NdBaInO₄-based mixed conductors,” *J. Phys. Chem. C*, 2016, 120, 6416–6426.
34. T. Ishihara, Y. Yan, T. Sakai and S. Ida, “Oxide ion conductivity in doped NdBaInO₄,” *Solid State Ionics*, 2016, 288, 262–265.
35. M. S. Islam, “Ionic transport in ABO₃ perovskite oxides: a computer modelling tour,” *J. Mater. Chem.*, 2000, 10, 1027–1038.
36. K.-D. Kreuer, S. J. Paddison, E. Spohr and M. Schuster, “Transport in proton conductors for fuel-cell applications: simulations, elementary reactions, and phenomenology,” *Chem. Rev.*, 2004, 104, 4637–4678.
37. M.-Y. Yoon, K.-J. Hwang, D.-S. Byeon, H.-J. Hwang and S.-M. Jeong, “Molecular dynamics simulation of the effect of dopant distribution homogeneity on the oxide ion conductivity of Ba-doped LaInO₃,” *J. Power Sources*, 2014, 248, 1085–1089.
38. Y. Wang, M. Klenk, K. Page and W. Lai, “Local structure and dynamics of lithium garnet ionic conductors: A model material Li₅La₃Ta₂O₁₂,” *Chem. Mater.*, 2014, 26, 5613–5624.
39. S. Hayward and N. Go, “Collective variable description of native protein dynamics,” *Annu. Rev. Phys. Chem.*, 1995, 46, 223–250.
40. S. T. Roweis and L. K. Saul, “Nonlinear dimensionality reduction by locally linear embedding,” *Science*, 2000, 290, 2323–2326.
41. J. B. Tenenbaum, V. De Silva and J. C. Langford, “A global geometric framework for nonlinear dimensionality reduction,” *Science*, 2000, 290, 2319–2323.
42. M. Ceriotti, G. A. Tribello and M. Parrinello, “Simplifying the representation of complex free-energy landscapes using sketch-map,” *Proc. Natl. Acad. Sci. U. S. A.*, 2011, 108, 13023–13028.
43. R. R. Coifman, I. G. Kevrekidis, S. Lafon, M. Maggioni and B. Nadler, “Diffusion maps, reduction coordinates, and low dimensional representation of stochastic systems,” *Multiscale Model. Simul.*, 2008, 7, 842–864.
44. A. L. Ferguson, A. Z. Panagiotopoulos, P. G. Debenedetti and I. G. Kevrekidis, “Systematic determination of order parameters for chain dynamics using diffusion maps,” *Proc. Natl. Acad. Sci. U. S. A.*, 2010, 107, 13597–13602.
45. C. Chen, Z. Lu and F. Ciucci, “Data mining of molecular dynamics data reveals Li diffusion characteristics in garnet Li₇La₃Zr₂O₁₂,” *Sci. Rep.*, 2017, 7, 40769.

Chapter II Oxygen diffusion mechanism in acceptor-doped NBIO

46. C. Chen, Z. M. Baiyee and F. Ciucci, "Unraveling the effect of La A-site substitution on oxygen ion diffusion and oxygen catalysis in perovskite BaFeO₃ by data-mining molecular dynamics and density functional theory," *Phys. Chem. Chem. Phys.*, 2015, 17, 24011–24019.
47. C. Chen, D. Chen and F. Ciucci, "A molecular dynamics study of oxygen ion diffusion in A-site ordered perovskite PrBaCo₂O_{5.5}: data mining the oxygen trajectories," *Phys. Chem. Chem. Phys.*, 2015, 17, 7831–7837.
48. I. T. Todorov, W. Smith, K. Trachenko and M. T. Dove, "DL_POLY_3: new dimensions in molecular dynamics simulations via massive parallelism," *J. Mater. Chem.*, 2006, 16, 1911–1918.
49. C. Tealdi, L. Malavasi, C. A. Fisher and M. S. Islam, "Disproportionation, dopant incorporation, and defect clustering in perovskite-structured NdCoO₃," *J. Phys. Chem. B*, 2006, 110, 5395–5402.
50. G. Lewis and C. Catlow, "Potential models for ionic oxides," *J. Phys. C: Solid State Phys.*, 1985, 18, 1149.
51. C. Fisher and M. Islam, "Defect, protons and conductivity in brownmillerite-structured Ba₂In₂O₅," *Solid State Ionics*, 1999, 118, 355–363.
52. J. D. Gale and A. L. Rohl, "The general utility lattice program (GULP)," *Mol. Simul.*, 2003, 29, 291–341.
53. M. D. Berg, O. Cheong, M. V. Kreveld and M. Overmars, Computational geometry: algorithms and applications, Springer-Verlag TELOS, 2008.
54. C. B. Barber, D. P. Dobkin and H. Huhdanpaa, "The quickhull algorithm for convex hulls," *ACM Trans. Math. Soft.*, 1996, 22, 469–483.
55. M. Ester, H.-P. Kriegel, J. Sander and X. Xu, et al., "A density-based algorithm for discovering clusters in large spatial databases with noise," *KDD*, 1996, pp. 226–231.
56. E. Schubert, J. Sander, M. Ester, H. P. Kriegel and X. Xu, "DBSCAN revisited, revisited: why and how you should (still) use DBSCAN," *ACM Trans. Database Syst.*, 2017, 42, 19.
57. H.-P. Kriegel, P. Kroger, J. Sander and A. Zimek, Wiley Interdiscip. Rev.: Data Min. Knowl. Discovery, 2011, 1, 231–240.
58. R. D. Shannon, "Revised effective ionic radii and systematic studies of interatomic distances in halides and chalcogenides," *Acta Crystallogr., Sect. A: Cryst. Phys., Diffr., Theor. Gen. Crystallogr.*, 1976, 32, 751–767.

Chapter II Oxygen diffusion mechanism in acceptor-doped NBIO

59. X. He, Y. Zhu, A. Epstein and Y. Mo, “Statistical variances of diffusional properties from ab initio molecular dynamics simulations,” *npj Comput. Mater.*, 2018, 4, 18.
60. J. Kilner, “Fast oxygen transport in acceptor doped oxides,” *Solid State Ionics*, 2000, 129, 13–23.
61. H. Mehrer, “Diffusion in solids: fundamentals, methods, materials, diffusion-controlled processes,” *Springer Science & Business Media*, 2007, vol. 155.
62. N. J. de Klerk, E. van der Maas and M. Wagemaker, “Analysis of diffusion in solid-state electrolytes through MD simulations, improvement of the Li-ion conductivity in Beta-Li₃PS₄ as an example,” *ACS Appl. Energy Mater.*, 2018, 1, 3230–3242.
63. Z. I. Botev, J. F. Grotowski and D. P. Kroese, et al., *Ann. Stat.*, 2010, 38, 2916–2957.

II.6 Supporting information

Outline of supporting information:

1. Example input files of NcBIO c6.25% 1500K (N σ T) for DLPOLY calculations
2. Matlab code for producing the complex information cell
3. Matlab code for 3D convex hull classification method
4. Figure S2.1 The complete information cell of NBIO at 1900K.
5. Figure S2.2 The lattice parameters *a b c* of pure and AE-doped NBIO as a function of temperature and dopant amount. (AE= Ca, Sr, Ba).
6. Figure S2.3 One representative oxygen ion trajectory.
7. Figure S2.4 jumps conditions of NcBIO c9.375% 1500K.
8. Figure S2.5 jumps conditions of NcBIO c15.625% 1500K.
9. Figure S2.6 The MSD curves of all oxygen ions of NcBIO c18.75% 1900K along different direction.

Example input files of NcBIO c6.25% 1500K (N σ T) for DLPOLY calculations

CONTROL file

```
NCBIO  maille      3*4*4
integrator      leapfrog
```

Chapter II Oxygen diffusion mechanism in acceptor-doped NBIO

```
temperature      1500.0
pressure         0.001
ensemble        nst hoover 0.1 0.1
steps           100000
equil           20 000
scale           10
print           1000
stack           500
stats           1000
timestep        0.0005
cutoff          10.00
delr width      0.5000
ewald precision 1.0E-6
job time        144000.00
close time      100000.00
finish
```

FIELD file

```
NCBIO maille 3*4*4
UNITS eV
MOLECULES 8
Neodymium
NUMMOLS 180
ATOMS 1
Nd          144.242      3.000
FINISH
Calcium
NUMMOLS 12
ATOMS 1
Ca          40.078      2.000
FINISH
Barium
NUMMOLS 192
ATOMS 1
Ba          137.327     2.000
FINISH
Indium
NUMMOLS 192
ATOMS 1
In          114.818     3.000
FINISH
Oxygen1
NUMMOLS 192
ATOMS 1
O1          15.9994     -2.000
FINISH
Oxygen2
NUMMOLS 192
ATOMS 1
```

Chapter II Oxygen diffusion mechanism in acceptor-doped NBIO

```
O2          15.9994      -2.000
FINISH
Oxygen3
NUMMOLS 189
ATOMS 1
O3          15.9994      -2.000
FINISH
Oxygen4
NUMMOLS 189
ATOMS 1
O4          15.9994      -2.000
FINISH
VDW 26
O1 Nd buck 1379.9 0.36072 22.59
O1 Ca buck 1228.9 0.3372 0.00
O1 Ba buck 931.7 0.3949 0.00
O1 In buck 1495.6 0.3310 4.325
O2 Nd buck 1379.9 0.36072 22.59
O2 Ca buck 1228.9 0.3372 0.00
O2 Ba buck 931.7 0.3949 0.00
O2 In buck 1495.6 0.3310 4.325
O3 Nd buck 1379.9 0.36072 22.59
O3 Ca buck 1228.9 0.3372 0.00
O3 Ba buck 931.7 0.3949 0.00
O3 In buck 1495.6 0.3310 4.325
O4 Nd buck 1379.9 0.36072 22.59
O4 Ca buck 1228.9 0.3372 0.00
O4 Ba buck 931.7 0.3949 0.00
O4 In buck 1495.6 0.3310 4.325
O1 O1 buck 22764.30 0.1490 43.00
O1 O2 buck 22764.30 0.1490 43.00
O1 O3 buck 22764.30 0.1490 43.00
O1 O4 buck 22764.30 0.1490 43.00
O2 O2 buck 22764.30 0.1490 43.00
O2 O3 buck 22764.30 0.1490 43.00
O2 O4 buck 22764.30 0.1490 43.00
O3 O3 buck 22764.30 0.1490 43.00
O3 O4 buck 22764.30 0.1490 43.00
O4 O4 buck 22764.30 0.1490 43.00
CLOSE
```

Matlab code for producing the complex information cell

```
clear
```

```
close all
```

```
% Read the trajectories coordinates of all ions obtained by MD simulation, e.g. the coordinates  
generated by HISTORY file with VMD.1
```

Chapter II Oxygen diffusion mechanism in acceptor-doped NBIO

```
DATA=load('data_MD.dat','-ascii');
```

```
% The lattice parameter of compounds.  $a=[ax \ ay \ az]$ .  $na$  is the number of unit cells along  $a$  direction, the same is for  $b$  and  $c$  respectively.
```

```
ax=27.4569856338;
```

```
ay=0;
```

```
az=0.1645871838;
```

```
bx=0;
```

```
by=24.3745847321;
```

```
bz=0;
```

```
cx=-7.7636119933;
```

```
cy=0;
```

```
cz=32.3640450323;
```

```
na = 3;
```

```
nb = 4;
```

```
nc = 4;
```

```
% Because the origin of all coordinates in HISTORY file produced by DLPLOY is  $[0.5*(ax+bx+cx), 0.5*(ay+by+cy), 0.5*(az+bz+cz)]$ , Now we transfer the origin of coordinate from  $([0.5*(ax+bx+cx), 0.5*(ay+by+cy), 0.5*(az+bz+cz)])$  to  $[-0.5*(ax+bx+cx), -0.5*(ay+by+cy), -0.5*(az+bz+cz)]$ . Then all the coordinates will be positive.
```

```
origin=[0.5*(ax+bx+cx) 0.5*(ay+by+cy) 0.5*(az+bz+cz)];
```

```
DATA=DATA+origin;
```

```
% A is the reduced-unit cell in which all the coordinates will be transferred by periodic boundary condition.
```

```
A = [ax/na  ay/na  az/na;
```

```
      bx/nb  by/nb  bz/nb;
```

```
      cx/nc  cy/nc  cz/nc;];
```

```
InvA=inv(A');
```

```
% MD data in a reduced cell with fractional positions
```

```
DATA2=mod((InvA*DATA)',1);
```

```
% MD data in a reduced cell with xyz positions
```

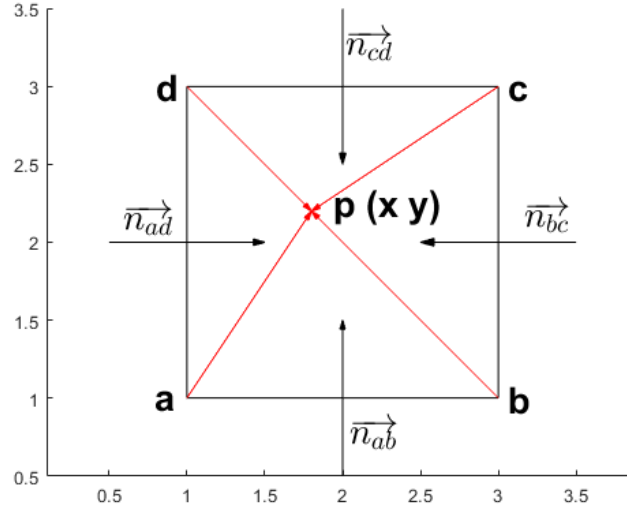
```
DATA3=(A'*DATA2)';
```

Matlab code for 3D convex hull classification method

```
%% Here the Matlab code of 3D convex hull classification method (Figure 2.3) is attached. The geometric criterion of whether the point is inside the 2D or 3D convex hull is: when a point is inside or on the convex hull, the dot production between the vector from any convex vertex to this point and any normal vector of this convex vertex is more than 0. The normal vector of
```

Chapter II Oxygen diffusion mechanism in acceptor-doped NBIO

this convex vertex means that all the normal vectors of line segments (2D) or faces (3D) including this vertex. For example, as shown in the figure behind, when an arbitrary point p is inside or on the square abcd, we can get $\vec{ap} \cdot \vec{n}_{ab} \geq 0$ and $\vec{ap} \cdot \vec{n}_{ad} \geq 0$. The same is for \vec{bp} with \vec{n}_{ab} and \vec{n}_{bc} etc. ²



clear

close all

%coexp is the coefficient of expansion of standard convex hull.

coexp=1.15;

%read the standard convex hull and then adjust the size of this convex hull. In this work, the standard convex hull is the 3D data of NdBaInO₄ 1900K (Figure S2.1) and the coefficient expansion is 15%.

data=textread('points of standard convex hull.txt');

dataN(:,1)=(data(:,1)-mean(data(:,1)))*coexp+mean(data(:,1));

dataN(:,2)=(data(:,2)-mean(data(:,2)))*coexp+mean(data(:,2));

dataN(:,3)=(data(:,3)-mean(data(:,3)))*coexp+mean(data(:,3));

convexH=convhulln(dataN);

[nc,~]=size(convexH);

% read all the test points, here the test points are all 3D oxygen coordinates.

testP=textread('test points.txt');

[n,~]=size(testP);

% build normal vectors

ab=dataN(convexH(:,1,:),:)-dataN(convexH(:,2,:),:);

ac=dataN(convexH(:,1,:),:)-dataN(convexH(:,3,:),:);

Chapter II Oxygen diffusion mechanism in acceptor-doped NBIO

```
normalV = cross(ab,ac,2);

% scale normal vectors to unit length
module = sqrt(sum(normalV.^2,2));
normalV = normalV.*repmat(1./ module,1,3);

% center point of the convex hull
center = mean(dataN,1);

% all vertexes in the plane of each simplex in the convex hull
vertex = dataN (convexH (:,1),:);

% ensure the normal vectors pointing inwards
difference = sum((repmat(center,nc,1) - vertex).* normalV,2);
k = difference<0;
normalV (k,:) = - normalV (k,:);

% We want to test if: dot production ((testpoint - vertex),Normal) >= 0, if so for all faces of
the convex hull, then p is inside the convex hull. Change this to dot production (testpoint,
Normal) >= dot(vertex, Normal)
NorVer = sum(normalV.* vertex,2);

% if n is too large, we need to worry about the dot product grabbing huge chunks of memory.
in = false(n,1);
memblock = 1e6;
blocks = max(1,floor(n/(memblock/nc)));
NorVerN = repmat(NorVer,1,length(1:blocks:n));

for i = 1:blocks
    j = i:blocks:n;
    if size(NorVerN,2) ~= length(j)
        NorVerN = repmat(NorVer,1,length(j));
    end
    in(j) = all((normalV * testP (j,:) - NorVerN) >= 0,1)';
end
```

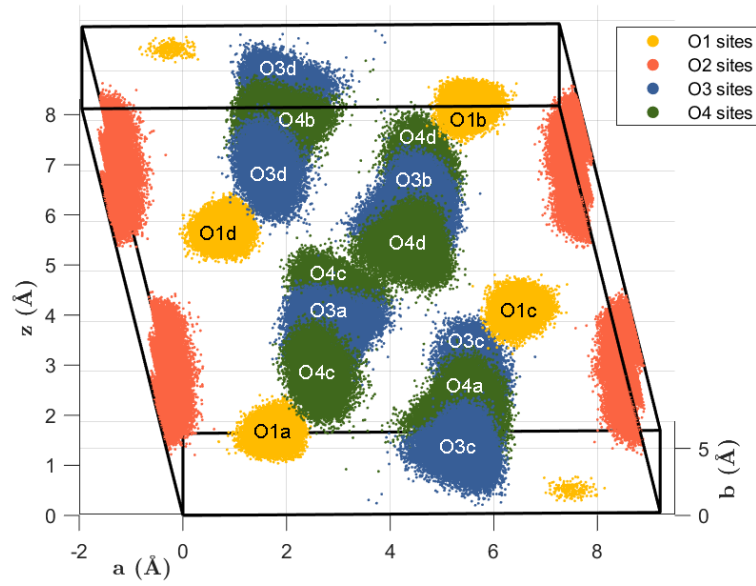
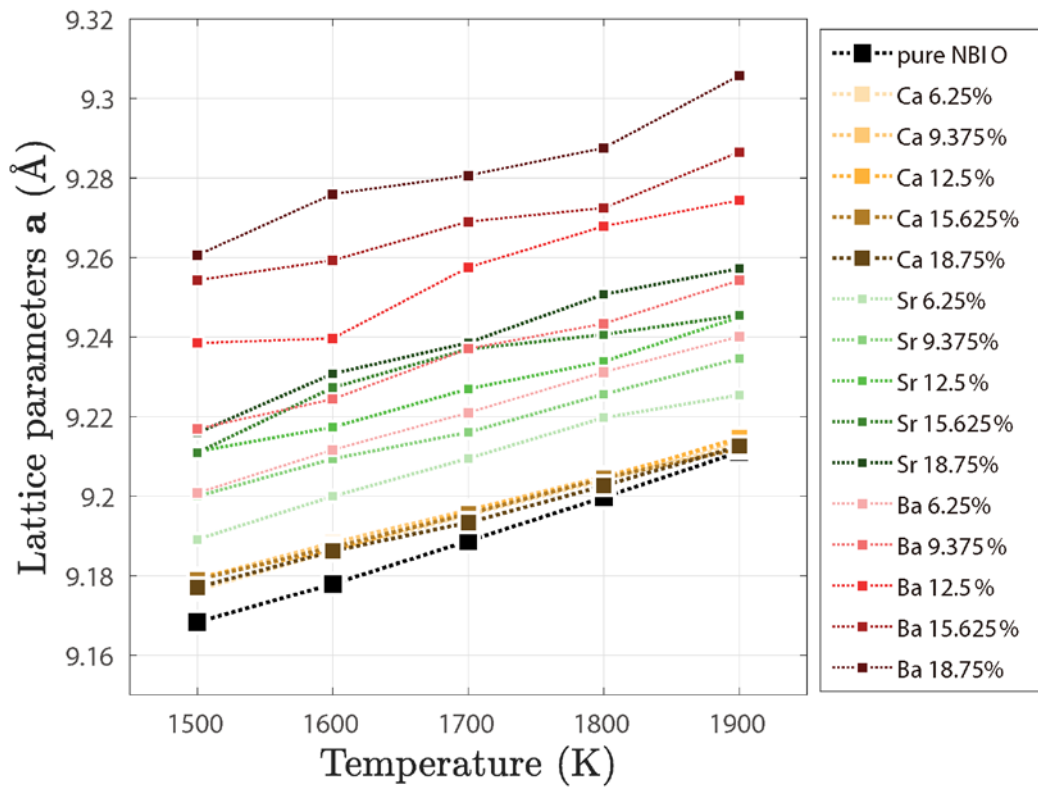


Figure S2.1 The complete information cell of NBIO at 1900K.

Compared with the complete information cell of NBIO at 1500K (**Figure 2.2**), the size of each oxygen site clusters increase due to a higher temperature.



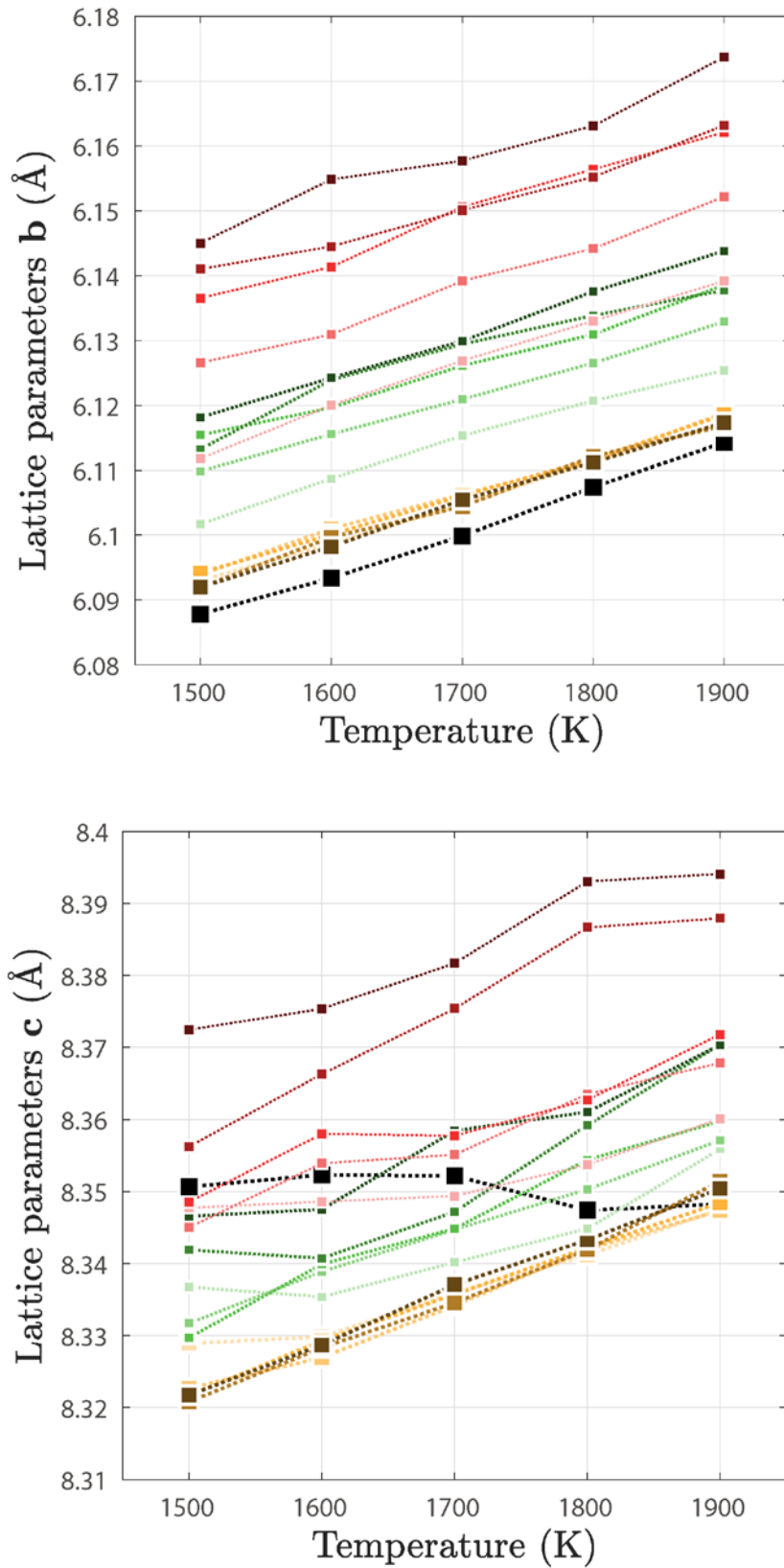


Figure S2.2 The lattice parameters a b c of pure and AE-doped NBIO as a function of temperature and dopant amount. (AE= Ca, Sr, Ba).

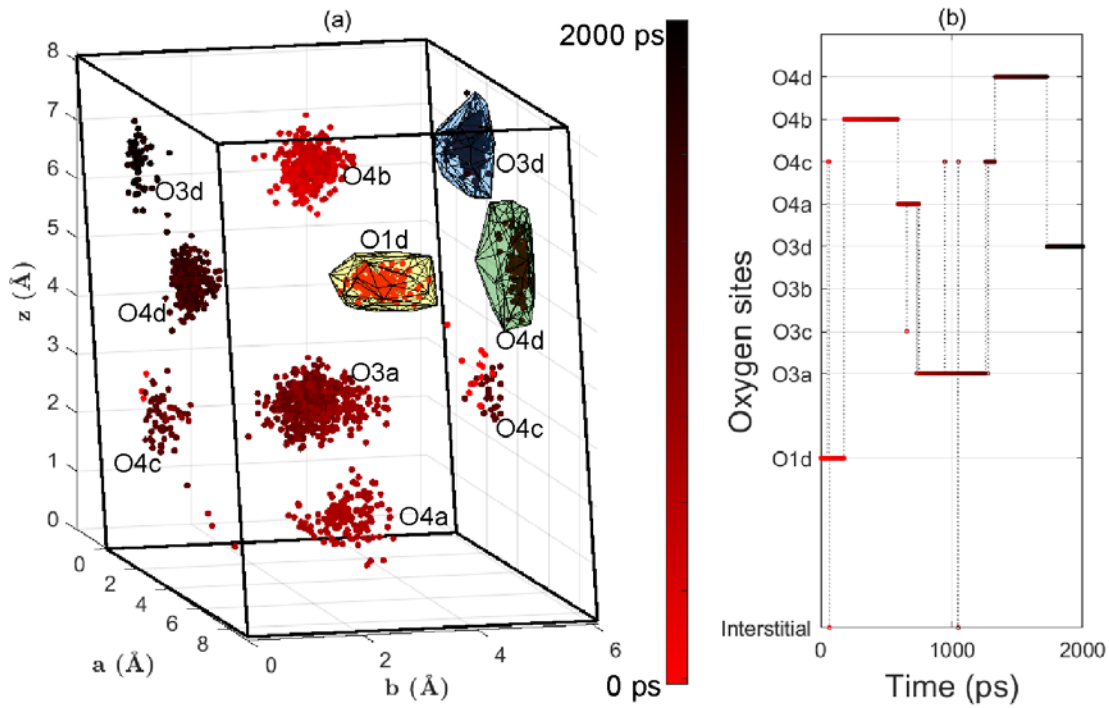


Figure S2.3 One representative oxygen ion trajectory in NcBIO c18.75% 1500K.

One oxygen ion was traced by using convex hull classification method. The color change of color bar (from red to black) represents the evolution of simulation time, all these dots stand for this oxygen ion at different timesteps, the darker color, the later timestep. We can find clearly the variation of the belonging cluster of this oxygen ion with the pass of simulation time by recognizing the changing dots colors. The change clusters of this ion can be described roughly as O1d (178ps) \rightarrow O4b (410ps) \rightarrow O4a (144ps) \rightarrow O3a (544ps) \rightarrow O4c (52ps) \rightarrow O4d (399ps) \rightarrow O3d (273ps).

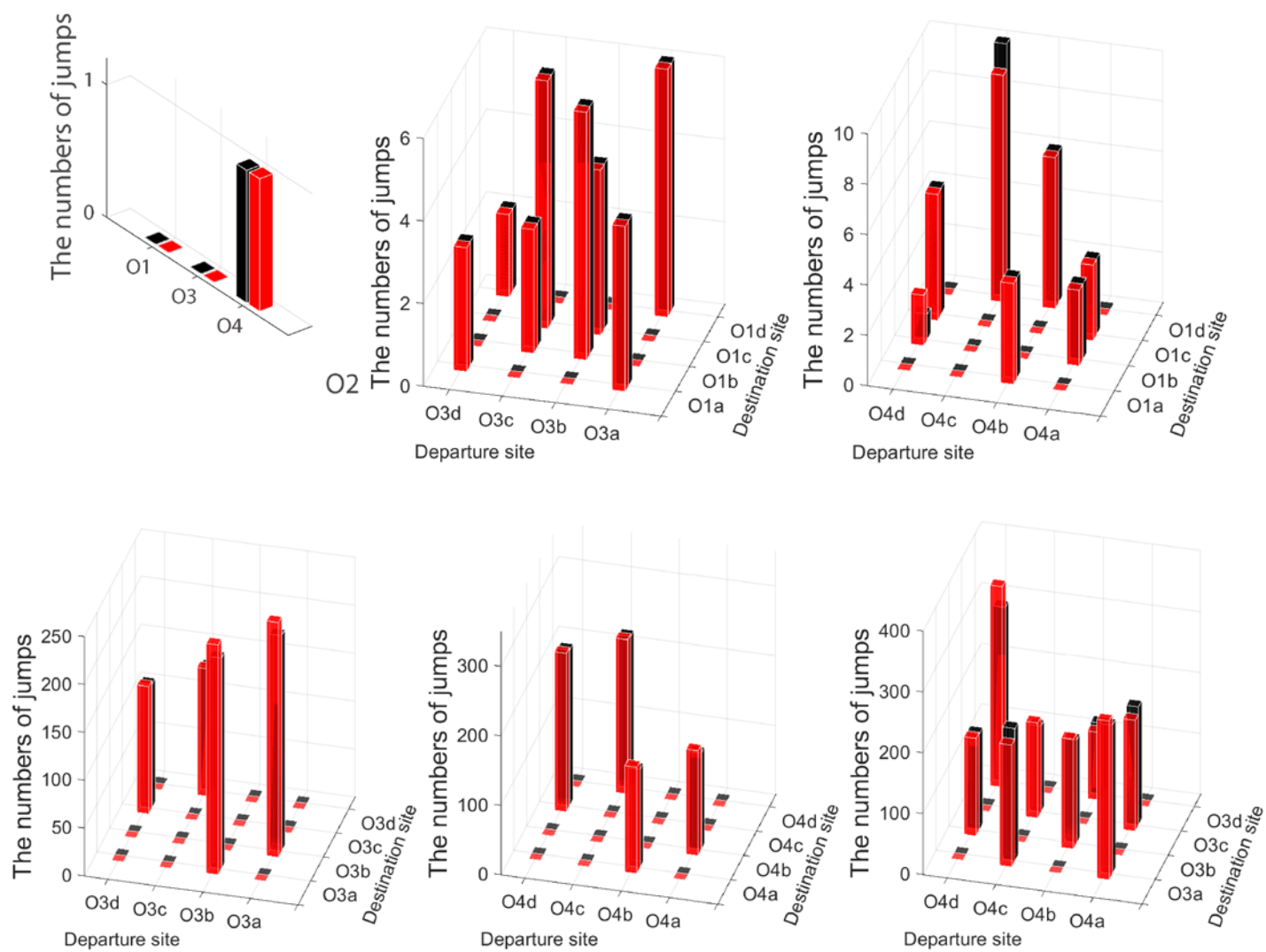


Figure S2.4 Detailed jump analysis between different sites in NcBIO c9.375% 1500K. Red column represents results by convex hull classification methods (CHC), while black stands for DBSCAN.

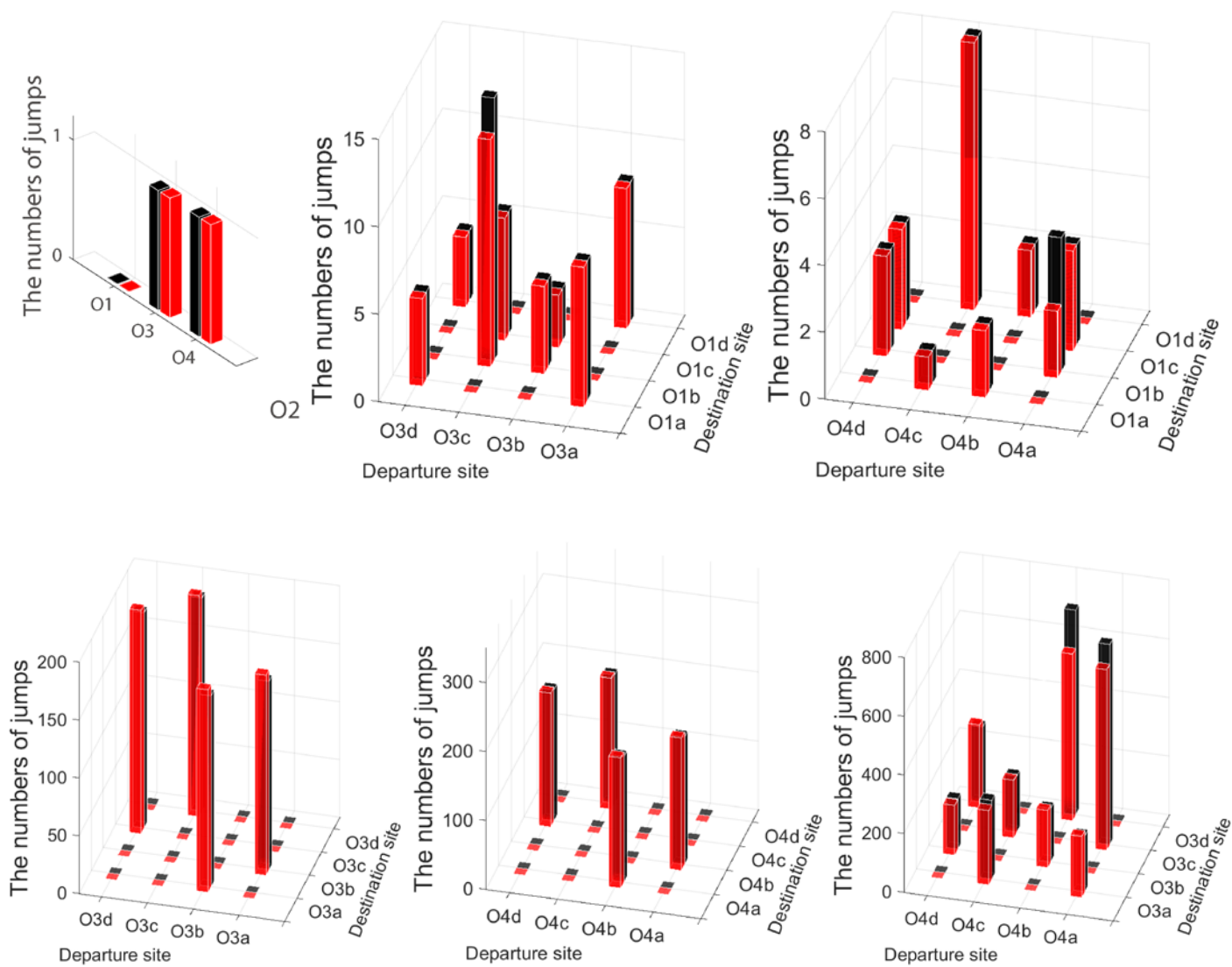


Figure S2.5 Detailed jump analysis between different sites in NcBIO c15.625% 1500K. Red column represents results by convex hull classification methods (CHC), while black stands for DBSCAN.

Chapter II Oxygen diffusion mechanism in acceptor-doped NBIO

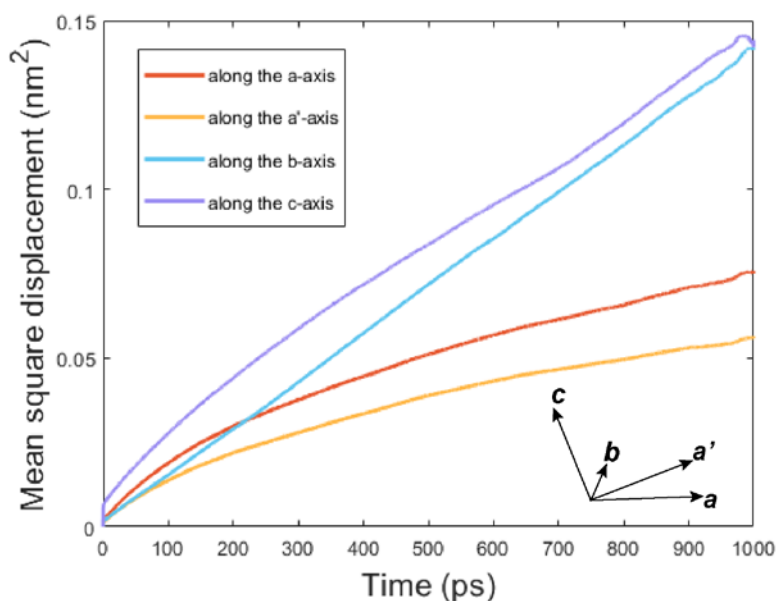


Figure S2.6 The MSD curves of all oxygen ions of NcBIO c18.75% 1900K along different direction.

In **Figure S2.6**, the MSD curves along four different directions are presented: a , b , c and a' , where a b c are the primitive vectors of unit cell along $[1\ 0\ 0]$, $[0\ 1\ 0]$ and $[\cot\beta, 0, 1]$ respectively, β is the angle between a and c . a' , with the direction of $[1, 0, -\cot\beta]$, is on the ac plane and perpendicular to c . Though O2 is the barrier for oxygen diffusion along the a direction, oxygen ions diffuse inside unit cell resulting in the values of MSD of a and a' are not 0. Besides the oxygen ions diffuse along c direction will contribute to a direction, resulting in the values of MSD a is larger than MSD a' . The oxygen diffusion mainly happens along b and c direction, which is also proved in **Figure S2.6**, the MSD curves of b and c are similar and the top two highest.

References

1. Humphrey, W., Dalke, A. and Schulten, K., "VMD - Visual Molecular Dynamics", *J. Molec. Graphics*, 1996, vol. 14, pp. 33-38.
2. <https://uk.mathworks.com/matlabcentral/fileexchange/10226-inhull>

Chapter III oxygen diffusion mechanism in donor-doped NBIO

Abstract

Understanding fundamental aspects of oxygen diffusion is important to develop new materials for Solid Oxide Fuel Cells. Molecular dynamics simulations have been widely adopted since they can provide highly relevant information on the relationship between atomic-scale mechanisms and macroscopic diffusion coefficients. In this work, $\text{NdBaIn}_{1-x}\text{M}_x\text{O}_{4+x/2}$ ($\text{M}=\text{Ti}, \text{Zr}$) compounds have been studied by MD simulation focusing on oxygen diffusion. Bond valence summation (BVS) has been used as an additional tool to find the possible oxygen interstitial position. From MD simulations, Titanium might be preferred as a dopant compared to Zirconium since the diffusion coefficient of Ti-doped compounds are significantly higher, confirming recent experimental results. MD simulations allowed confirming that interstitial oxygen ions concentrate on a specific crystallographic position (*4e Wyckoff position of $P2_1/c$ space group*, [0.5766 0.7567 0.8959]), in good agreement with BVS calculations. DBSCAN machine learning algorithm was adopted to track the trajectory of each oxide ion and further obtain the oxygen diffusion path. An interstitialcy mechanism was found in the temperature range 1500 K - 1900 K. Oxygen diffusion is highly anisotropic, occurring mainly in the *b-c* plane, involving only two of the four lattice oxygen sites, namely O3 and O4 and the interstitial sites. The other two lattice oxygen sites do not participate to the diffusion process in these donor-doped compounds and even constitute a barrier for the oxygen diffusion along *a* direction. Finally, a residence time analysis of oxygen ions confirms that ions have different motion abilities depending on the considered crystallographic site.

Molecular dynamic study of oxygen diffusion in $\text{NdBaIn}_{1-x}\text{M}_x\text{O}_{4+x/2}$ (M= Ti, Zr)

III.1 Introduction

Solid Oxide Fuel Cells (SOFCs) offer an efficient way to convert hydrogen and air into electricity and heat with reduced emission of green-house gases compared to many conventional power generation routes.[1][2] Materials for SOFCs would advantageously present high oxygen ion diffusion coefficients, whatever their role as electrolyte or electrode materials. Then, understanding oxygen diffusion mechanisms in SOFCs materials is important since this will allow identifying the diffusion bottlenecks or fast routes and thus help finding the next generation of new materials.[1], [3] Numerous SOFC materials were indeed studied by Molecular Dynamics (MD) simulations since such simulation can provide a precise insight of oxygen diffusion at the atomistic scale. Chroneos *et al.* thoroughly studied the $\text{La}_2\text{NiO}_{4+\delta}$ and $\text{Pr}_2\text{NiO}_{4+\delta}$ compounds with K_2NiF_4 structure and concluded that oxygen diffusion is highly anisotropic, occurring almost entirely *via* an interstitialcy mechanism in the *a-b* plane.[4]–[8] Ciucci *et al* proposed a data-mining approach for the analysis of molecular dynamic simulations in $\text{Ba}_{1-x}\text{La}_x\text{FeO}_{2.5+x/2}$ and $\text{PrBaCo}_2\text{O}_{5.5}$ compounds, approach by which atoms trajectories information were much more effectively used.[9]–[11] Tealdi *et al* explored $\text{La}_{1.54}\text{Sr}_{0.46}\text{Ga}_3\text{O}_{7.27}$ and suggested an interstitialcy or cooperative-type mechanism involving the concerted knock-on motion of interstitial and lattice oxide ions.[12]–[14] In our group, we also investigated the double perovskite cobaltite compounds, $\text{REBaCo}_2\text{O}_{5.5}$ (RE=Nd, Gd, La, Y). Our results revealed that oxygen diffusion was driven by the presence of vacancies in both the rare-earth and the cobalt planes, while Ba-containing planes act as a barrier for oxygen diffusion.[15]–[18]

Recently, NdBaInO_4 and its derived compounds were presented as promising electrolyte candidates by Fujii *et al.*[19]–[22] These authors discovered that NdBaInO_4

Chapter III oxygen diffusion mechanism in donor-doped NBIO

belong to a new perovskite-related structure family and Sr^{2+} substitution for Nd^{3+} would enhance the oxide ion conductivity through the creation of oxygen vacancies.[19], [20] Ishihara *et al.* proved that Ti doping on In site in NdBaInO_4 *i.e.* a donor-doping approach is also effective to increase the oxide ion conductivity. In this case, the optimized amount of Ti was found to be around 20 mol%.[21] In our previous work, we discussed the oxygen diffusion mechanism in acceptor-doped $\text{Nd}_{1-x}\text{AE}_x\text{BaInO}_{4-x/2}$ (AE=Ca, Sr, Ba) compounds by means of MD simulations. More specifically, we used two classification methods, Convex hull classification and DBSCAN, to associate precisely oxygen ions to specific crystallographic sites and capture the oxygen jumps between those sites. A detailed oxygen ions vacancy diffusion mechanism was then proposed.

In this work, we performed MD simulations in donor-doped $\text{NdBaIn}_{1-x}\text{M}_x\text{O}_{4+x/2}$ (M=Ti, Zr) compounds to understand the diffusion mechanism of oxygen ions. BVS methods were used to find the possible positions of oxygen interstitial ions. MD simulations were performed for different doping levels and temperatures. These MD simulations helped identifying which dopant (nature, concentration) gives the best oxygen diffusion coefficient and, on the other side, allowed identifying the oxygen diffusion mechanism. For this, a DBSCAN approach was used to associate precisely oxygen ions to specific crystallographic sites. An interstitialcy mechanism could be proposed to explain the oxygen diffusion pathway.

III.2 Methods

III.2.1 Bond valence summation (BVS)

The bond valence analysis is a simple and useful tool for the identification of ion transport pathways in both crystalline and amorphous ion conductors.[23]–[26] “Accessible” sites for mobile ions A in a local structure model are identified using empirical relationships between the bond length R and a so-called bond valence S_{A-X} :

$$S_{A-X} = \exp[(R_0 - R)/b]$$

Chapter III oxygen diffusion mechanism in donor-doped NBIO

Where R_0 and b are the empirical parameters.[27] The mismatch of the bond valence sum $V(A)$:

$$|\Delta V(A)| = \left| \sum_X S_{A-X} - V_{id}(A) \right|$$

over the S_{A-X} from all adjacent counterions X approaches the ideal valence $V_{id}(A)$ (*i.e.* its oxidation state). BVS map provides then information on probable ion transport paths. Indeed, isosurfaces of fixed $|\Delta V(A)|$ for a certain ion type A may be identified as most probable regions of the material that A ions can reach.[23] In this study; the BVS map of oxygen ions of NdBaInO₄ was calculated by the software PyAbstantia.[28]

III.2.2 Molecular dynamic simulation

MD simulations were done assuming the chemical formula NdBaIn_{1-x}M_xO_{4+x/2} (M=Ti, Zr) and varying x so as to obtain 16 different dopant concentrations, from $x=2\%$ to $x=31.25\%$. The simulation box consisted of a supercell containing $3 \times 4 \times 4$ unit cells, in which the dopant were introduced randomly. The oxygen interstitial ions were distributed randomly on the Wyckoff positions obtained from BVS calculations. We tested 8 different simulation temperatures from 1500 K to 1900 K. MD simulations were performed using the DLPOLY classic code.[29] Interaction between ions were described by a long range Coulombic term calculated by Ewald Summation, and a short range Buckingham pair potential. For Coulombic interactions, we use the formal charges of +3, +2, +3, +4 and -2 for Nd, Ba, In, RE and O ions respectively. The used Buckingham potential is described by:

$$\varphi_{ij} = A_{ij} \exp\left(-\frac{r}{\rho_{ij}}\right) - \frac{C_{ij}}{r^6} \quad (3.1)$$

Where r is the distance between the ions i and j , and A_{ij} , ρ_{ij} , C_{ij} are potential parameters specific to each ion pair whose values are given in **Table 3.1**. The set of potentials was taken from previous studies, which were shown to reproduce correctly oxide materials properties.[30]–[32] As a proof of the potential validity, an energy minimization approach was employed using GULP code to determine the pristine lattice parameters ($a=9.038 \text{ \AA}$, $b=6.009 \text{ \AA}$, $c=8.308 \text{ \AA}$, $\beta=103.674^\circ$), which are within 0.66% the ones

Chapter III oxygen diffusion mechanism in donor-doped NBIO

found experimentally ($a=9.095 \text{ \AA}$, $b=6.049 \text{ \AA}$, $c=8.256 \text{ \AA}$, $\beta=103.404^\circ$).[19], [33] Each system was first equilibrated at the desired temperature and zero pressure for 20,000 time steps (with a time step duration of 0.5 fs) in the isothermal-isobaric (N σ T) ensemble with Nose-Hoover thermostat. Afterwards, the equilibrium lattice parameters were calculated with 80,000 time steps more. Then, simulations were performed in the NVT mode during 100,000 time steps. Finally, NVE simulations were realized corresponding to 2,000,000 time steps. All the ions trajectories coordinates will be dumped every 1000 time steps to the trajectory file.

Interaction	A / eV	ρ / \AA	C / eV. \AA^6
Nd ³⁺ —O ²⁻	1379.9	0.3607	22.59
Ba ²⁺ —O ²⁻	931.7	0.3949	0.00
In ³⁺ —O ²⁻	1495.6	0.3310	4.325
Ti ⁴⁺ —O ²⁻	754.2	0.3879	0.00
Zr ⁴⁺ —O ²⁻	1453.8	0.3500	0.00
O ²⁻ —O ²⁻	22764.3	0.1490	43.00

Table 3.1 Interatomic Buckingham potentials used for molecular dynamic simulations. M-O interactions are taken from: Nd-O, O-O,[30] Ba-O, Ti-O and Zr-O,[31] In-O[32].

III.2.3 Density-based spatial clustering of applications with noise (DBSCAN)

DBSCAN is one of the most common clustering algorithms used in unsupervised machine learning to separate clusters of high density from clusters of low density.[34]–[36] Considering that DBSCAN is a density based clustering algorithm, it does a great job in seeking areas in the data that have a high density of observations, versus areas of the data that are not very dense. Each cluster is the largest set of points connected by density, and the shape of clusters can be arbitrary. This point is important since it allows

Chapter III oxygen diffusion mechanism in donor-doped NBIO

finding crystallographic sites without any assumption on the position nor on the shape of the trajectory followed by a vibrating atom. In this approach, interstitials are defined as the set of points in the database not belonging to any cluster corresponding to a given crystallographic site of the considered structure. Using DBSCAN approach, there are two parameters to define in the clustering process, Eps (distance threshold) and $MinPts$ (minimum cluster size, which must be chosen greater or equal 3). These two parameters should be modified prudentially to have a reasonable classification result.[34]–[36]

III.3 Results and discussions

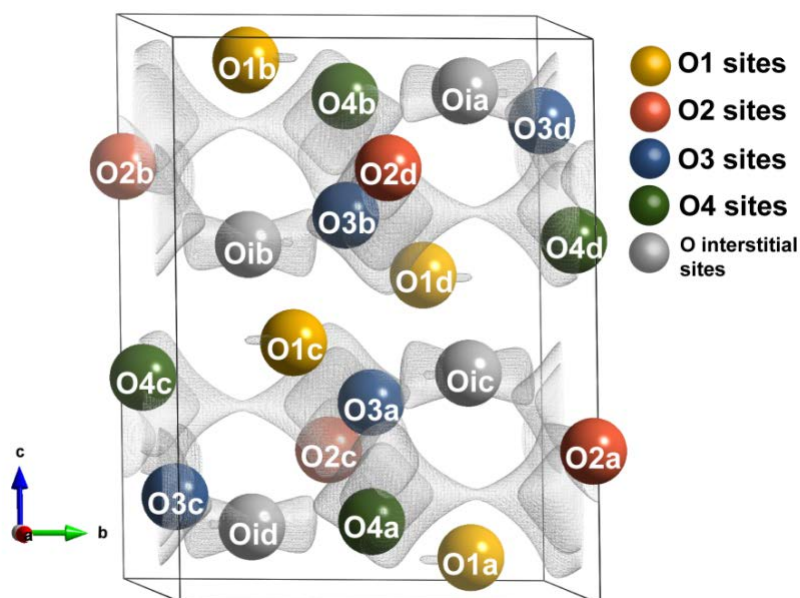


Figure 3.1 Isosurfaces for value of the oxygen BV mismatch $|\Delta V(O^{2-})| = 0.15$ in NdBaInO₄

In NdBaInO₄ (NBIO), there are seven independent sites, namely Nd, Ba, In, O1, O2, O3, and O4, all located on the general (4e) Wyckoff position of the space group $P2_1/c$ (see Supplementary Information **Table S3.1** for details).[19] We named the four O1 sites in the cell as O1a, O1b, O1c and O1d respectively (The same notation is also adopted for the other oxygen sites). Through this BVS map, the possible oxygen

Chapter III oxygen diffusion mechanism in donor-doped NBIO

interstitial ions positions could be obtained. Indeed, in **Figure 3.1**, we plot the BVS isosurface for oxygen ion with $|\Delta V(O^{2-})| = 0.15$ valence unit (v.u.). From this figure, all the oxygen ions of the pristine compound are on an isosurface connected to the original crystallographic site, except for 4 isosurfaces. These 4 isosurfaces with a peanut shape (**Figure 3.2b**), may be associated to 4 hypothetical interstitial sites (Oia Oib Oic Oid). These isosurfaces are nevertheless very extended so we decreased the value of $|\Delta V(O^{2-})|$ to locate the interstitial position more precisely. For $|\Delta V(O^{2-})| = 0.05$ (see **Figure S3.1**), the geometric center of these 4 isosurfaces can also be associated to a $(4e)$ Wyckoff position of the $P2_1/c$ space group with coordinates $[0.575 \ 0.750 \ 0.893]$.

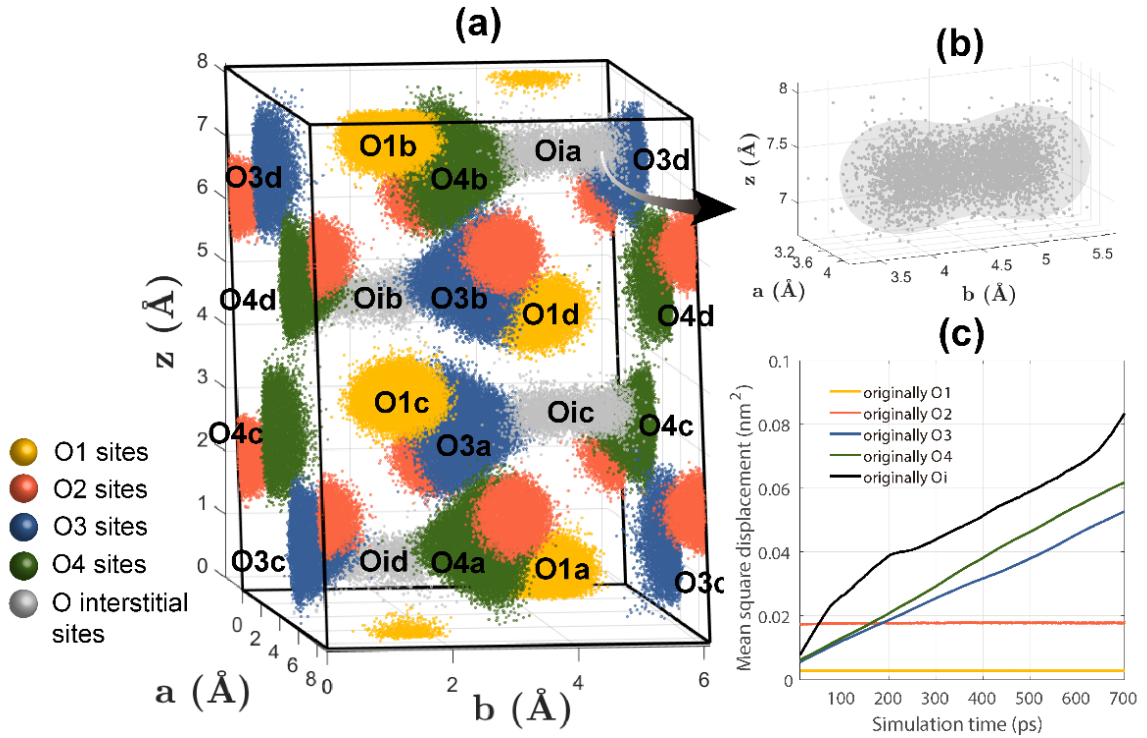


Figure 3.2 (a) The complete information unit cell of $\text{NdBaIn}_{1-x}\text{Ti}_x\text{O}_{4+x/2}$ $x=9.375\%$ at 1500K. (b) Oia cluster is enlarged and presented aside. (c) The MSD curves of different oxygen ion of $\text{NdBaIn}_{1-x}\text{Ti}_x\text{O}_{4+x/2}$ $x=9.375\%$ at 1500K without direction.

After NVE steps, we get the trajectory coordinates of all ions every 1000 time steps in the trajectory file. All oxygen ions coordinates were then refolded into one unit cell

Chapter III oxygen diffusion mechanism in donor-doped NBIO

according to periodic boundary condition. We name this unit cell containing all the oxygen ion coordinates: the “complete information cell”. A DBSCAN classification was used to associate each oxygen ion to specific crystallographic sites. **Figure 3.2a** shows the complete information cell of $\text{NdBaIn}_{1-x}\text{Ti}_x\text{O}_{4+x/2}$ $x=9.375\%$ at 1500K. It also shows the clustering results through coloring after applying DBSCAN. Most oxygen ions vibrate around their equilibrium positions resulting in 34 oxygen ions clusters. Originally, we have randomly arranged oxygen ions at the interstitial sites calculated by BVS. After MD simulations, we observe that the interstitial oxygen ions actually remain for a significant time at these 4 interstitial sites (4 grey clusters), validating then the correctness of the interstitial positions found by BVS. As an example and from the MD simulation with $x=9.375\%$ and $T=1500$ K, the geometric center of the interstitial cluster is found at Wyckoff position [0.5766 0.7567 0.8959], which is fully consistent with BVS results. The shape of this cluster is similar that of a peanut, which is actually similar to the shape of BVS interstitial isosurface, shown in **Figure S3.1**. Compared with the other methods, including neutron diffraction,[37]–[39] DFT calculation,[40], [41] and geometrical calculation,[42] BVS appears once more as simpler and highly effective to find interstitial ion sites. MSD curves were obtained and are drawn in the **Figure 3.2c** for a temperature of 1500 K. It shows that the atoms originally located on O1 and O2 sites only vibrate around their equilibrium position. The ions originally located on O3 and O4 sites have MSDs similar to those originally located on O_i sites. This presentation confirms that O1 and O2 sites do not participate to the diffusion process while atoms on O3, O4 and O_i sites tend to mix due to this diffusion process.

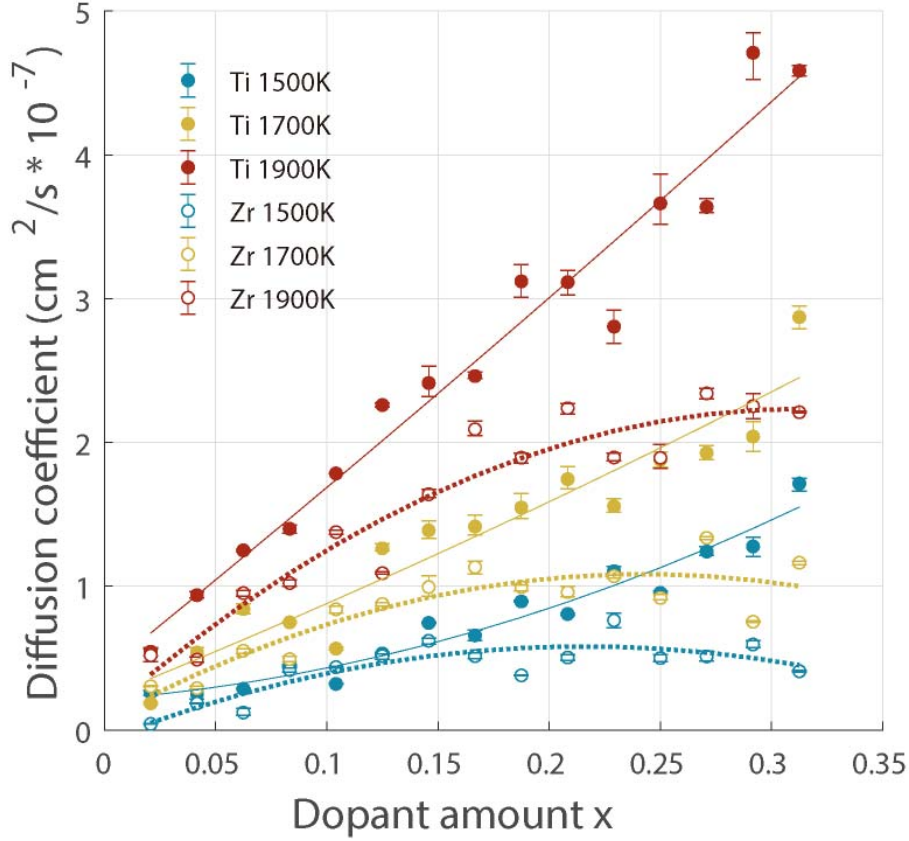


Figure 3.3. Diffusion coefficient with respect to the dopant amount and temperature of $\text{NdBa}(\text{Ti}/\text{Zr})_x\text{In}_{1-x}\text{O}_{4+x/2}$.

Before entering into the details of the atomic-scale mechanism, we will first focus on the macroscopic properties which can also be deduced from the simulation. MD simulations are interesting for determining long range oxygen diffusion coefficients. We thus performed an analysis of the mean square displacement (MSD) of oxygen ions as a function of doping level and temperature. Oxygen diffusion coefficients can be calculated from the slopes of MSD curves according to the Einstein's law:

$$\langle |r_i(t) - r_i(0)|^2 \rangle = 6Dt + \text{constant} \quad (3.2)$$

where $r_i(t)$ is the position of the i -th particle at time t , $|r_i(t) - r_i(0)|$ is the displacement of the oxygen ion i from its initial position, t is the simulation time, D is the oxygen diffusion coefficient. At this stage, we assume a 3D diffusion process, even if a further analysis would induce to consider a 2D process. The constant value is

Chapter III oxygen diffusion mechanism in donor-doped NBIO

generally associated with the purely vibrational motion of ions around their crystallographic site. In our case, the diffusion coefficient was fitted in the 200-800 *ps* time range, where a linear behavior was observed. As shown in **Figure 3.3**, for Ti dopant, the oxygen diffusion coefficient continuously increases with the increase of dopant concentration and temperature. For Zr, we see that initially diffusion coefficient rises rapidly with the increase of dopant concentration but, beyond approximately $x=16\%$, diffusivity tends to be constant. Comparing to experimental results, Ishihara *et al.* indicate that doping with Ti on In site ($\text{NdBaIn}_{0.8}\text{Ti}_{0.2}\text{O}_4$, $\log(\sigma/S \text{ cm}^{-1}) = -2.5$ at 1173K) is more effective for increasing the oxide ion conductivity, compared to Zr doping ($\text{NdBaIn}_{0.8}\text{Zr}_{0.2}\text{O}_4$, $\log(\sigma/S \text{ cm}^{-1}) = -3.0$ at 1173K).[21] This is also verified in our calculations. Indeed, with the same dopant concentration and temperature, oxygen diffusion coefficients of Ti-doped compounds are always larger than those of Zr-doped ones. Besides Ishihara *et al.* compared the ion conductivity of different Ti dopant concentration and proposed that the optimized amount of Ti-doping for In site is around 20 mol%.[21] We have calculated the logarithm of oxygen diffusion coefficients as a function of the inverse of temperature of different Ti dopant concentration (**Figure S3.4**). We did not find such an optimal value for doping but found that the activation energy of oxygen self-diffusion $\text{NdBaIn}_{1-x}\text{Ti}_x\text{O}_{4+x/2}$ varies little of a wide range of compositions. Indeed, for $x= 10.41\%$, 20.83% , 25% , 29.17% , the activation energies were found to be 0.91 eV, 0.83 eV, 0.84 eV and 0.82 eV respectively.

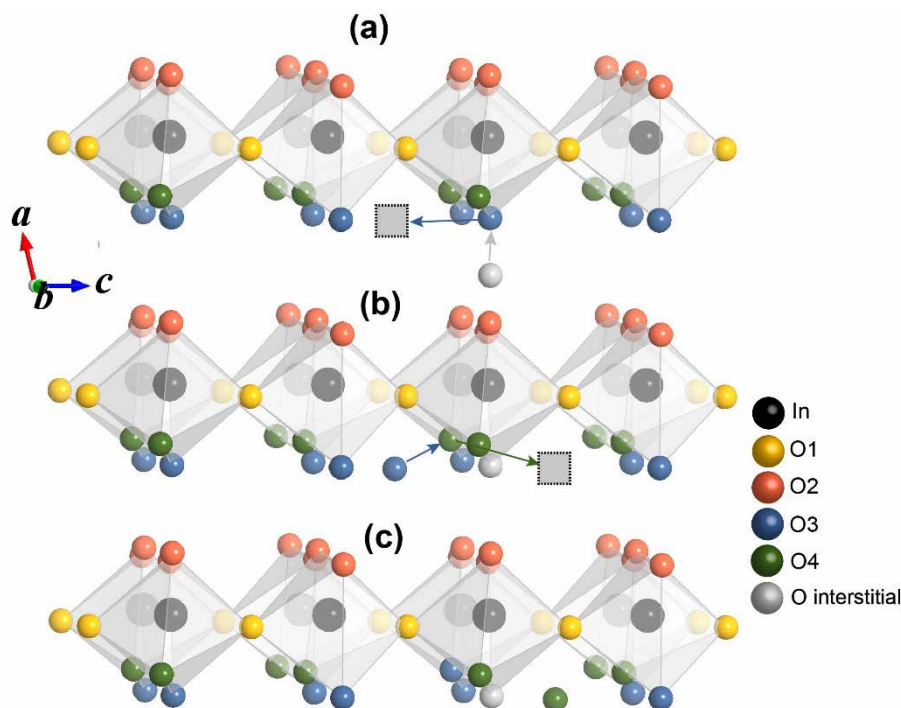


Figure 3.4 (a–c): An example of the time resolved diffusion process of an oxygen ion of NdBaIn_{1-x}Ti_xO_{4+x/2} $x=1.04\%$ at 1500K. Vacant sites relevant to the diffusion process are indicated by grey squares. **(4a)** initial configuration **(4b)** intermediate configuration **(4c)** final configuration. Only the first layer was plotted for the sake of clarity in **4b** and **4c**.

Once identified that both Ti and Zr doping induce oxygen ion conductivity, we need to understand how this occurs, taking into account that the additional oxygen ions induced by donor-doping go to some specific interstitial positions as mentioned above. By following some specific atoms and before performing a deepest pathway analysis, we were able to understand some features of the diffusion mechanism. A representative snapshot of oxygen ion diffusion is presented in **Figure 3.4**. In this figure, the grey oxygen ion (interstitial oxygen) is originally located at one interstitial site between chains of InO₆ octahedrons. This interstitial ion remained on this interstitial site for about 2.5 ps. Then, it replaced the formerly occupied and closest O3 site, while this O3 ion moved to the unoccupied interstitial site (grey square). The intermediate configuration is shown in **Figure 3.4b**. The kicked-out O3 ion vibrated during ~14 ps

Chapter III oxygen diffusion mechanism in donor-doped NBIO

at this interstitial site, and then pushed away the neighboring O4 ion. This O4 ion was then pushed forward another interstitial site. This sequence reveals that diffusion process occurs through an interstitialcy mechanism. Such mechanism is collective because it involves at least two atoms displacement simultaneously. In this system, these two ions are one oxygen interstitial ion and one specific oxygen ion on NdBaInO₄ crystallographic oxygen sites, namely O3 or O4 sites as shown below.

		Departure site																
		O1a	O1b	O1c	O1d	O2	O3a	O3b	O3c	O3d	O4a	O4b	O4c	O4d	Oia	Oib	Oic	Oid
Destination site	O1a	-	0	0	0	0	0	0	0	0	0	0	0	0	0	0	0	0
	O1b	0	-	0	0	0	0	0	0	0	0	0	0	0	0	0	0	0
	O1c	0	0	-	0	0	0	0	0	0	0	0	0	0	0	0	0	0
	O1d	0	0	0	-	0	0	0	0	0	0	0	0	0	0	0	0	0
	O2	0	0	0	0	-	0	0	0	0	0	0	0	0	0	0	0	0
	O3a	0	0	0	0	0	-	0	0	0	0	0	3	0	0	16	52	15
	O3b	0	0	0	0	0	0	-	0	0	0	0	0	3	18	42	14	0
	O3c	0	0	0	0	0	0	0	-	0	0	1	0	0	13	0	19	26
	O3d	0	0	0	0	0	0	0	0	-	0	1	0	0	25	13	0	18
	O4a	0	0	0	0	0	0	0	2	0	-	0	0	0	12	0	19	27
	O4b	0	0	0	0	0	0	0	0	1	0	-	0	0	0	18	33	21
	O4c	0	0	0	0	0	1	0	1	0	0	0	-	0	61	15	0	23
	O4d	0	0	0	0	0	0	3	0	0	0	0	0	-	23	34	9	0
	Oia	0	0	0	0	0	0	14	15	24	20	59	0	20	-	0	0	0
	Oib	0	0	0	0	0	19	42	0	14	0	21	12	31	0	-	0	0
	Oic	0	0	0	0	0	51	18	13	0	14	0	36	15	0	0	-	0
Oid	0	0	0	0	0	15	0	28	18	26	18	23	0	0	0	0	-	

Table 3.2 The number of jumps between two different sites in NdBaIn_{1-x}Ti_xO_{4+x/2} x=9.375% at 1500K. The jumps mainly occur within in O3↔Oi and O4↔Oi pairs

Chapter III oxygen diffusion mechanism in donor-doped NBIO

which are highlighted in grey and yellow respectively.

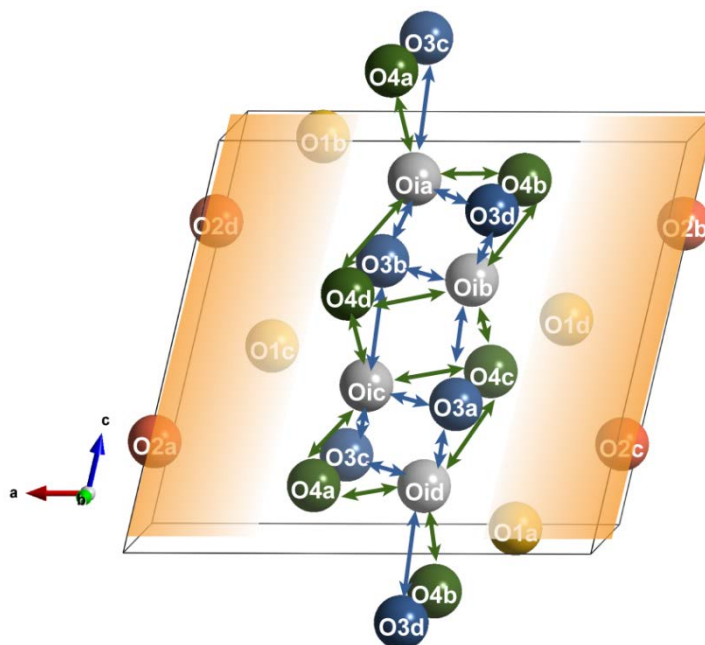


Figure 3.5 Viewing the oxygen diffusion path from opposite *b* direction in NdBaIn_{1-x}M_xO_{4+x/2}.

Through DBSCAN, we could analyze the cluster association of one given oxygen ion with time and thus obtain the precise trajectory of this ion from site to site (**Figure S3.5**). Considering all the oxygen ion trajectories, a detailed oxygen ion jumps table can be achieved, shown in **Table 3.2**. From this table, we notice that the most important jumps appear to be O3↔O_i and O4↔O_i jumps, with a 47.21% and 51.39% probability, respectively. Ions present on O1 and O2 sites do not jump to any other site, *i.e.*, they do not participate to the diffusion process. Similarly, no jump could be found among O3↔O3, O4↔O4, and O_i↔O_i, and only a few jumps could be found between O3 and O4 (the number of jumps over total jumps is about 1.39%). Connecting sites between which jumps exist by arrows, we obtain **Figure 3.5**, in which it becomes more evident that a long-range pathway exists. Oxygen ions at the interstitial sites will act as a “bridge” to connect O3 and O4, resulting in a fast diffusion channel. Each interstitial oxygen site will interact with the three nearest O3 and O4 sites. Oxygen diffusion occurs entirely in the *b-c* plane and is thus highly anisotropic.

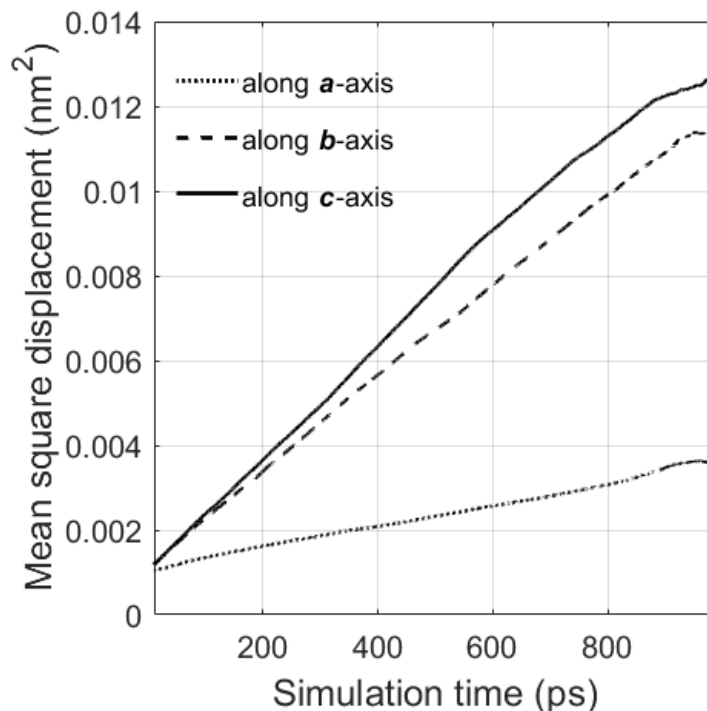


Figure 3.6 The MSD curves of all oxygen ions of $\text{NdBaIn}_{1-x}\text{Ti}_x\text{O}_{4+x/2}$ $x=9.375\%$ 1500K along different directions. a, b, c are the primitive vectors of NdBaInO_4 unit cell.

The anisotropy of diffusion can also be proved from MSD curves along different directions (**Figure 3.6**). In this figure, the MSD curves along the three different directions a, b, c are plotted, where a, b, c are the primitive vectors of the unit cell along $[1\ 0\ 0]$, $[0\ 1\ 0]$ and $[\cot\beta, 0, 1]$ respectively, β being the angle between a and c . The MSD curves of b and c are similar and show higher slopes. The value of MSD curve along the a direction keeps a low slope, being this slope essentially due to the contribution along the c -axis (not perpendicular to a -axis) and thus confirming the proposed diffusion mechanism.

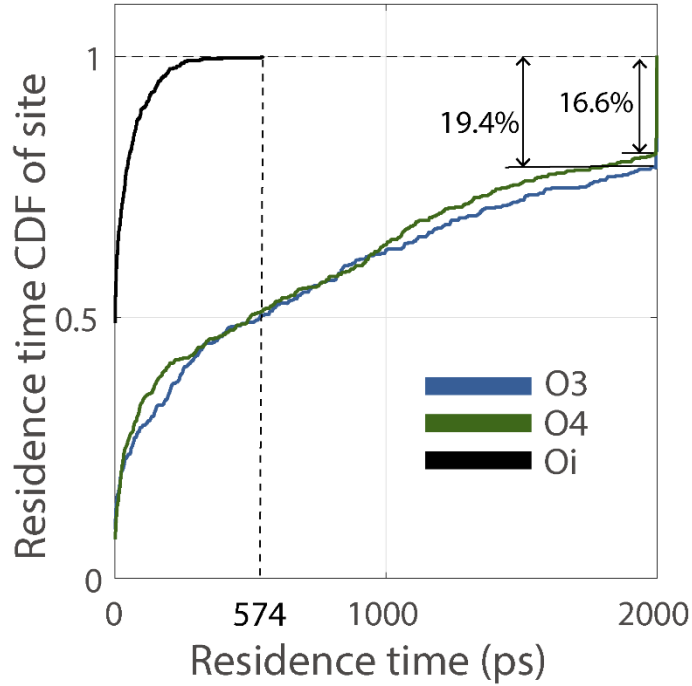


Figure 3.7 Cumulative distribution function of oxygen residence time at different oxygen site in $\text{NdBaIn}_{1-x}\text{Ti}_x\text{O}_{4+x/2}$ $x=9.375\%$ at 1500K.

With the help of DBSCAN classification, we can find out how many oxygen atoms have visited one given oxygen site and how long each oxygen atom stayed at this site. Therefore, the oxygen residence time of this site can be considered as a random variable. The cumulative distribution function (CDF) of this random variable can be obtained by the Gaussian kernel density estimation with automatic determination of the kernel bandwidth.[43] The CDFs of the residence time of different oxygen sites are shown in **Figure 3.7**. The CDF of a continuous random variable can be expressed as the integral of its probability density function. The curve of O_i approach 1 quickly, we have $f_{CDF_{O_i}}(x = 200 \text{ ps}) = 0.973$, *i.e.*, the probability of oxygen ions to stay at the interstitial site for less than 200 ps is 97.3%. Besides, $f_{CDF_{O_i}}(x = 574 \text{ ps}) = 1$, no oxygen ion will rest interstitial site longer than 574 ps. The curves of O_3 and O_4 increase at obvious lower rate than O_i , and in this specific case, 19.4% of O_3 ions and 16.6% of O_4 ions stay at their original sites during the whole simulation process. Our residence time analysis confirms that O_3 and O_4 sites have a stronger ability to constrict

Chapter III oxygen diffusion mechanism in donor-doped NBIO

the movement of oxygen ions than Oi site, while oxygen ions would not stay at the terminal interstitial site (Oi site) too long. For O1 and O2 sites, these two sites have the strongest abilities to trap oxygen, and these two sites do not participate in the oxygen diffusion.

III.4 Conclusions

In this work, we have made a specific analysis route for figuring out the oxygen diffusion mechanism in $\text{NdBaIn}_{1-x}\text{M}_x\text{O}_{4+x/2}$ ($\text{M}=\text{Ti}, \text{Zr}$) compound. Firstly, we operated the Bond Valence Summation (BVS) calculation to locate the possible oxygen interstitial position ($4e$ site [0.575 0.750 0.893]). Secondly, Molecular dynamics simulations were performed. The interstitial oxygen ion Wyckoff position calculated by MD is ($4e$ site [0.5766 0.7567 0.8959]), confirming the results of BVS calculation. At the meantime, lattice parameters, macroscopic diffusion coefficients, activation energy of self-diffusion have been obtained. Finally, DBSCAN (a machine learning algorithm) was adopted to associate precisely oxygen ions to specific crystallographic sites. Based on this classification method, we determined the jump numbers from site to site, the oxygen ion diffusion path and we performed a residence time analysis. An interstitialcy mechanism was predicted in the temperature range 1500K-1900K. Oxygen sites participate differently to the oxygen diffusion process. Oi are connectors that connect two participants (O3 and O4). while O1 and O2 can be considered as barriers. Oxygen diffusion occurs entirely in the plane b - c . Though this work concentrates on a series of specific compounds, we propose that the analysis route can be extrapolated to some other oxygen hyperstoichiometry compounds.

III.5 Notes and references

- [1] A. Chroneos, B. Yildiz, A. Tarancon, D. Parfitt, and J. A. Kilner, "Environmental

Chapter III oxygen diffusion mechanism in donor-doped NBIO

- Science Oxygen diffusion in solid oxide fuel cell cathode and electrolyte materials: mechanistic insights from atomistic simulations,” *Energy Environ. Sci.*, vol. 4, pp. 2774–2789, 2011.
- [2] B. C. H. Steele and A. Heinzl, “Materials for fuel-cell technologies,” *Nature*, vol. 414, no. 6861, pp. 345–352, 2001.
- [3] A. Tarancón, M. Burriel, J. Santiso, S. J. Skinner, and J. A. Kilner, “Advances in layered oxide cathodes for intermediate temperature solid oxide fuel cells,” *J. Mater. Chem.*, vol. 20, no. 19, pp. 3799–3813, 2010.
- [4] A. Chroneos, D. Parfitt, J. A. Kilner, and R. W. Grimes, “Anisotropic oxygen diffusion in tetragonal $\text{La}_2\text{NiO}_{4+\delta}$: Molecular dynamics calculations,” *J. Mater. Chem.*, vol. 20, no. 2, pp. 266–270, 2010.
- [5] D. Parfitt, A. Chroneos, J. A. Kilner, and R. W. Grimes, “Molecular dynamics study of oxygen diffusion in $\text{Pr}_2\text{NiO}_{4+\delta}$,” *Phys. Chem. Chem. Phys.*, vol. 12, no. 25, pp. 6834–6836, 2010.
- [6] D. Parfitt, A. Chroneos, A. Tarancón, and J. A. Kilner, “Oxygen ion diffusion in cation ordered/disordered $\text{GdBaCo}_2\text{O}_{5+\delta}$,” *J. Mater. Chem.*, vol. 21, no. 7, pp. 2183–2186, 2011.
- [7] I. D. Seymour, A. Chroneos, J. A. Kilner, and R. W. Grimes, “Defect processes in orthorhombic $\text{LnBaCo}_2\text{O}_{5.5}$ double perovskites,” *Phys. Chem. Chem. Phys.*, vol. 13, no. 33, pp. 15305–15310, 2011.
- [8] A. Kushima, D. Parfitt, A. Chroneos, B. Yildiz, J. A. Kilner, and R. W. Grimes, “Interstitialcy diffusion of oxygen in tetragonal $\text{La}_2\text{CoO}_{4+\delta}$,” *Phys. Chem. Chem. Phys.*, vol. 13, no. 6, pp. 2242–2249, 2011.
- [9] C. Chen, D. Chen, and F. Ciucci, “A molecular dynamics study of oxygen ion diffusion in A-site ordered perovskite $\text{PrBaCo}_2\text{O}_{5.5}$: Data mining the oxygen trajectories,” *Phys. Chem. Chem. Phys.*, vol. 17, no. 12, pp. 7831–7837, 2015.
- [10] C. Chen, Z. M. Baiyee, and F. Ciucci, “Unraveling the role of La A-site substitution on oxygen ion diffusion and oxygen catalysis in perovskite BaFeO_3 by data-mining molecular dynamics and density functional theory.” *Phys. Chem.*

Chapter III oxygen diffusion mechanism in donor-doped NBIO

- Chem. Phys.*, vol. 17, no. 37, pp. 24011–24019, 2015.
- [11] C. Chen, Z. Lu, and F. Ciucci, “Data mining of molecular dynamics data reveals Li diffusion characteristics in garnet $\text{Li}_7\text{La}_3\text{Zr}_2\text{O}_{12}$,” *Sci. Rep.*, vol. 7, no. January, pp. 1–8, 2017.
- [12] C. Tealdi, C. Ferrara, P. Mustarelli, and M. S. Islam, “Vacancy and interstitial oxide ion migration in heavily doped $\text{La}_{2-x}\text{Sr}_x\text{CoO}_{4\pm\delta}$,” *J. Mater. Chem.*, vol. 22, no. 18, pp. 8969–8975, 2012.
- [13] C. Tealdi, P. Mustarelli, and M. S. Islam, “Layered $\text{LaSrGa}_3\text{O}_7$ -based oxide-ion conductors: Cooperative transport mechanisms and flexible structures,” *Adv. Funct. Mater.*, vol. 20, no. 22, pp. 3874–3880, 2010.
- [14] C. Tealdi, C. Sprefico, and P. Mustarelli, “Lithium diffusion in $\text{Li}_{1-x}\text{FePO}_4$: The effect of cationic disorder,” *J. Mater. Chem.*, vol. 22, no. 47, pp. 24870–24876, 2012.
- [15] J. Hermet, B. Dupé, and G. Dezanneau, “Simulations of $\text{REBaCo}_2\text{O}_{5.5}$ (RE=Gd, La, Y) cathode materials through energy minimisation and molecular dynamics,” *Solid State Ionics*, vol. 216, pp. 50–53, 2012.
- [16] J. Hermet, G. Geneste, and G. Dezanneau, “Molecular dynamics simulations of oxygen diffusion in $\text{GdBaCo}_2\text{O}_{5.5}$,” *Appl. Phys. Lett.*, vol. 97, no. 17, p. 174102, 2010.
- [17] Y. Hu *et al.*, “Oxygen diffusion mechanism in the mixed ion-electron conductor $\text{NdBaCo}_2\text{O}_{5+x}$,” *J. Mater. Chem.*, vol. 22, no. 36, pp. 18744–18747, 2012.
- [18] G. Dezanneau, J. Hermet, and B. Dupé, “Effects of biaxial strain on bulk 8% yttria-stabilised zirconia ion conduction through molecular dynamics,” *Int. J. Hydrogen Energy*, vol. 37, no. 9, pp. 8081–8086, 2012.
- [19] K. Fujii *et al.*, “New Perovskite-Related Structure Family of Oxide-Ion Conducting Materials NdBaInO_4 ,” *Chem. Mater.*, vol. 26, no. 3, pp. 2488–2491, 2014.
- [20] K. Fujii, M. Shiraiwa, Y. Esaki, M. Yashima, S. J. Kim, and S. Lee, “Improved oxide-ion conductivity of NdBaInO_4 by Sr doping,” *J. Mater. Chem. A*, vol. 3,

Chapter III oxygen diffusion mechanism in donor-doped NBIO

- no. 22, pp. 11985–11990, 2015.
- [21] T. Ishihara, Y. Yan, T. Sakai, and S. Ida, “Oxide ion conductivity in doped NdBaInO₄,” *Solid State Ionics*, vol. 288, pp. 262–265, 2016.
- [22] X. Yang, S. Liu, F. Lu, J. Xu, and X. Kuang, “Acceptor Doping and Oxygen Vacancy Migration in Layered Perovskite NdBaInO₄-Based Mixed Conductors,” *J. Phys. Chem. C*, vol. 120, no. 12, pp. 6416–6426, 2016.
- [23] S. Adams, “Bond valence analysis of structure – property relationships in solid electrolytes,” *J. Power Sources*, vol. 159, pp. 200–204, 2006.
- [24] S. Adams, “Modelling ion conduction pathways by bond valence pseudopotential maps,” *Solid State Ionics*, vol. 137, pp. 1351–1361, 2000.
- [25] S. Adams and R. P. Rao, “materials by computational design pss solidi,” *Phys. Status Solidi A*, vol. 1753, no. 8, pp. 1746–1753, 2011.
- [26] I. D. Brown, “Recent Developments in the Methods and Applications of the Bond Valence Model,” *Chem. Rev.*, no. 109, pp. 6858–6919, 2009.
- [27] I. D. Brown and D. Altermatt, “Bond-Valence Parameters Obtained from a Systematic Analysis of the Inorganic Crystal Structure Database,” *Acta Crystallogr. Sect. B*, vol. 244, no. 2, pp. 244–247, 1985.
- [28] S. NISHIMURA, “<https://shinichinishimura.github.io/pyabst/#>.”
- [29] I. T. Todorov, W. Smith, K. Trachenko, and M. T. Dove, “DL_POLY_3: New dimensions in molecular dynamics simulations via massive parallelism,” *J. Mater. Chem.*, vol. 16, no. 20, pp. 1911–1918, 2006.
- [30] C. Tealdi, L. Malavasi, C. A. J. Fisher, and M. S. Islam, “Disproportionation, dopant incorporation, and defect clustering in perovskite-structured NdCoO₃,” *J. Phys. Chem. B*, vol. 110, no. 11, pp. 5395–5402, 2006.
- [31] G. V Lewis and C. R. A. Catlow, “Potential models for ionic solids,” *J. Phys. C Solid State Phys.*, vol. 18, pp. 1149–1161, 1985.
- [32] C. Fisher, “Defect, protons and conductivity in brownmillerite-structured Ba₂In₂O₅,” *Solid State Ionics*, vol. 118, no. 3–4, pp. 355–363, 1999.
- [33] J. D. Gale and A. L. Rohl, “The General Utility Lattice Program (GULP),” *Mol.*

Chapter III oxygen diffusion mechanism in donor-doped NBIO

- Simul.*, vol. 29, pp. 291–341, 2003.
- [34] M. Ester, H.-P. Kriegel, S. Jorg, and X. Xu, “A Density-Based Clustering Algorithms for Discovering Clusters,” *Kdd*, vol. 96, no. 34, pp. 226–231, 1996.
- [35] T. N. Tran, K. Drab, and M. Daszykowski, “Revised DBSCAN algorithm to cluster data with dense adjacent clusters,” *Chemom. Intell. Lab. Syst.*, vol. 120, pp. 92–96, 2013.
- [36] E. Schubert, J. Sander, M. Ester, H. P. Kriegel, and X. Xu, “DBSCAN Revisited, Revisited: Why and How You Should (Still) Use DBSCAN,” *ACM Trans. Database Syst.*, vol. 42, no. 3, pp. 1–21, 2017.
- [37] S. J. Skinner, “Characterisation of $\text{La}_2\text{NiO}_{4+\delta}$ using in-situ high temperature neutron powder diffraction,” *Solid State Sci.*, vol. 5, no. 3, pp. 419–426, 2003.
- [38] K. Cornell, H. Wipf, U. Stuhr, and A. V. Skripov, “A neutron diffraction study of the interstitial sites of deuterium in the A-15 compound Ti_3Ir ,” *Solid State Commun.*, vol. 101, no. 8, pp. 569–573, 1997.
- [39] M. Ceretti *et al.*, “Low temperature oxygen diffusion mechanisms in $\text{Nd}_2\text{NiO}_{4+\delta}$ and $\text{Pr}_2\text{NiO}_{4+\delta}$ via large anharmonic displacements, explored by single crystal neutron diffraction,” *J. Mater. Chem. A*, vol. 3, no. 42, pp. 21140–21148, 2015.
- [40] Y. Ma, “Simulation of interstitial diffusion in graphite,” *Phys. Rev. B*, vol. 76, no. 7, pp. 2–6, 2007.
- [41] D. E. Jiang and E. A. Carter, “Diffusion of interstitial hydrogen into and through bcc Fe from first principles,” *Phys. Rev. B*, vol. 70, no. 6, pp. 1–9, 2004.
- [42] C. Jiang, S. A. Maloy, and S. G. Srinivasan, “A computational method to identify interstitial sites in complex materials,” *Scr. Mater.*, vol. 58, no. 9, pp. 739–742, 2008.
- [43] Z. I. Botev, J. F. Grotowski, and D. P. Kroese, “Kernel density estimation via diffusion,” *Ann. Stat.*, vol. 38, no. 5, pp. 2916–2957, 2010.

III.6 Supporting information

Labels	site	x	y	z	g
Nd	4e	0.45255	0.74754	0.10772	1
Ba	4e	0.14906	0.2520	0.03297	1
In	4e	0.83218	0.2559	0.2066	1
O1	4e	0.18290	0.80251	0.04752	1
O2	4e	-0.01160	-0.0098	0.26951	1
O3	4e	0.38400	0.5426	0.32956	1
O4	4 ^e	0.64914	0.5054	0.12922	1

Table S3.1 The Wyckoff positions of different ions in NdBaInO₄, g is the Occupancy factor.¹

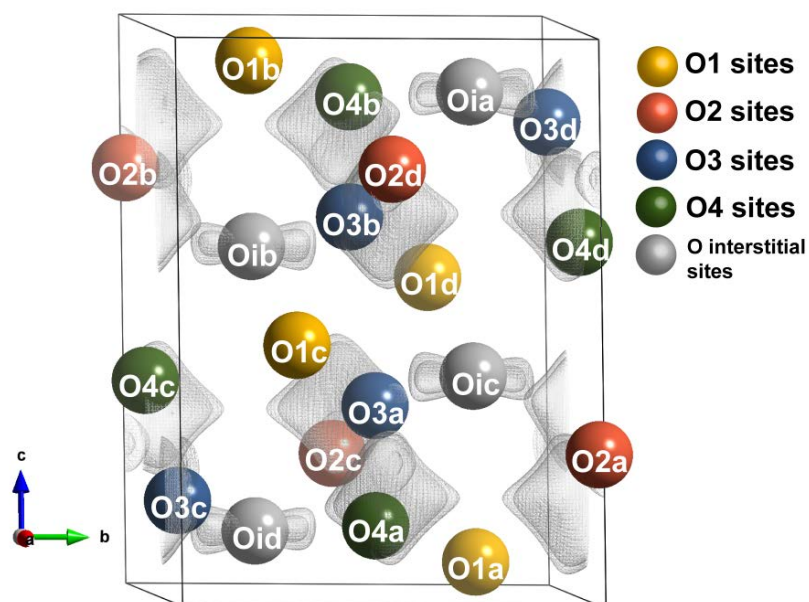


Figure S3.1 Isosurfaces for value of the oxygen BV mismatch $|\Delta V(O^{2-})| = 0.05$ in NdBaInO₄. The less value of $|\Delta V(O^{2-})|$, the more precise interstitial position we can obtain.

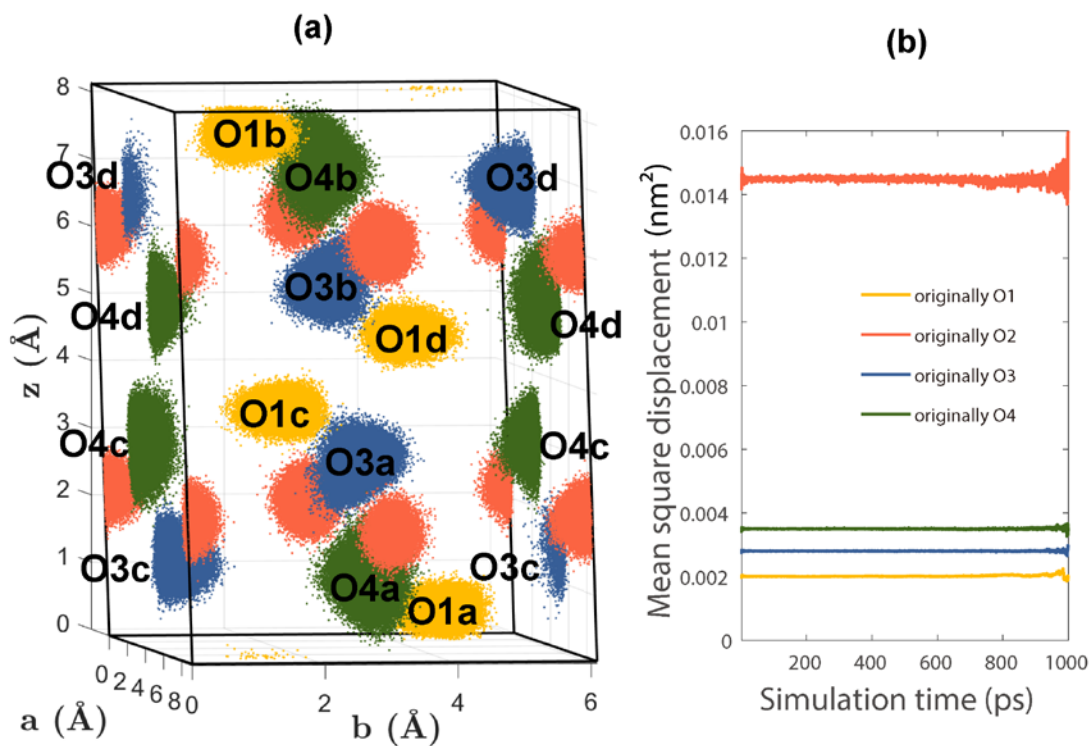


Figure S3.2 (a) Complete information unit cell of NbBaInO₄ 1500K. (b) The MSD curves of different oxygen ion in NdBaInO₄

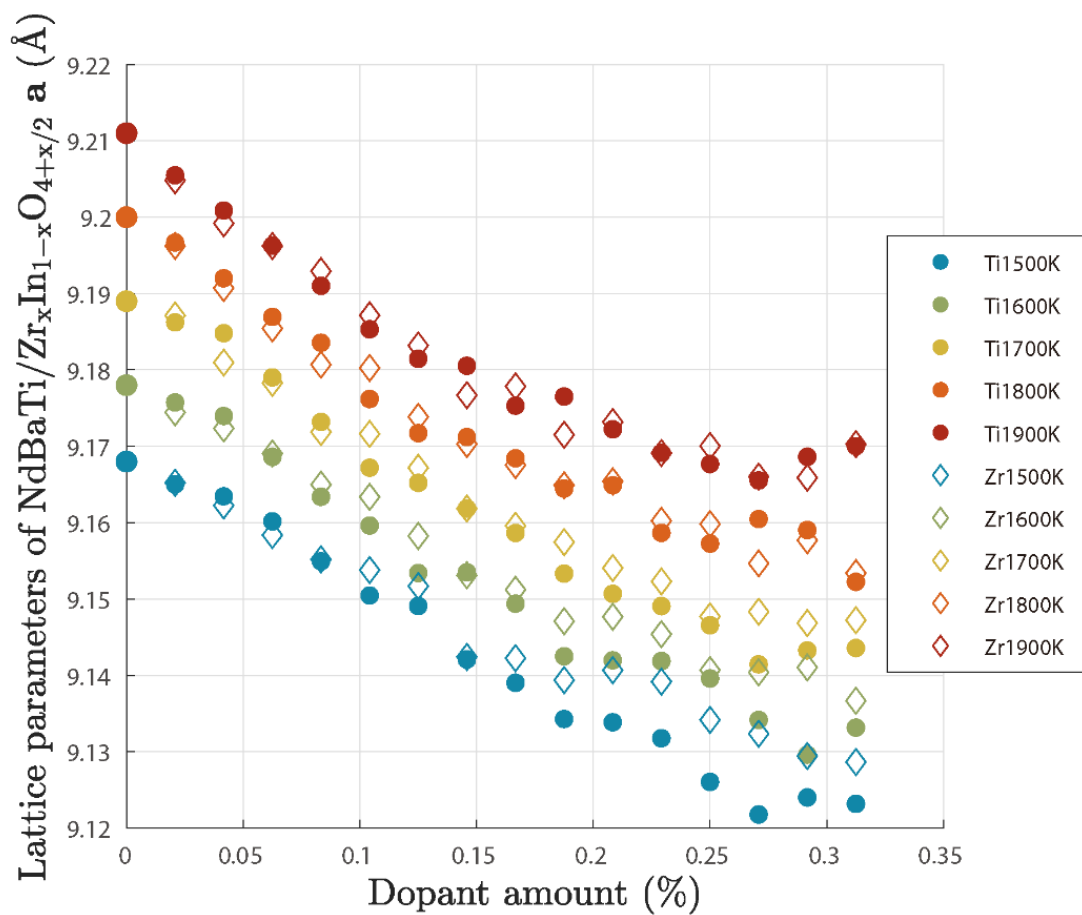


Figure S3.3 Lattice parameters a (\AA) of $\text{NdBa}(\text{Ti/Zr})_x\text{In}_{1-x}\text{O}_{4+x/2}$ as a function of temperature and dopant concentration.

The max value of lattice parameters a are found at pure NdBaInO_4 of each temperature. Lattice parameter decreases with the increase of dopant concentration. With the same dopant amount and temperature, the values of a of Ti doped compounds are slightly lower than those of Zr doped ones. This can be attributed to the difference in ion size between dopants and hosting In ion, *i.e.*, $r(\text{Ti}^{4+}) = 0.745 \text{\AA} < r(\text{Zr}^{4+}) = 0.86 \text{\AA} < r(\text{In}^{3+}) = 0.94 \text{\AA}$.²

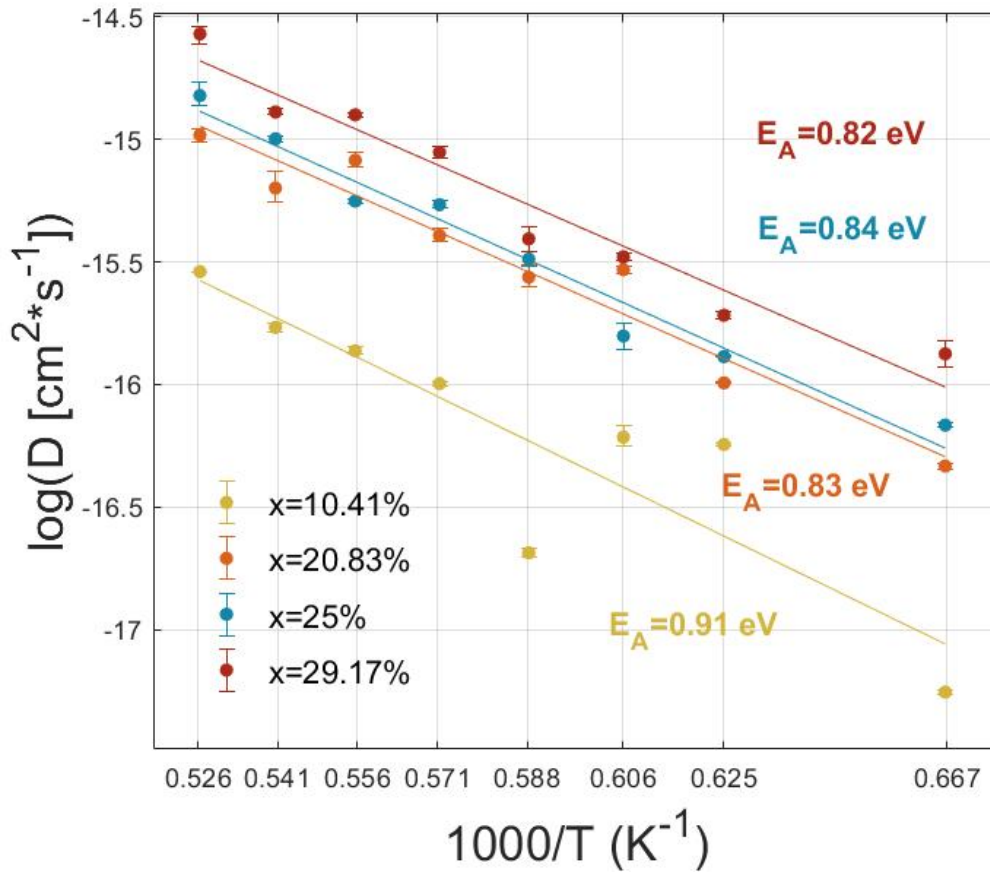


Figure S3.4 Calculated logarithm of oxygen diffusion coefficients as a function of the inverse of temperature of $\text{NdBaIn}_{1-x}\text{Ti}_x\text{O}_{4+x/2}$ ($x= 10.41\%$, 20.83% , 25% , 29.17%).

Diffusion coefficient D can be expressed as a function of temperature T through:

$$D = D_0 \cdot \exp\left(-\frac{E_A}{k_B T}\right)$$

Where k_B being the Boltzmann constant, D_0 a pre-exponential factor and E_A the activation energy of the diffusion process. The activation energy for oxygen diffusion can be obtained by fitting the logarithm of oxygen diffusion coefficient with the reciprocal of temperature as shown in **Figure S3.4**.

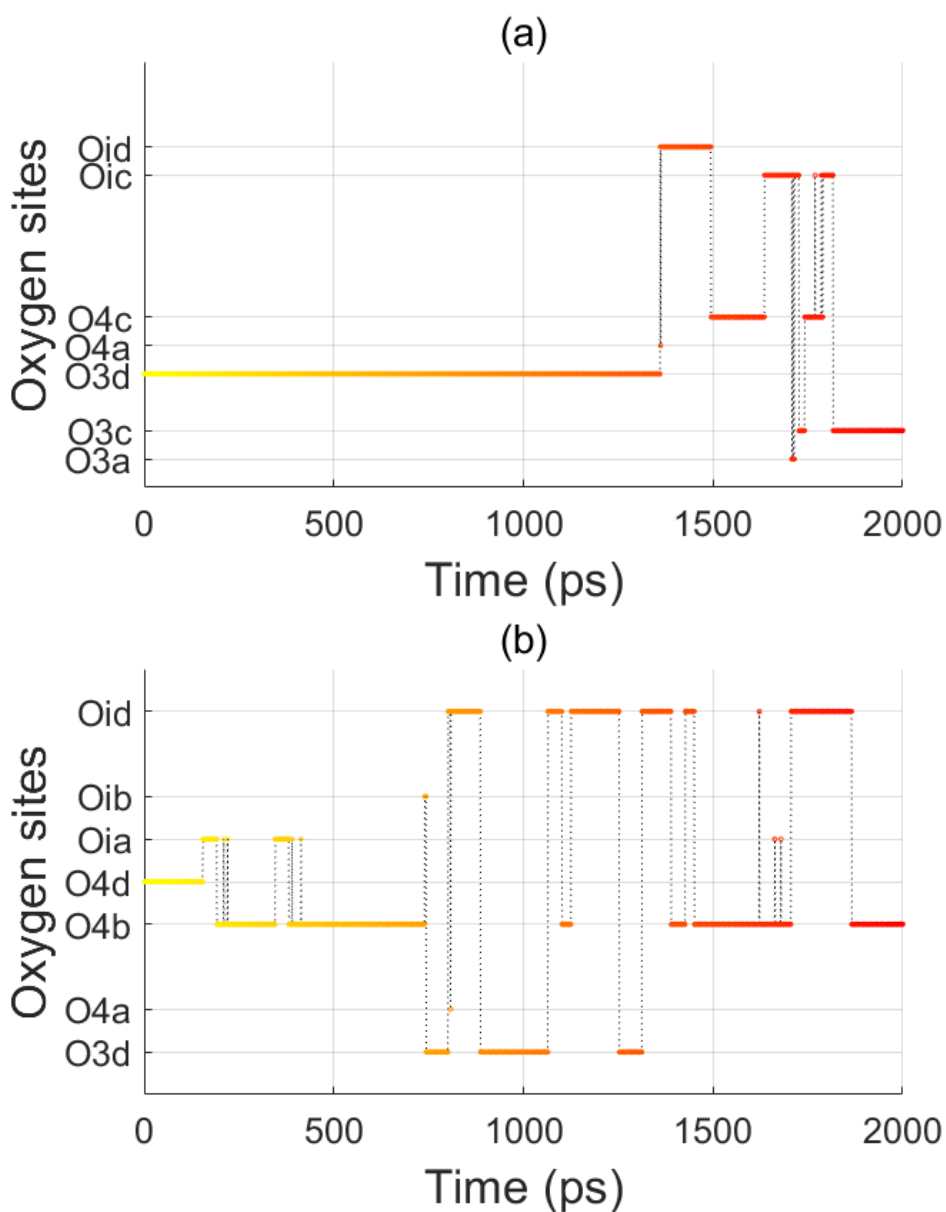


Figure S3.5 Trajectories of two selected oxygen ion with the evolution of simulation time in $\text{NdBaIn}_{1-x}\text{Ti}_x\text{O}_{4+x/2}$ $x=9.375\%$ at 1500K.

Notes and references

- 1 K. Fujii, Y. Esaki, K. Omoto, M. Yashima, A. Hoshikawa, T. Ishigaki and J. R. Hester, *Chem. Mater.*, 2014, **26**, 2488–2491
- 2 R. D. Shannon, *Acta crystallographica section A: crystal physics, diffraction, theoretical and general crystallography*, 1976, **32**, 751–767.

Chapter III oxygen diffusion mechanism in donor-doped NBIO

Chapter IV Hydride diffusion mechanism in LaHO family

Abstract

Oxyhydrides are promising hydride ion conductors for electrochemical devices. The understanding of H⁻ diffusion mechanisms is still at its infancy: for now, only a few Density Functional Theory calculations allowed to anticipate some of the most favorable pathways at the atomic scale in different materials. Due to the lack of available force field for H⁻, no study involving large scale or long-time simulations has been reported, which would provide a precise link between atom motions and macroscopic diffusion coefficients. To fill such a gap, the present work combines (1) DFT calculations in order to build an interatomic potential taking into account the structural and elastic properties of the various polymorphic forms of LaHO and (2) classical Molecular Dynamics calculations based on the developed potential to study the hydride ion diffusion mechanism in LaHO. The hydride ion diffusion mechanism is explored in the two most stable forms of LaHO, namely α -LaHO and β -LaHO. In pure α -LaHO, two different steps in the diffusion process were identified, the first one induced by a cooperative motion of hydride ions within a unit block, the second one leading to a jump between the same hydride-ions unit blocks. As a whole, the long-range diffusion is highly anisotropic, occurring mainly along with a and b directions. In pure β -LaHO, the hydride diffusion mechanism is also identified, having in this case only a slight anisotropic character. The activation energies for hydride diffusion in non-defective α -LaHO and β -LaHO are calculated to be 1.3 and 2.2 eV, respectively. Due to its low hydride migration energy and its higher conductivity, the α -LaHO structural form has more potential for low-temperature devices. Finally, we try to evaluate the influence of potential defects on hydride ion diffusion properties. We prove that a small number of anionic defects may significantly alter the diffusion mechanism leading to much lower diffusion activation energies.

Hydride diffusion mechanisms in LaHO family: A computational study

IV.1 Introduction

Ion conducting materials with different mobile ion species have been thoroughly studied both experimentally and theoretically, *e.g.*, Li-ion conductors, [1]-[6] O-ion conductors,[7]-[15] and proton conductors,[16], [17] etc. The exploration of proton-conducting oxides, where H is in the ionized state H^+ , has been the object of intense researches due to their potential ability to fill the gap between low-temperature organic proton-conductors and high-temperature oxide ion conductors.[18] Specific studies have in particular focused on the influence of dopant on hydration, proton-dopant association, migration energies in perovskite-type compounds like $BaSnO_3$, $BaZrO_3$, or $BaCeO_3$. [17], [19]–[21] Significant works have also allowed identifying more precisely how the quantum nature of protons is involved in the diffusion process in oxide materials.[22], [23] More recently, several works have focused on hydride containing compounds (H^-) with promising performances for the next-generation of electrochemical energy conversion systems.[18], [24]-[36]

The efforts to discover new H^- conductors have followed two strategies, the first one based on metal hydride compounds[25], the other one on oxyhydride materials[24], [37]–[39]. Irvine *et al.* show that barium hydride BaH_2 presents a hydride ion conductivity of 0.2 S/cm at 903 K, which is an order of magnitude larger than that of state-of-the-art proton-conducting perovskites or oxide ion conductors at this temperature.[25] Concerning oxyhydride materials, Kobayashi *et al.*[33] discovered the new $La_{2-x-y}Sr_{x+y}LiH_{1-x+y}O_{3-y}$ ($0 \leq x \leq 1$, $0 \leq y \leq 2$, $0 \leq x + y \leq 2$) compound, in which they measured a high H^- conductivity of 0.12 mS/cm at 573 K. They also built an all-solid-state $TiH_2/o-La_2LiHO_3/Ti$ cell and proved the feasibility of developing solid

Chapter IV Hydride diffusion mechanism in LaHO family

electrochemical devices based on H^- conductors. Bai *et al.* studied the H^- diffusion mechanism of $\text{La}_{2-x-y}\text{Sr}_{x+y}\text{LiH}_{1-x+y}\text{O}_{3-y}$ with first-principles calculations. They confirmed the good stability and chemical robustness of this material with K_2NiF_4 structure. They also identified that the fast H^- diffusion is mediated by H^- vacancies and showed through calculations that aliovalent doping with Na^+ , K^+ , and Rb^+ instead of Sr^{2+} in $\text{Sr}_2\text{LiH}_3\text{O}$ could enhance H^- ionic conductivity.[30] Kageyama *et al.* expanded the lanthanide oxyhydrides family LnHO ($\text{Ln} = \text{La}, \text{Ce}, \text{Pr}, \text{Nd}$) series to include $\text{Ln} = \text{Sm}, \text{Gd}, \text{Tb}, \text{Dy}, \text{Ho},$ and Er . They showed that anion-ordered fluorite-derived structure ($P4/nmm$) is observed for larger Ln^{3+} ions (La-Nd) while a more classical disordered fluorite structure ($Fm\bar{3}m$) is observed for smaller Ln^{3+} (Sm-Er), this transition being driven by the size flexibility of hydride anion.[28] Besides, they found unexpectedly two novel high-pressure polymorphs of lanthanum oxyhydride. When the pressure changes from ambient pressure to 3 GPa and then to 5 GPa, the structure of LaHO evolves from anion-ordered fluorite structure α -LaHO ($P4/nmm$) to PbCl_2 -type structure γ -LaHO ($Pnma$) and then to Fe_2P -type structure δ -LaHO ($P\bar{6}2m$).[31] While the anion-ordered phase α -LnHO ($\text{Ln} = \text{La}, \text{Nd}$) exhibits measurable hydride conductivity (e.g., 2.3×10^{-5} S/cm for NdHO at 300 °C), the disordered fluorites phases do not. Finally, Hosono *et al.* studied the oxygen-doped LaH_3 ($\text{LaH}_{3-2x}\text{O}_x$) and showed it has an optimum ionic conductivity of 2.6×10^{-2} S cm^{-1} for $x=0.24$ at 615 K.[18]

In the present paper, we aim to explore more deeply the LaHO family, taking benefit from the existence of different well-known structural forms. More concretely, we have studied the hydride ion diffusion mechanism in both α -LaHO ($P4/nmm$) and β -LaHO ($Pnma$), which are the most commonly reported forms at ambient pressure.[24], [31], [40] Our approach is based on both DFT and classical molecular dynamics simulations. Molecular dynamics (MD) simulation has the unique advantage of being able to deal with large-scale systems (other thousands of atoms), *i.e. sizes* otherwise difficultly accessible to first-principle calculations. Yet, the unavailability of a force field for H^-

has precluded the use of Molecular Dynamics in the LaHO system until now. In this work, we remediate to this lack of knowledge by developing, from first-principles, a new set of interatomic potentials for the LaHO system, which reproduces most features of LaHO polymorphic forms. Then, using MD simulations, we derive a coherent picture of the hydride ion diffusion mechanism in defective and non-defective α -LaHO and β -LaHO structural forms.

IV.2 Computational techniques

IV.2.1 First-principle calculation

Density Functional Theory (DFT) calculations were performed using the Projector Augmented-Wave (PAW)[41] approach implemented in the Vienna Ab initio Simulation Package (VASP).[42] All calculations were performed using the Perdew–Burke–Ernzerhof (PBE), and Perdew-Burke-Ernzerhof revised for solids (PBEsol) generalized-gradient approximation (GGA) functional.[43] The plane wave cutoff energies were set to 800 eV, and integration in reciprocal space was performed with $6 \times 6 \times 6$ Monkhorst-Pack k-point meshes. Structural optimizations were conducted with full degrees of freedom relaxation (cell volume, cell shape, and atomic positions) using a conjugate gradient algorithm, converging forces to 10^{-7} eV/Å and electronic energies to 10^{-8} eV.

The climbing-image nudged elastic-band (CI-NEB)[44] calculations were performed to determine the different energy barriers of H^- migration. The forces of CI-NEB were converged within 0.01 eV/Å. A single Γ -centered $1 \times 1 \times 1$ k-point was used. All CI-NEB calculations for α -LaHO were based on supercells with $1 \times 1 \times 2$ unit cells, while for β -LaHO, $1 \times 2 \times 2$ unit cells was adopted. Calculation with higher density reciprocal space meshes give qualitatively similar results. (More details see **Figure S4.1**)

IV.2.2 Derivation of Interatomic potentials

A full set of classical interatomic potential for LaHO was obtained by employing the General Utility Lattice Program (GULP), which allows to reproduce DFT-calculations.[45] In this paper, the Buckingham and Coulomb potentials were used to describe the short-range and long-range interaction:

$$\varphi_{ij} = A_{ij} \exp\left(-\frac{r_{ij}}{\rho_{ij}}\right) - \frac{C_{ij}}{r_{ij}^6} + \frac{q_i q_j}{r_{ij}}$$

Where r_{ij} is the distance between the ions i and j , and A_{ij} , ρ_{ij} , C_{ij} are potential parameters specific through an empirical fitting for each ion pair, q_i , and q_j are charges on the ions. The three terms on the right-hand side constitute the repulsion, the dispersion, and the Coulomb terms, respectively.

The potential fitting procedure adopted was the following: Firstly, structural data (atomic positions and lattice parameters), elastic tensors of 6 different materials, including α -LaHO (Table S4.1), β -LaHO (Table S4.2), La₂O₃[46] (Table S4.3), LaH₃[46] (Table S4.4), γ -LaHO (Table S4.5) and δ -LaHO (Table S4.6), were calculated with first-principle calculations using both PBE and PBEsol potentials. Secondly, except for γ -LaHO and δ -LaHO, the data of the other four materials were used for potential fitting by GULP. Finally, the properties of all 6 materials were calculated in MD simulations using the fitted potential and compared with experimental and DFT results.[45]

Interactions	A / eV	ρ / Å	C / eV Å ⁶
La ^{2.4+} — H ^{0.8-}	1259.77	0.3073	0.00
La ^{2.4+} — O ^{1.6-}	2197.85	0.3180	0.00
O ^{1.6-} — O ^{1.6-}	13803.26	0.21601	0.00
La ^{2.4+} — La ^{2.4+}	459.38	0.1236	0.00

Table 4.1 Optimized interatomic Buckingham potentials, as obtained from the fitting

of PBE-functional DFT calculations

Two interatomic potentials were obtained corresponding to the fitting of PBE and PBEsol calculations, and are presented in **Table 4.1** and in **Table S4.7**. After many attempts with formal charges, partial charges were finally adopted with values of +2.4, -0.8, and -1.6 C for La, H, and O ions, respectively. The use of partial charges was the only way to reproduce structural and elastic properties since the use of formal charges +3, -2, and -1 C for La, O, and H led systematically to very stiff materials. The core-shell model[47], which introduces ion polarization, has also been tested but, due to the highly symmetric character of the considered structural forms, it always led to a low improvement of the model. We also observed that the dispersion coefficient C_{ij} increases to unreasonably high values during fitting, most likely to prevent the O and H ions from repelling each other too much. Despite its elementary form, our model with partial charges reproduces with great accuracy the different structural forms of LaHO and their elastic properties. Indeed, in all cases, the cell parameters are reproduced within 1%, the fractional atomic position are reproduced to a precision of 1/100, and the elastic coefficients are most often reproduced with less than a 10% error. Considering the very diverse nature of the materials used in the fit, namely oxides, hydrides, oxyhydrides, we consider that the proposed potential works indeed very correctly. Diffusion being in nature a highly anharmonic process, we also calculated the evolution of cell parameters with temperature through MD calculations (see below) and once more the proposed potential reproduces reasonably well the experimental evolution (see **Figure 4.1**).

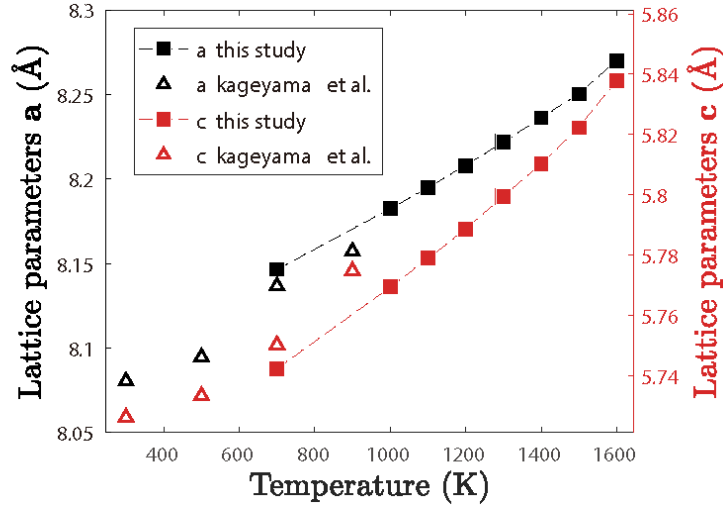


Figure 4.1 Evolution of α -LaHO lattice parameters as a function of temperature. Comparison with experimental data provided by Professor Kageyama.[24]

IV.2.3 Molecular dynamic simulation

The α -LaHO unit cell structure was firstly optimized by DFT calculation and then expanded to a $5 \times 5 \times 5$ supercell, representing 3000 ions in total. For defective supercells, presenting 2% H interstitials, 2% H vacancies, and 2% O vacancies, we introduced these defects randomly using the software ATOMSK[48]. Three different original configurations were produced for each type of defective lattice. For pure β -LaHO and its defective configurations, the procedure was similar except that the supercell contains $5 \times 10 \times 5$ unit cells. MD simulations were performed with the DLPOLY classic code[49] with 8 simulation temperatures (from 700K to 1600K). Interactions between ions are described by a long-range Coulombic term calculated by Ewald Summation, and a short-range Buckingham pair potential. For Coulombic interactions, we use the formal charges of +2.4, -0.8, and -1.6 for La, H, and O ions, respectively. The parameters determining the Buckingham potential are described in **Table 4.1**, which corresponds to the potential fitted on PBE DFT calculations. Each system was first equilibrated at the desired temperature and zero pressure for 20,000-time steps (with a time step duration of 0.5 fs) in the isothermal-isobaric ($N\sigma T$)

Chapter IV Hydride diffusion mechanism in LaHO family

ensemble with Nose-Hoover thermostat. Afterwards, the equilibrium lattice parameters were calculated with additional 80,000-time steps. Simulations were then performed in the NVT ensemble during 100,000-time steps. Finally, NVE simulations were realized, corresponding to 2,000,000 time steps. Ions trajectories coordinates were recorded every 1000-time or 100-time steps to the trajectory file. The convex hull classification method has been used for associating each ion trajectory to a specific Wyckoff site.[11] After NVE simulation, the diffusion coefficients were computed by monitoring the slope of the ion's mean squared displacement (MSD):

$$\bar{D} = \lim_{t' \rightarrow +\infty} \frac{\langle [x_i(t+t') - x_i(t)]^2 \rangle}{6t'}$$

where \bar{D} is the diffusion coefficient, $x_i(t)$ is the particle's instantaneous position, t' the lag time, and $\langle \dots \rangle$ denotes the ensemble average. Furthermore, according to the Arrhenius equation, \bar{D} can be expressed as a function of temperature T:

$$\bar{D} = D_0 \cdot \exp\left(-\frac{E_A}{k_B T}\right)$$

Where k_B being the Boltzmann constant, D_0 a pre-exponential factor, and E_A the activation energy of the diffusion process.

IV.3 Results and discussion

IV.3.1 General results of MD simulations in α -LaHO and β -LaHO phases

MD simulations allow obtaining relevant information concerning the vibration and potential diffusion of atoms in both α -LaHO and β -LaHO phases. In the **Figure 4.2**, we plot the mean square displacements (MSD) of all atoms in both phases at two different temperatures. This figure evidences that diffusion is hardly observed at low temperature since all types of atoms seem only to vibrate around their original position. At higher temperature, the MSD curve tends to follow, for the hydride ion, a straight line with a non-zero slope, from which a diffusion coefficient can be extracted. For α -LaHO, MSD

curves also evidence a marked anisotropy with a much smaller slope along the c -direction.

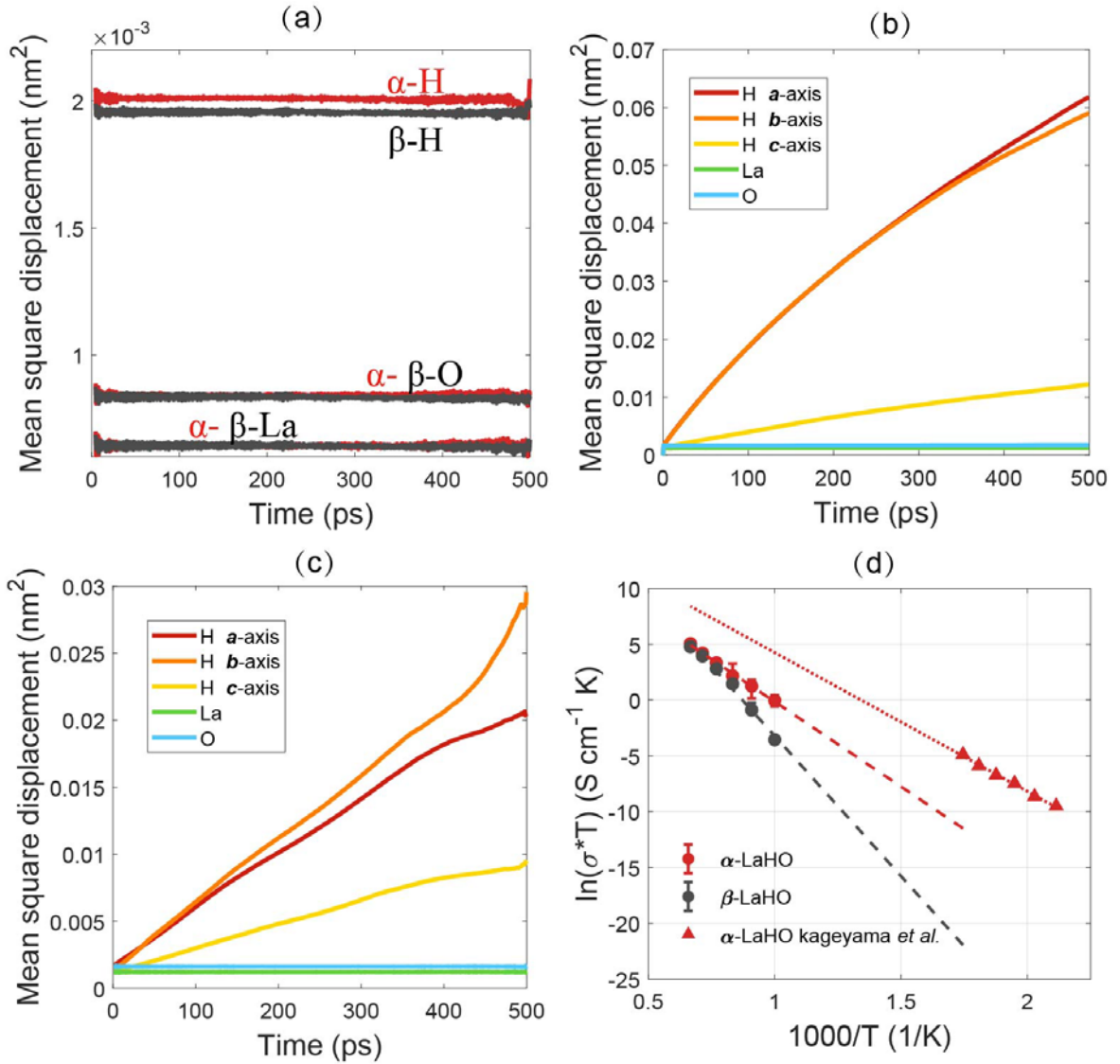


Figure 4.2 (a) MSD curves of La, H, O ions in α , β -LaHO at 700 K (b) MSD curves of La, H, O ions in α -LaHO at 1200 K. a , b , c are the primitive vectors of α -LaHO unit cell. (c) MSD curves of La, H, O ions in β -LaHO at 1200 K. (d) The ion conductivity as a function of temperature in α , β -LaHO compared to experimental data from Prof. Kageyama's group[24]

The diffusion coefficient as extracted from MSD curve can also be converted into ionic conductivity σ using the Nernst-Einstein equation[50]:

Chapter IV Hydride diffusion mechanism in LaHO family

$$\sigma = \frac{e^2}{Vk_B T} (N_+ z_+^2 \overline{D_+} + N_- z_-^2 \overline{D_-})$$

It states that the conductivity is proportional to the diffusion coefficients of the ionic species and to their concentration. where e is the elementary charge, V and T are the volume and the temperature, and $\overline{D_{\pm}}$, z_{\pm} , N_{\pm} are respectively the diffusion coefficient, charge, and the number of cations and anions. The conductivities of non-defective α - and β -LaHO are shown in **Figure 4.2d**. The conductivity of α -LaHO is larger and exposes an exponential growth trend with increasing temperature. Kageyama et al. have measured the bulk conductivity of α -LaHO at from 473K to 573 K and achieved $1.32 \times 10^{-5} \text{ S cm}^{-1}$ at 573K.[24] For α -LaHO, We obtain a hydride conductivity of $9.68 \times 10^{-4} \text{ S cm}^{-1}$ at 1000 K. This value is smaller than the one expected from an extrapolation of experimental data. Nevertheless, the activation energy for α -LaHO through MD calculations (1.3 eV) is similar to the one reported for conductivity measurements (1.01 eV).[24]

IV.3.2 Hydride diffusion mechanism in non-defective α -LaHO

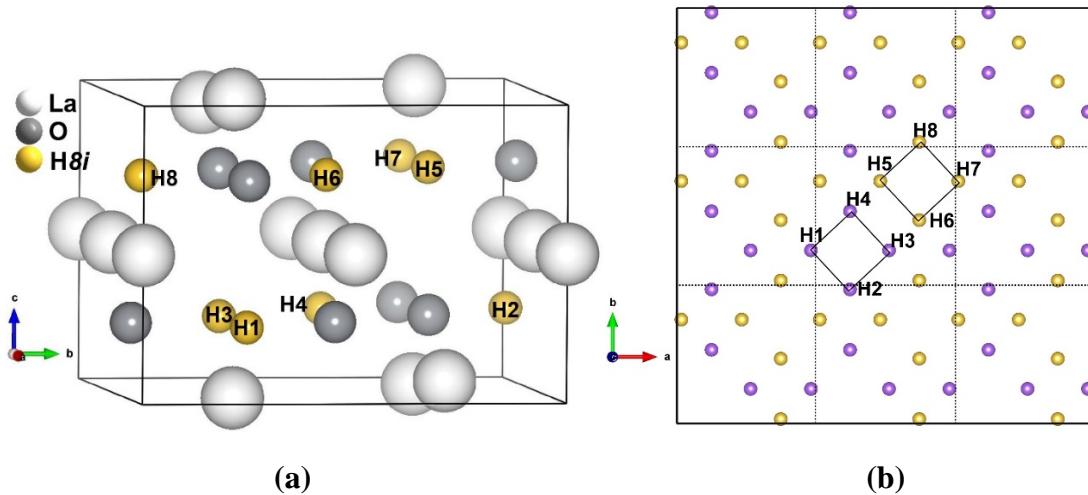


Figure 4.3 (a) Tetragonal unit cell of α -LaHO. (b) $3 \times 3 \times 1$ unit cells of α -LaHO view from z -direction. The violet balls represent for the hydride H1-H4 with $z \approx 0.24$, while the yellow balls are the hydrides H5-H8 with $z \approx 0.76$. Four hydrides (H1 to H4) construct a square according to periodic boundary condition.

The unit cell of α -LaHO is presented in **Figure 4.3a**, with the atomic positions given in **Table S4.1**. In one unit cell, there are 8 La, 8 H, and 8 O ions, respectively. Depending on the z coordinate value, the 8 H ions might be divided into two groups: H1 to H4 ($z \approx 0.24$) belong to one group (bottom layer), H5 to H8 ($z \approx 0.76$) belong to the other group (top layer). H1 to H4 (resp. H5 to H8) form a square where H atom groups are separated by the different z coordinates (**Figure 4.3b**). As discussed below, these squares constitute blocks in which a collective motion of hydrogen atoms could be observed. We can also mention the previously identified interstitial positions[24], which are located on the $(2b)$, $(2c)$ and $(4d)$ Wyckoff positions.

In **Figure 4.4**, we present the results of MD simulations in α -LaHO at 700 K and 1100 K. In this figure, each dot represents a hydride-ion position at a given time. The colour of each dot is decided after associating a given hydride position to a specific crystallographic site, following a convex hull procedure as described exhaustively in a previous article.[11] In this figure, H1 and H5, H2 and H6, H3 and H7, H4 and H8 are coloured in yellow, brown, blue and dark red, respectively. The hydride-ion positions which do not belong to any of the original position were associated with the closest potential interstitial sites, namely $(2c)$ and $(4d)$, with the respective colour green and pink. In **Figure 4.4**, one can appreciate two essential mechanisms in the long-range hydride-ion diffusion process: (1) hydride ions can exchange positions *within* a hydrogen block by going through the $(2c)$ interstitial site (green dots at the center of the square of hydrogen atoms in **Figure 4.4a**); (2) one (or two) hydride ions can jump *between* hydrogen blocks using the $(4d)$ interstitial site (pink dots between squares of hydrogen in **Figure 4.4b**). A detailed description of these two mechanisms is given below.

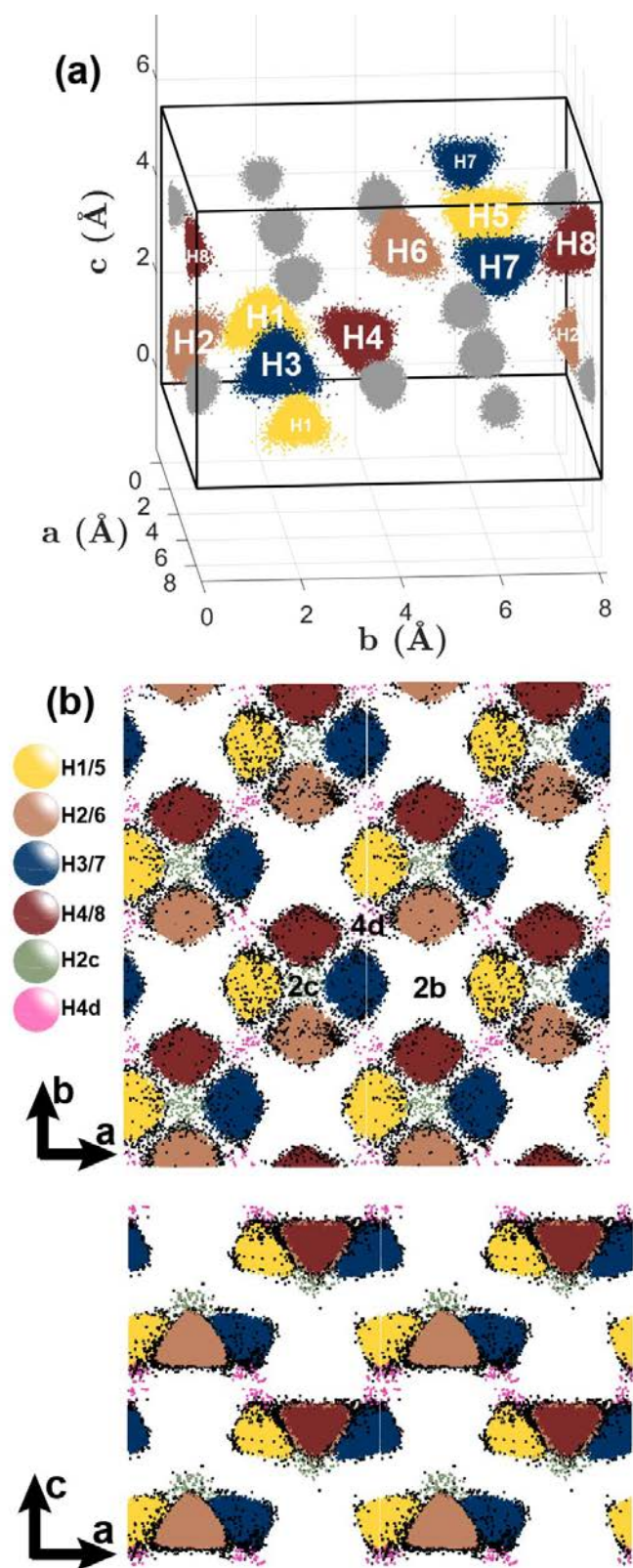


Figure 4.4 Representation of hydride-ion positions all along with the MD simulation and association to specific crystallographic sites following the convex hull approach. (a) the complete information cell of α -LaHO at 700 K (b) Projection of hydride ions

Chapter IV Hydride diffusion mechanism in LaHO family

positions at 1100 K along the c and b axis.

In the case of the intra-block diffusion mechanism, which occurs with the exchange of hydride ions through the assistance the $(2c)$ interstitial site, we note that Kageyama *et al.* already suggested that interstitial H⁻ may locate on the $(2c)$ position based on neutron powder diffraction experiments[24]. However, they described that $(2c)$ interstitial site to be located at (0.25, 0.25, 0.692). Here, we suggest that this coordinate is $\sim(0.25\ 0.25\ 0.422)$ in agreement with all our calculations. Indeed, not only the Bond Valence Sum (BVS) isosurfaces, but also the trajectories of molecular dynamics simulations and the DFT calculations confirm the validity of this interstitial position. Bond valence analysis is a simple method for the identification of ion transport pathways in crystalline ion conductors.[51], [52] “Accessible” sites for mobile ions A in a local structure model are identified using empirical relationships between the bond length R and a so-called bond valence: $S_{A-X} = \exp[(R_0 - R)/b]$, where R_0 and b are empirical parameters.[51], [52] The mismatch of the BVS, $|\Delta V(A)| = |\sum_X S_{A-X} - V_{id}(A)|$, over the S_{A-X} from all adjacent counter ions X approaches the ideal valence $V_{id}(A)$. Isosurfaces of fixed $|\Delta V(A)|$ for a certain ion type A thus may be approximately identified with regions that A can reach. The BVS map of the hydride of α -LaHO was calculated using PyAbstantia[53] and is shown in **Figure 4.5**. The grey surfaces in this figure represent the isosurfaces where the different bond valence sum for a hydride (the difference between observed BVS and the ideal valence of a hydride (i.e., 1)) is $|\Delta V(H^-)|=0.30$ valence units (v.u.). H1 to H4 on their crystallographic sites, plus the $(2c)$ interstitial position form a square-base pyramid, with the $(2c)$ interstitial position being the apex of the pyramid. When we lower the value of $|\Delta V(H^-)|$ for the isosurface representation, we can refine the $(2c)$ interstitial site position to be (0.25 0.25 0.422). Similarly, the center of mass of the $(2c)$ convex after the analysis of MD simulation was found to be (0.249 0.249 0.447).

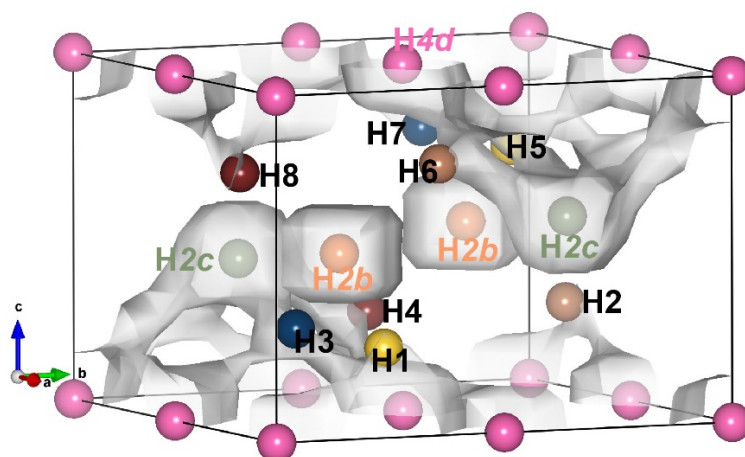


Figure 4.5 Isosurfaces for the value of the hydride BV mismatch $|\Delta V(H^-)| = 0.30$ in the α -LaHO unit cell. H1/H5, H2/H6, H3/H7, H4/H8 are colored in yellow, brown, blue and dark red, respectively. H 2b (orange), H 2c (green), and H 4d (pink) are interstitial positions, at Wyckoff positions (0.25 0.75 0.5), H 2c (0.25 0.25 0.422), H 4d (0 0 0) respectively

Once the precise position of the (2c) position has been refined, it is important to identify the role of such an interstitial site in the diffusion process. As mentioned above, H1 to H4, with the same z coordinate, constitutes a square of hydride ions. Within this block, four different types of collective jumps were identified which contribute to the mixing of hydride positions within the block:

- Exchange n° 1: One hydride ion at (8i) site jumps to the (2c) site, and comes back. Any hydride among H1 to H4 can jump into their associate (2c) site, and reciprocally a hydride ion located at (2c) site can fill an empty (8i) site. We performed CI-NEB calculations to investigate H^- migration along this pathway. The migration barrier is $\Delta E_{8i \rightarrow 2c} = 0.607 \text{ eV}$, as shown in **Figure 4.6a**. The full H^- migration path from CI-NEB was shown in **Figure S4.2**.

- Exchange n°2 : hydrides ions on the same edge exchange their position, with the help of the (2c) site: two hydrides on the same edge would exchange their positions, as shown in **Figure 4.6b**. H1 will move to the (2c) site, while H4 will migrate the H1 site at the same time. Next step, H1 will jump to the original H4 site, which realizes the

Chapter IV Hydride diffusion mechanism in LaHO family

exchange process. The $2c$ site is like a transit station that provides temporary accommodation for one hydride ion. The CI-NEB results also confirm this. As shown in **Figure S4.3**, the nine images correspond to the nine energy points of mechanism 2 in **Figure 4.6b**. The migration barrier is $\Delta E_{exchange2} = 1.039 \text{ eV}$ and image 3 is the transition state that the system free energy is the highest. It should be noted that this mechanism is not adapted to the two hydrides on the diagonal. The snapshot of this process (about 200 fs) is presented by VMD[54] (**Figure S4.4**).

- Exchange n°3: three hydride ions swap their places, with the help of the ($2c$) site. Any three of the four H hydrides can swap positions. H1 initially moves to the $2c$ transition state; meanwhile, H4 jumps to the original H1 site and H3 heads for the original H4 site. Eventually, H1 at ($2c$) site will return to the vacancy left by H3, as shown in mechanism 3 in **Figure 4.6c**. The energy barrier of this process is 1.242 eV. The optimized CI-NEB diffusion path and the VMD evidence are shown in **Figure S4.5** and **Figure S4.6**, respectively.

- Exchange n°4: four hydrides (H1 to H4) rotate, without the help of the ($2c$) site. The four hydride ions constituting the block turn clockwise or counterclockwise with the energy barrier of 1.540 eV. (**Figure 4.6d**) In this case, no hydride ion is seen to occupy the $2c$ position.

From this analysis, it is difficult to anticipate which exchange mechanisms will be favored since these different exchanges involve a different number of atoms (1, 2, 3, 4 atom(s) involved for exchange n°1, 2, 3, 4 respectively).

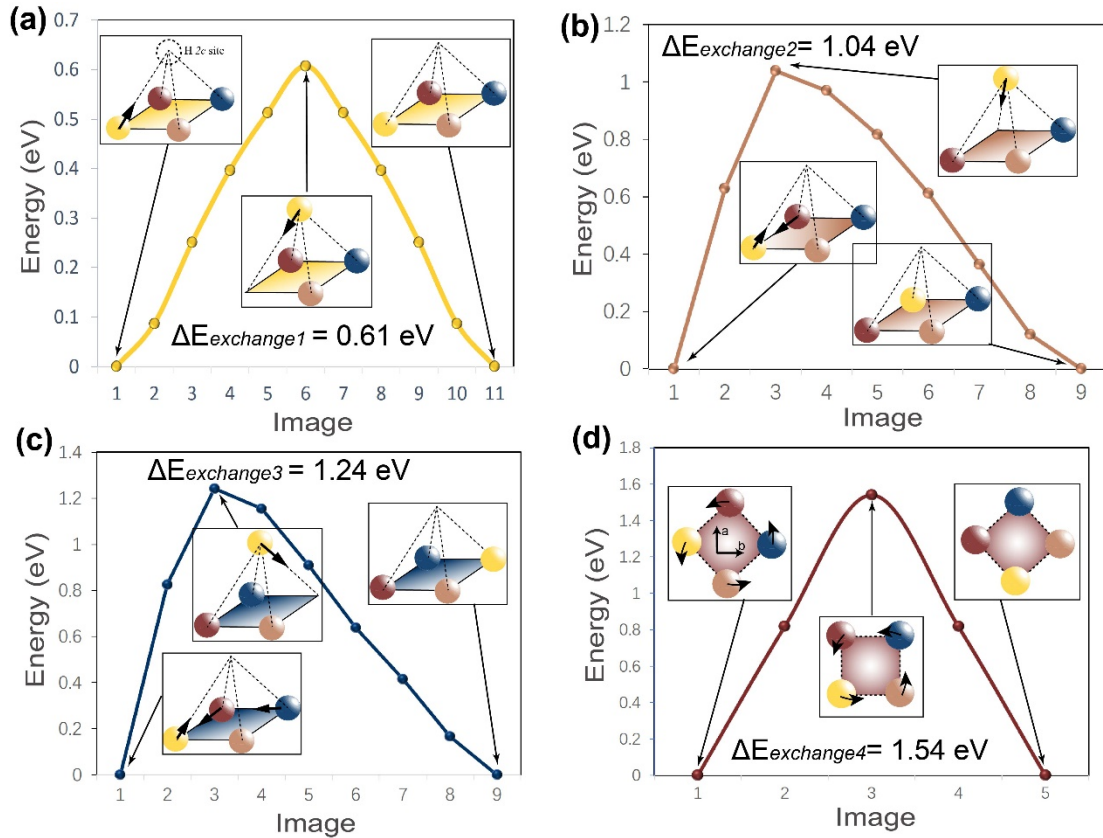


Figure 4.6 DFT calculations and scheme of the hydride ion transfer within the unit-block containing four hydrogens in the α -LaHO phase (a) exchange mechanism n°1 (b) exchange mechanism n°2 (c) exchange mechanism n°3 (d) exchange mechanism n°4.

After identifying how diffusion can potentially occur inside the unit block made of 4 hydride-ions, we describe here how hydride ions can jump from one block to another. This step is mandatory (as well as the other one) to ensure long-range diffusion. We thus calculated by DFT the energy cost for transferring one hydride-ion to the two possible (*4d*) and (*2b*) sites. We found that transferring one hydride ion from a (*8i*) to the closest (*4d*) site represents an energy cost of 1.02 eV, while jumping from (*8i*) site to (*2b*) site represents an energy cost 1.67 eV *i.e.*, the highest one. This confirms the pre-eminent role of the interstitial (*4d*) site in the inter-block diffusion of hydride anions, which is indeed what is observed through MD simulation as mentioned previously, while the (*2b*) site never appears to be occupied. (**Figure 4.4b**)

This analysis of exchange/diffusion mechanisms through DFT calculations can be

complemented by the MD trajectory analysis to quantify more precisely the most frequent exchange/jumps events. The positions of each H hydride-ion can be followed along with the MD simulation and associated to the different possible sites, through the convex hull approach. From this, the jump statistics of all hydride-ions can be analyzed in a straightforward way. The occurrence of the different exchange mechanisms within the unit block can also be followed. **Figure 4.7a** shows the jump statistics of H ions (1000 atoms for 1000 steps) after a MD simulation at 1100K. The highest number of “jumps” appears at the diagonal of $(8i)$ sites, corresponding in fact to the atoms remaining on their crystallographic site *i.e.* to vibrating atoms. Then, we see that the second largest number of jumps are related to intra-block exchanges of positions or jumps to the interstitial site $(2c)$. These represent ~90% of the total of jumps, the rest ~10% corresponding to jumps to the interstitial $(4d)$ site or to another block. These numbers evolve with temperature as shown in **Figure 4.7b**. Interesting in the jump analysis is also the fact that the rotation (also named exchange $n^{\circ}4$) of the four hydride-ions within a block is a relatively frequent process. We indeed counted 123 rotation cases at 1100 K (**Figure 4.7b**), representing more than 20% of the identified atom diffusion processes. Among the rotation cases, we counted 65 anti-clockwise and 58 clockwise rotations, respecting thus approximately the equal probability of occurrence. The rotation process lasts around 150 fs, and the detailed molecular dynamics rotation is shown in **Figure S4.8**. As a whole, the diffusion path of the hydride-ion is thus highly anisotropic and occurring mainly in the *a-b* plane.

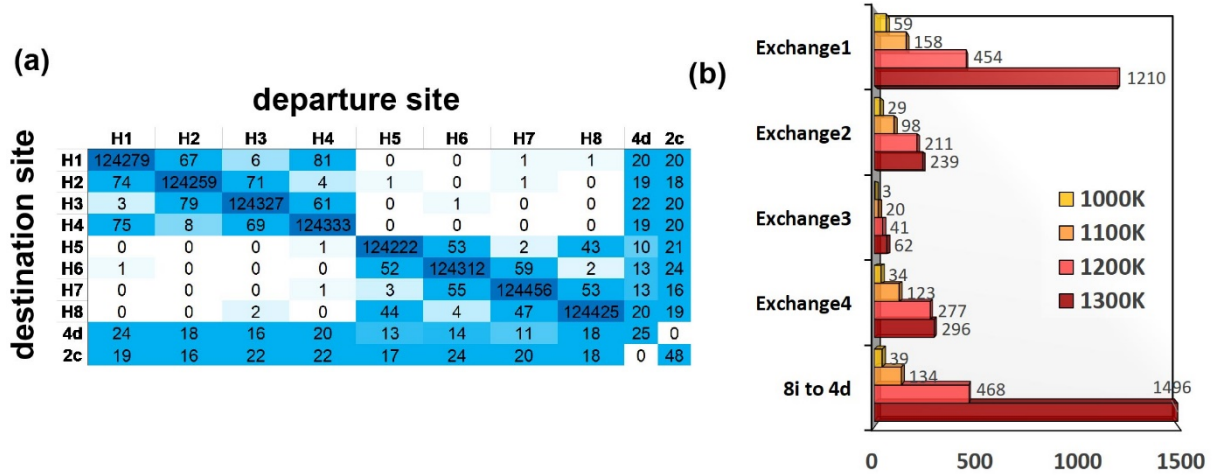


Figure 4.7 Analysis of hydride-ion movements in α -LaHO (a) Number of jumps between two different sites in α -LaHO at 1100K based on 1000 H^- with 1000 timesteps. (b) The occurrence of the five exchange/diffusion mechanisms as a function of temperature.

IV.3.3 Hydride diffusion mechanism in non-defective β -LaHO

β -LaHO is the second form of LaHO at ambient pressure.[55] The structure of this material is shown in **Figure 4.8a**. The unit cell contains 4 La, H, O ions. The free energy of β -LaHO as deduced from DFT calculations to be 0.056 eV per formula unit smaller than that of α -LaHO, which indicates that β -LaHO should be the experimental phase observed under normal pressure. In the $1 \times 1 \times 2$ supercell of **Figure S4.12**, H1 and H4 can be considered to form a group because they are geographically closer (the distance d_{H1-H4} is 2.639 Å), while H2 and H3 constitute the other group. Short distance opens up possibilities for their direct exchange, as shown below. As done previously for the α -LaHO phase, we performed Bond Valence calculations to identify potential interstitial sites. The isosurfaces of bond valence sum $|\Delta V(H^-)|=0.20$ is shown for β -LaHO in **Figure 4.8a**. Each hydride site is surrounded by a "ham" shape isosurface, which allows identifying an associated interstitial ion position. The exact interstitial position is obtained by reducing the value $|\Delta V(H^-)|$ during BV calculations. When $|\Delta V(H^-)|=0.10$, the Wyckoff position of the interstitial site is identified to be a (4c)

position with coordinates (0.897 0.25 0.711). This interstitial position was also refined from DFT calculations, and we obtained the (4*c*) Wyckoff position with coordinates (0.903 0.25 0.7068), which is consistent with the results obtained by BVS calculation.

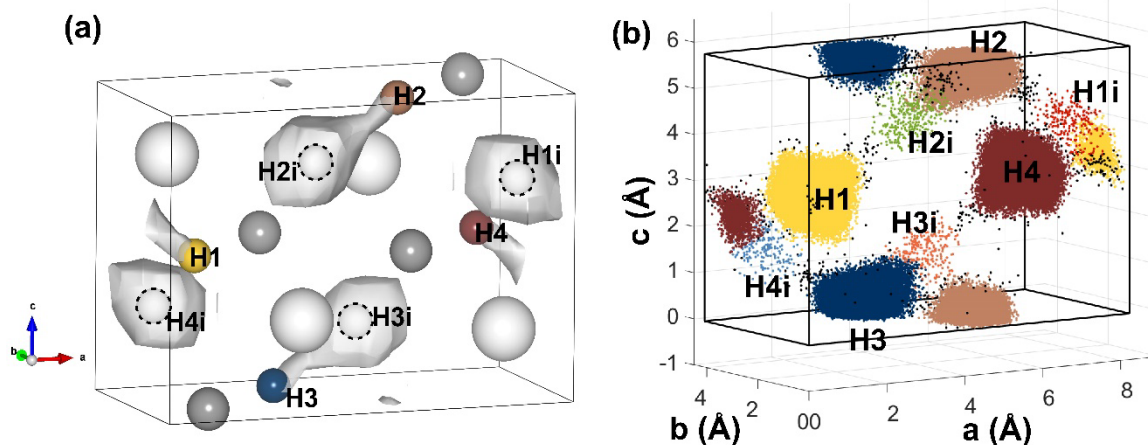


Figure 4.8 Representation of the β -LaHO form. (a) Isosurfaces for the value of the hydride BV mismatch ($|\Delta V(H^-)| = 0.20$), where the H1 to H4 positions are drawn in yellow, brown, blue and dark red, respectively. Interstitial (4*i*) sites are drawn by dotted line ball. (b) The complete information unit cell of β -LaHO at 1200K after convex hull assignment

After MD calculations, the coordinates of hydride ions were classified by convex hull classification, as shown in **Figure 4.8b**. This figure reveals that H indeed occupies its original crystallographic sites as given in the original β -LaHO description but also the interstitial sites as deduced from BVS. This phenomenon is observed whatever the temperature. These interstitial positions might thus play an important role in the hydride-ion diffusion mechanism in non-defective β -LaHO. As described here, One hydride-ion can indeed jump to one of its three nearest interstitial positions. Herein, H2 is selected as an example and the three nearest interstitial positions to H2 are H2i ($d_1 = 2.027 \text{ \AA}$), H3i ($d_2 = 2.391 \text{ \AA}$), and H1i ($d_3 = 2.843 \text{ \AA}$). **(Figure S4.12) Figure 4.9a** illustrates the statistics of jumps between the different sites. It can be seen that the jumping times from H2 to any of the interstitial site is inversely proportional to the

Chapter IV Hydride diffusion mechanism in LaHO family

distance. Hardly any jumps occurred between H2 and H4i because the distance is too long (about 4.890 Å). We have calculated the energy barriers required for all these three different jumps, and the results are shown in **Figure 4.9b**. Each hydride ion will more naturally jump to its closest interstitial position (e.g. H2 jump to H2i), which requires a migration energy of approximately 0.98 eV. For the other two distances, the energy barriers are close to each other $\Delta E_{H2 \rightarrow H3i} \approx \Delta E_{H2 \rightarrow H1i} \sim 1.3$ eV. By itself, such transfer of a hydride-ion to an interstitial is only effective in terms of diffusion if there is a concomitant movement of another hydride ion. This correlated two-ion exchange mechanism corresponds to the situation when, for instance, H2 and H3 (respectively H1 and H4) swap their position directly. The optimized movements of atoms for this exchange process are shown in **Figure S4.13**, where we can see that H2 first jumps to H2i (with travel distance d_1). At the same time, H3 directly migrates to the vacancy left by H2 (travel distance d_{H2-H3}), and then the hydride at H2i jumps to H3 (travel distance d_2). A similar exchange path is presented in **Figure S4.14**, where H2 will first jump to H3i site (travel distance d_2). Next step, H3 will head for the vacancy left by H2 (travel distance d_{H2-H3}). Meanwhile, H at H3i site will go to the vacancy left by H3 (travel distance d_1). Both paths are feasible from DFT calculations with an equivalent energy barrier in both cases of 1.45 eV. Differing from α -LaHO limited diffusion along c direction, H^- in β -LaHO can diffuse almost isotropically as shown in the MSD curves (**Figure 4.2c**) and **Figure 4.9c**. The interstitial site provides temporary accommodation for H^- which makes possible the long-range diffusion.

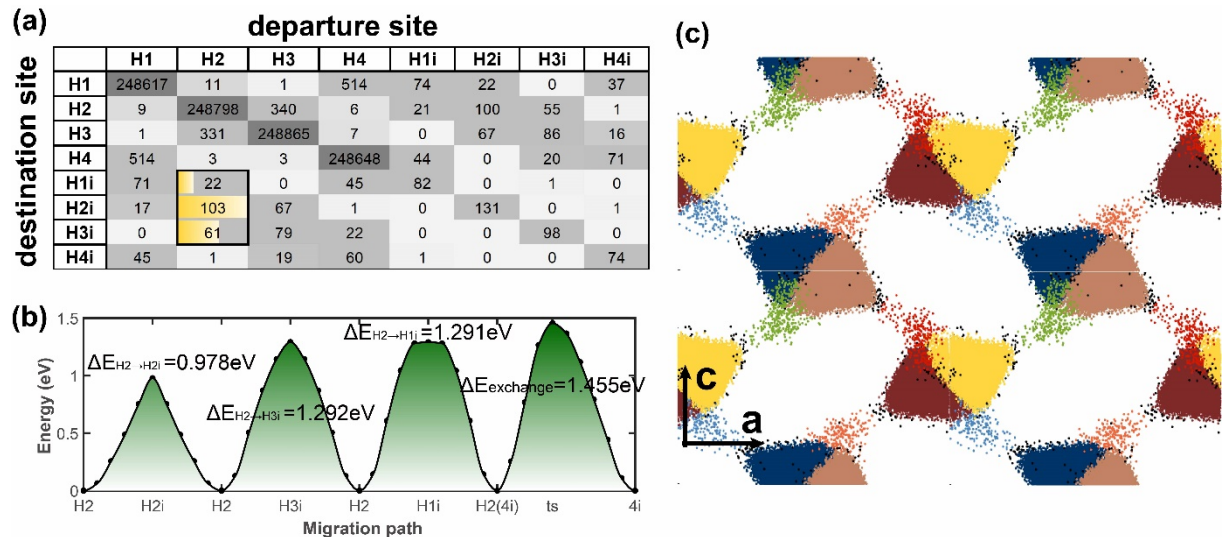


Figure 4.9 (a) Analysis of jumps from MD simulations in β -LaHO at 1200K. The analyzed system is the same size as **Figure 4.7a** (1000 H⁻ with 1000 timesteps). (b) Energy profile of H⁻ migration along different pathways from CI-NEB calculations. (c) Projection along the b axis of the hydride ion positions in β -LaHO at 1200 K.

IV.3.4 Influence of defects on hydride diffusion mechanisms in α and β -LaHO

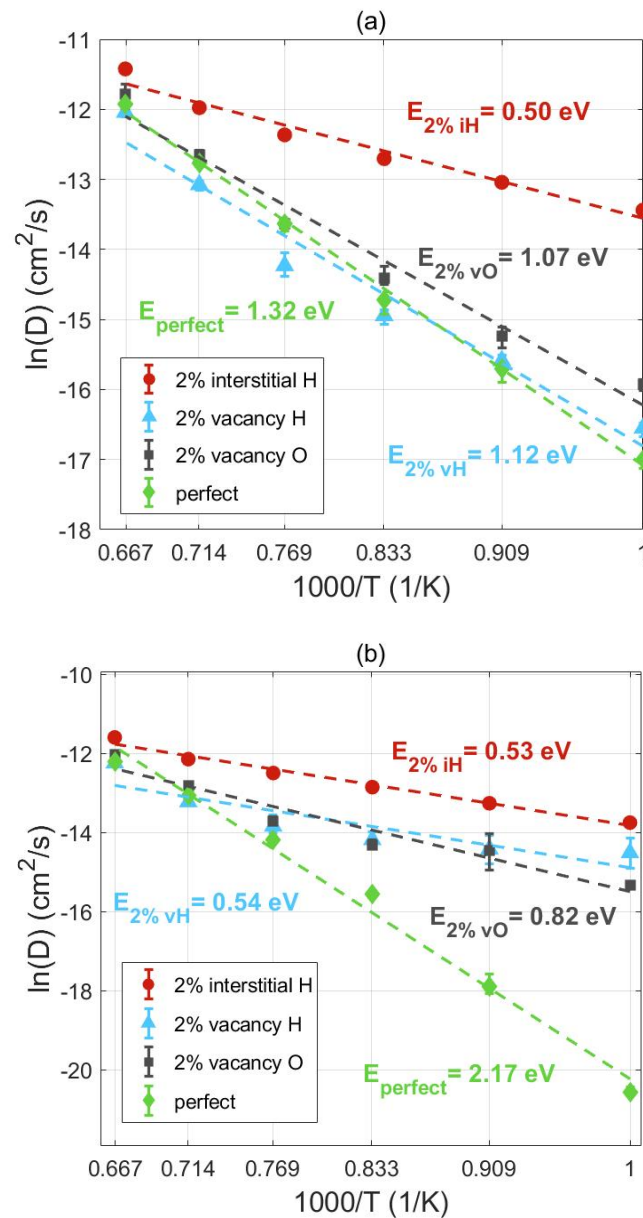


Figure 4.10 Calculated logarithm of H⁻ diffusion coefficients as a function of

Chapter IV Hydride diffusion mechanism in LaHO family

temperature as deduced from MD simulations in non-defective and defect containing configurations for (a) the α -LaHO form (b) the β -LaHO form.

In **Figure 4.10**, we present the macroscopic diffusion coefficients as a function of the inverse of temperature for both the pure α -LaHO and β -LaHO and for the same structures after deliberately introducing defects. Since diffusion can be driven by the presence of vacancies and/or interstitial ions, we tested the influence of such defects on the diffusion properties. We thus introduced the following defects:

- 2% additional interstitial hydride ions
- 2% hydride ion vacancies
- 2% oxygen ion vacancies

These defects we introduced randomly in the $5 \times 5 \times 5$ and the supercells in the α -LaHO and β -LaHO phases, respectively, and further MD simulations were performed. In this case, additional charges were compensated by Fuchs correction, as performed within the DLPOLY Classic package.[49]

As mentioned previously, for the pure phases (green diamonds in **Figure 4.10**), the hydride ion diffusivity on the α -LaHO phase (**Figure 4.10a**) is characterized by an activation energy of 1.3 eV while that of β -LaHO phase is 2.2 eV. As evidenced in **Figure 4.10a**, introducing vacancy defects does not greatly affect the behaviour of diffusing hydride ions, in α -LaHO, although oxygen vacancies decrease the activation energy slightly and increase the total diffusion coefficient. Hence, from the small difference of slope between vacancy-doped (oxygen or hydride) and non-defective cells, we conclude that the diffusion mechanism changes very little with the presence of such defects in α -LaHO. The analysis of pure α -LaHO shows that hydride diffusion mechanism of α -LaHO is a combination of collective motion within a unit-block and the interstitial jump to $4b$ site. The α -LaHO pristine structure thus already has all the ingredients to present a high hydride-ion conductivity, and thus the creation of vacancies appears to have a small effect on hydride ion diffusivity. Interestingly, the

Chapter IV Hydride diffusion mechanism in LaHO family

introduction of additional hydride ions leads to a large enhancement of diffusion properties by diminishing the hydride migration energy from 1.34 eV in the case of non-defective α -LaHO to 0.5 eV in the case of 2% extra H⁻ interstitials. However, the feasibility of such doping remains to be proven.

For β -LaHO, as shown in **Figure 4.10b**, all considered defects decrease the hydride diffusion activation energy significantly. Differing from α -LaHO, increasing the number of hydride ion vacancies in β -LaHO appears as an efficient strategy to increase diffusion. In this case, the main diffusion mechanism switches from interstitial to vacancy-driven with direct jumps between H2 and H3 sites (or H1 and H4 sites) without the need for correlated motions of atoms. While the hydride diffusion activation energy of pure β -LaHO is 2.171 eV, it diminishes to 0.5-0.8 eV once defects are introduced.

As discussed above, the possible solution to improve the conductivity of α -LaHO is to add interstitial H⁻. The hydride diffusion along *a-b* plane of 2% H⁻ interstitial α -LaHO at 1100K is shown in **Figure 4.11a**. Compared with non-defective α -LaHO (**Figure 4.4b**), the hydride ion clusters of *2c* (green) and *4d* (pink) are denser and the interstitial ions can be detected easily (**Figure 4.11b**). At 0 ps, the *2c* site of one-unit block was filled with a H⁻ (green ball). After 0.5 ps, this *2c* H⁻ kicked another H⁻ at *8i* site to *4d* site and occupied the *8i* site. This is a typical interstitialcy behaviour using *2c-8i-4d* sites. At 1 ps, the kicked out *4d* hydride will push one hydride at *8i* site of another unit block to *4d* site. This is the second type of interstitialcy behaviour involving *4d-8i-4d* sites. These two basic types of behaviours were identified to be the main diffusion mechanisms, strengthening the diffusion coefficient as shown in **Figure 4.10a**.

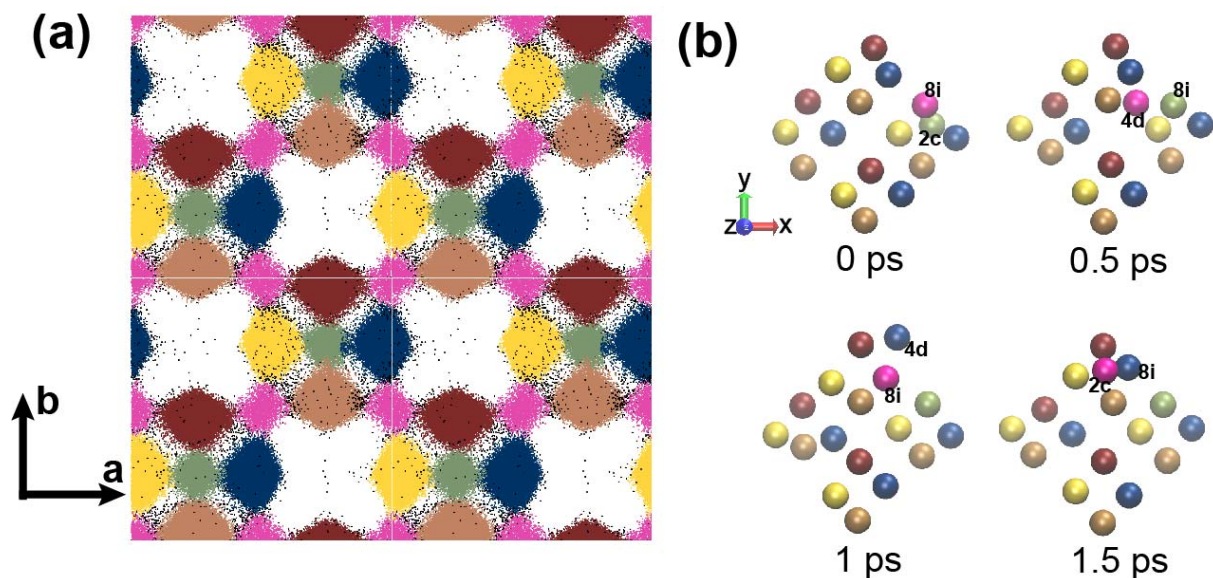


Figure 4.11 (a) The hydride diffusion in 2% H⁻ interstitial α -LaHO at 1100K. The legend of **Figure 4.4b** is also adopted here. (b) Snapshot of the interstitial mechanism of 2% H⁻ interstitial α -LaHO by VMD[54].

For β -LaHO, adding both interstitial H⁻ or/and H⁻ vacancy can be good choices to enhance H⁻ diffusion. In the case of 2% H⁻ interstitials, as shown in **Figure S4.15**, the H⁻ cluster size increases highly, and interstitial atoms can also be detected easily. While adding H⁻ vacancies, the number of direct jumps within one group (H2/H3 or H1/H4) can be 10-30 times higher than in non-defective β -LaHO as shown in **table S4.9**. The diffusion mechanism of 2% H⁻ vacancy will turn into a vacancy-driven one. As presented in **Figure S4.16**, the MSD of H⁻ *b* direction is much higher than that with *a* and *c* directions. The diffusion path of H⁻ is shown in **Figure S4.16b**. With close physical distances, hydrides pairs form a fast channel for diffusion.

IV.4 Conclusion

In the present study, we have shown that the lanthanide oxyhydrides LaHO can be accurately modelled using simple interatomic analytic models fitted on DFT calculations. The potential consisting of a long-range Coulomb term and a short-range Buckingham term is obtained by fitting DFT calculation including the lattice

Chapter IV Hydride diffusion mechanism in LaHO family

parameters and elastic tensors of α -LaHO, β -LaHO, La_2O_3 , and LaH_3 . The as-developed potential reproduces not only the data used in the fit but also the structural and elastic properties of the high-pressure form of Lanthanum oxyhydrides, namely γ -LaHO and δ -LaHO and the experimental evolution of cell parameters. This new potential, combined with DFT calculations, has been employed to study the hydride diffusion mechanisms in α -LaHO and β -LaHO.

In α -LaHO, after applying BVS, MD and DFT calculations, the (2c) and (4d) interstitial sites were shown to play in a decisive role in the diffusion process. This diffusion process includes mainly 2 steps: the first one involving most often the (2c) site and corresponding to hydride-ion exchanges with a unit block, the second one involving the (4d) site and corresponding to jumps between those blocks. The introduction of vacancies is shown to improve only slightly the hydride-ion diffusion by favouring the exchanges between sites. The (4d) position is shown to act as a bridge that connects hydride-ion blocks, resulting in a diffusion that occurs mainly along *a* and *b* direction. In β -LaHO, the hydride diffusion also occurs through interstitial sites, but the overall diffusion coefficient is much more limited. In this phase, the introduction of oxygen or hydride ion vacancies is shown to greatly increase the diffusion coefficient. These results have thus provided highly relevant information to enhance the diffusion coefficients in α -LaHO and β -LaHO phases. It may also constitutes good starting point for studying other lanthanide oxyhydrides compounds.

IV.5 Notes and references

- [1] Y. Zhu, X. He, and Y. Mo, "First principles study on electrochemical and chemical stability of solid electrolyte-electrode interfaces in all-solid-state Li-ion batteries," *J. Mater. Chem. A*, vol. 4, no. 9, pp. 3253–3266, 2016.
- [2] A. Van Der Ven, Z. Deng, S. Banerjee, and S. P. Ong, "Rechargeable Alkali-Ion Battery Materials : Theory and Computation," *Chem. Rev.*, 2020.
- [3] Y. Zhang *et al.*, "Unsupervised discovery of solid-state lithium ion conductors,"

Chapter IV Hydride diffusion mechanism in LaHO family

- Nat. Commun.*, vol. 10, no. 1, pp. 1–7, 2019.
- [4] X. He, Y. Zhu, and Y. Mo, “Origin of fast ion diffusion in super-ionic conductors,” *Nat. Commun.*, vol. 8, no. May, pp. 1–7, 2017.
- [5] M. Burbano, D. Carlier, F. Boucher, B. J. Morgan, and M. Salanne, “Sparse Cyclic Excitations Explain the Low Ionic Conductivity of Stoichiometric $\text{Li}_7\text{La}_3\text{Zr}_2\text{O}_{12}$,” *Phys. Rev. Lett.*, vol. 116, no. 13, pp. 1–6, 2016.
- [6] S. Fang, D. Bresser, and S. Passerini, “Transition Metal Oxide Anodes for Electrochemical Energy Storage in Lithium- and Sodium-Ion Batteries,” *Adv. Energy Mater.*, vol. 10, no. 1, 2020.
- [7] A. Chroneos, B. Yildiz, A. Tarancón, D. Parfitt, and J. A. Kilner, “Oxygen diffusion in solid oxide fuel cell cathode and electrolyte materials: Mechanistic insights from atomistic simulations,” *Energy Environ. Sci.*, vol. 4, no. 8, pp. 2774–2789, 2011.
- [8] A. Tarancón, S. J. Skinner, R. J. Chater, F. Hernández-Ramírez, and J. A. Kilner, “Layered perovskites as promising cathodes for intermediate temperature solid oxide fuel cells,” *J. Mater. Chem.*, vol. 17, no. 30, pp. 3175–3181, 2007.
- [9] C. Tealdi, C. Ferrara, P. Mustarelli, and M. S. Islam, “Vacancy and interstitial oxide ion migration in heavily doped $\text{La}_{2-x}\text{Sr}_x\text{CoO}_{4\pm\delta}$,” *J. Mater. Chem.*, vol. 22, no. 18, pp. 8969–8975, 2012.
- [10] C. Chen, D. Chen, Y. Gao, Z. Shao, and F. Ciucci, “Computational and experimental analysis of $\text{Ba}_{0.95}\text{La}_{0.05}\text{FeO}_{3-\delta}$ as a cathode material for solid oxide fuel cells,” *J. Mater. Chem. A*, vol. 2, no. 34, pp. 14154–14163, 2014.
- [11] C. Li, H. Dammak, and G. Dezanneau, “Identification of oxygen diffusion mechanisms in $\text{Nd}_{1-x}\text{AE}_x\text{BaInO}_{4-x/2}$ (AE = Ca, Sr, Ba) compounds through molecular dynamics,” *Phys. Chem. Chem. Phys.*, vol. 21, no. 38, pp. 21506–21516, 2019.
- [12] Y. Hu *et al.*, “Oxygen diffusion mechanism in the mixed ion-electron conductor $\text{NdBaCo}_2\text{O}_{5+x}$,” *J. Mater. Chem.*, vol. 22, no. 36, pp. 18744–18747, 2012.
- [13] Y. Z. Wang, E. Bevilion, A. Chesnaud, G. Geneste, and G. Dezanneau,

Chapter IV Hydride diffusion mechanism in LaHO family

- “Atomistic simulation of pure and doped BaSnO₃,” *J. Phys. Chem. C*, vol. 113, no. 47, pp. 20486–20492, 2009.
- [14] chi chen, Z. M. Baiyee, and F. Ciucci, “Multi-phase semicrystalline microstructures drive exciton dissociation in neat plastic semiconductors,” *Phys. Chem. Chem. Phys.*, vol. 3, pp. 10715–10722, 2015.
- [15] C. Tealdi, P. Mustarelli, and M. S. Islam, “Layered LaSrGa₃O₇-based oxide-ion conductors: Cooperative transport mechanisms and flexible structures,” *Adv. Funct. Mater.*, vol. 20, no. 22, pp. 3874–3880, 2010.
- [16] A. Ottochian, G. Dezanneau, C. Gilles, P. Raiteri, C. Knight, and J. D. Gale, “Influence of isotropic and biaxial strain on proton conduction in Y-doped BaZrO₃: A reactive molecular dynamics study,” *J. Mater. Chem. A*, vol. 2, no. 9, pp. 3127–3133, 2014.
- [17] J. Hermet, M. Torrent, F. Bottin, G. Dezanneau, and G. Geneste, “Oxide ion and proton transport in Gd-doped barium cerate: A combined first-principles and kinetic Monte Carlo study,” *J. Mater. Chem. A*, vol. 2, no. 24, pp. 9055–9066, 2014.
- [18] K. Fukui *et al.*, “Characteristic fast H⁻ ion conduction in oxygen-substituted lanthanum hydride,” *Nat. Commun.*, vol. 10, no. 1, pp. 1–8, 2019.
- [19] J. Hermet, F. Bottin, G. Dezanneau, and G. Geneste, “Thermodynamics of hydration and oxidation in the proton conductor Gd-doped barium cerate from density functional theory calculations,” *Phys. Rev. B - Condens. Matter Mater. Phys.*, vol. 85, 2012.
- [20] G. Geneste, A. Ottochian, J. Hermet, and G. Dezanneau, “Proton transport in barium stannate: classical, semi-classical and quantum regimes,” *Phys. Chem. Chem. Phys.*, vol. 17, pp. 19104–19118, 2015.
- [21] É. Bévilion and G. Geneste, “Hydration properties of BaSn_{0.875}M_{0.125}O_{3-δ} substituted by large dopants (M=In, Y, Gd, and Sm) from first principles,” *Phys. Rev. B - Condens. Matter Mater. Phys.*, vol. 77, pp. 1–11, 2008.
- [22] E. Fabbri, D. Pergolesi, and E. Traversa, “Materials challenges toward proton-

Chapter IV Hydride diffusion mechanism in LaHO family

- conducting oxide fuel cells: A critical review,” *Chemical Society Reviews*. pp. 4355–4369, 2010.
- [23] K. D. Kreuer, “Proton-Conducting Oxides,” *Annu. Rev. Mater. Res.*, vol. 33, no. 1, pp. 333–359, 2003.
- [24] H. Ubukata *et al.*, “Hydride Conductivity in an Anion-Ordered Fluorite Structure LnHO with an Enlarged Bottleneck,” *Chem. Mater.*, vol. 31, no. 18, pp. 7360–7366, 2019.
- [25] M. C. Verbraeken, C. Cheung, E. Suard, and J. T. S. Irvine, “High H⁻ ionic conductivity in barium hydride,” *Nat. Mater.*, vol. 14, no. 1, pp. 95–100, 2015.
- [26] Y. Kobayashi *et al.*, “An oxyhydride of BaTiO₃ exhibiting hydride exchange and electronic conductivity,” *Nat. Mater.*, vol. 11, no. 6, pp. 507–511, 2012.
- [27] S. Yamaguchi, “Large, soft, and polarizable hydride ions sneak around in an oxyhydride,” *Science (80-.)*, vol. 351, no. 6279, pp. 1262–1263, 2016.
- [28] H. Yamashita *et al.*, “Chemical Pressure-Induced Anion Order-Disorder Transition in LnHO Enabled by Hydride Size Flexibility,” *J. Am. Chem. Soc.*, vol. 140, no. 36, pp. 11170–11173, 2018.
- [29] M. C. Verbraeken, E. Suard, and J. T. S. Irvine, “Structural and electrical properties of calcium and strontium hydrides,” *J. Mater. Chem.*, vol. 19, no. 18, pp. 2766–2770, 2009.
- [30] Q. Bai, X. He, Y. Zhu, and Y. Mo, “First-Principles Study of Oxyhydride H⁻ Ion Conductors: Toward Facile Anion Conduction in Oxide-Based Materials,” *ACS Appl. Energy Mater.*, vol. 1, no. 4, pp. 1626–1634, 2018.
- [31] T. Broux *et al.*, “High-Pressure Polymorphs of LaHO with Anion Coordination Reversal,” *J. Am. Chem. Soc.*, vol. 141, no. 22, pp. 8717–8720, 2019.
- [32] O. J. Hernandez *et al.*, “Site Selectivity of Hydride in Early-Transition-Metal Ruddlesden-Popper Oxyhydrides,” *Inorg. Chem.*, 2018.
- [33] G. Kobayashi *et al.*, “Pure H⁻ conduction in oxyhydrides,” *Science (80-.)*, vol. 351, no. 6279, pp. 1314–1317, 2016.
- [34] T. Yamamoto *et al.*, “Selective Hydride Occupation in BaVO_{3-x}H_x (0.3 ≤ x ≤ 0.8)

Chapter IV Hydride diffusion mechanism in LaHO family

- with Faceand Corner-Shared Octahedra,” *Chem. Mater.*, 2018.
- [35] M. Matsuo and S. I. Orimo, “Lithium fast-ionic conduction in complex hydrides: Review and prospects,” *Adv. Energy Mater.*, vol. 1, no. 2, pp. 161–172, 2011.
- [36] Z. Ren, J. Yu, Y. Li, and C. Zhi, “Tunable Free-Standing Ultrathin Porous Nickel Film for High Performance Flexible Nickel–Metal Hydride Batteries,” *Adv. Energy Mater.*, vol. 8, no. 12, pp. 1–12, 2018.
- [37] C. Tassel *et al.*, “High-Pressure Synthesis of Manganese Oxyhydride with Partial Anion Order,” *Angew. Chemie - Int. Ed.*, vol. 55, no. 33, pp. 9667–9670, 2016.
- [38] F. Denis Romero, A. Leach, J. S. Möller, F. Foronda, S. J. Blundell, and M. A. Hayward, “Strontium vanadium oxide-hydrides: ‘square-planar’ two-electron phases,” *Angew. Chemie - Int. Ed.*, vol. 53, no. 29, pp. 7556–7559, 2014.
- [39] Y. Tang *et al.*, “Metal-Dependent Support Effects of Oxyhydride-Supported Ru, Fe, Co Catalysts for Ammonia Synthesis,” *Adv. Energy Mater.*, vol. 8, no. 36, pp. 1–9, 2018.
- [40] B. Malaman and J. F. Brice, “Etude structurale de l’hydruro-oxyde LaHO par diffraction des rayons X et par diffraction des neutrons,” *J. Solid State Chem.*, vol. 53, no. 1, pp. 44–54, 1984.
- [41] P. E. Blöchl, “Projector augmented-wave method,” *Phys. Rev. B*, vol. 50, p. 17953, 1994.
- [42] G. Kresse and J. Hafner, “Ab initio molecular dynamics for liquid metals,” *Phys. Rev. B*, vol. 47, p. 558, 1993.
- [43] J. P. Perdew, K. Burke, and M. Ernzerhof, “Generalized gradient approximation made simple,” *Phys. Rev. Lett.*, vol. 77, p. 3865, 1996.
- [44] G. Henkelman, B. P. Uberuaga, and H. Jónsson, “Climbing image nudged elastic band method for finding saddle points and minimum energy paths,” *J. Chem. Phys.*, vol. 113, pp. 9901–9904, 2000.
- [45] J. D. Gale and A. L. Rohl, “The General Utility Lattice Program (GULP),” *Mol. Simul.*, vol. 29, pp. 291–341, 2003.
- [46] A. Jain *et al.*, “Commentary: The materials project: A materials genome

Chapter IV Hydride diffusion mechanism in LaHO family

- approach to accelerating materials innovation,” *APL Mater.*, vol. 1, no. 1, 2013.
- [47] G. V. Lewis and C. R. A Catlow, “Potential models for ionic oxides,” *J. Phys. C Solid State Phys.*, 1985.
- [48] P. Hirel, “Atomsk: A tool for manipulating and converting atomic data files,” *Comput. Phys. Commun.*, vol. 197, pp. 212–219, 2015.
- [49] I. T. Todorov, W. Smith, K. Trachenko, and M. T. Dove, “DL_POLY_3: New dimensions in molecular dynamics simulations via massive parallelism,” *J. Mater. Chem.*, vol. 16, pp. 1911–1918, 2006.
- [50] A. France-Lanord and J. C. Grossman, “Correlations from Ion Pairing and the Nernst-Einstein Equation,” *Phys. Rev. Lett.*, vol. 122, no. 13, p. 136001, 2019.
- [51] S. Adams, “Modelling ion conduction pathways by bond valence pseudopotential maps,” *Solid State Ionics*, vol. 137, pp. 1351–1361, 2000.
- [52] S. Adams, “Bond valence analysis of structure – property relationships in solid electrolytes,” *J. Power Sources*, vol. 159, pp. 200–204, 2006.
- [53] S. NISHIMURA, “<https://shinichinishimura.github.io/pyabst/#>.” .
- [54] W. Humphrey, A. Dalke, and K. Schulten, “VMD: Visual molecular dynamics,” *J. Mol. Graph.*, vol. 14, pp. 33–38, 1996.
- [55] N. Zapp, H. Auer, and H. Kohlmann, “YHO, an Air-Stable Ionic Hydride,” *Inorg. Chem.*, vol. 58, no. 21, pp. 14635–14641, 2019.

IV.6 Supporting information

α -LaHO tetragonal	Experimental (300 K)	DFT PBE	Fitted potential 1	DFT PBEsol	Fitted Potential 2
Cell parameters					
a (Å)	8.08051(3) ¹ 8.074(1) ²	8.084	8.0697 (-0.18%)	8.0041	7.9877 (-0.20%)
c (Å)	5.72639(6) ¹ 5.739(1) ²	5.7177	5.6848 (-0.58%)	5.6578	5.6261 (-0.56%)
Atomic positions :					
La1 (<i>2a</i>)	(0.7500	0.2500	0.0000)		
La2 (<i>2c</i>)	(0.2500	0.2500	z_{La2})		
La3 (<i>4e</i>)	(0.0000	0.0000	0.5000)		
O (<i>8i</i>)	(0.2500	y_O	z_O)		
H (<i>8i</i>)	(0.2500	y_H	z_H)		
z_{La2}	0.9479(3) ¹ 0.959(2) ²	0.9422	0.9460 (+0.40%)	0.9428	0.9450 (+0.23%)
y_O	0.5086(3) ¹ 0.501(1) ²	0.4859	0.4829(-0.62%)	0.4861	0.4830 (-0.64%)
z_O	0.7463(3) ¹ 0.747(3) ²	0.7411	0.7378(-0.45%)	0.7412	0.7374 (-0.51%)
y_H	0.5263(5) ¹ 0.505(2) ²	0.5193	0.5258 (+1.25%)	0.5190	0.5259 (+1.33%)
z_H	0.2556(7) ¹ 0.268(8) ²	0.2429	0.2357(-2.96%)	0.2431	0.2352 (-3.25%)
Elastic coefficients					
C₁₁ (GPa)	-	170.7	164.8 (-3.45%)	181.4	175.2 (-3.42%)
C₁₂ (GPa)	-	64.0	68.8 (+7.50%)	66.9	75.3 (+12.56%)
C₁₃ (GPa)	-	66.2	61.9 (+6.50%)	74.1	67.5 (-8.90%)
C₃₃ (GPa)	-	152.6	161.1 (+5.57%)	159.2	171.1 (+7.47%)
C₄₄ (GPa)	-	52.9	52.4 (-0.95%)	56.1	55.2 (-1.60%)
C₆₆ (GPa)	-	52.4	55.9 (+6.68%)	50.9	58.4 (+14.73%)

Table S4.1 Comparison of experimental and calculated properties in α -LaHO, with tetragonal structure and space group: *P4/nmm* (129). Calculations are based on DFT (PBE, PBEsol) and on the associated derived interatomic potential.

Chapter IV Hydride diffusion mechanism in LaHO family

β -LaHO Orthorhombic	DFT PBE	Fitted potential 1	DFT PBEsol	Fitted Potential 2
Cell parameters				
a (Å)	8.0662	8.088463(+0.28%)	7.9785	8.00784 (+0.37%)
b (Å)	4.0455	4.019223(-0.65%)	4.0082	3.97724 (-0.77%)
c (Å)	5.7275	5.692954(-0.60%)	5.6700	5.63424 (-0.63%)
Atomic positions :				
La ($4c$)	(x_{La}	0.25000	z_{La})
O ($4c$)	(x_O	0.25000	z_O)
H ($4c$)	(x_H	0.25000	z_H)
x_{La}	0.37217	0.37557 (+0.91%)	0.37234	0.37579 (+0.93%)
z_{La}	0.28103	0.27785 (-1.13%)	0.28093	0.27833 (-0.93%)
x_O	0.14127	0.14382 (+1.81%)	0.14098	0.14376 (+1.97%)
z_O	0.01155	0.01770 (+53.25%)	0.01139	0.01798(+57.86%)
x_H	0.10473	0.09812 (-6.31%)	0.10475	0.09792 (-6.52%)
z_H	0.51171	0.52053 (+1.72%)	0.51189	0.52099 (+1.78%)
Elastic coefficients				
C_{11} (GPa)	166.1	163.4 (-1.63%)	175.5	174.1(-0.80%)
C_{12} (GPa)	63.9	67.9 (+6.26%)	67.3	74.0 (+9.96%)
C_{13} (GPa)	64.9	60.7 (-6.47%)	72.0	66.0 (-8.33%)
C_{22} (GPa)	173.8	164.9 (-5.12%)	184.8	174.6 (-5.52%)
C_{23} (GPa)	67.5	63.1 (-6.51%)	75.3	68.5 (-9.03%)
C_{33} (GPa)	152.5	161.5 (+5.90%)	157.5	170.3 (+8.13%)
C_{44} (GPa)	49.5	49.2 (-0.61%)	53.1	51.1 (-3.77%)
C_{55} (GPa)	54.45	58.8 (+7.99%)	59.2	63.2 (+6.76%)
C_{66} (GPa)	50.9	55.1 (+8.25%)	49.8	57.6 (+15.66%)

Table S4.2 Comparison of calculated properties in β -LaHO, with orthorhombic structure and space group: $Pnma$ (62). Calculations are obtained from DFT (PBE, PBEsol) and from the derived interatomic potentials.

Chapter IV Hydride diffusion mechanism in LaHO family

	DFT PBE	Fitted potential 1	DFT PBEsol	Fitted Potential 2
Cell parameters				
a (Å)	5.5654	5.6269(+1.11%)	5.5025	5.57608(+1.34%)
Atomic positions :				
La (0.0000 0.0000 0.0000)				
H1 (0.2500 0.2500 0.2500)				
H2 (0.0000 0.0000 0.5000)				
Elastic coefficients				
C ₁₁ (GPa)	87.4	95.6 (+9.38%)	87.6	97.6 (+11.42%)
C ₁₂ (GPa)	76.3	87.0 (+14.02%)	83.4	88.5 (+6.12%)
C ₄₄ (GPa)	78.2	83.2 (+6.39%)	73.1	83.7 (+14.50%)

Table S4.3 Comparison of Experimental and calculated properties (PBE, interatomic potential derived from PBE, PBEsol, interatomic potential derived from PBEsol) in **LaH₃**, cubic, Space group : Fm-3m (225). This structure was used for the fitting of potential.

	DFT PBE	Fitted potential 1	DFT PBEsol	Fitted Potential 2
Cell parameters				
a (Å)	3.9378	3.94996(+0.31%)	3.9094	3.91680 (+0.19%)
c (Å)	6.1819	6.17863 (-0.05%)	6.0433	6.0474 (+0.07%)
Atomic positions :				
La (0.3333 0.6666 z_{La})				
O1 (0.3333 0.6666 z_o)				
O2 (0.0000 0.0000 0.5000)				
z_{La}	0.24737	0.24657 (-0.32%)	0.24536	0.24533 (-0.01%)
z_o	0.64535	0.66289(+2.72%)	0.64592	0.66376 (+2.76%)
Elastic coefficients				
C ₁₁ (GPa)	198.8	187.5 (-5.68%)	216.9	206.3 (-4.89%)
C ₁₂ (GPa)	118.4	129.3 (+9.21%)	133.5	144.6 (+8.31%)
C ₁₃ (GPa)	77.4	69.2 (-10.59%)	88.1	77.9 (-11.58%)
C ₁₄ (GPa)	33.1	43.9 (+32.63%)	30.3	45.9 (+51.49%)
C ₂₄ (GPa)	-33.1	-43.9 (+32.63%)	-30.3	-45.9 (+51.49%)
C ₃₃ (GPa)	130.4	110.7 (-15.11%)	137.6	114.7 (-16.64%)
C ₄₄ (GPa)	57.1	62.2 (+8.93%)	64.1	69.6 (+8.58%)
C ₆₆ (GPa)	40.2	29.1 (-27.61%)	41.7	30.8 (-26.14%)

Chapter IV Hydride diffusion mechanism in LaHO family

Table S4.4 Comparison of Experimental and calculated properties (PBE, interatomic potential derived from PBE, PBEsol, interatomic potential derived from PBEsol) in La_2O_3 , hexagonal, Space group: $P-3m1$ (164). This structure was used for the fitting of potential.

	Experimental (300 K)	DFT PBE	Fitted potential 1	DFT PBEsol	Fitted Potential 2
Cell parameters					
a (Å)	6.4116(1) ³	6.4355	6.34516(-1.40%)	6.3058	6.27664(+2.72%)
b (Å)	3.9161(1) ³	3.9146	3.95259 (+0.97%)	3.8724	3.91645(+2.72%)
c (Å)	7.0823(1) ³	7.0854	7.12467 (+0.55%)	7.0434	7.05219(+2.72%)
Atomic positions :					
La (x_{La} 0.25000 z_{La})					
O (x_{O} 0.25000 z_{O})					
H (x_{H} 0.25000 z_{H})					
x_{La1}	0.2766(1) ³	0.2778	0.26590 (-4.28%)	0.27574	0.26610 (-3.50%)
z_{La1}	0.3987(1) ³	0.39789	0.41562 (+4.46%)	0.39742	0.41613(+4.71%)
x_{O}	0.1512(5) ³	0.15063	0.15232 (+1.12%)	0.15211	0.15223(+0.08%)
z_{O}	0.0820(4) ³	0.07941	0.09806(+23.49%)	0.07889	0.09811(+24.36%)
x_{H}	0.0268(4) ³	0.02866	0.00898(-68.59%)	0.02724	0.00868(-68.13%)
z_{H}	0.6696(4) ³	0.66823	0.64184 (-3.94%)	0.67187	0.64179(-4.48%)
Elastic coefficients					
C_{11} (GPa)		88.6	131.7(+48.65%)	95.3	137.1(+43.86%)
C_{12} (GPa)		43.7	41.5 (-5.03%)	54.2	45.3 (-16.42%)
C_{13} (GPa)		66.8	60.1 (-10.03%)	72.3	65.8 (-8.99%)
C_{22} (GPa)		154.5	152.8 (-1.10%)	167.0	164.8 (-1.32%)
C_{23} (GPa)		84.4	80.9 (-4.15%)	95.8	92.6 (-3.34%)
C_{33} (GPa)		189.3	152.3 (-19.55%)	205.2	167.9 (-18.18%)
C_{44} (GPa)		40.2	27.5 (-31.59%)	44.5	28.9 (-35.06%)
C_{55} (GPa)		49.0	39.9 (-18.57%)	51.6	43.6 (-15.50%)
C_{66} (GPa)		35.7	44.0 (+23.25%)	44.6	45.5 (+2.02%)

Table S4.5 Comparison of Experimental and calculated properties (PBE, interatomic potential derived from PBE, PBEsol, interatomic potential derived from PBEsol) in γ -**LaHO** (Orthorhombic, High pressure form), Space group: $Pnma$ (62). This structure was **not** used for the fitting of potential.

Chapter IV Hydride diffusion mechanism in LaHO family

	Experimental (300 K)	DFT PBE	Fitted potential 1	DFT PBEsol	Fitted Potential 2
Cell parameters					
a (Å)	6.1681(1) ³	6.1778	6.24338(+1.06%)	6.1026	6.16643(+1.05%)
c (Å)	3.6036(1) ³	3.6012	3.58062(-0.57%)	3.5668	3.53286(-0.95%)
Atomic positions :					
La (1b)	(0.0000	0.0000	0.0000)		
La2 (2c)	(0.3333	0.6666	0.5000)		
O (3g)	(x _O	0.0000	0.0000)	
H (3f)	(x _H	0.0000	0.5000)	
x _O	0.5932(5) ³	0.59533	0.59240 (-0.49%)	0.59442	0.59199 (-0.41%)
x _H	0.2390 ³	0.24558	0.24262 (-1.21%)	0.24517	0.24211 (-1.25%)
Elastic coefficients					
C ₁₁ (GPa)		195.0	214.5 (+10.0%)	207.9	230.4(+10.82%)
C ₁₂ (GPa)		69.0	74.3 (+7.68%)	74.2	78.7 (+6.06%)
C ₁₃ (GPa)		66.7	54.1 (-18.89%)	81.5	59.4 (-27.12%)
C ₂₂ (GPa)		195.0	214.5 (+10.0%)	207.9	230.4 (+10.82%)
C ₃₃ (GPa)		245.1	248.5 (+1.39%)	260.4	266.4 (+2.30%)
C ₄₄ (GPa)		54.7	52.6 (-3.84%)	60.6	58.0 (-4.29%)
C ₆₆ (GPa)		63.0	70.1 (+11.27%)	66.9	75.8 (+13.03%)

Table S4.6 Comparison of Experimental and calculated properties (PBE, interatomic potential derived from PBE, PBEsol, interatomic potential derived from PBEsol) in δ -LaHO (Hexagonal, high pressure form), Space group : P-62m (189). This structure was **not** used for the fitting of potential.

Interactions	A / eV	$\rho / \text{Å}$	C / eV Å^6
La ^{2.4+} — H ^{0.8-}	1151.04	0.3088	0.00
La ^{2.4+} — O ^{1.6-}	2938.74	0.3019	0.00
O ^{1.6-} — O ^{1.6-}	16976.43	0.21601	0.00
La ^{2.4+} — La ^{2.4+}	460.51	0.1236	0.00

Table S4.7 Interatomic potentials as obtained from the fitting of PBEsol-functional DFT calculations.

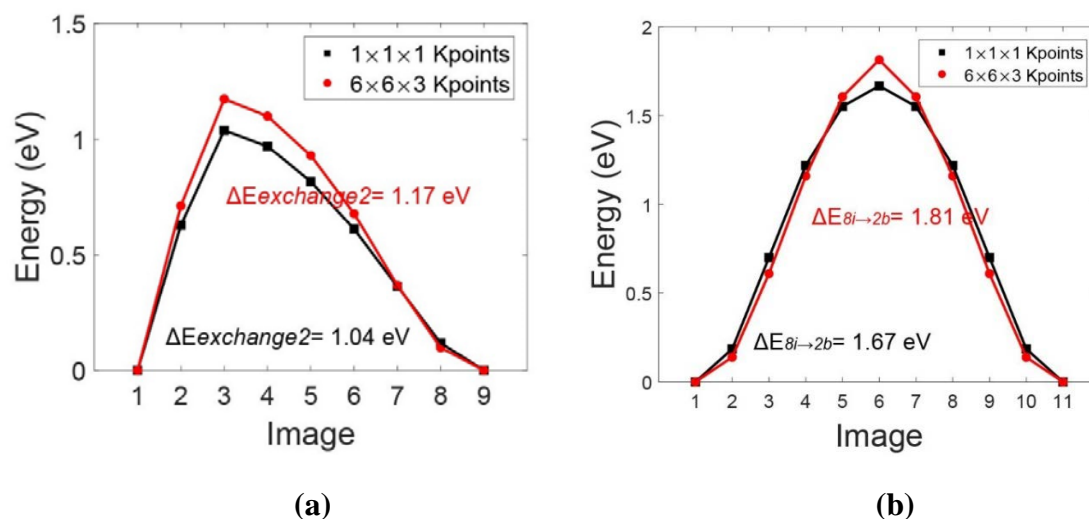


Figure S4.1 The CI-NEB energy landscape of two different pathways in α -LaHO for different density reciprocal space meshes. The red curve represents $6 \times 6 \times 3$ Kpoints, while the black one is $1 \times 1 \times 1$ Kpoints. (a) The exchange mechanism n^2 , the black curve is identical to that of **Figure 4.6b**. (b) one H^- move from $8i$ site to $2b$ site, and come back to $8i$ site.

Because of computing time/memory issues, a single Γ -centered $1 \times 1 \times 1$ k-point was adopted. The higher density reciprocal space meshes will produce similar energy values as shown in **Figure S4.1**.

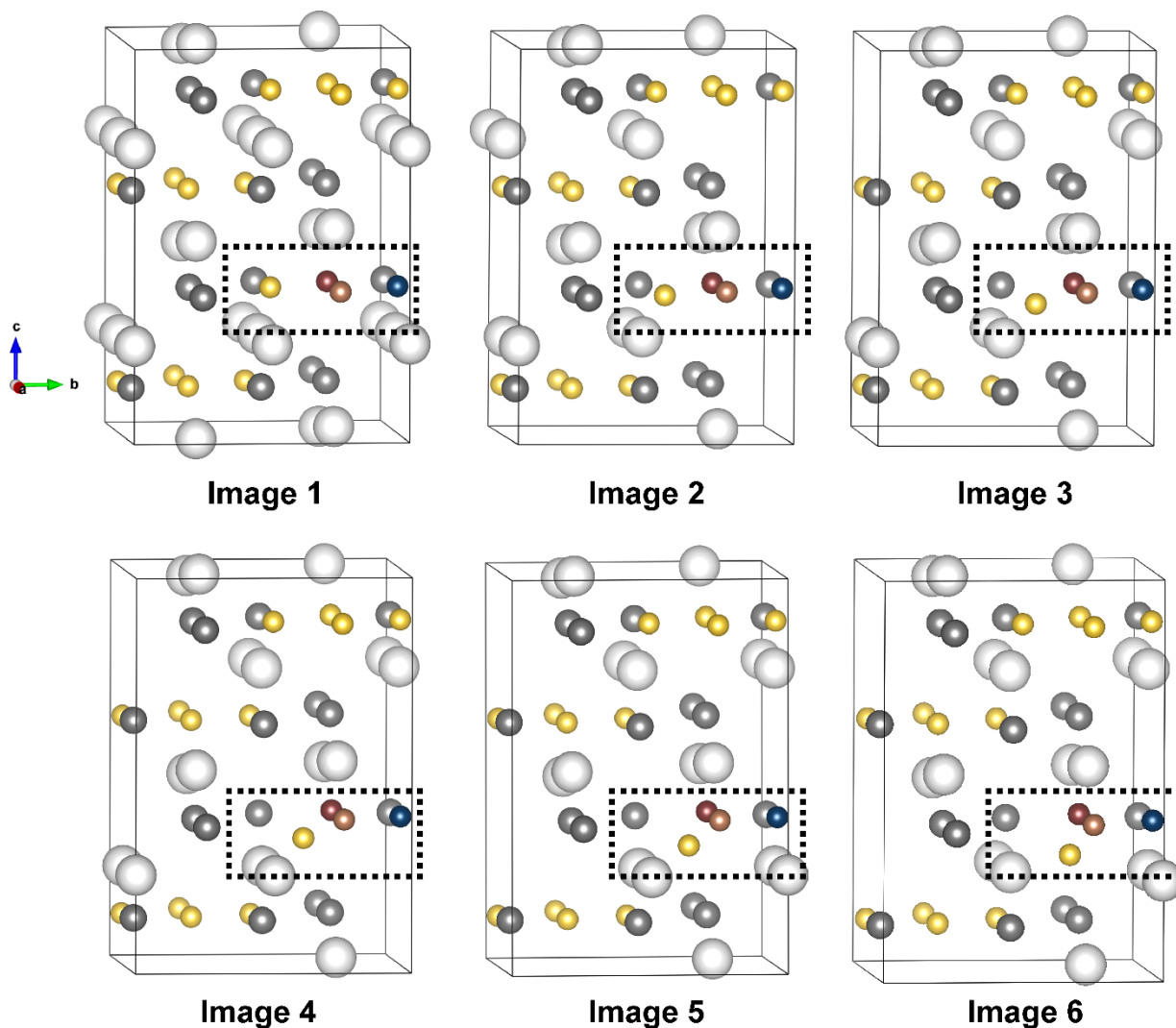


Figure S4.2 Exchange n° 1 The detailed pathway of hydride ion transfer from $8i$ to $2c$ sites. Only hydrides in the dotted frame are focused. H1, H2, H3, and H4 in the dotted frame are coloured in yellow, brown, blue, and dark red. The other hydrides are all coloured in yellow. This drawing method is adopted to all the CI-NEB figures followed behind.

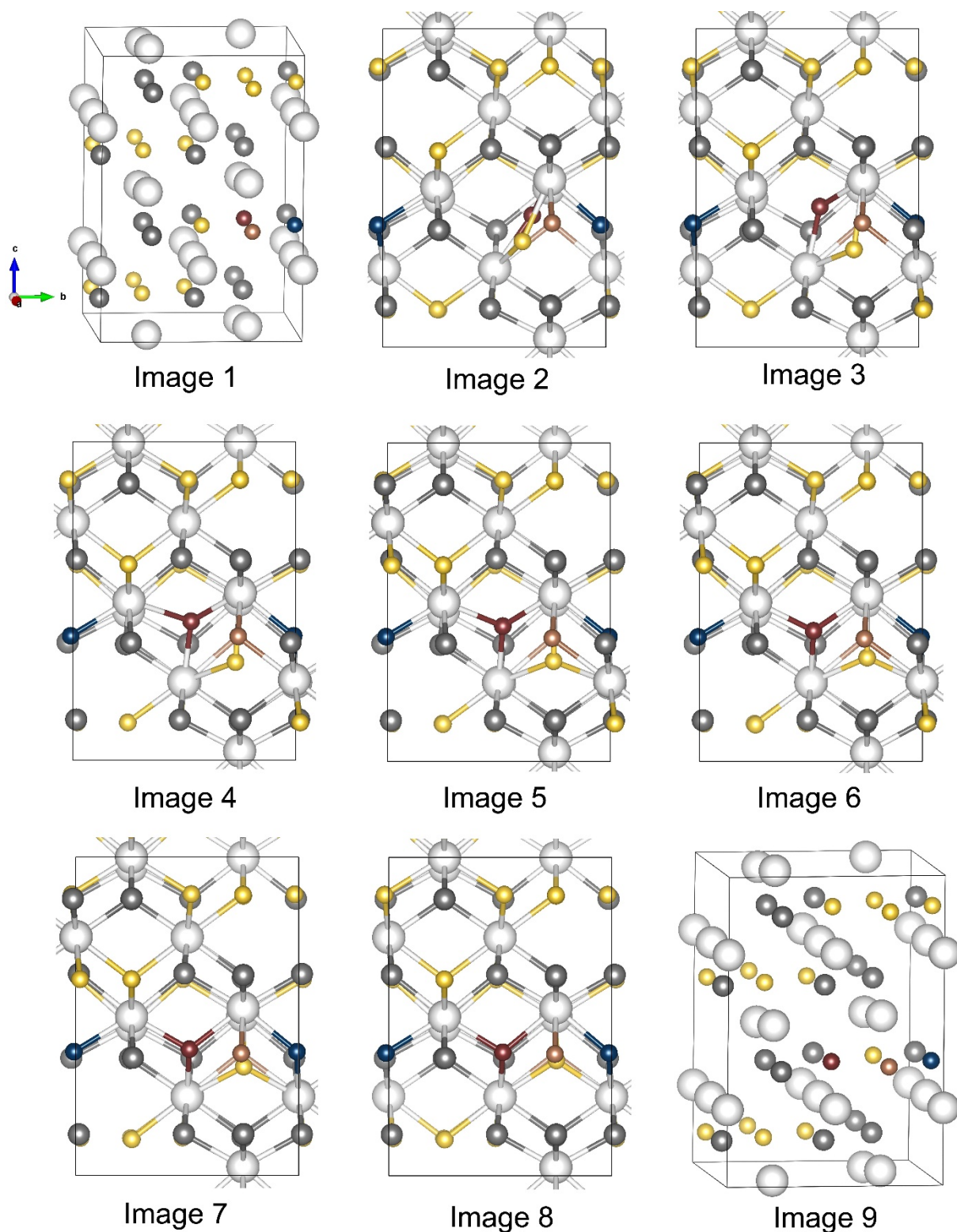


Figure S4.3 Exchange n° 2 The optimized diffusion path of two hydrides exchange positions calculated by CI-NEB. The configuration with the highest free energy is the one corresponding to image 3.

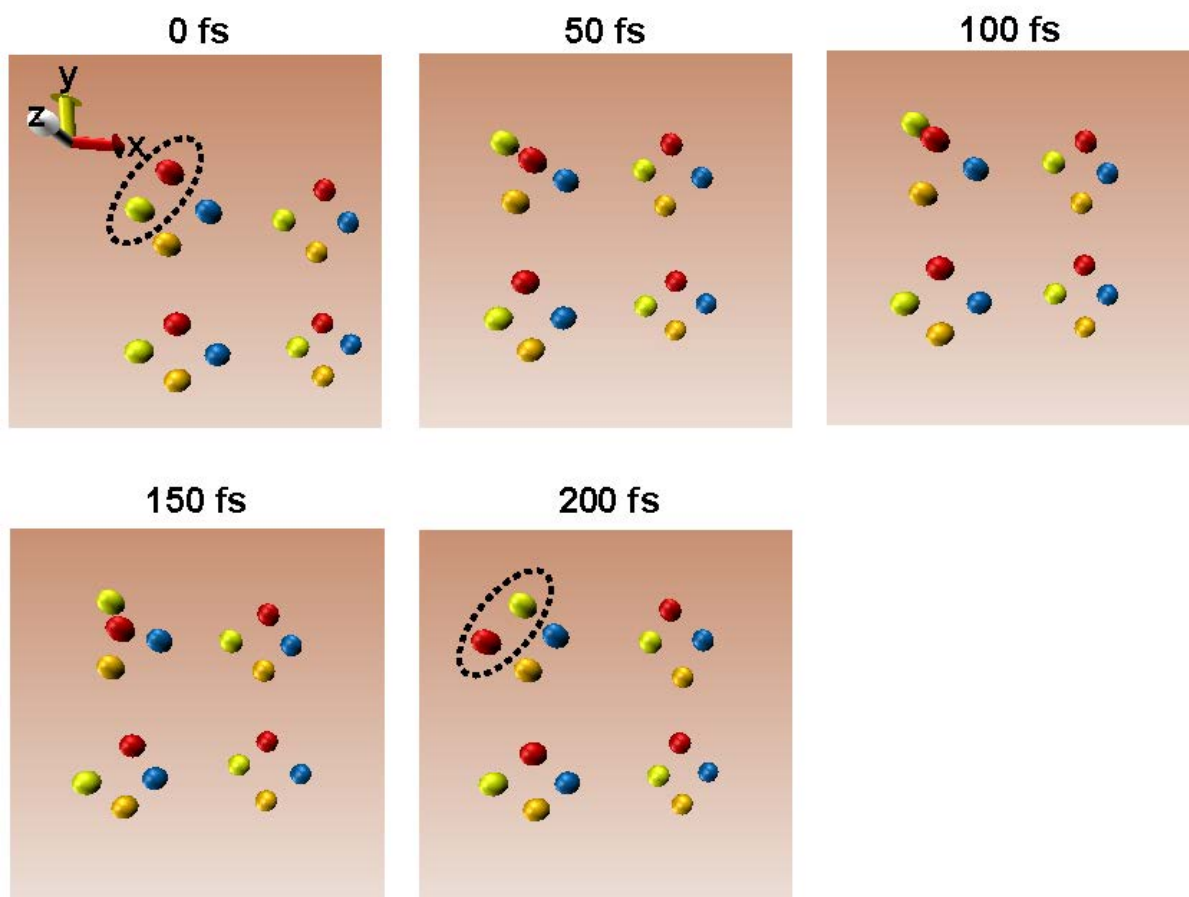


Figure S4.4 Exchange n° 2 VMD⁴ evidence of two hydride ions exchanging their positions. The yellow and dark red ions surrounded by the dotted frame change their positions. The snapshot was captured in the α -LaHO trajectory of NVE simulation with time interval 50 fs at 1100 K. The yellow ball (H1) move from H1 site to H4 site from 0 fs to 100 fs, while the dark red ball (H4) occupied the H2c site from 50 fs to 150 fs.

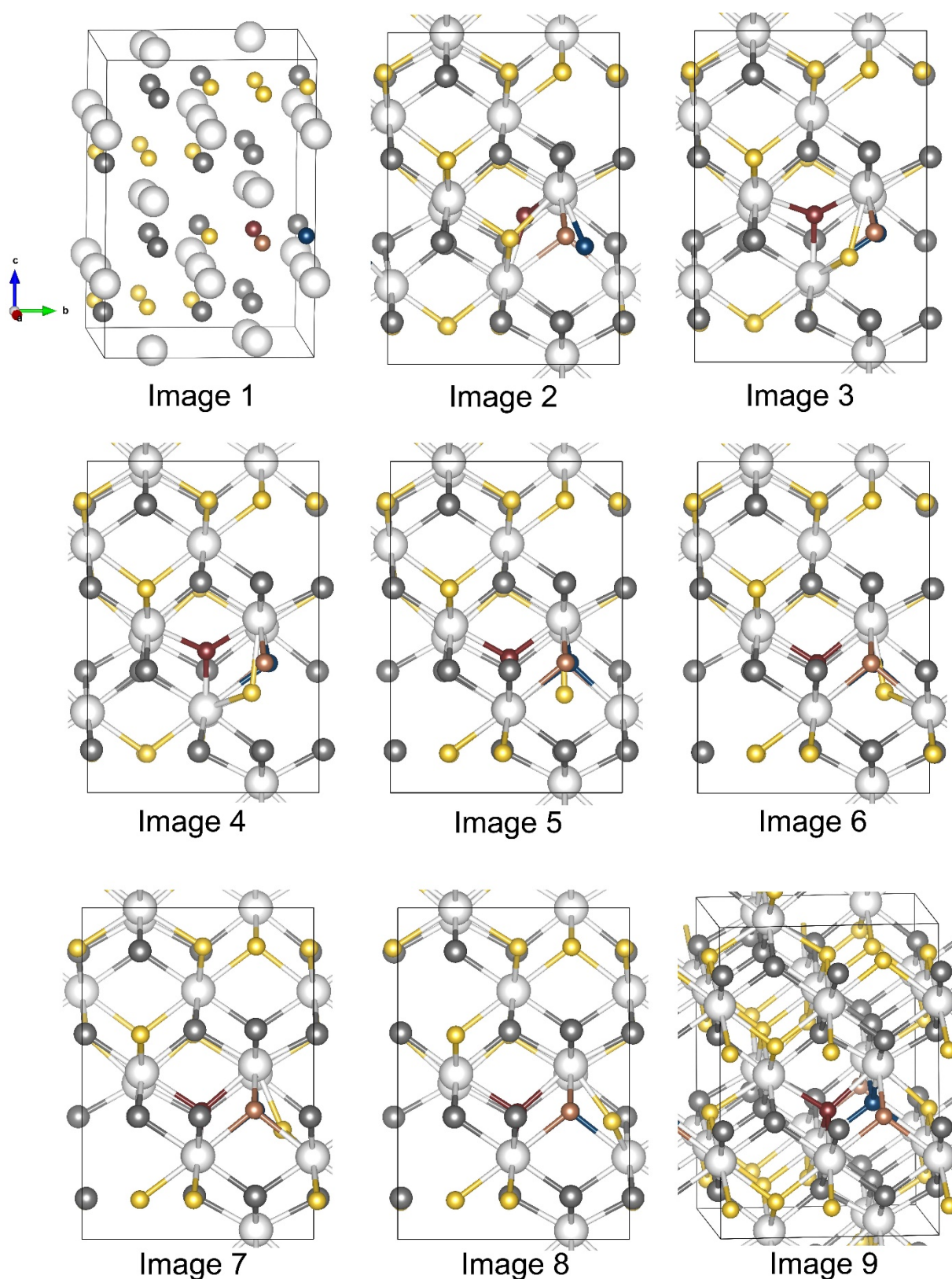


Figure S4.5 Exchange n° 3 The optimized diffusion path of three hydrides exchange positions calculated by CI-NEB. The configuration with the highest free energy is the one corresponding to image 3.

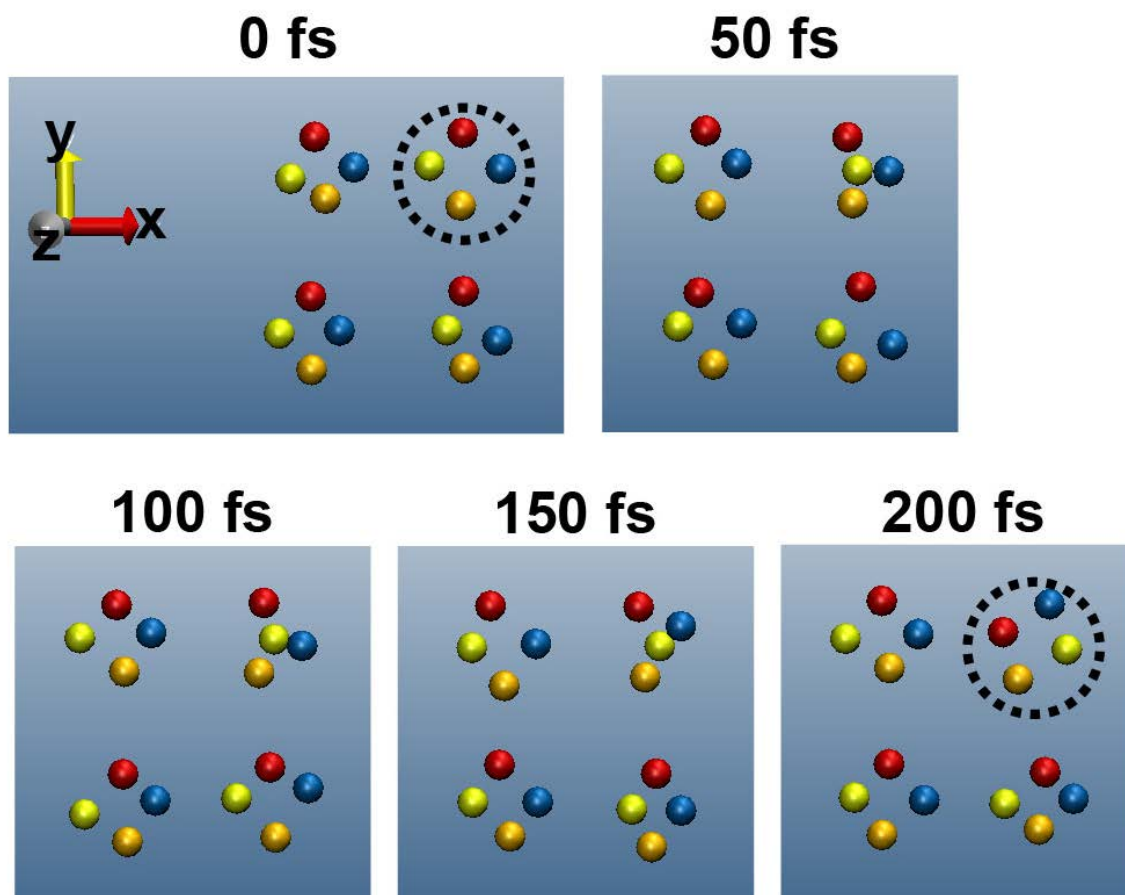


Figure S4.6 Exchange n° 3 VMD evidence of three hydrides exchanging their positions.

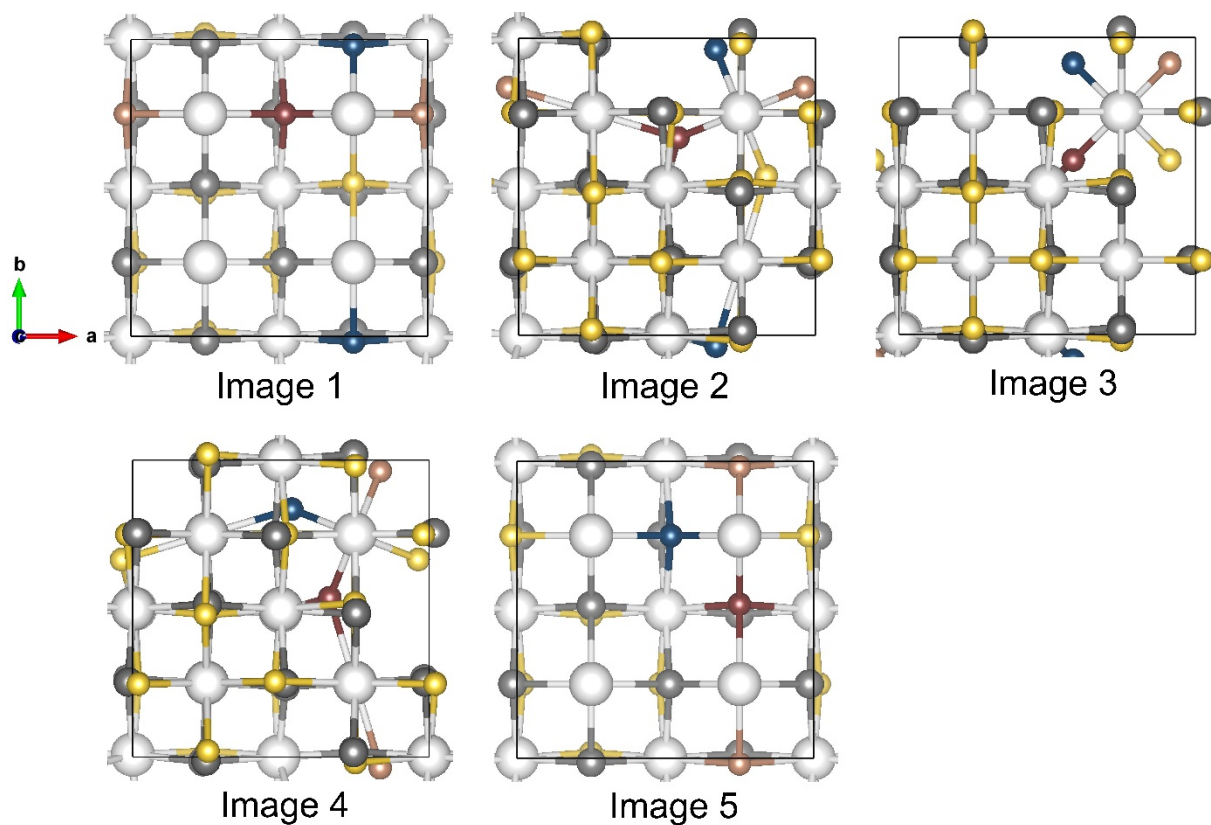


Figure S4.7 Exchange n° 4 The optimized diffusion path of four hydrides rotate by CI-NEB. The configuration with the highest free energy is the one corresponding to image 3

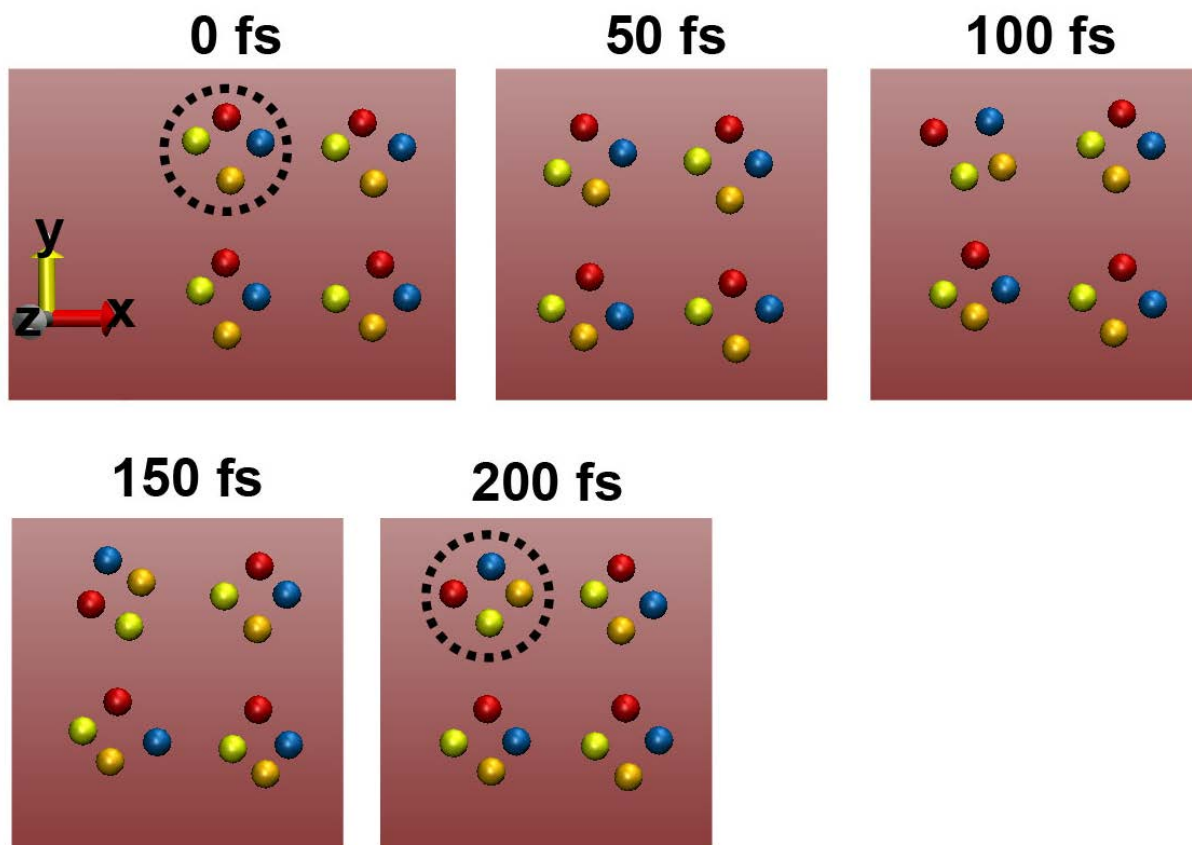
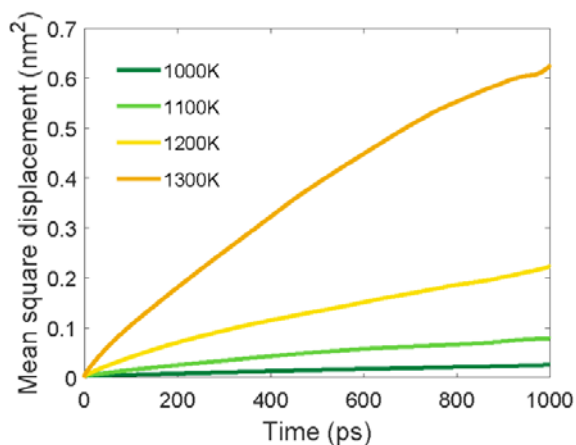
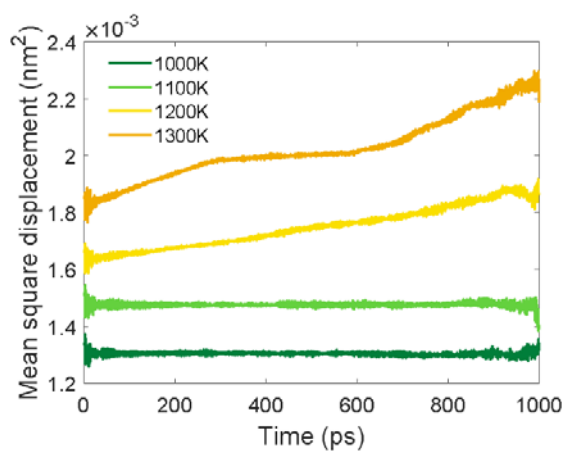


Figure S4.8 Exchange n° 4 VMD evidence of four hydrides rotate.

Chapter IV Hydride diffusion mechanism in LaHO family



(a)



(b)

Figure S4.10 (a) The MSD curves of H^- at four different temperature of $\alpha\text{-LaHO}$. (b) The MSD curves of O^{2-} at four different temperature of $\alpha\text{-LaHO}$.

Occupancy	1000K	1100K	1200K	1300K
O^{2-} in H^- sites	0	0	0.163%	0.300%
O^{2-} in O^{2-} sites	1	99.999%	99.834%	99.698%
H^- in H^- sites	99.871%	99.745%	99.129%	97.984%
H^- in O^{2-} sites	0	0	0.162%	0.298%

Table S4.8 The occupancy rate of different ions in different ion sites with the change of temperature calculated by applying the convex hull statistic method⁵.

Chapter IV Hydride diffusion mechanism in LaHO family

In **Figure S4.10b**, when the temperature is 1000K and 1100K, the MSD curve of the oxygen ion is a constant value. When the temperature increased to 1200K, the MSD curve of the oxygen ion is slightly increased. When we compare the MSD curves of hydrides and oxygen ions (**Figure S4.10**), we can find that the mean square displacement of oxygen ions is much smaller than that of hydrides. Overall, oxygen ions play a very limited role in diffusion compared with hydrides.

In **table S4.8** it can be found that at 1000K and 1100K, the occupancy rate of oxygen ions in the O^{2-} site is almost 1, indicating that at these two temperatures, the oxygen ions only vibrate at their equilibrium positions, which is also reflected in the MSD curve of oxygen ions in **Figure S4.10**. When the temperature rises to 1200K, the occupancy rate of oxygen ions in O^{2-} site and H^- site are 99.834% and 0.163%, respectively. Besides, the occupancy rate of hydride in the O^{2-} site is 0.162%. It indicates that a tiny number of oxygen ions jumped to the position of H 8i, resulting in the creation of oxygen vacancies. The hydrides will then occupy this oxygen vacancy and achieve greater long-range diffusion. In summary, oxygen ions can provide oxygen vacancies to enhance the diffusion of hydrides at higher temperatures ($\geq 1200K$) but the effect is limited.

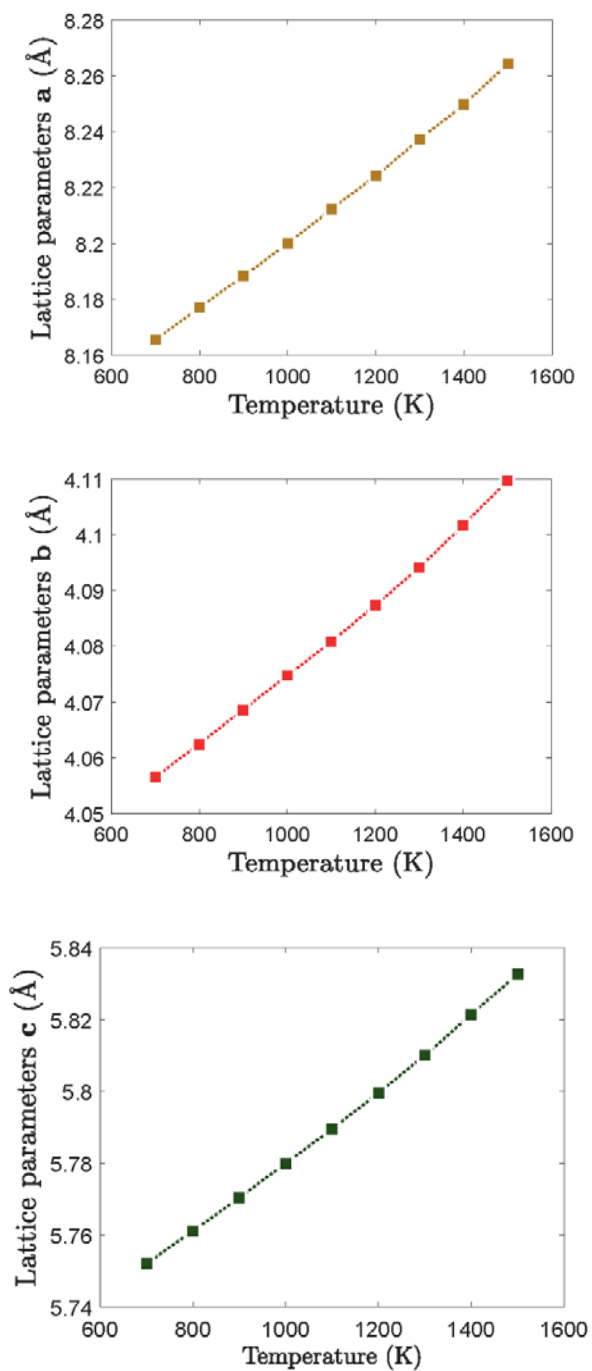


Figure S4.11 The lattice parameter of β -LaHO as a function of temperature by the MD simulation results.

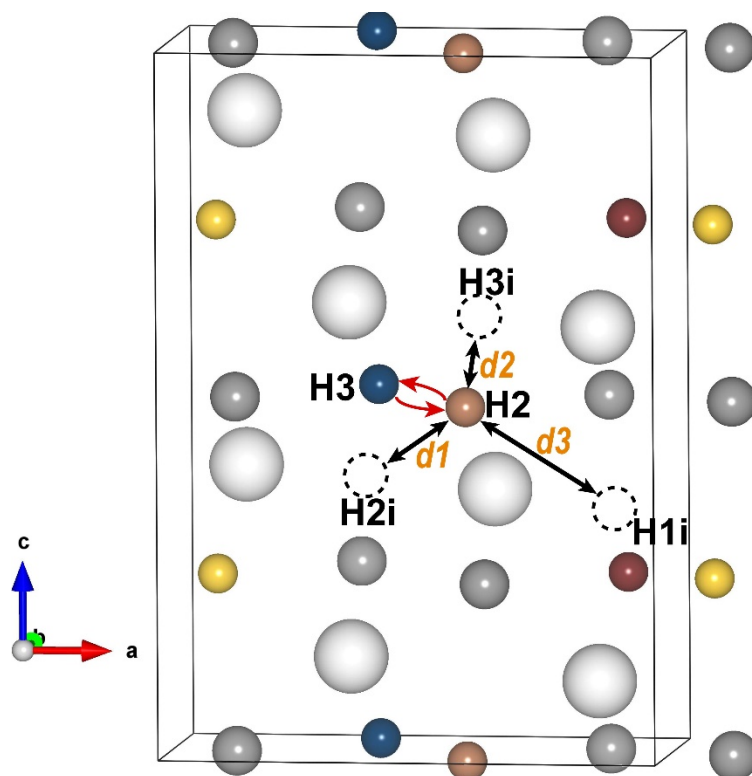


Figure S4.12 The $1 \times 1 \times 2$ β -LaHO unit cells. H1, H2, H3 and H4 are coloured in yellow, brown, blue and dark red respectively. According to periodic boundary condition, H1 and H4 (yellow and dark red balls) are geographically near and can be considered as one group. The same is for H2 and H3 group. The red arrows represent that in one group (H2/H3 or H1/H4), they can swap their positions. Besides, each H can jump to the nearest three interstitial positions. e.g. H2 can jump to H2i, H3i and H1i.

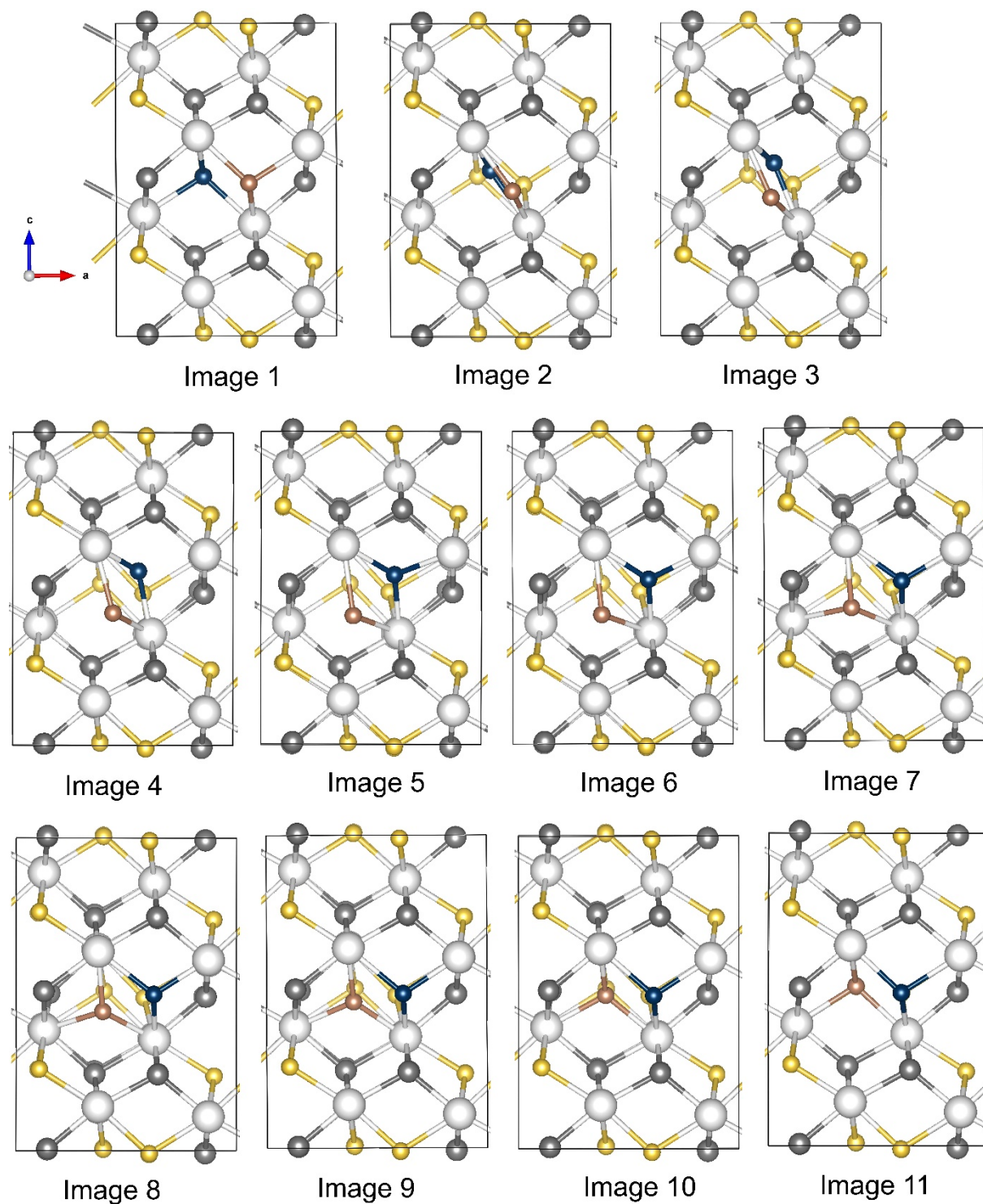


Figure S4.13 The optimized diffusion path 1 of two H^- exchange position in $\beta\text{-LaHO}$ by CI-NEB. The configuration with the highest free energy is the one corresponding to image 5.

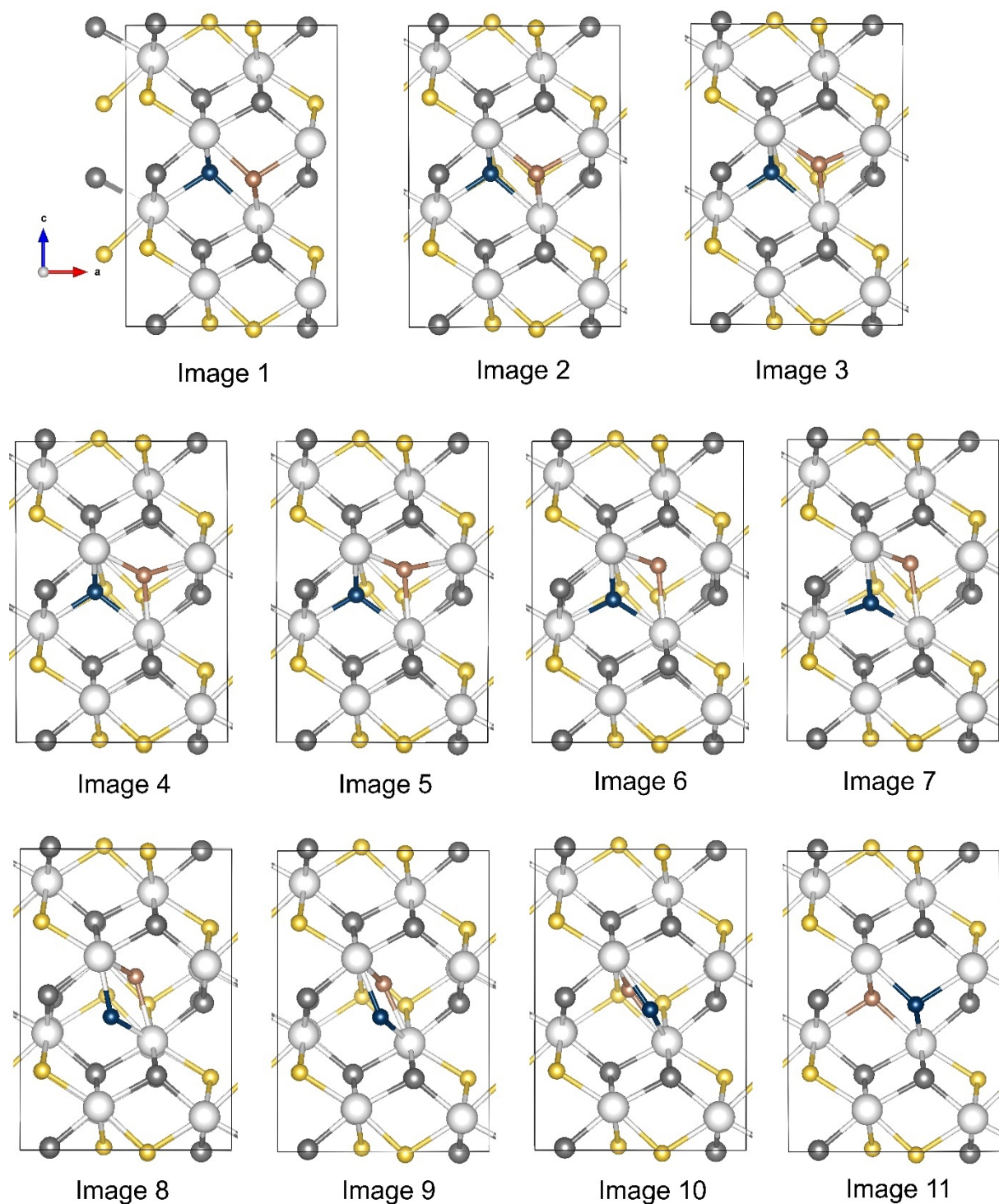


Figure S4.14 The optimized diffusion path 2 of two H^- exchange position in β -LaHO by CI-NEB. The configuration with the highest free energy is the one corresponding to image 7. The free energy of image 7 is identical to that of image 5 of **Figure S4.13**. (1.455 eV higher than the ground state of image 1)

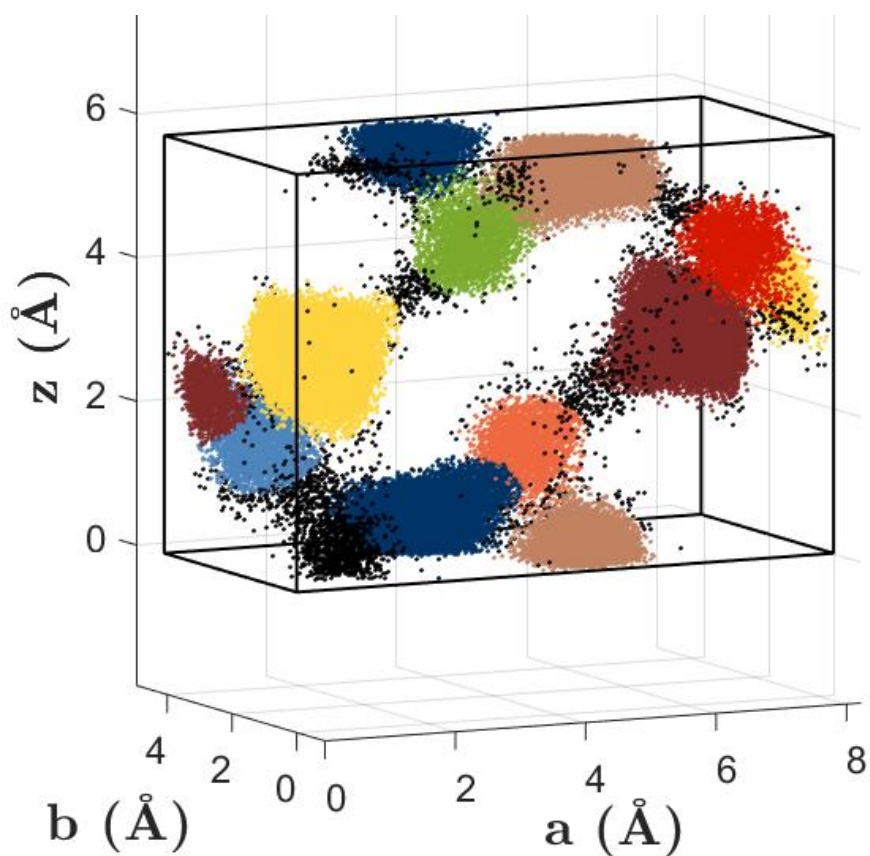


Figure S4.15 The complete information unit cell of 2% H interstitial β -LaHO at 1200K.

The interstitial H- clusters become more visible compared to the case of pure β -LaHO.

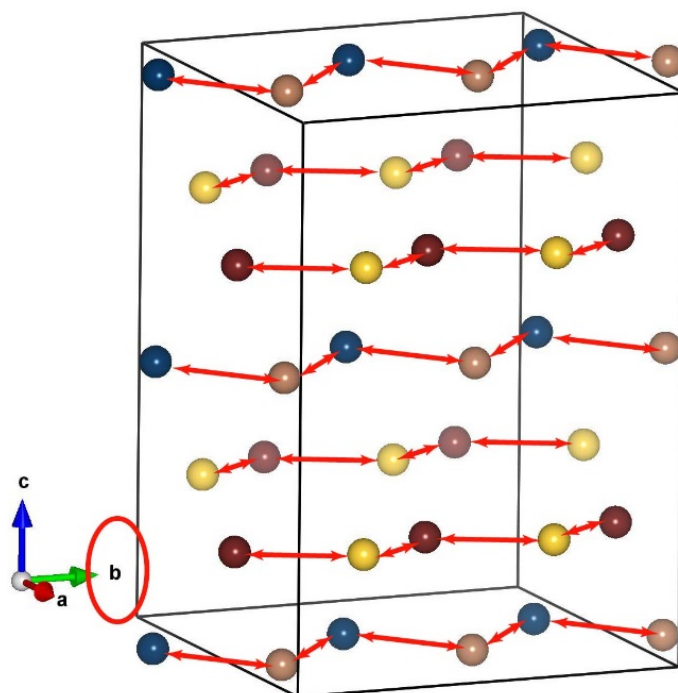
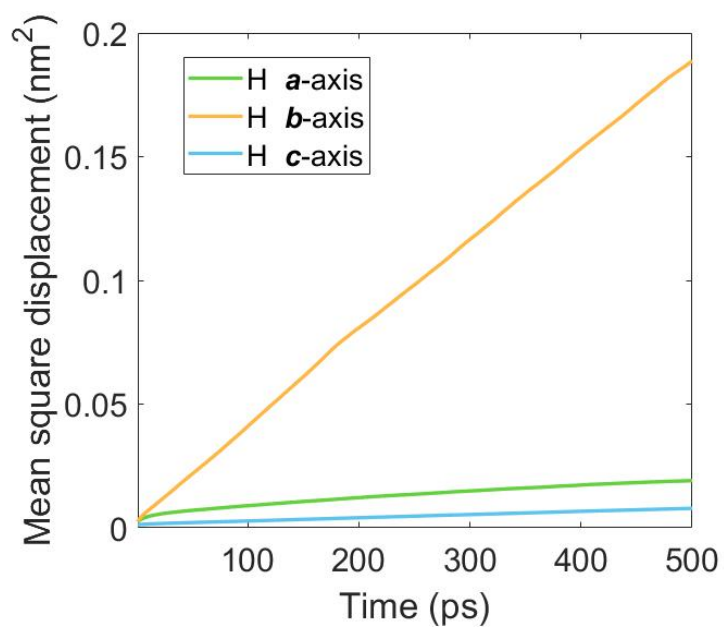


Figure S4.16 (a) The MSD curves of different ions in 2% H- vacancy β -LaHO at 1200K.

(b) The diffusion path of H- in 2% H- vacancy β -LaHO.

Destination site	Departure site							
	H1	H2	H3	H4	H1i	H2i	H3i	H4i
H1	238578	7	5	6202	50	11	0	45
H2	3	233617	9053	3	13	69	45	0
H3	5	9056	233875	4	0	43	72	16
H4	6198	5	3	238021	32	2	12	59
H1i	51	10	0	34	17	0	0	0
H2i	13	62	50	0	0	13	0	0
H3i	0	45	75	10	0	0	24	0
H4i	47	0	13	60	0	0	0	16

Table S4.9 The number of jumps between two different sites in 2% H⁻ vacancy β -LaHO at 1200K.

There are 9056 jumps from H2 to H3 and 9053 jumps in the opposite direction, which is well above the number of jumps in pure β -LaHO.

References:

- 1 H. Ubukata, T. Broux, F. Takeiri, K. Shitara, H. Yamashita, A. Kuwabara, G. Kobayashi and H. Kageyama, *Chem. Mater.*, 2019, **31**, 7360–7366.
- 2 B. Malaman and J. F. Brice, *J. Solid State Chem.*, 1984, **53**, 44–54.
- 3 T. Broux, H. Ubukata, C. J. Pickard, F. Takeiri, G. Kobayashi, S. Kawaguchi, M. Yonemura, Y. Goto, C. Tassel and H. Kageyama, *J. Am. Chem. Soc.*, 2019, **141**, 8717–8720.
- 4 W. Humphrey, A. Dalke and K. Schulten, *J. Mol. Graph.*, 1996, **14**, 33–38.
- 5 C. Li, H. Dammak and G. Dezanneau, *Phys. Chem. Chem. Phys.*, 2019, **21**, 21506–21516.

Chapter V Hydride diffusion mechanism in $\text{LaH}_{3-2x}\text{O}_x$

Abstract

$\text{LaH}_{3-2x}\text{O}_x$ are promising H^- ion conductors reported by Hosono *et al.*[1] Herein, we performed classical molecular dynamics simulation to study the diffusion mechanism of hydride ions in this series of compounds. Our simulations are based on a previously reported potential, which was developed to simulate LaHO phases. Our simulations indicate that the four different hydrogen sites in $\text{LaH}_{3-2x}\text{O}_x$ play different roles in the diffusion process. We also show that the progressive substitution by oxygen ions make the diffusion mechanism changing from an isotropic to a bi-dimensional process. This behaviour is mainly due to the fact that oxygen ions repel hydrogen ions modifying the occupancy of the different hydrogen sites significantly and inducing a 2D diffusion. Finally, we demonstrate that the main bottleneck for diffusion occurs between two well-identified hydrogen sites. This bottleneck can be adjusted by playing on the rare-earth nature.

Molecular dynamics study of oxygen-substituted lanthanum hydride

V.1 Introduction

Hydride ions, H^- , can be a promising charge carrier in the next-generation of electrochemical energy storage systems with high voltage and high energy density.[2]-[12] Recently, Hosono *et al.* [1] discovered a new oxyhydride family $\text{LaH}_{3-2x}\text{O}_x$ with a very high H^- conductivity. From Neutron Powder Diffraction, they found that this material has the tetragonal structure with the space group of $P4/nmm$, with a very slightly distorted structure compared to the original cubic one of LaH_3 . Analyses of NPD data allowed obtaining relevant information about the oxygen dopant site, the evolution of hydrogen positions relatively to the original LaH_3 structure. They also obtained an optimized ionic conductivity of $2.6 \times 10^{-2} \text{ S cm}^{-1}$ and a high transport number (>0.99) for hydride ion conduction is observed at $T = 340 \text{ }^\circ\text{C}$ for $x = 0.24$. At these intermediate temperatures, this conductivity is the highest reported to date among hydride ion conductors. Upon increasing the oxygen content x , the relatively high activation energy of 1.2–1.3 eV remains almost unchanged. They conclude that the light mass and high polarizability of H^- , and the structural framework composed of densely packed H^- in $\text{LaH}_{3-2x}\text{O}_x$, are crucial factors that impose the temperature dependence of the diffusion process.

In the present paper, we studied the diffusion mechanism of H^- in $\text{LaH}_{3-2x}\text{O}_x$ through classical molecular dynamics simulations. The potential used, initially developed by fitting the structural and elastic properties of LaHO family, is shown here to reproduce many of the features observed in the $\text{LaH}_{3-2x}\text{O}_x$ system. From molecular dynamics simulation, we are able to extract macroscopic data like cell parameters, diffusion coefficients, and conductivity. From these simulations, we can also understand more deeply how oxygen doping affects the hydride ion diffusion mechanism. We indeed

provide a complete view of the diffusion path, occupancy rate, and residence time on the different sites as a function of the oxygen doping level. Finally, We discuss the potential influence of the rare-earth radius for hydride ion diffusion in other $\text{LnH}_{3-2x}\text{O}_x$.

V.2 Molecular dynamic simulation

MD simulations were performed considering seven different chemical formulas $\text{LaH}_{3-2x}\text{O}_x$, from x varying from 0 to 0.75. Each configuration consists of a supercell containing $9 \times 8 \times 6$ tetragonal unit cells. The number of La ions in the different configurations is 864, while the numbers of H and O ions change with composition.

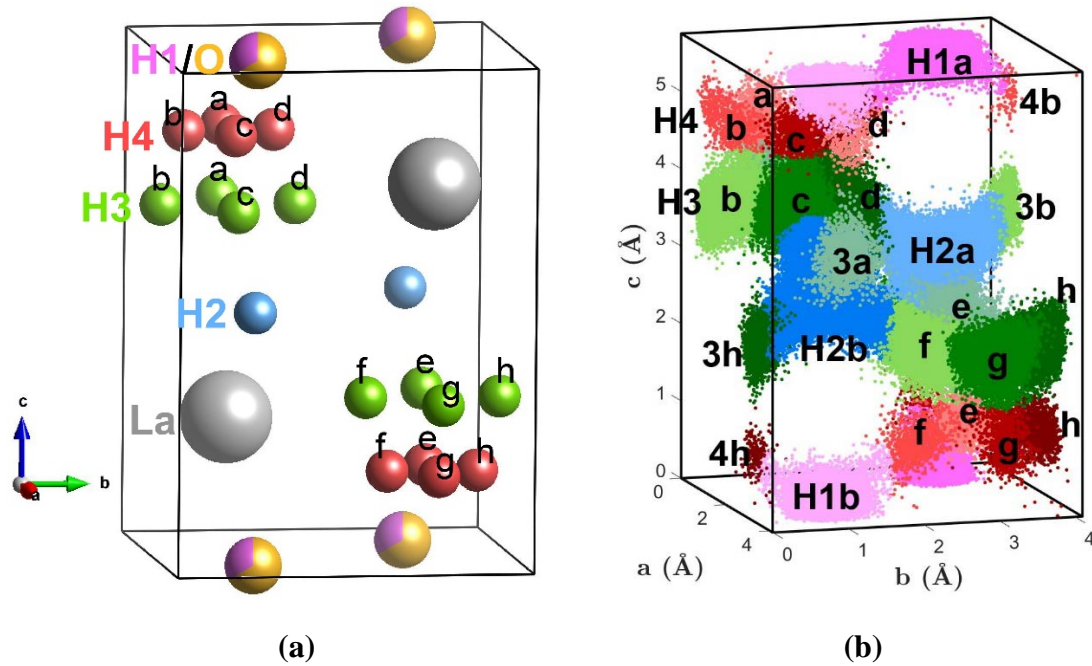


Figure 5.1 (a) Unit cell of tetragonal $\text{LaH}_{3-2x}\text{O}_x$. as represented in the space group is $P4/nmm$. The La at (0.25 0.25 0.2481), O1/H1 at (0.75 0.25 0), H2 at (0.75 0.25 0.5), H3 at (0.25 0.062 0.670), and H4 at (0.25 0.124 0.816) ions are represented by grey, yellow, pink, blue, green and red representatively. (b) The complete information unit cell of $\text{LaH}_2\text{O}_{0.5}$ at 300 K.

For building the different configurations, it is important to remind the main features of the $\text{LaH}_{3-2x}\text{O}_x$ tetragonal structure. The unit cell of $\text{LaH}_{3-2x}\text{O}_x$, as proposed by Hosono

Chapter V Hydride diffusion mechanism in $\text{LaH}_{3-2x}\text{O}_x$

et al., is shown in **Figure 5.1(a)**. There are five independent sites, namely La, O1/H1, H2, H3, and H4, expressed in the tetragonal space group $P4/nmm$. From NPD, the description and positions of the different sites in $\text{LaD}_2\text{O}_{0.5}$ (D is the deuterium, NPD results can be referred from [1]) were as follows: La lies on a $(2c)$ position at (0.25, 0.25, 0.2481). O1/H1 lies on a $(2a)$ position at (0.75, 0.25, 0), since oxygen ion was shown to substitute specifically H1 in this structure. H2 lies also on a $(2a)$ position at (0.75, 0.25, 0.5). Finally, H3 and H4 lie both on a $(8i)$ position at (0.062, 0.6704, 0.1070) and (0.124, 0.816, 0.063) respectively. A similar structure was observed for $\text{LaD}_{1.5}\text{O}_{0.75}$ [1]. For our simulation, the supercells were built according to this scheme, specifically with oxygen substituting the hydrogen atoms on H1 site. Instead of filling H3 and H4 positions with one hydrogen atom per 8 possible sites, we built the tetragonal cell by putting the hydrogen atom on the average position between those sites. This position corresponds to the octahedral $(8c)$ site at (0.5, 0.5, 0.5) in the original LaH_3 cubic cell. It is worth mentioning that the splitting of this site in the LaH_3 cubic cell was observed experimentally at low temperature, and the transition from an ordered to a disordered phase was given to be at ~250-270 K [13]–[15]. After filling the La, O1/H1, H2, H3/H4 sites, we finally adjusted the total hydrogen composition by creating vacancies on this last specific site. Concerning LaH_3 , despite its structure is reported to be cubic, we modeled this composition considering both the cubic and the tetragonal structures. All these processes (substitution, removal of atoms) were performed with the software ATOMSK.[16] For each doped composition, three different original configurations were created, and all the final properties presented were averaged over these three configurations. We systematically tested 12 different simulation temperatures from 300 K to 1400 K. MD simulations were performed using the DLPOLY classic code.[17] Interaction between ions is described by a long-range Coulombic term calculated by Ewald Summation and a short-range Buckingham pair potential. For Coulombic interactions, we use the formal charges of +2.4, -0.8, and -1.6 for La, H, and O ions, respectively. The parameters determining the Buckingham potential are described in **Table 4.1**. Each system was first equilibrated at the desired

Chapter V Hydride diffusion mechanism in $\text{LaH}_{3-2x}\text{O}_x$

temperature and zero pressure for 20,000 timesteps (with a time step duration of 0.2 fs) in the isothermal-isobaric (N σ T) ensemble with Nose-Hoover thermostat. Afterwards, the equilibrium lattice parameters were calculated with 80,000 timesteps more. Then, simulations were performed in the NVT mode during 100,000 timesteps. Finally, NVE simulations were realized, corresponding to 2,000,000 time steps. All the ions trajectories coordinates will be dumped every 2000 time steps to the trajectory file.

V.3 Results and discussions

In a previous study, we already showed that we could reproduce LaH_3 DFT calculations within ~1% for cell parameters and within 10-15% for elastic coefficients. The other LaHO oxyhydride compounds, also used in the fit, were reproduced with greater accuracy. We presented in **Figure 5.2** the volume of unit cells of all $\text{LaH}_{3-2x}\text{O}_x$ as a function of temperature and compared to experimental results. It shows that upon oxygen substitution, the calculated unit-cell volume increases following a non-linear law, similar to the one observed experimentally (insert figure of **Figure 5.2**). The simulation results are close to experimental ones with a difference between calculated and experimental values smaller than 2%, a range of errors frequently observed with DFT calculations. Calculations at higher temperatures indicate that oxygen-doping also allows diminishing the thermal expansion coefficient.

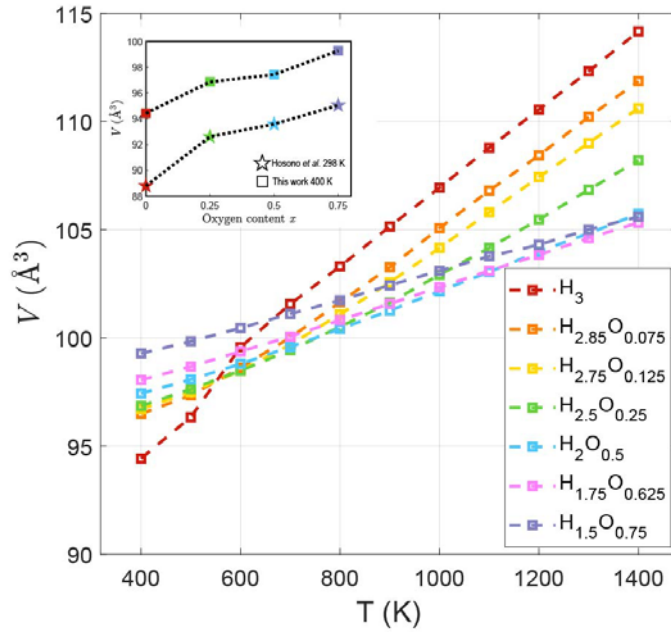


Figure 5.2 Evolution of unit-cell volumes for $\text{LaH}_{3-2x}\text{O}_x$ as calculated from MD calculations as a function of temperature and comparison with previous experimental results at 298 K [1].

Concerning pure LaH_3 and whatever the temperature (≥ 350 K), we observed no difference between the tetragonal and cubic structures, the tetragonal cell parameters becoming $a_{tetra} \times \sqrt{2} = a_{cubic}$, and $c_{tetra} = c_{cubic}$. Interestingly, both structures reflect the splitting of the H3/H4 sites in the tetragonal structure (H_{oct} in the cubic structure). We show in **Figure 5.3** the density map of two different planes for protons in LaH_3 at 600 K. We clearly observed the specific cubic shape (red area in **Figure 5.3**) of the H3/H4 block in the tetragonal structure and observed that these sites are more clearly resolved as temperature goes down. The measured distance between H3 and H4 in the diagonal of the H3/H4 cube is 1.43 \AA at 400 K, to be compared with the one 0.66 \AA and 0.76 \AA observed respectively from NMR and neutron diffraction at low and room temperature [14], [18]. At high temperature, H3 and H4 sites hardly can be distinguished, which impedes a further analysis of jumps in the tetragonal structure for this composition (as shown below). Below 250 K, none of the tetragonal or cubic cells allows describing the structure correctly since we can never relax the supercell to find a zero-pressure tensor.

Chapter V Hydride diffusion mechanism in $\text{LaH}_{3-2x}\text{O}_x$

This could be associated to a structural transition as reported in several previous works[13]. Nevertheless, the LaH_3 Debye temperature being 382 K[13], MD simulations at a lower temperature may also suffer some bias and unwanted atomic displacements.

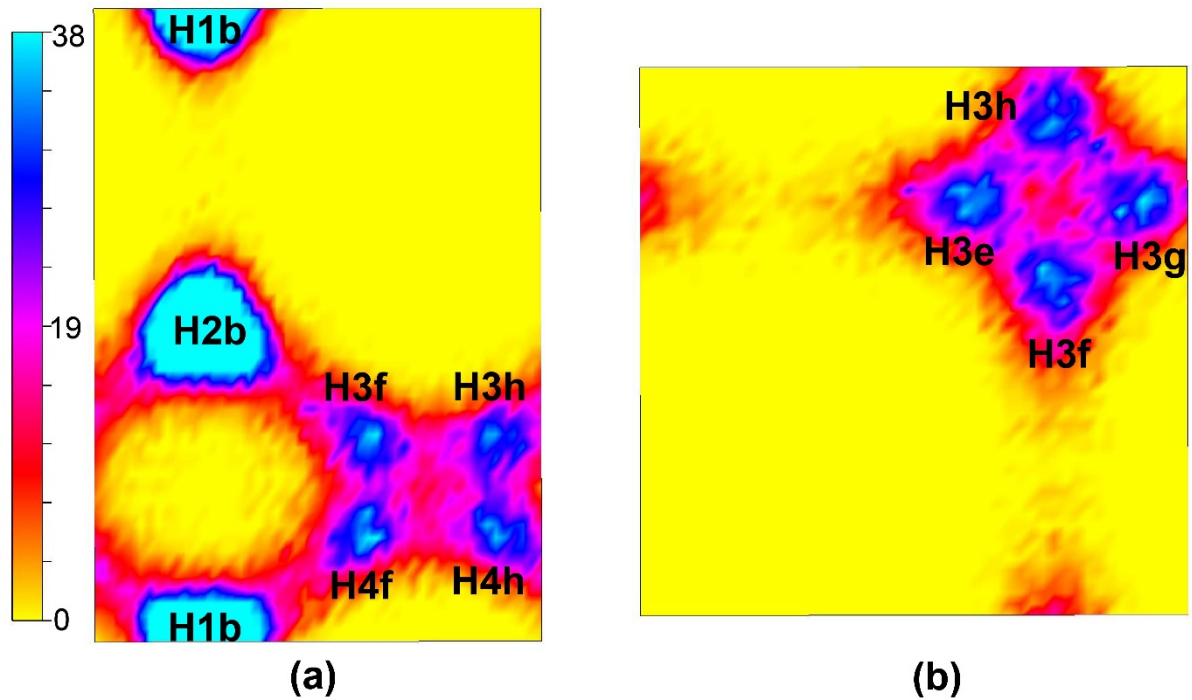


Figure 5.3 Density maps for hydride ions in tetragonal structure LaH_3 at 600 K (a) (1 0 0) plane (b) (0 0 1) plane.

The diffusion coefficient and the bulk conductivity of $\text{LaH}_{3-2x}\text{O}_x$ are shown in **Figure 5.4**. There exist no significant differences in the diffusion coefficient and activation energy among the different compositions. The migration activation energies range from 0.22-0.26 eV for x varying from 0 to 0.75. These calculated activation energies are in line with the previous results obtained from DFT calculations revealing H^- local migration energies from 0.04 to 0.2 eV. These values can also be compared to NMR results on pure LaH_3 showing a hydrogen relaxation activation energy of 0.14(1) eV [14] at $\sim 275\text{K}$. Similarly, an activation energy of 0.15(1) eV for long-range hydrogen diffusion was found in LaD_3 deduced from quasi-elastic neutron scattering [15].

Chapter V Hydride diffusion mechanism in $\text{LaH}_{3-2x}\text{O}_x$

Finally, the conductivities we deduced from MD simulation at 600 K are in the range $0.9\text{-}3.0 \text{ S.cm}^{-1}$ for $x = 0 - 0.75$, which are very close to the value 1.38 S.cm^{-1} at 607 K, reported previously and deduced from AIMD calculations.[1] This series of experimental and computational results nevertheless contrasts with the experimental conductivity measurements reported by Hosono *et al.*, showing much higher activation energy of 1.0-1.3 eV and an ionic conductivity at 600 K two orders of magnitude smaller.[1] This contradiction has already been discussed by Hosono *et al.*, who discarded the possibility of having measured grain boundary conductivity instead of bulk after performing high-pressure experiments. Some additional work seems necessary to lever such contradiction.

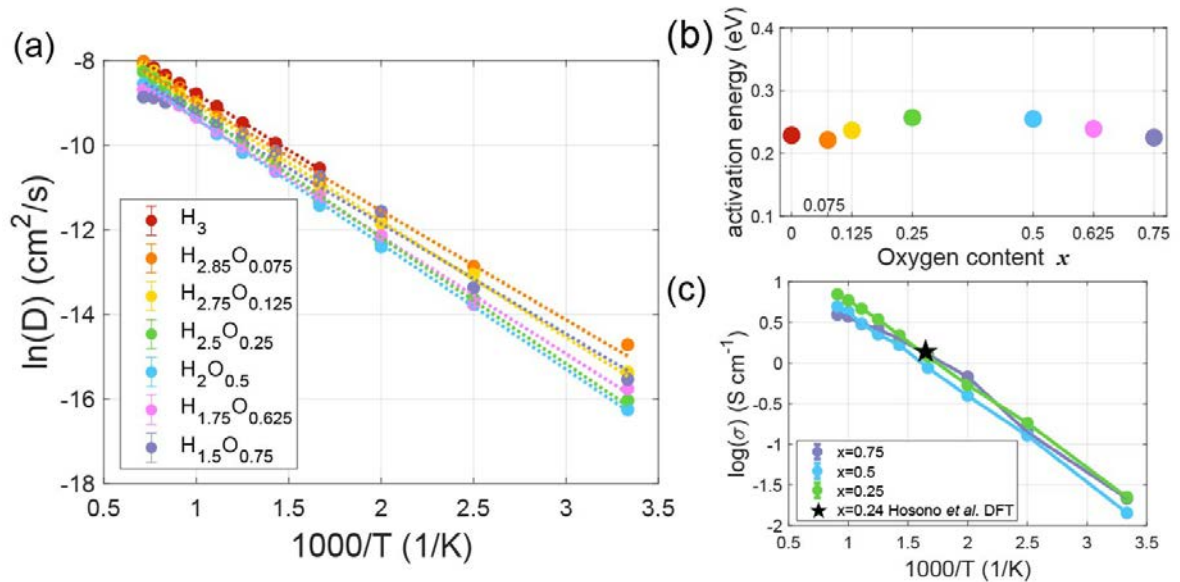


Figure 5.4 Evolution of hydride ion transport properties in $\text{LaH}_{3-2x}\text{O}_x$ (a) Hydride diffusion coefficient (b) activation energies (c) conductivity

After the NVE simulation, we obtain the trajectory coordinates of all H^- ions. These coordinates were then refolded into a one single unit-cell. We name this unit cell containing all the H^- coordinates: the “complete information cell”. A convex hull classification was used to associate each H^- to specific crystallographic sites, following a procedure presented in previous articles (see before). More than 95% of the hydride ions could be associated naturally to a given site, but when a hydride ion was found

Chapter V Hydride diffusion mechanism in $\text{LaH}_{3-2x}\text{O}_x$

outside any convex, it could be considered as interstitial and would then be associated to the nearest site. **Figure 5.1b** shows the complete information cell for $\text{LaH}_2\text{O}_{0.5}$ *i.e.*, $x = 0.5$ at 300 K. It also shows, through coloring, the clustering results after applying convex hull classification considering the tetragonal structure. Through convex hull classification, we could analyze the cluster association of one given H^- ion with time and thus obtain the precise trajectory of this ion from site to site. Such a fine description of hydride jumps is shown in **Table S5.1** for $\text{LaH}_2\text{O}_{0.5}$ (*i.e.* $x = 0.5$) at 300 K. From this table, the most frequent jumps are $\text{H2} \leftrightarrow \text{H3}$ and $\text{H3} \leftrightarrow \text{H3}$, representing 42.94% and 46.57% of the total number of jumps respectively. The proportions of $\text{H1} \leftrightarrow \text{H4}$, $\text{H3} \leftrightarrow \text{H4}$, and $\text{H4} \leftrightarrow \text{H4}$ are 3.00%, 5.28%, and 1.77%, respectively. The number of jumps involving the H1 site, where oxygen ions are substituting hydride ions, is thus the smallest. The energies barriers of $\text{H2} \leftrightarrow \text{H3}$ and $\text{H1} \leftrightarrow \text{H4}$ as calculated by Honoso *et al.* through DFT are 0.04 eV and 0.24 eV, respectively, confirming thus the potential predominance of $\text{H2} \leftrightarrow \text{H3}$ jumps.[1]

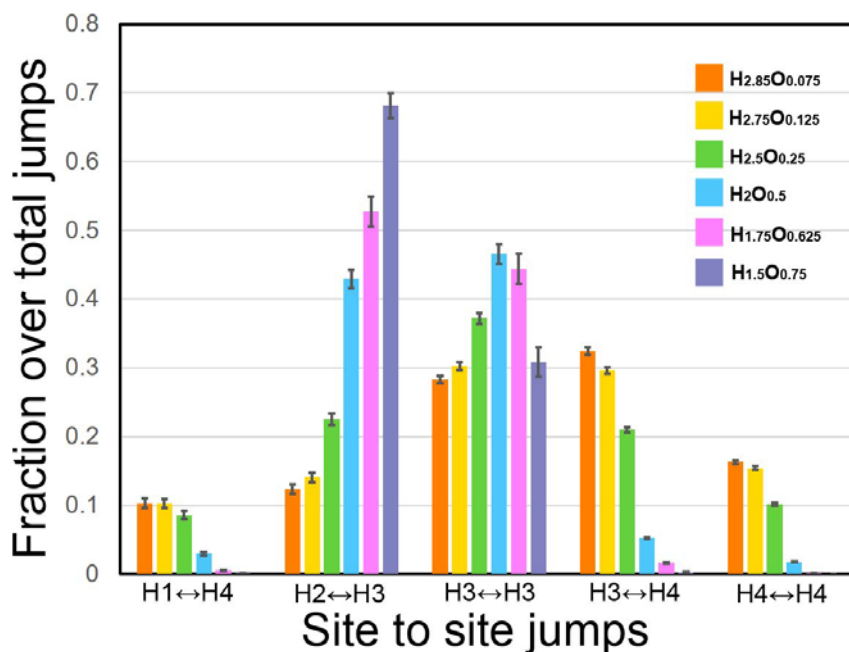


Figure 5.5 The fraction of different site jumps over the total jumps in different compositions at 300 K.

We calculated the jumps statistics of all partially substituted compositions, as shown in **Figure 5.5**. We observe that the relative proportion of jumps evolve drastically with

Chapter V Hydride diffusion mechanism in $\text{LaH}_{3-2x}\text{O}_x$

oxygen doping. The relative weight of jumps involving H1 and H4 sites is diminishing continuously with oxygen doping; On the opposite, while $\text{H3} \leftrightarrow \text{H3}$ jumps remain almost constant, $\text{H2} \leftrightarrow \text{H3}$ jumps are increasing strongly with oxygen doping. It seems from this analysis that the presence of oxygen atoms on H1 not only naturally impedes hydride ion to jump on this site but also repels hydride ions coming to the H4 site, which is close to O1/H1 site. This evolution of jumps frequency will induce a transition from a 3D diffusion to a 2D diffusion process as shown in the following.

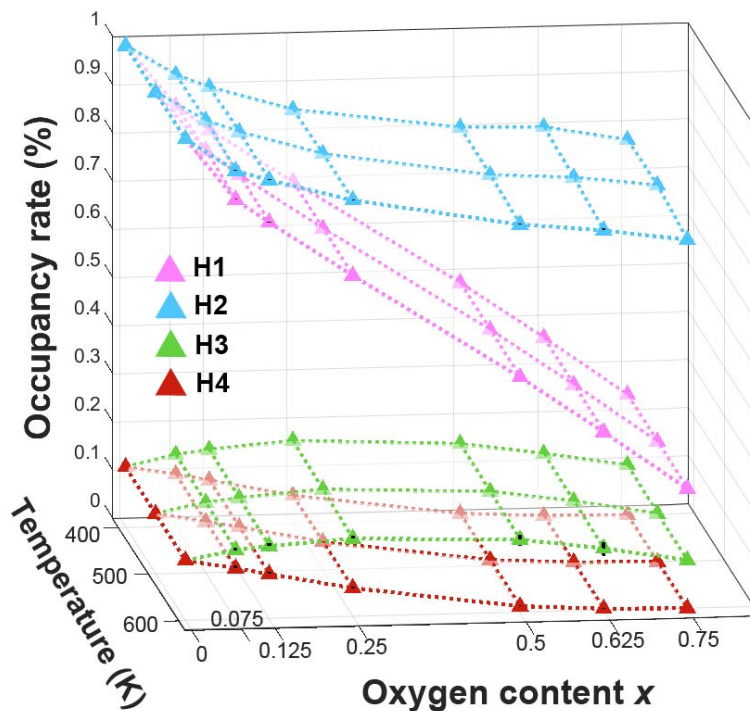
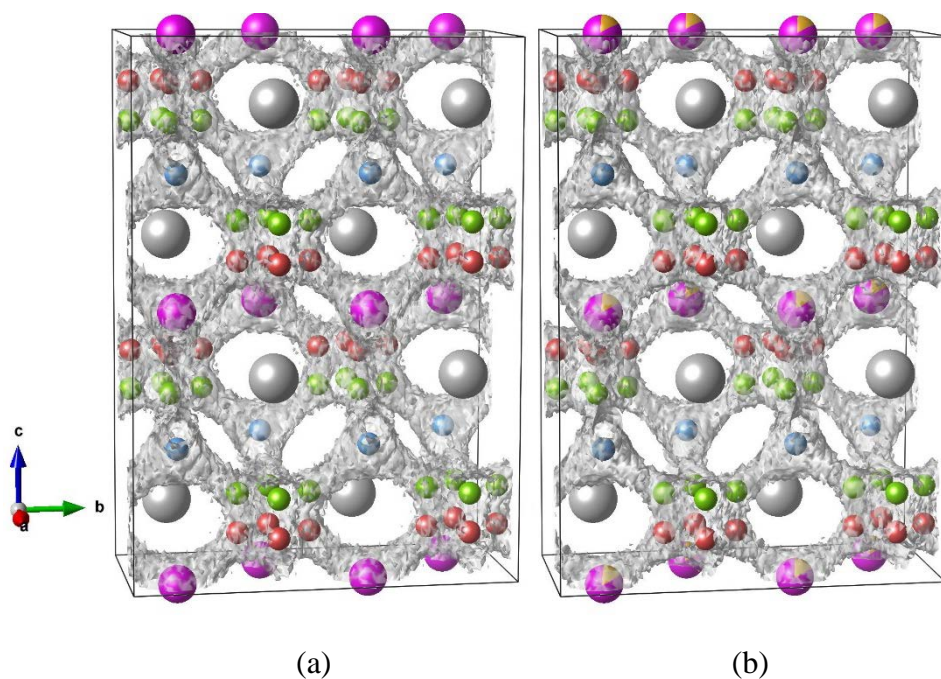


Figure 5.6 The occupancy rate of different sites by hydride ions as a function of temperature and composition.

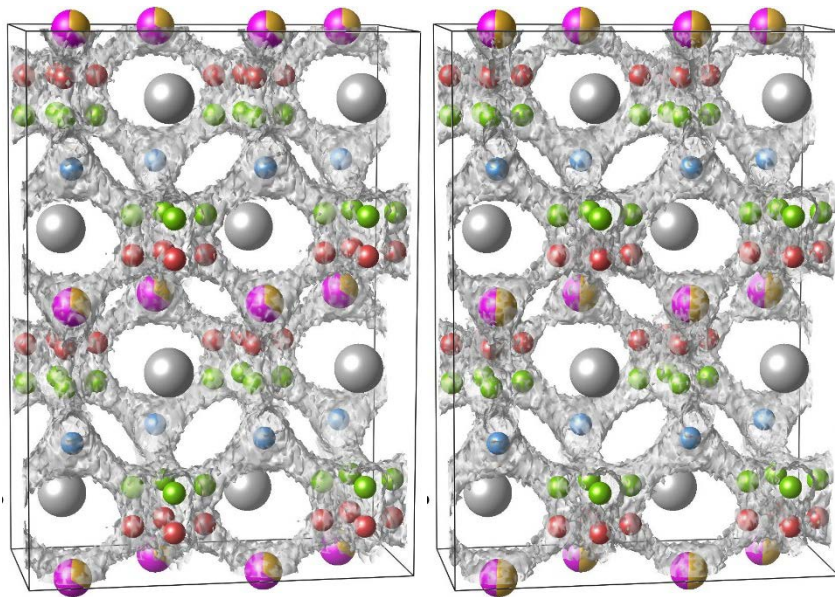
From the convex hull analysis, the site occupancy can also be determined as a function of temperature and oxygen content. O1/H1 occupancy by hydride ions is logically deeply affected by oxygen doping since O1 substitutes H1. The analysis (**Figure 5.6**) mainly reveals that the H2 site retains a relatively high occupancy rate. The most important information from this graph is that the H3 and H4 sites, which are equivalent

Chapter V Hydride diffusion mechanism in $\text{LaH}_{3-2x}\text{O}_x$

in LaH_3 , behave very differently as oxygen content increases. H4 site keeps a low occupancy rate, especially for $\text{LaH}_{1.5}\text{O}_{0.75}$, $\text{LaH}_{1.75}\text{O}_{0.625}$, and $\text{LaH}_2\text{O}_{0.5}$. The occupancy rates are almost zero, indicating that in these three compositions, the diffusion behaviour is limited along z -direction and mainly depends on H2 and H3 sites. Neutron diffraction refinements at 295 K showed that the occupancies of O1, H1, H2, H3, and H4 sites are 0.66(2) 0.343(2), 0.812(4), 0.107(1), and 0.063(1) in $\text{LaH}_2\text{O}_{0.5}$ respectively. This compares reasonably well with the results found here through MD calculations since the calculated occupancies of O1, H1, H2, H3, and H4 sites are 0.50, 0.343, 0.812, 0.107, and 0.063 respectively for the same temperature and composition. From **Figure 5.6**, we also observe that the presence of oxygen on O1/H1 site significantly affects the occupancy of H4 site. The double negative charge of oxygen ions probably repels hydride ions to come to H4 site, which combined with the concomitant presence of hydrogen vacancies with oxygen doping leads to an increase of H4 vacancies. It is also worth noting here that the occupancy rates hardly change with the change of temperatures.

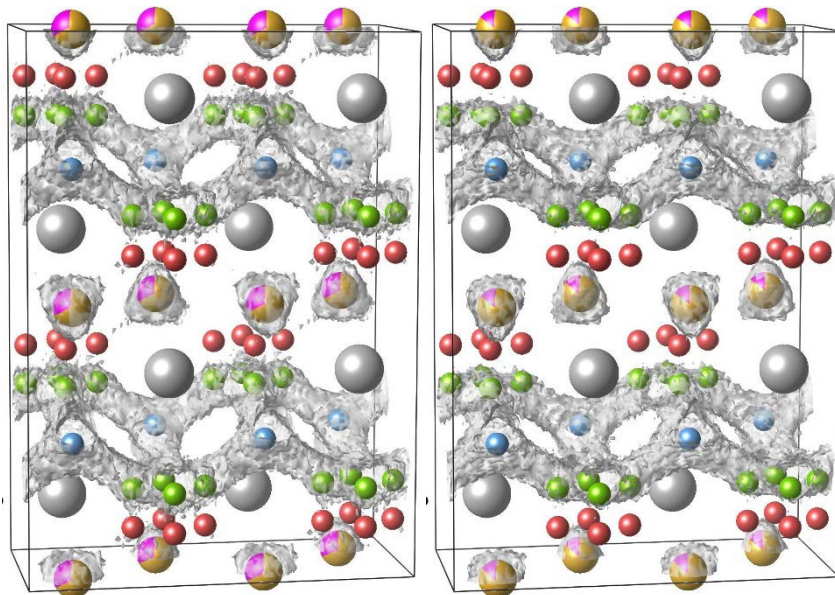


Chapter V Hydride diffusion mechanism in $\text{LaH}_{3-2x}\text{O}_x$



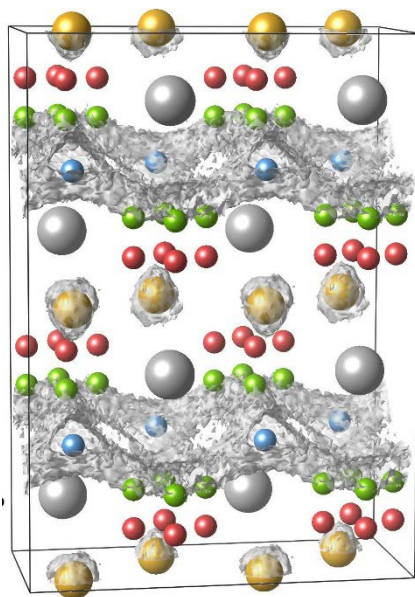
(c)

(d)



(e)

(f)



(g)

Figure 5.7 Hydride ion density maps showing the evolution from a 3D to a 2D diffusion process at 600K with increasing oxygen content in $\text{LaH}_{3-2x}\text{O}_x$ (a) LaH_3 (b) $\text{LaH}_{2.85}\text{O}_{0.075}$ (c) $\text{LaH}_{2.75}\text{O}_{0.125}$ (d) $\text{LaH}_{2.5}\text{O}_{0.25}$ (e) $\text{LaH}_2\text{O}_{0.5}$ (f) $\text{LaH}_{1.75}\text{O}_{0.625}$ (g) $\text{LaH}_{1.5}\text{O}_{0.75}$. The H1/O ion was represented with pink/orange color.

This general behaviour of hydride ions upon oxygen content increase is confirmed by the analysis of residence time. With the help of convex hull classification, we can find out how many hydrides have visited one given H^- site, and how long each ion stayed at this site. The cumulative distribution function (CDF) of the residence time can be obtained by the Gaussian kernel density estimation with automatic determination of the kernel bandwidth.[19] The CDFs of the residence time of different H^- sites are shown in **Figure S5.1**. The faster the CDF curve approaches 1, the shorter the time in this site. For H3 and H4 sites, for any composition, CDF curves will reach 1 quickly, reflecting their transfer station roles. For H1 site, the residence time tends to increase with oxygen content, showing that hydride ions on H1 are participating less and less to the diffusion process. For H2 site, we observe just the opposite *i.e.*, the CDF curve tends faster to 1, indicating that H2 will play a major role in the diffusion process for high oxygen

contents.

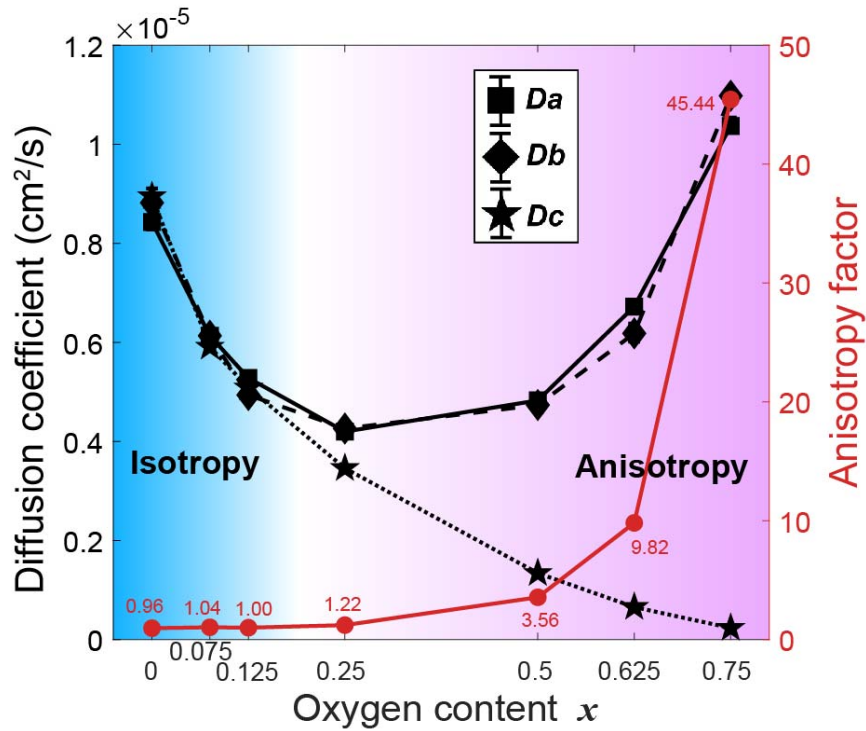


Figure 5.8 Diffusion coefficients along a , b , and c axes, and resulting anisotropy factor in $\text{LaH}_{3-2x}\text{O}_x$ at 600 K

All these aspects (occupancy, residence time, jumps) will naturally change the nature of the diffusion process, reflecting the impeding of the transfer of hydride ions along the c axis. We plot in **Figure 5.7** The density maps of hydride ions for all compositions at 600 K. The evolution from a 3D to a 2D process is clearly put into evidence. We also quantify the anisotropy factor by measuring the ratio between $\frac{D_{100}+D_{010}}{2}$ and D_{001} along (a), (b), and (c) directions, respectively. This anisotropy factor is plotted in **Figure 5.8** and reaches a value of 48 for $x = 0.75$.

V.4 Conclusion

In the present study, we adopted molecular dynamic simulations to model the $\text{LaH}_{3-2x}\text{O}_x$ using interatomic H^- potential developed in a previous study. This potential can produce reasonably many features observed experimentally. In particular, we observe

Chapter V Hydride diffusion mechanism in $\text{LaH}_{3-2x}\text{O}_x$

that oxygen doping induces a tetragonal distortion of the original cubic cell and also observe that this doping has important consequences on the hydride ion diffusion mechanism. As a whole, pure and doped $\text{LaH}_{3-2x}\text{O}_x$ all present a very high hydride ion diffusion coefficient with activation energies in the range 0.22-0.26 eV for x changing from 0 to 0.74. The presence of oxygen ions on O1/H1 site is shown to affect the distribution of hydride ions atoms by repelling them far away from O1/H1 site. The main consequence is that the hydride ion diffusion process switches from a 3D to a 2D process. This could potentially limit the diffusion coefficient, but the additional effect of hydride ion vacancies compensate in great part the loss of pathways due to oxygen doping.

V.5 Notes and references

- [1] K. Fukui *et al.*, “Characteristic fast H^- ion conduction in oxygen-substituted lanthanum hydride,” *Nat. Commun.*, vol. 10, no. 1, pp. 1–8, 2019.
- [2] H. Ubukata *et al.*, “Hydride Conductivity in an Anion-Ordered Fluorite Structure LnHO with an Enlarged Bottleneck,” *Chem. Mater.*, vol. 31, no. 18, pp. 7360–7366, 2019.
- [3] T. Yamamoto *et al.*, “The role of π -blocking hydride ligands in a pressure-induced insulator-to-metal phase transition in SrVO_2H ,” *Nat. Commun.*, vol. 8, no. 1, 2017.
- [4] Y. Kobayashi *et al.*, “An oxyhydride of BaTiO_3 exhibiting hydride exchange and electronic conductivity,” *Nat. Mater.*, vol. 11, no. 6, pp. 507–511, 2012.
- [5] A. Pishtshev and E. Strugovshchikov, “Computational Prediction of Ferro- and Piezoelectricity in Lead-Free Oxyhydrides $\text{Ln}_2\text{H}_4\text{O}$ ($\text{Ln} = \text{Y}, \text{La}$) ,” *Adv. Theory Simulations*, vol. 2, no. 12, p. 1900144, 2019.
- [6] Y. Iwasaki *et al.*, “Synthesis, crystal structure, and ionic conductivity of hydride

Chapter V Hydride diffusion mechanism in $\text{LaH}_{3-2x}\text{O}_x$

- ion-conducting Ln_2LiHO_3 ($\text{Ln} = \text{La}, \text{Pr}, \text{Nd}$) oxyhydrides,” *J. Mater. Chem. A*, vol. 6, no. 46, pp. 23457–23463, 2018.
- [7] C. Tassel *et al.*, “High-Pressure Synthesis of Manganese Oxyhydride with Partial Anion Order,” *Angew. Chemie - Int. Ed.*, vol. 55, no. 33, pp. 9667–9670, 2016.
- [8] S. Cornelius *et al.*, “Oxyhydride Nature of Rare-Earth-Based Photochromic Thin Films,” *J. Phys. Chem. Lett.*, vol. 10, no. 6, pp. 1342–1348, 2019.
- [9] X. Liu, T. S. Bjørheim, and R. Haugsrud, “Formation of defects and their effects on hydride ion transport properties in a series of K_2NiF_4 -type oxyhydrides,” *J. Mater. Chem. A*, vol. 6, no. 4, pp. 1454–1461, 2018.
- [10] Ø. S. Fjellvag, J. Armstrong, W. A. Sławiński, and A. O. Sjøstad, “Thermal and Structural Aspects of the Hydride-Conducting Oxyhydride La_2LiHO_3 Obtained via a Halide Flux Method,” *Inorg. Chem.*, vol. 56, no. 18, pp. 11123–11128, 2017.
- [11] Ø. S. Fjellvåg, K. H. Nygård, P. Vajeeston, and A. O. Sjøstad, “Advances in the LiCl salt flux method and the preparation of phase pure $\text{La}_{2-x}\text{Nd}_x\text{LiHO}_3$ ($0 \leq x \leq 2$) oxyhydrides,” *Chem. Commun.*, vol. 55, no. 26, pp. 3817–3820, 2019.
- [12] H. Harb, L. M. Thompson, and H. P. Hratchian, “On the linear geometry of lanthanide hydroxide (Ln-OH , $\text{Ln} = \text{La-Lu}$),” *Phys. Chem. Chem. Phys.*, vol. 21, no. 39, pp. 21890–21897, 2019.
- [13] K. Kai, K. A. Gschneidner, Jr, B. J. Beaudry, and D. T. Peterson, “Heat capacities of LaD_x and LaH_x ($1.9 \leq x \leq 3.0$) from 1 to 300 K,” *Phys. Rev. B*, vol. 40, no. 10, pp. 6591–6600, 1989.
- [14] R. G. Barnes, B. J. Beaudry, D. R. Torgeson, C. T. Chang, and R. B. Creel, “Hydrogen hopping rates and the order-disorder transitions in sub-stoichiometric lanthanum trihydride,” *J. Alloys Compd.*, vol. 253–254, pp. 445–448, 1997.
- [15] T. J. Udovic, Q. Huang, C. Karmonik, and J. J. Rush, “Structural ordering and

Chapter V Hydride diffusion mechanism in LaH_{3-2x}O_x

- dynamics of LaH_{3-x},” *J. Alloys Compd.*, vol. 293, pp. 113–117, 1999.
- [16] P. Hirel, “Atomsk: A tool for manipulating and converting atomic data files,” *Comput. Phys. Commun.*, vol. 197, pp. 212–219, 2015.
- [17] I. T. Todorov, W. Smith, K. Trachenko, and M. T. Dove, “DL_POLY_3: New dimensions in molecular dynamics simulations via massive parallelism,” *J. Mater. Chem.*, vol. 16, pp. 1911–1918, 2006.
- [18] J.J.Didisheim, K.Yvon, P.Fischer, W.Halg, and L.Schlapbach, “Neutron diffraction evidence for a structural phase transformation,” *Phys. Lett.*, vol. 78, no. 1, pp. 111–114, 1980.
- [19] Z. I. Botev, J. F. Grotowski, and D. P. Kroese, “Kernel density estimation via diffusion,” *Ann. Stat.*, vol. 38, no. 5, pp. 2916–2957, 2010.

V.6 Supporting information

Departure site

	H4a	H4b	H4c	H4d	H3a	H3b	H3c	H3d	H4e	H4f	H4g	H4h	H3e	H3f	H3g	H3h	H2a	H2b	H1a	H1b
H4a	899	76	4	22	200	38	2	10	0	0	0	0	0	0	0	0	0	4	1	99
H4b	79	480	25	11	18	97	18	1	0	0	0	0	0	0	0	0	1	2	77	4
H4c	1	28	601	46	2	34	122	19	0	0	0	0	0	0	0	0	0	4	1	29
H4d	29	11	34	519	11	3	32	136	0	0	0	0	0	0	0	0	1	2	149	0
H3a	203	25	1	11	14330	1341	242	1501	0	0	0	0	0	0	0	2	60	1375	0	6
H3b	34	93	40	2	1315	10862	1475	252	0	0	0	0	1	0	0	0	851	85	1	2
H3c	1	18	122	25	259	1496	13156	1006	0	0	0	0	1	0	0	0	45	1329	1	5
H3d	11	1	18	141	1501	229	1013	10664	0	0	0	0	2	0	0	0	1128	62	9	2
H4e	0	0	0	0	0	0	0	0	1135	60	6	99	175	9	3	18	3	2	38	4
H4f	0	0	0	0	0	0	0	0	53	777	6	18	13	37	5	2	0	2	0	102
H4g	0	0	0	0	0	0	0	0	6	6	640	68	2	5	124	18	5	1	69	4
H4h	0	0	0	0	0	0	0	0	94	15	67	1092	17	1	28	70	3	1	1	71
H3e	0	0	0	0	0	0	0	3	183	10	2	12	12761	1236	180	1195	1296	35	2	0
H3f	0	0	0	0	1	0	0	0	9	41	4	0	1253	12920	1606	237	46	921	0	0
H3g	0	0	0	0	0	0	0	0	2	3	132	28	171	1605	13134	1098	1190	44	13	1
H3h	0	0	0	0	1	0	0	0	18	1	13	72	1181	257	1084	12120	44	1326	0	3
H2a	1	1	0	2	62	845	58	1122	4	0	3	2	1304	42	1185	44	82880	18	1	0
H2b	4	3	4	1	1386	74	1336	55	0	1	0	1	40	916	62	1307	13	81387	0	1
H1a	1	76	2	148	1	1	0	12	38	2	73	0	1	0	12	0	0	0	52235	4
H1b	100	1	35	0	9	0	2	0	5	99	3	67	1	2	2	3	0	3	7	52526

Table S5.1 The number of jump between two different site in LaH_{3-2x}O_x x=0.5 at 300K.

The jumps mainly happen in O2↔O3 and O3↔O3 pairs which are highlighted in blue and green square respectively.

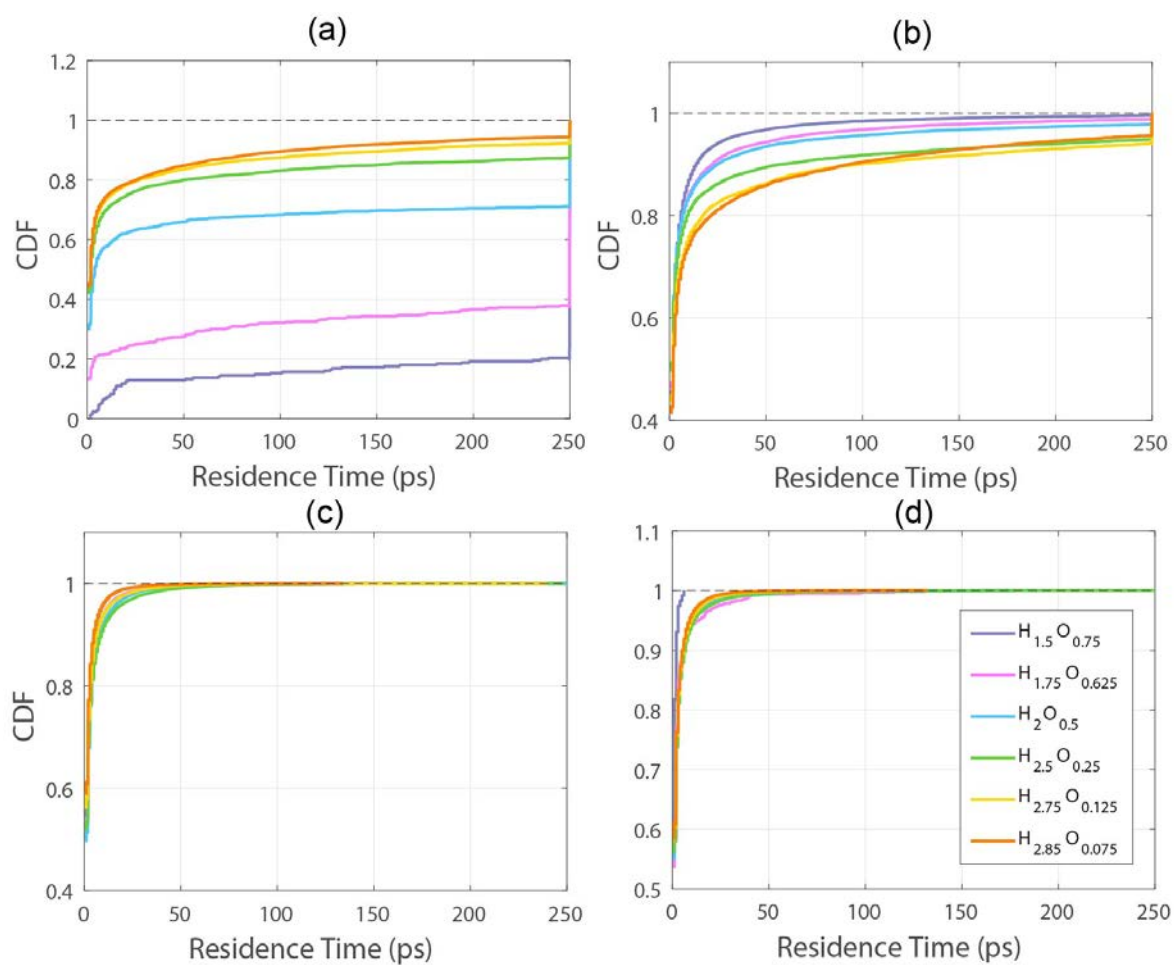
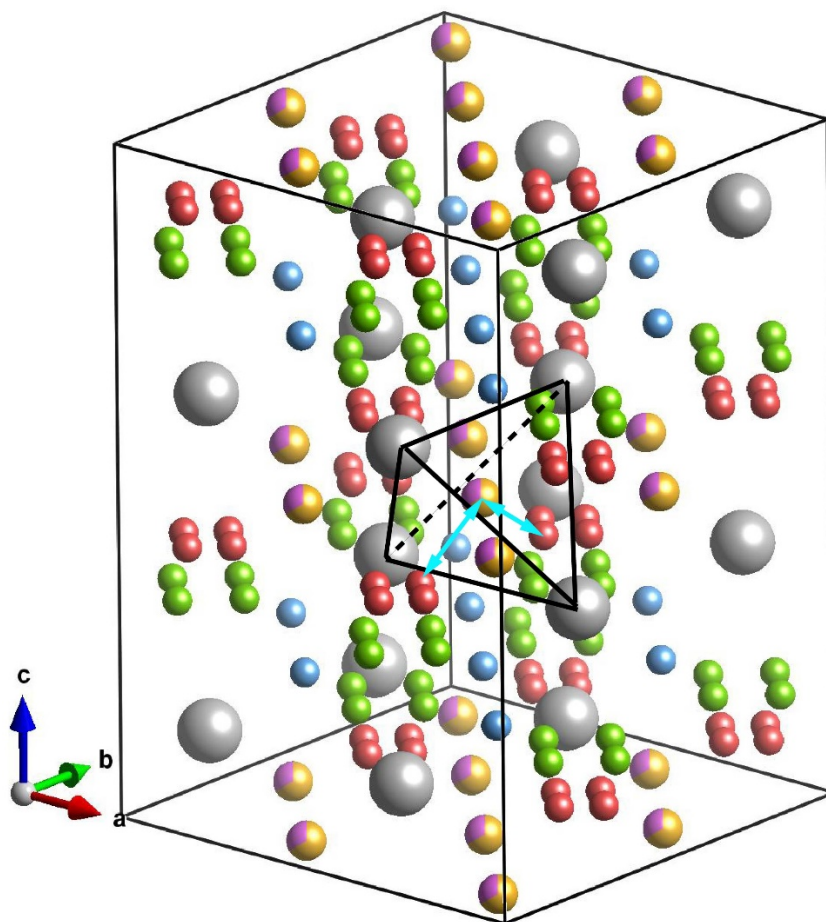
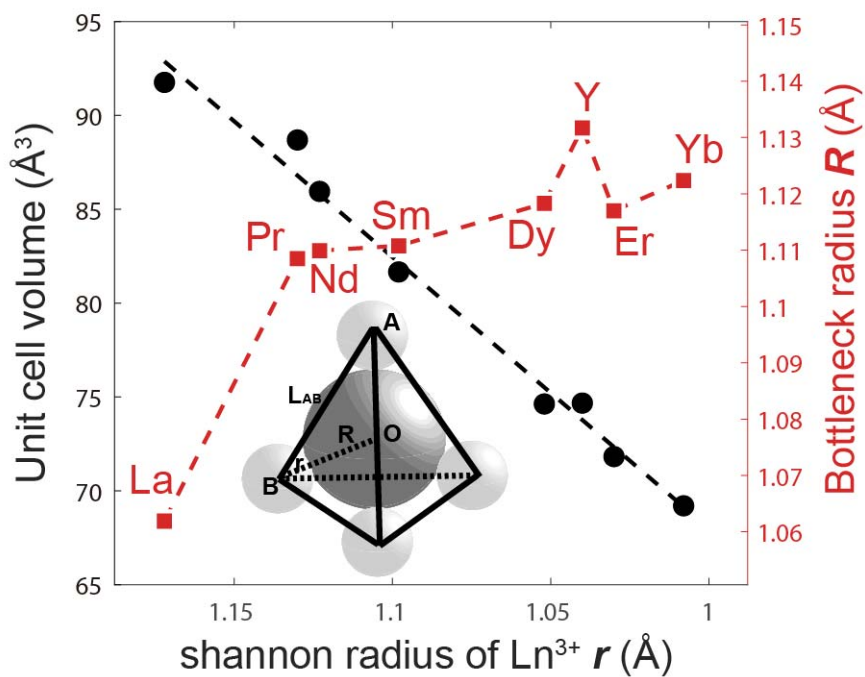


Figure S5.1 Cumulative distribution function of hydride residence time at different hydride site in $\text{LaH}_{3-2x}\text{O}_x$ at 300K. (a) H1 site (b) H2 site (c) H3 site (d) H4 site.



(a)



(b)

Chapter V Hydride diffusion mechanism in $\text{LaH}_{3-2x}\text{O}_x$

Figure S5.2 (a) In $2 \times 2 \times 2$ $\text{LaH}_{3-2x}\text{O}_x$ supercell, one regular tetrahedron was represented with four La vertices and H1 is the center of this regular tetrahedron. The blue arrows represent two diffusion paths of $\text{H1} \leftrightarrow \text{H4}$. The diffusion path correspond to the bottleneck radius of this regular tetrahedron. The legend is same to **Figure 5.1**. **(b)** The unit cell volume and the bottleneck radius as a function of Ln shannon radius in $\text{LnH}_2\text{O}_{0.5}$ (Ln= La, Pr, Nd, Sm, Dy, Y, Er, Yb). Schematic diagram of bottleneck radius is also presented, A and B ion is the Ln ion, r is the radius of Ln ion, R is the bottleneck radius.

For calculating the bottleneck radius, Density Functional Theory (DFT) calculations were performed using the Projector Augmented-Wave (PAW) approach implemented in the Vienna Ab initio Simulation Package (VASP).[2] All calculations were performed using the Perdew–Burke–Ernzerhof (PBE) generalized-gradient approximation (GGA) functional.[3] The systems were $\text{LnH}_2\text{O}_{0.5}$ with the supercell containing 16 Ln, 32 H and 8 O respectively. The plane wave cutoff energies were set to 800 eV, and integration in reciprocal space was performed with $2 \times 2 \times 2$ Monkhorst-Pack k-point meshes. Structural optimizations were conducted with full degrees of freedom relaxation (cell volume, cell shape, and atomic positions) using a conjugate gradient algorithm, converging forces to 10^{-5} eV/Å and electronic energies to 10^{-6} eV.

Notes and references

- [1] K. Fukui *et al.*, “Characteristic fast H^- ion conduction in oxygen-substituted lanthanum hydride,” *Nat. Commun.*, vol. 10, no. 1, pp. 1–8, 2019.
- [2] P. E. Blöchl, *Phys. Rev. B*, 1994, **50**, 17953.
- [3] G. Kresse and J. Hafner, *Phys. Rev. B*, 1993, **47**, 558.

Chapter VI General Conclusion

This work consists of four parts. Each part is based on one new ion conductor, and the associated anion diffusion mechanism is studied mainly by Classical Molecular dynamic (MD) simulations with/without Density functional theory calculations. Each material has been systematically investigated as a potential promising fast ion conductor.

The Chapter 2 focuses on the diffusion mechanism of the acceptor-doped NdBaInO₄ compound. The most important innovation of this part is that we propose two classification methods (convex hull classification method (CHC) and Density-based spatial clustering of applications with noise (DBSCAN)) to associate the trajectories of oxygen ion to specific crystallographic sites. Based on the residence site of each oxygen ion in every trajectory step, amounts of useful information can be shown, *i.e.*, the mean occupancy of each oxygen site, the jump rates from site to site, the oxygen ion diffusion path, and the residence time analysis. These two methods can be extended to all ion-conductors for detecting the diffusion bottlenecks and fast diffusion routes, which will help to design new fast-ion conductors. Nd_{1-x}AE_xBaInO_{4-x/2} (AE=Ca, Sr, Ba) compounds with four different oxygen sites have been chosen as an example to verify the feasibility of these two classification methods. The calculation results show that: The addition of Ca element hardly changes the lattice parameter of pure NBIO, while the lattice distortion of Ba-doped NBIO is the largest. The diffusion coefficients are $D_{Ca(O)} > D_{Sr(O)} > D_{Ba(O)}$, indicating that Ca is the most favorable doping element while Ba is the worst. Four different oxygen sites (O1 to O4) are shown to play different roles in the diffusion process. We could classify these oxygen sites in the function of their participation in the diffusion process as $O3 \approx O4 > O1 \gg O2$. The MSD curves, site occupancy rate, site-to-site jumps, and residence analysis can all describe the differences between these four sites. Specially, the activation migration enthalpies $\Delta H_{O3 \rightarrow O3}$, $\Delta H_{O3 \rightarrow O4}$ and $\Delta H_{O4 \rightarrow O4}$ are calculated to be 0.186 eV, 0.227 eV, and

Chapter VI General Conclusion

0.233 eV respectively, which are lower than $\Delta H_{O1 \rightarrow O3}$ 0.769 eV and $\Delta H_{O1 \rightarrow O4}$ 0.793 eV. A main and a secondary diffusion paths were thus proposed. For the main diffusion path, ions migrate along the **b** and **c** directions on O3 and O4 sites. For the secondary diffusion path, a small proportion of O1 sites will interact with the O3 and O4 sites. The diffusion is limited along the **a** direction due to the O2 barrier sites. This work shows that the proposed approach can deal with complex diffusion mechanisms and can thus be extrapolated to other compounds. The followed three parts all adopt these two methods to analyze the ion trajectories.

In Chapter 3, the oxygen diffusion mechanism in donor-doped NdBaInO₄ compound (NdBaIn_{1-x}M_xO_{4+x/2} (M=Ti, Zr)) was described. We used the Bond Valence Summation (BVS) calculation to locate the possible oxygen interstitial position (*4e* site [0.575 0.750 0.893]). Furthermore, Molecular dynamics simulations were performed and DBSCAN was adopted to associate precisely oxygen ions to specific crystallographic sites. The interstitial oxygen ion Wyckoff position calculated by MD is (*4e* site [0.577 0.757 0.896]), confirming the results BVS calculation. An analysis routine similar to that of chapter 2 was adopted allowing to describe the lattice cell parameters, the macroscopic diffusion coefficients, the activation energy of self-diffusion, the jump rates from site to site, the oxygen ion diffusion path, and the residence time analysis. An interstitialcy mechanism was demonstrated in the temperature range 1500 K-1900 K. Oxygen sites were shown to participate differently to the oxygen diffusion process. Oxygen interstitials O_i play a major role in connecting the two participant sites, O3 and O4, while O1 and O2 do not play any role. Oxygen diffusion is shown to occurs entirely in the **b-c** plane.

In Chapter 4, we have developed a new interatomic potential in the La-H-O system, which can model the lanthanide oxyhydrides LaHO accurately. The potential consists of a long-range Coulomb term and a short-range Buckingham term based on partial charges, and it is derived by fitting lattice parameters and elastic tensors of α -LaHO, β -

Chapter VI General Conclusion

LaHO, La₂O₃, and LaH₃ calculated by DFT calculation. The potential can also reproduce the structural and elastic properties of the high-pressure form of Lanthanum oxyhydrides, namely γ -LaHO and δ -LaHO and the experimental evolution of cell parameters. After this development, the hydride ion diffusion mechanism of α -LaHO and β -LaHO were studied using this new potential, together with DFT calculations. For pure α -LaHO, two different steps in the diffusion process were identified, the first one induced by a cooperative motion of hydride ions within a unit block, the second one leading to a jump between the same hydride-ions unit blocks. As a whole, the long-range diffusion is highly anisotropic, occurring mainly along with *a* and *b* directions. In pure β -LaHO, each hydride site has its attached interstitial site that plays a key role in H⁻ diffusion. Finally, the influence of potential defects on hydride ion diffusion properties was analyzed. Adding a small number of anionic defects may significantly alter the diffusion mechanism leading to much lower diffusion activation energies.

In Chapter 5, we adopted the interatomic La-H-O potential produced in chapter 4 to model the LaH_{3-2x}O_x. This new material shows good performance concerning H⁻ conduction and is considered as the new promising oxyhydride for energy devices. Our potentials can reproduce the experimental crystalline data correctly. The self-diffusion activation energy of H⁻ in this series of compounds ranges from 0.22-0.26 eV with *x* changing from 0 to 0.75. As the oxygen content increases, the original diffusion mechanism involving all sites changes progressively, and for high oxygen contents, hydride ions diffusions involve only the four H3 and the H2 sites, while H1/O1 site represents a barrier for hydride ion diffusion. Besides, due to the repulsive effect of oxygen ions on H1/O1 site, with the increase of oxygen ions, there are fewer and fewer hydrogen H⁻ in the H4 position and the role of H4 in diffusion becomes less and less important. As a result, as oxygen content increases, the diffusion of hydrogen ions becomes highly anisotropic even if keeping a high value of diffusion coefficient.

As a whole, our study constitutes a valuable work, as it exposes to the scientific community methodological aspects for the analysis of MD trajectories and applied

Chapter VI General Conclusion

them to NdBaInO₄ based compounds, as it develops for the first time a new potential for oxyhydrides, as it explains long-range diffusion mechanisms in several compositions of high relevance for the scientific community namely LaHO and LaH_{3-2x}O_x.

Titre : Mécanismes de diffusion d'ions dérivés de simulations atomiques dans des conducteurs superioniques

Mots clés : dynamique moléculaire; DFT; Conducteurs d'ions oxygène; Oxyhydrides; Mécanisme de diffusion ionique.

Résumé : L'objectif principal de cette thèse est d'étudier le mécanisme de diffusion anionique dans divers matériaux en utilisant la simulation par dynamique moléculaire et les calculs ab initio.

nous présentons deux chapitres traitant de l'influence du dopage aliovalent dans la phase NdBaInO_4 . Dans le chapitre 2, nous étudions les composés $\text{Nd}_{1-x}\text{AE}_x\text{BaInO}_{4-x/2}$ ($\text{AE} = \text{Ca}, \text{Sr}, \text{Ba}$) et nous déterminons précisément le mécanisme de diffusion de la lacune d'oxygène. Dans le chapitre 3, nous suggérons que la diffusion de l'oxygène dans les composés $\text{NdBaIn}_{1-x}\text{M}_x\text{O}_{4+x/2}$ ($\text{M}=\text{Ti}, \text{Zr}$) dits « dopé donneur » est basée sur un mécanisme de diffusion interstitielle. Dans le chapitre 4, nous avons tout d'abord calculé les structures cristallines et les tenseurs élastiques des six matériaux α -LaHO, β -LaHO, γ -LaHO, δ -LaHO, La_2O_3 et LaH_3 par des calculs de premier principe.

Ensuite, nous avons créé un nouveau champ de

force pour le système La-H-O en ajustant les informations issues des calculs DFT. Les nouveaux champs de force créés ont été adoptés pour explorer le mécanisme de diffusion des deux formes les plus stables de LaHO (α -LaHO, β -LaHO). Les résultats de dynamique moléculaire fournissent des informations importantes sur les chemins et mécanismes de diffusion dans ces deux matériaux. Par ailleurs, le champ de force développé fournit potentiellement un outil de recherche puissant pour d'autres oxyhydrides de lanthanides. Au chapitre 5, nous avons étudié la famille $\text{LaH}_{3-2x}\text{O}_x$ en nous basant sur les potentiels interatomiques développés au chapitre 4. Nous prouvons que l'incorporation d'ions oxygène affecte fortement le mécanisme de diffusion des ions hydrides, le rendant hautement anisotrope. Enfin, le chapitre 6 résume les conclusions les plus pertinentes tirées de ce travail.

Title : Ion diffusion mechanisms derived from atomic simulations in fast ion conductors

Keywords : Molecular dynamic simulation; DFT; Oxygen-ion conductors; Oxyhydrides; Ion diffusion mechanism.

Abstract : The main purpose of this thesis is to study the anion diffusion mechanism of various materials by using molecular dynamics simulation and first-principles calculations.

We present two chapters dealing with the influence of aliovalent doping in NdBaInO_4 . In chapter 2, we study $\text{Nd}_{1-x}\text{AE}_x\text{BaInO}_{4-x/2}$ ($\text{AE} = \text{Ca}, \text{Sr}, \text{Ba}$) and we determine precisely the oxygen vacancy diffusion mechanism. In chapter 3, we suggest that the oxygen diffusion in donor-doped $\text{NdBaIn}_{1-x}\text{M}_x\text{O}_{4+x/2}$ ($\text{M}=\text{Ti}, \text{Zr}$) is based on an interstitial diffusion mechanism. In chapter 4, firstly, we calculated the crystal structures and the elastic tensors of the six materials α -LaHO, β -LaHO, γ -LaHO, δ -LaHO, La_2O_3 , and LaH_3 through first-principle calculations.

Secondly, we created a new force field for the La-H-O system by fitting DFT information. The new-born force fields were further adopted to explore the diffusion mechanism of the two most stable forms in the LaHO family (α -LaHO, β -LaHO). The results show that the force field provides important information about diffusion pathways in both materials. This force field potentially provides a powerful research tool for lanthanide oxyhydrides. In chapter 5, we studied the $\text{LaH}_{3-2x}\text{O}_x$ family based on the interatomic potentials developed during chapter 4. We prove that the incorporation of oxygen ions strongly affects the hydride ion diffusion mechanism, making it highly anisotropic. Finally, chapter 6 summarizes the most relevant conclusions derived in this work.